FACULTY
OF MATHEMATICS
AND PHYSICS
Charles University

DOCTORAL THESIS

Kateřina Pleiner Sládková

Tidally induced deformation of icy moons

Department of Geophysics

Supervisor of the doctoral thesis: RNDr. Ondřej Souček, Ph.D.
Study programme: Physics
Study branch: Physics of the Earth and Planets

Prague 2023

I declare that I carried out this doctoral thesis independently, and only with the cited sources, literature and other professional sources. It has not been used to obtain another or the same degree.

I understand that my work relates to the rights and obligations under the Act No. 121/2000 Sb., the Copyright Act, as amended, in particular the fact that the Charles University has the right to conclude a license agreement on the use of this work as a school work pursuant to Section 60 subsection 1 of the Copyright Act.

In .... date ....

Author's signature

Mamince,
protože bez ní by bylo všechno těžší, ne-li nemožné.

First of all, I would like to thank my family; almost nothing would be possible without them. My mom, for being my biggest fan no matter what, and for the endless babysitting, without which I would have never finished my dissertation. To my dad for his material support, without which I wouldn't have even started my studies. To my siblings for knowing how to make fun of me at the right time so that I never take myself too seriously. To Míša for the neverending discussions and IT support. To Štěpán for coming in time so that I wouldn't go crazy and to Kuba for putting up with me through it all.

Next, I would like to thank my supervisor, Ondřej Souček, for being the best supervisor one could ask for and for his endless help and patience (with my stupid mistakes and forgetfulness).

Additionally, I thank all my fellow office cohabitants mainly for their friendship and valuable advice, but also for other menial tasks such as watering the flowers and scanning forgotten materials during home offices. I also thank František Galovlič for providing the 1D code for computing the spring slider model with the rate and state friction model and Klara Kalousová for supplying the code for the europan models and the practical advice. And thanks to the entire Geophysical department for the pleasant working environment (despite the crazy heat).

Last but not least, a huge shout out to Kasárna Karlín for the chance to celebrate all the partial successes and hopefully the last one, too.

This research received funding from projects Charles University (namely GA UK with project number 304217 and SVV, project numbers: SVV-2018-260447, SVV-2019-260447 and SVV 115-09/260581) and the Czech Science Foundation through projects No. 19-10809S and No. 22-20388S. The work was supported by The Ministry of Education, Youth and Sports from the Large Infrastructures for Research, Experimental Development and Innovations project IT4Innovations National Supercomputing Center—LM2018140, and by the Charles University project SVV 115-09/260581.

Title: Tidally induced deformation of icy moons

Author: Kateřina Pleiner Sládková

Department: Department of Geophysics

Supervisor: RNDr. Ondřej Souček, Ph.D., Mathematical Institute of Charles University

Abstract: Within this Ph.D. project, we have developed and validated a modeling methodology for the evaluation of the influence of friction in regional and global models of tidal deformation in icy bodies. We focus on the role of friction in two specific scenarios: (i) strike-slip faults within Europa's ice shell (expanding the model by Kalousová et al. (2016)), and (ii) the frictional behavior of fault system known as 'tiger stripes' at the south pole of Enceladus, building upon the 3D model of Enceladus' ice shell developed by Souček et al. (2019).

Ad (i), we have developed a mathematical model predicting slip at the strike-slip fault, its neighboring bulk's deformation, and the region's thermal evolution driven by two dissipative processes. First, our investigation focuses on the mechanism of meltwater generation, where results indicate a limited potential for generating near-subsurface meltwater and its confinement to the fault region. Second, we confirmed the physical validity of the 'tidal walking' concept, a theoretical model for generating lateral offsets on Europa's strike-slip faults. We show that fault penetration across the entire shell or reaching a sufficiently low-viscosity zone is necessary for producing observable offset, which is unlikely under current europan conditions. Also, our model's quantitative assessment of the associated surface heat fluxes indicates that measuring thermal anomalies on Europa's surface might lead to the differentiation of active faults.

Ad (ii), we extended the numerical model by Souček et al. (2019), by including Coulomb-type friction in the description of tiger stripes, which introduces a mechanical asymmetry in the response of faults between the periods of normal loading and unloading, resulting in a stress redistribution with potential geomorphological implications. We also observe an intriguing correlation between the brightness of the plumes and tangential displacement at the faults, and the strong dependence of Enceladus' tidal deformation on the friction coefficient. Finally, we present a proof-of-concept for incorporating a more realistic rate and state frictional model in future 3D models of Enceladus' ice shell.

Keywords: Mohr-Coulomb friction on faults, tidally induced strike-slip motion, thermo-mechanical evolution of icy shell, frictional heating, rate and state friction

Contents

Preface

An in-depth examination of the icy moons in the outer Solar system through space missions, namely Cassini-Huygens (exploring Saturn's system) and Galileo (investigating Jupiter's system), yielded unexpected findings. Rather than lifeless rocky bodies, these missions revealed dynamically active entities. While the notion of water presence on Europa had been theorized decades ago, the most astounding revelation came with the identification of active vapor plumes on Enceladus. This discovery not only demonstrated the availability of sufficient energy to propel water at speeds exceeding the escape velocity, providing a remarkable link between Enceladus' geysers and Saturn's E ring but also confirmed the existence of liquid water. But where does this energy originate? And how is it possible to sustain an ocean in such a small and distant celestial body where solar radiation is feeble? The answer lies in the phenomenon of tides.

Most people commonly understand tides as the daily motion of the sea level. The dynamical cause of this phenomenon is the interplay between gravity and centrifugal forces in a binary (or more complex) system of a planet and its moon. In the icy moon context (Saturn and Enceladus or Jupiter and Europa), tides may have a huge dynamical impact on such an interacting system, affect the orbital characteristics, and, due to the incessant distorting of the moon's/planet's shape, generate dissipative heat that provides the source for internal dynamics and/or may sustain a liquid ocean.

Since the initial revelation of vapor plumes on Enceladus, similar plumes have been observed on Europa, and subsurface oceans have been confirmed on several moons within the outer Solar system. Tides continue to provide explanations for an increasing number of questions. Nevertheless, many aspects evade complete understanding, such as the timing of plume activity on Enceladus, the underlying reasons for the suggested presence of subsurface water lakes on Europa, and the mechanism behind the lateral offset on Europa's strike-slip faults, known as "tidal walking". This thesis endeavors to approach comprehensive answers to these inquiries by enhancing numerical models of tidal deformation through the inclusion of friction.

1. Icy moons - geology and tides

In this chapter, we will provide a brief overview of the two icy moons that are the focus of our study, namely Europa and Enceladus. We will present essential geological information to establish the necessary context and introduce the fundamental concept of tides, which serve as the primary driving force behind the modeled dynamical phenomena.

1.1 Europa

1.1.1 Exploration and interior structure

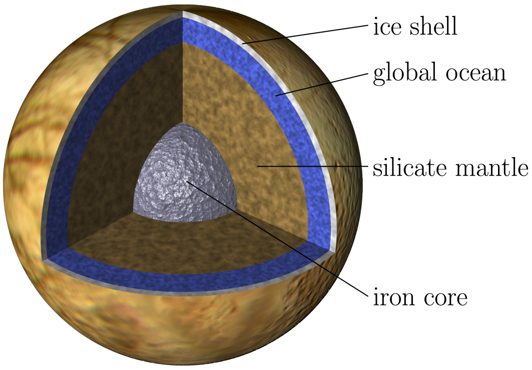

Figure 1.1: The interior structure of Europa. Background image: courtesy of JPL NASA.

Galileo Galilei discovered the four large Jovian moons - Europa, Io, Ganymede, and Callisto - in 1610. Amongst these (nowadays called Galilean satellites) Europa is the smallest with a radius of 1565 kilometers. The first spacecraft views of Europa were provided by the Pioneer 10 (launched in 1972) and Pioneer 11 (launched in 1973) missions. Subsequently, the Voyager 1 and 2 flybys in 1979 delivered the initial evidence of geological activity on Europa (e.g., Smith et al., 1979a,b).

A significant breakthrough in our understanding of Europa occurred with the arrival of the Galileo spacecraft in 1996. This mission provided high-resolution images and measurements that allowed for inferences about the moon's internal structure, including the potential presence of liquid water. Gravitational data, as presented by Anderson et al. (1997), indicated that Europa is fully differentiated, featuring a metallic core, a silica mantle, and an outer layer of water, see Figure 1.1. Magnetic measurements conducted by Khurana et al. (1998) and Kivelson et al. (2000) revealed that the water layer consists of a global ocean beneath an ice shell. This confirmation of liquid water made Europa one of the first celestial bodies in space where the presence of such an ocean was verified.

The increasing knowledge about Europa continues to fuel our intrigue. The presence of a young surface and recent observations of water plumes (Roth et al. (2014), Sparks et al. (2016), Sparks et al. (2017), Jia et al. (2018)) strongly suggest that Europa is a geologically active celestial body. The morphological evidence further indicates the possibility of near-surface meltwater, which could potentially make Europa's water, and a hypotetical life, more accessible compared to other celestial bodies. These remarkable characteristics have positioned Europa as a significant target for space missions with immense astrobiological potential. Currently, there are two ongoing space missions dedicated to exploring Europa.

- **Europa Clipper** National Aeronautics and Space Administration's mission with a launch target on October 2024 (`https://europa.nasa.gov`)
- **JUICE** European Space Agency's mission targeting Jupiter and three of its icy moons in depth (Ganymede, Callisto and Europa) launched in 2023 (`https://sci.esa.int/juice`).

Europa's ice shell

The thickness and thermal structure of Europa's outer ice shell are still not well constrained. Estimates of the shell's thickness range from less than 10 kilometers to more than 40 kilometers (Billings and Kattenhorn, 2005). Regarding the thermal state, the circular features observed on the surface suggest the occurrence of convection during their formation (Pappalardo et al., 1998). However, the current thermal state of the ice shell remains unclear (Barr et al., 2009). Determining whether the shell is in a convective or conductive state depends on the thickness and viscosity structure of the ice shell. Currently, no observations provide a definitive assessment of its state.

Pappalardo et al. (1999) proposed a model combining a brittle layer at the top with a ductile (possibly convecting) layer at the bottom. On the other hand, Hussmann and Spohn (2004) demonstrated that the thickness and, consequently, the thermal state of the ice shell could have varied by several tens of kilometers over the course of Europa's evolution.

1.1.2 Europa's geomorphology

Europa has a relatively high geometric albedo of 0.67 (Buratti and Veverka, 1983) caused by the presence of water ice. Pure ice lies on the leading hemisphere, while on the trailing hemisphere, hydrated salts or hydrated sulfuric acid have been suggested (McCord et al., 1998; Carlson et al., 1999), see the mosaic of the leading hemisphere and real color image of the heading hemisphere on Figure 1.2. On Europa's geologically young surface (Bierhaus et al., 2009, 40 - 90 Myr) global tension prevails while crustal convergence features are harder to spot (Kattenhorn et al., 2009). While many fracture patterns can be correlated with diurnal tidal forces and the long-term effects of non-synchronous rotation, these forces are not sufficient to explain all patterns; additional stress sources are required, such as orbital evolution, polar wander, finite obliquity, ice shell thickening, endogenic forcing by convection and diapirism or secondary effects driven by strike-slip faulting and plate flexure (Kattenhorn et al., 2009).

Extensional tectonics

Several lines of evidence support the extensional formation model suggested for the majority of landforms on Europa's surface:

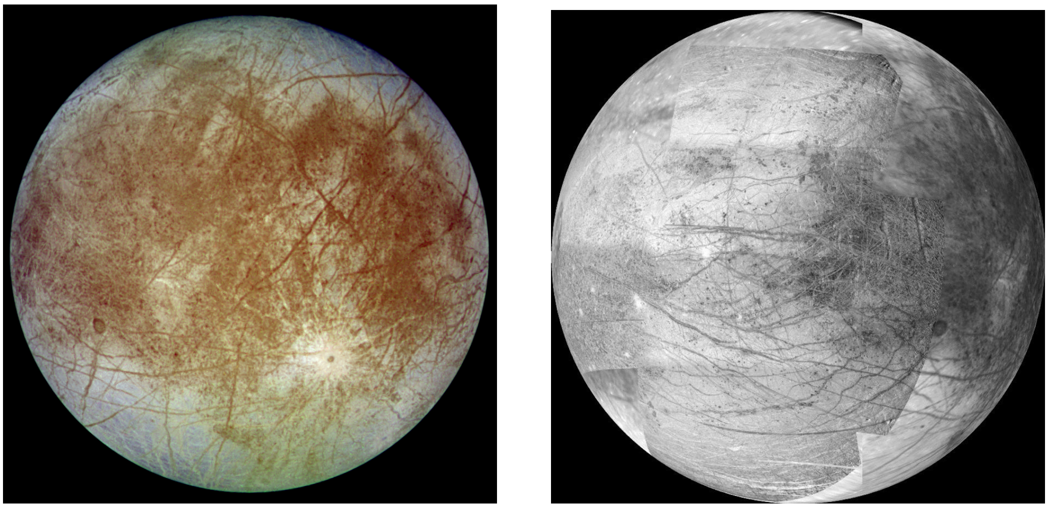

Figure 1.2: Left: trailing hemisphere of Europa taken by the Galileo spacecraft, right: a mosaic of the leading hemisphere. Courtesy of NASA/JPL Caltech.

1. Ice is mechanically weak under tension at europan conditions.
2. Europa's near-surface experiences tensional stresses on a daily basis due to the oscillating tidal bulges caused by gravitational interactions with Jupiter and other Jovian moons.
3. Some of the lineaments (linear features) on Europa's surface appear in multiple parallel sets, resembling tension joints observed on Earth.
4. Most lineaments on Europa's surface do not show lateral offsets, indicating pure extensional deformation.
5. Clear evidence of complete dilational separation of parts of the ice shell can be observed in images captured by the Galileo spacecraft; see "Dilational bands" below.

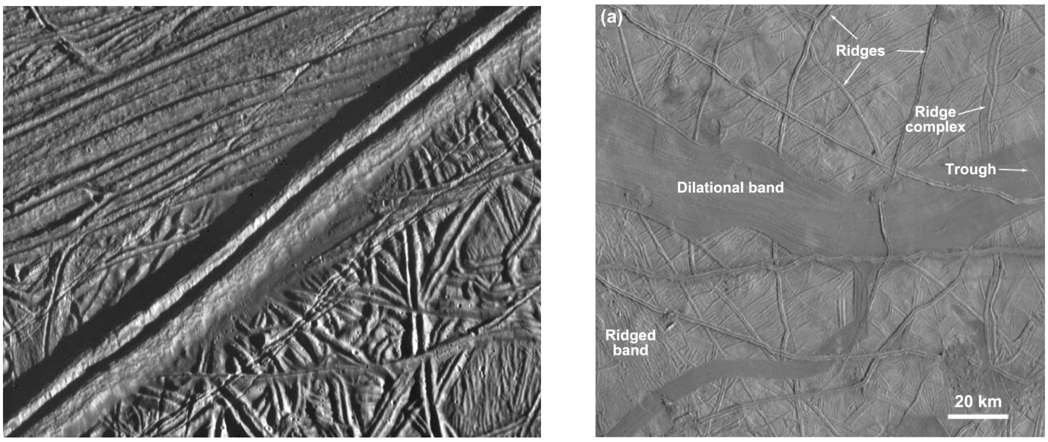

Figure 1.3: Left: Double ridge (mosaic of two pictures taken by Galileo, image courtesy of NASA/JPL-Caltech). Right: Several examples of features on Europa's surface (Kattenhorn et al., 2009).

We now briefly describe the extensional features found on europan surface in more detail.

Ridges

Ridges are a few to a thousand kilometers long, with topography up to hundreds of meters and characteristic width of hundreds of meters (with a maximum of five kilometers), see Figure 1.3. They can be found in the oldest ridged plains, but they are also part of some of the youngest geological regions, making them the most persistent feature on Europa.

Formation models include volcanism, tidal squeezing, diapirism, compression, and shear heating. In addition, Dombard et al. (2013) proposed a cryovolcanic sill model (see Chapter 2 for more information). Regardless of the precise formation mechanism, each individual ridge has been built in a relatively short period of time, with estimates varying from ten thousand (Nimmo and Gaidos, 2002; Melosh and Turtle, 2004) to up to thirty thousand years (Greenberg et al., 1998).

Cycloids

Since the cycloid's lengths range from hundreds to thousands of kilometers, they were first recognized even on Voyager images; see Figure 1.4. Each segment of a cycloid, typically tens of kilometers long, is linked to the adjacent one by a cusp. Except for one possibly analogous feature in the south pole of Enceladus, cycloids are unique features in the whole Solar System.

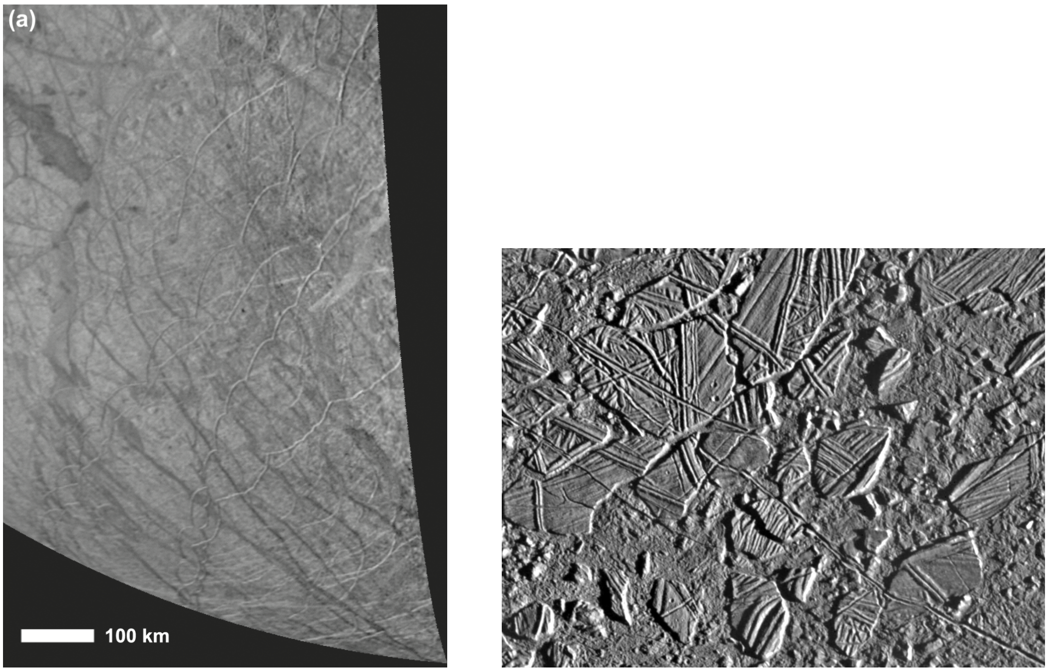

Figure 1.4: Left: Cycloid from Kattenhorn et al. (2009). Right. Chaos terrain. Image courtesy of NASA/JPL-Caltech.

Hoppa et al. (1999a,b) proposed that cycloids formed due to tensile cracking in response to diurnally varying tidal stresses. As the orientations of the principal stresses rotate, and the magnitudes oscillate at any location on the surface during the orbital period, the cycloids develop perpendicular to the rotating direction of maximum tensile stress with a substantial speed of three to five kilometers per hour, or even more (Lee et al., 2005).

Dilational bands

The dilational bands (see the right part of Figure 1.3) are composed of a new crustal material that intruded between the progressively dilating walls of a tensional fracture; hence they represent a proof of resurfacing process. They are typically hundreds of kilometers long and less than thirty kilometers wide (commonly a few kilometers), with a topography elevated up to two hundred meters with respect to the surrounding area.

Two categories of dilational bands can be found on Europa: smooth and lineated. They have formed either by the dilatational cracks penetrating the shell completely and exposing the water to freeze as a new smooth material (Tufts et al., 2000) or through the brittle part of the shell dilating slowly enough for the ductile ice to undergo buoyant upwelling.

Troughs

Troughs (see the right part of Figure 1.3) are the youngest extensional features identified on Europa; they probably gave rise to most of the others. These tension fractures assumably initiated at the surface and then propagated downwards up to a certain depth which is dependent on the stress available to overcome the overburden pressure.

Hoppa et al. (1999a) calculated that troughs would penetrate less than approximately sixty-five meters if formed by diurnal stresses; however, if crack-tip stresses and porous ice are considered, the cracks can pierce even several kilometers deep ice shell. Taking into account additional stresses due to the nonsynchronous rotation, up to thirteen kilometers thick ice shell might be ruptured by the throughs (Lee et al., 2005).

Normal faults

The last form of extensional tectonics observed on Europa is normal faulting, evidenced by fault scarps showing a component of vertical motion for which a deviatoric tension is necessary. The majority of normal faults are present as fine striations within lineated bands comparable to Earth‘s mid-ocean ridges. Normal faulting has also extended some of the dilational bands after their original formation. Rarely a vertical displacement of approximately 300 meters is present in ridged plains (Nimmo and Schenk, 2006).

Compressive tectonics

Even though Europa has probably experienced cooling and thickening of the ice shell, which could partly explain the prevalence of extension, given the number of extensional features, some contraction should be visible on the current surface. Nevertheless, compressive tectonics is scarce.

On Earth, apart from subduction, which was suggested for Europa by Kattenhorn and Prockter (2014), compression can occur along deformation bands, and pressure-solution surfaces, by the development of thrust faults or through elastic warping and folding.

Folding

Folding is manifested via parallel folds within the dilational bands. Even though folds may relax due to the presence of warm and thus ductile ice, according to Dombard and McKinnon (2006), the relaxation is so slow that folds should be visible in current images.

Convergence bands

Convergence bands are places where tectonic reconstruction reveals a zone of missing crust. Two types are present, either those driven by the motion along strike-slip faults or those along zones of pre-existing weakness. Another possibility lies in the misidentification of convergence bands as dilational bands.

Contraction across ridges

Some of the double ridges present evidence of lateral offset, which can be partially driven by convergence. Nimmo and Gaidos (2002) suggested that heating may result in a more mobile wedge of ice alongside a shearing lineament, causing localized weakness, where contraction may be accommodated. According to Vetter (2005), ridges that also exhibit contraction show a larger amount of strike-slip. If most of the contraction would be accommodated across ridges (Bader and Kattenhorn, 2008), then a minimal amount of convergence would be needed elsewhere since they are the most ubiquitous landform on the surface.

Lateral shearing

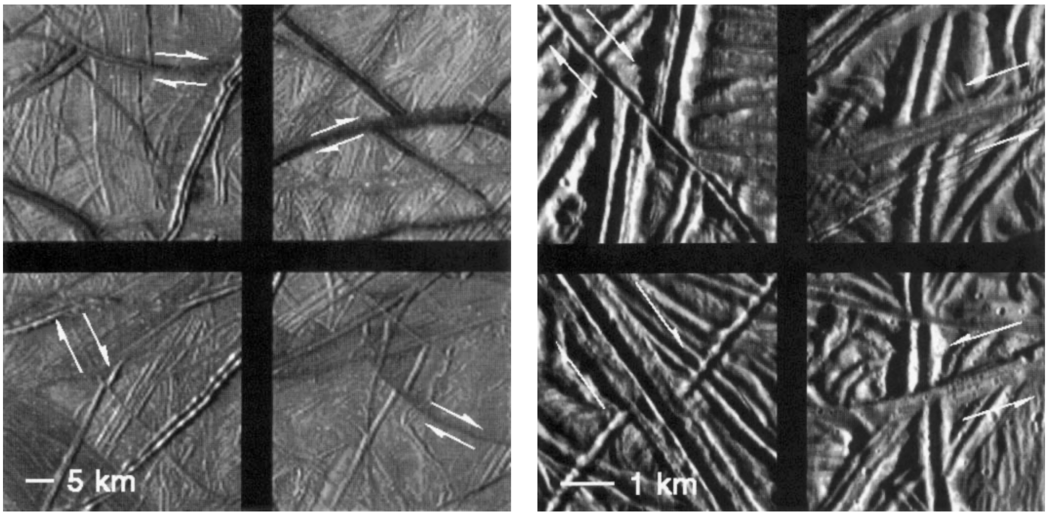

Figure 1.5: Examples of lateral offset from Hoppa et al. (1999a), on the left examples of right-lateral motion in the wedges region, on the right both left- and right-lateral motion in the Conamara Chaos region.

The lateral offset occurs on Europa, probably thanks to the reactivation of existing faults; see Chapter 2 and Figure 1.5. Since troughs, ridges, and dilational bands have originated from extension, they are all prone to reactivation by diurnal stresses; however, in general, the offset can develop on any lineament and is also observed on normal faults in the form of oblique-slip motions. Based on the observations of cumulative offsets on Galileo images (more than hundreds of meters are needed for distinguishing the offset) Kattenhorn (2004) divides strike-slip faults on Europa into ridge-like and band-like.

The ridge-like faults probably developed from throughs, and the offset was formed later, possibly leading to the development of ridges (Nimmo and Gaidos, 2002; Kalousová et al., 2016). Concerning the band-like strike-slip faults, the timing of the development of offset is much more difficult, as it is unclear whether it developed prior, during, or after dilation. According to Kattenhorn (2004), on examined band-like faults, the strike-slip offsets accumulated while dilatating. Band-like faults have typical lateral offsets of tens of kilometers (e.g., 77 km along Astypalaea Linea), whereas the offsets for ridge-like faults usually range from hundreds of meters to several kilometers (Hoppa et al., 2000) with an extreme case of 83 km (Sarid et al., 2002).

Since lateral offset is not visible on all ridges, two formation scenarios are possible: either other processes are needed for the ridge production, and they can produce ridges separately, or sometimes the shear motion is strong enough to heat the ice to construct the ridge but results in zero or unresolvable cumulative offset.

Chaotic terrain

One-quarter of Europa‘s surface is occupied by the chaotic terrains formed through the disruption of the preexisting surface into isolated plates and lumpy matrix material between these plates (Carr et al., 1998). Conamara chaos is a prominent example of chaotic terrain, with approximately sixty percent of its area taken by the matrix and the rest by the blocks (Spaun et al., 1998). Domes, spots, and pits together called lenticulae (small features) can also host chaotic terrains.

The disrupted terrain plates usually measure from one to twenty kilometers across and are topographically elevated with respect to the surrounding matrix. Many of them have moved from their original position, some rotated around their vertical axes, and several have tilted (Spaun et al., 1998). The surrounding matrix is formed by a collection of ice pieces sized from tens of meters up to a kilometer.

Several formation models have been proposed: melting through the ice shell (Greenberg et al., 1999), thermally or compositionally buoyant diapirs, or even a hybrid model of the previous two. Also, an exogenic impact was proposed by Billings and Kattenhorn (2003). And finally, a lense collapse model, where water lenses formed due to eutectic melting at three kilometers depth and have allowed ice blocks to move and subsequently refreeze (Schmidt et al., 2011).

1.2 Enceladus

1.2.1 Exploration and interior structure

Enceladus is a small moon of Saturn with a radius of 252 kilometers and the highest albedo (0.99) in the whole Solar System caused by fresh, clean ice covering the surface. Enceladus was discovered by William Herschel in 1789 (Herschel, 1790) and named 60 years later by his son John after a Greek mythological giant.

The understanding of Enceladus is tightly connected to the discovery (and understanding) of the Saturn's E ring, which is being fed by Enceladus' cryovolcanism (Postberg et al., 2008). The Pioneers 10's and 11's flybys of Saturn led to the discovery of Saturn's F ring, skipping the letter E in the naming of the rings in anticipation of E ring discovery, later confirmed by Voyager 1's images (Showalter et al., 1991).

The first spacecraft images of Enceladus were provided by Voyager 1 in 1980, followed by a closer look from the Voyager 2 mission in 1981, showing few craters and numerous smooth areas together with extensive linear cracks (Dougherty et al., 2018). The two Voyager missions brought the first direct indication of current activity. The high albedo, together with the peak in the density of Saturn's E ring near the orbit of Enceladus (Showalter et al., 1991) and the expected short lifetime of E ring particles, hinted at the possibility of geyser-like activity on Enceladus (Haff et al., 1983; Pang et al., 1984).

A major breakthrough in understanding Enceladus came with the Cassini mission, which entered Saturn's orbit in 2004. The magnetometer observations in the two first flybys revealed apparent perturbations near Enceladus, explained by the MAG team as a diffuse extended atmosphere. Consequently, the MAG team advocated for reducing the height of the third flyby to mere 173 km.

In July 2005, many Cassini instruments simultaneously discovered geysers emanating water vapour and ice particles from the south pole of Enceladus resupplying the E ring (Dougherty et al., 2018). Thereupon, Enceladus became the main focus of Cassini's extended missions, namely the Cassini Equinox Mission (2008 - 2010) and the Cassini Solstice Mission (2012 - 2017), providing us with an enormous amount of information, which are being processed until today.

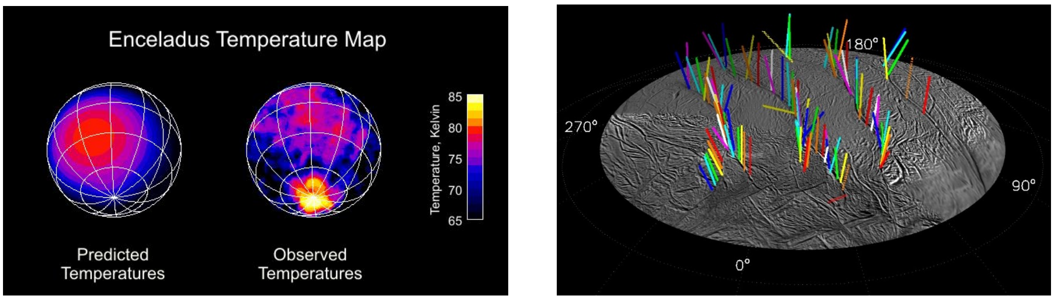

Figure 1.6: Left: Comparison of expected thermal profile of Enceladus and an actual infrared (heat) radiation measured during the third flyby (courtesy of NASA/JPL/GSFC). Right: A 3D map of all 98 jets emanating from the tiger stripes (Porco et al., 2014).

In 2005, the temperature map of Enceladus showed large anomalies on the south pole, see Figure 1.6 left, from where the active geysers are emanating. The jets erupt from fractures near the south pole, informally called "tiger stripes" (Porco et al., 2006), see Figures 1.6 and 1.7 right. The activity of the jet plumes varies significantly depending on the position of Enceladus in its orbit, indicating that it is related to periodic variations in tidal stress (Hurford et al., 2007; Hedman et al., 2013; Nimmo et al., 2014; Ingersoll et al., 2020). However, until today the temporal variations in the activity have not been completely explained by any model.

The plume samples collected by Cassini were shown to include molecular hydrogen and silica nanoparticles hinting at a hydrothermal system connected to the silicate-rich core (Hsu et al., 2015; Waite et al., 2017; Schoenfeld et al., 2023), making Enceladus one of the top candidates for hosting extraterrestrial life (Angelis et al., 2021). On Earth, the hydrothermal systems aspire for the origin of life, and even today, they still are an active ecosystem. On the other hand, if life requires surface environments for its origin and if panspermia has not been effective on Enceladus, then its ocean might be habitable but uninhabited. To resolve this enigma, near-term missions are being planned to search for biomolecules in plume materials. Analogous environments to the subsurface ocean on an icy moon include dark, anoxic water bodies virtually sealed by ice, anaerobic chemoautotrophic microbial ecosystems, and low-temperature alkaline hydrothermal vents.

Enceladus is differentiated into a silicate - possibly porous (Choblet et al., 2017) - core and a water layer. The joint inversion of the gravity (Iess et al., 2014), topography (Tajeddine et al., 2017), and libration data (Thomas et al., 2016) points at the presence of a global ocean beneath a thin ice shell, see Figure 1.7.

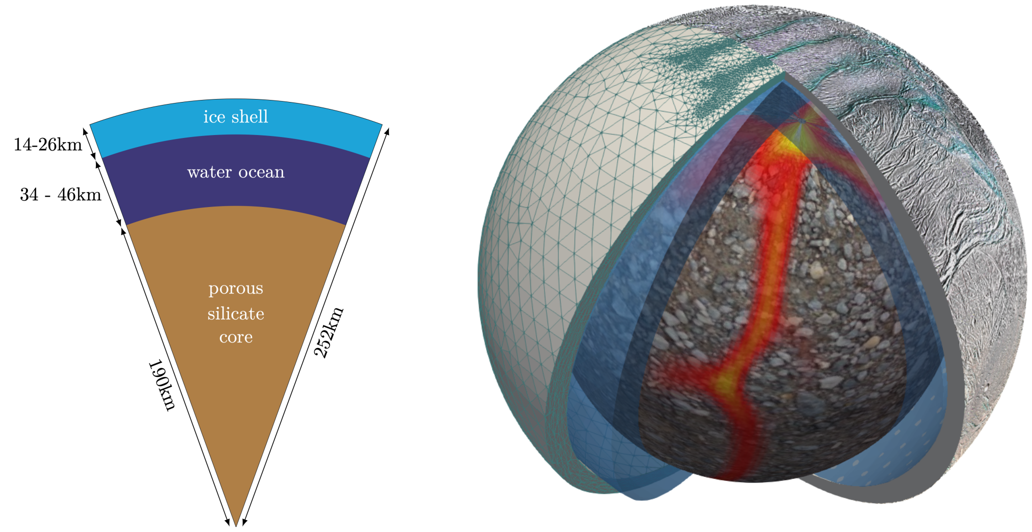

Figure 1.7: Left: A sketch of the approximate inner structure of Enceladus. Right: A visualization of our mathematical model of Enceladus with finite element mesh refined in the vicinity of tiger stripes, the image is turned, “tiger stripes” and their mesh representation are shown in the north pole. Image courtesy of Ondřej Souček.

1.2.2 Enceladus’ geomorphology

Based on Voyager 2’s highest resolution coverage Smith et al. (1982) showed that the surface of Enceladus has distinct provinces with different crater densities confined by major tectonic contacts. The provinces were called cratered terrain, cratered plains, ridged plains, and smooth plains. This diversity has been later on specified with the usage of better-resolution data to cratered terrain, trailing hemisphere terrain, leading hemisphere terrain, and south polar terrain, see Figure 1.8 from Crow-Willard and Pappalardo (2015). The massive differences

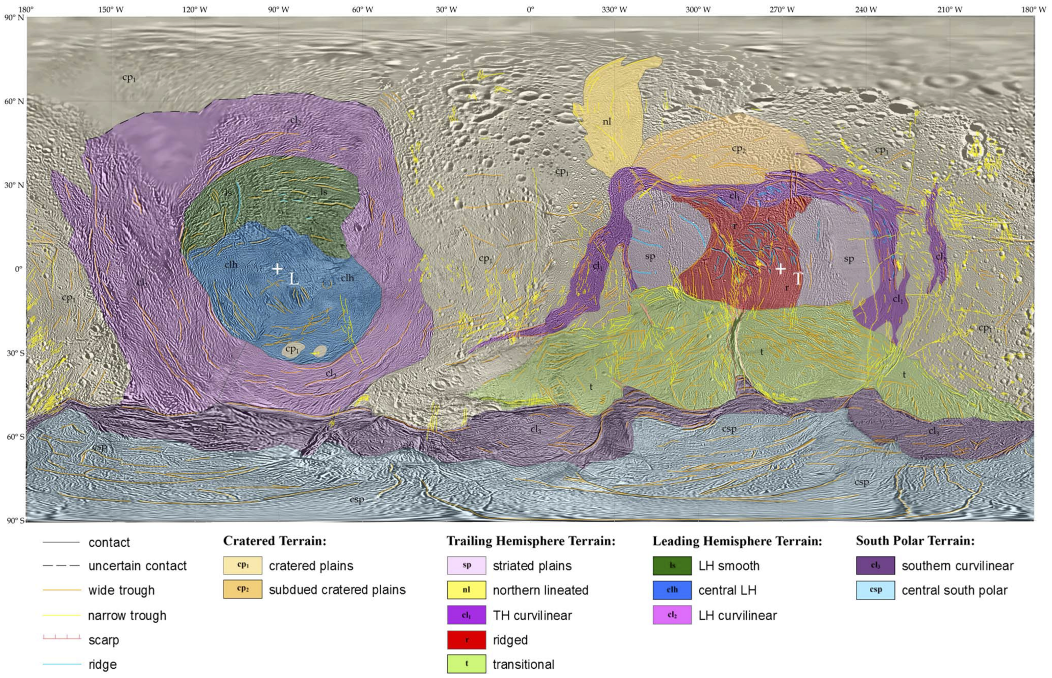

Figure 1.8: Simple cylindrical global image mosaic with superimposed map units and structures from Crow-Willard and Pappalardo (2015). Crosses mark the leading point (L) and trailing point (T).

between the tectonic terrains of leading and trailing hemispheres, cratered terrain, and the geologically active south polar terrain imply complex history and probably several different endogenic processes taking place in the ice shell.

South Polar Terrain (SPT)

The geologically youngest area of Enceladus - the South Polar Terrain (SPT) - is characterized by a low topography surrounded by a tectonic belt (Patterson et al., 2018). The SPT might have formed in the south pole, or it might have migrated as a mass anomaly. The whole area is massively fractured with four sub-parallel linear depressions (the tiger stripes) standing out, see Figure 1.9. Damascus, Baghdad, Cairo, and Alexandria are approximately 2 kilometers wide and 130 kilometers long features spaced 35 kilometers apart. The tiger stripes correlate with the pattern of increased heat flux (e.g., Spencer et al., 2018) and the positions of Enceladus' jet plumes, see Figure 1.6 and Porco et al. (2006).

In addition to the major tiger stripes faults, there are other fractures in the SPT region of Enceladus with different orientations (Patthoff and Kattenhorn, 2011). The origin of these fractures has been suggested to be the result of long-term effects of non-synchronous rotation stresses or gravitational collapse along a shallow detachment fault above a thermal anomaly (Patthoff and Kattenhorn, 2011; Yin and Pappalardo, 2015). The deformation of the polygonal tectonic belt that encloses the SPT, the spoke-like chasmata that extend radially northward from the SPT, and the tectonic dissection of relatively older terrains around the SPT have probably been affected by the tectonic activity in SPT as well (Patterson et al., 2018).

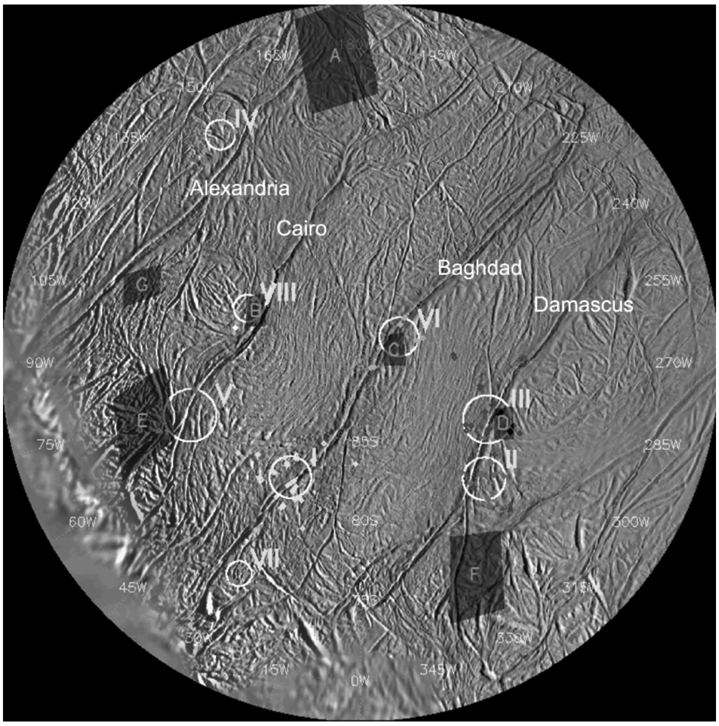

Figure 1.9: Polar stereographic projection of Enceladus' south polar region with noted names of the tiger stripes (Goldstein et al., 2018).

Trailing and Leading Hemisphere Polar Terrains (THT and LHT)

The intermediate stage of Enceladus's geological activity is recorded within older (based on crater densities (Crow-Willard and Pappalardo, 2015; Kinczyk et al., 2017)) Trailing Hemisphere Terrains (THT) and younger Leading Hemisphere Terrains (LHT). As the SPT, both these areas are partially or fully enclosed by the circumferential belts. In addition, two distinct areas (Cufa Dorsa and Ebony Dorsum) lying in the THT, share structural characteristics with SPT and possibly record tectonic deformation over multiple generations.

The LHT resembles the SPT even more with its complete belt and ridges with throughs in the central region. The similarities between the three regions also mirror the coronae of a uranian satellite Miranda which has a similar size as Enceladus with a radius of approximately 235 kilometers. Since the tectonized terrains of Enceladus (as in Miranda's case) are placed along the principal inertia axis, long-lived mass anomalies have been suggested as the formation mechanisms for THT and LHT. However, the connection between the formation of these terrains (SPT, THT, and LHT) is still feeble since features similar to the tiger stripes, and the Y-shaped structural discontinuities have not yet been found in the latter two.

Cratered plains

The earliest stages of geological activity can be observed in the cratered plains, where crater density analysis suggests age of more than a billion years. The presence of subsurface heat flows is indicated by the observation of topographic basins and topographically relaxed craters. Subdued ridges and troughs in the equatorial regions, together with anomalously low small-crater densities, hint at an ancient resurfacing event. Although pit chains orientation points at much more recent activity, possibly produced due to nonsynchronous rotation stresses.

Summary

Altogether the geological evidence indicates that at least some of the tectonic history of Enceladus is related to the global tidal deformation of the ice shell, while other geological structures are consistent with a nonsynchronous rotation of the ice shell above the global ocean on a timescale ranging from a hundred thousand to million years.

1.3 Tides on icy moons

Tides represent a physical phenomenon resulting from a localized imbalance between the gravitational force exerted by the companion body and the centrifugal force acting on the adjacent and distant sides of the moon, leading to its deformation. The measurement of tidal response serves as a universal method for investigating the interior structure of moons. Similar to the tides experienced in Earth's oceans, the tides exerted on moons also exhibit variations on a diurnal timescale, where the mechanical response of the body is primarily elastic. Although relatively small, anelastic effects resulting from viscoelasticity, plasticity, internal friction, and the dissipation of mechanical energy can contribute significantly to the internal energy budget over geological timescales. Consequently, these processes gradually modify the internal structure of the moon, leading to changes in its tidal response and facilitating feedback among its thermal, orbital, and rotational evolution. Particularly on icy moons like Europa or Enceladus, tidal forcing potentially acts as a substantial energy source, enabling the formation and long-term sustenance of internal oceans.

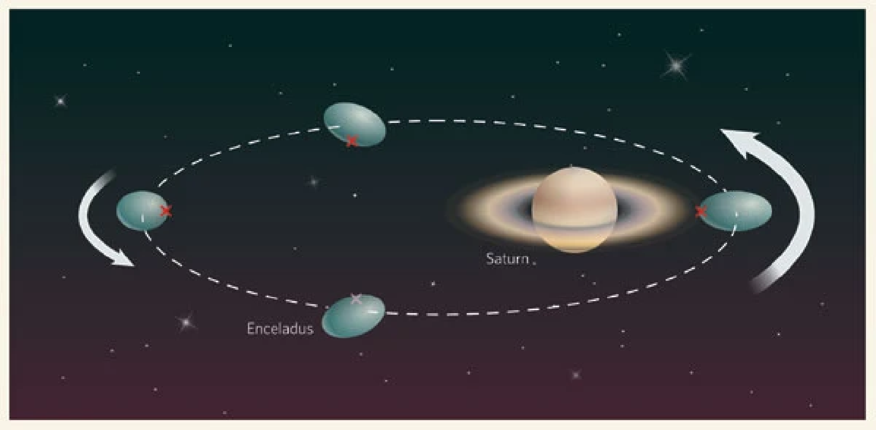

Figure 1.10: Figure from Dombard (2007) showing Enceladus‘ tidal bulge varying in size (exaggerated) due to its eccentric orbit. Since the orbital and rotational motions are out of phase, the position of Enceladus's tidal bulge oscillates around a fixed point (red crosses; pink cross indicates the point on the far side of the planet).

Let us now focus on Enceladus and examine the tidal forces acting upon it. As depicted in Figure 1.10 from Dombard (2007), Enceladus follows a slightly elliptical orbit around Saturn, characterized by a small but nonzero eccentricity of $e = 0.0047$, which is maintained by a 2:1 orbital resonance with Dione. Enceladus is in a state of synchronous rotation, meaning that its revolution around Saturn takes the same time as its revolution around its own orbit. Under the influence of tidal forces, Enceladus undergoes distortion, assuming an ellipsoidal shape with its longest axis pointing toward Saturn. Due to its eccentric orbit, the tidal bulge on Enceladus differs between the apocenter and the pericenter. Additionally, according to Kepler's second law, the orbital velocity also varies throughout the orbit. As a result, the rotational and orbital motions of Enceladus exhibit a slight phase difference. Consequently, the line connecting the planet and the satellite oscillates around a fixed point on the moon's surface, as illustrated in Figure 1.10. The combined effect of these mechanisms leads to a cyclic deformation of Enceladus' shape, resulting in the dissipation of internal energy on a diurnal timescale. This dissipation of energy, occurring over the long term, drives geological activity on the moon.

In the case of Europa, a similar tidal mechanism operates, as its eccentricity is excited by the Laplace resonance with Io and Ganymede, with a mean motion ratio of 4:2:1. While Ganymede circles once around Jupiter, Europa orbits twice, and Io passes around four times.

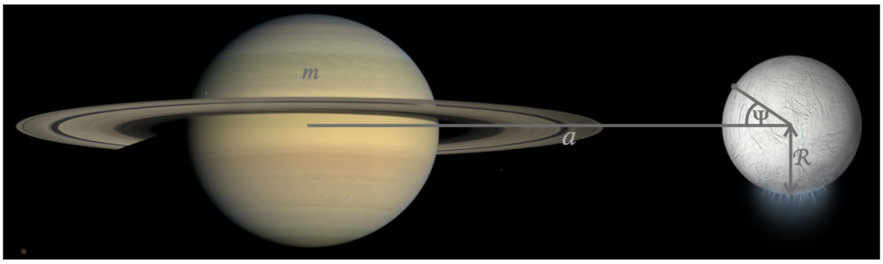

Figure 1.11: Saturn and its moon Enceladus with denoted m, a, Ψ and $\mathcal{R}$ from tidal potential in eq. 1.1. Images of Saturn and Enceladus: courtesy of NASA/JPL/Space Science Institute. The image is not to scale.

The dissipation of tidal energy can be quantified by precise astrometric observations of a moon's orbit over time (e.g., Lainey et al., 2009). Since the magnitude and phase of tidal deformation are influenced by the moon's internal structure and directly impact the amount of internal heating, understanding tidal deformation is crucial for comprehending a moon's energy budget and investigating its internal structure (Kleer et al., 2019). Tidal forces can be best described and examined in terms of the tidal potential characterizing the gravity influence of the companion body. To the second order in eccentricity, the net tidal disturbing potential can be expressed as (Hemingway et al., 2018):

$$V_{\mathrm{tidal}}(\Psi) = \frac{Gm\mathcal{R}^2}{a^3} P_2(\cos\Psi), \tag{1.1}$$

where Ψ is the angle from the axis connecting the centers of the two bodies at an arbitrary point on the satellite's surface, G is the universal gravitational constant, m is the mass of the parent body, $\mathcal{R}$ is the radius of the satellite, a is the distance between the centers of the two bodies, and P_2 is the degree-2 Legendre polynomial, see Figure 1.11.

Since Enceladus is roughly a million times less massive than Saturn and its orbit is synchronous with its mean rotation rate, we can rewrite the potential in terms of spin rate $\omega^2 = Gm/a^3$. Moreover, Enceladus's obliquity is close to zero (<0.001, (Chen and Nimmo, 2011; Baland et al., 2016)), meaning that Enceladus's spin axis is nearly normal to its orbital plane, which allows us to rewrite Ψ through colatitude ϑ and longitude ϕ as $\cos\psi = \cos\phi \sin\vartheta$. Hence the tidal potential of Enceladus as a function of colatitude and longitude can be expressed as follows:

$$V_{\mathrm{tidal}}(\vartheta, \phi) = \omega^2 R^2 \left(\frac{1}{2} Y_{20}(\vartheta, \phi) - \frac{1}{4} Y_{22}(\theta, \phi) \right), \tag{1.2}$$

where Y_{20}, Y_{22} are the spherical harmonic functions.

In Europa's case, we can also use the spin rate since Jupiter is approximately forty thousand times more massive than Europa. However, the usage of colatitude and longitude would be more complicated since Europa's obliquity is not well constrained and is likely to be around 0.1° (Bills et al., 2009).

2. Strike-slip faults on Europa - generation of meltwater and tidal walking

In this part of the thesis, we explore two phenomena related to strike-slip faults on Europa by means of numerical modeling: the **generation of near subsurface meltwater** (Section 2.1) and the **development of lateral offset** through a process called "tidal walking" (Section 2.2).

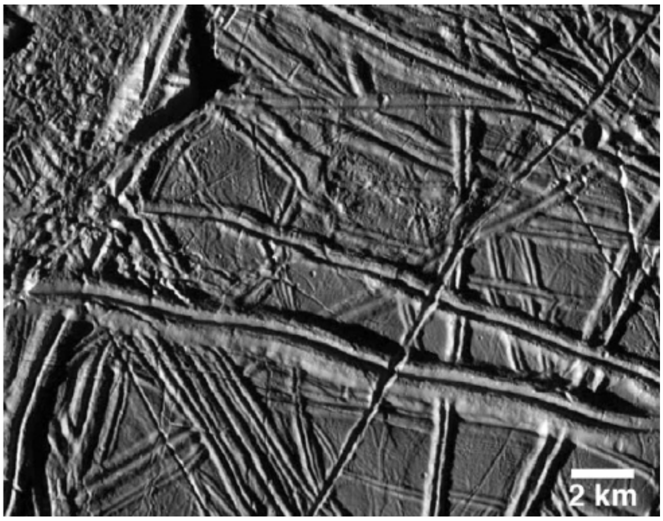

Figure 2.1: Figure from Pappalardo (2010) showing a set of double ridges on Europa.

Two types of morphological terrains observed on the surface of Europa hint at the presence of near-surface water. The first one is a *double ridge*, see Figure 2.1, the most ubiquitous landform on Europa, consisting of a central crack or trough flanked by two raised edifices, up to a few hundred meters high and less than 5 kilometers wide (Kattenhorn et al., 2009). Dombard et al. (2013) observed fractures on the double ridge flanks and suggested a formation mechanism where the ridge is grown due to underlain cryomagmatic sill, which locally heats and thins the lithosphere, see Figure 2.2.

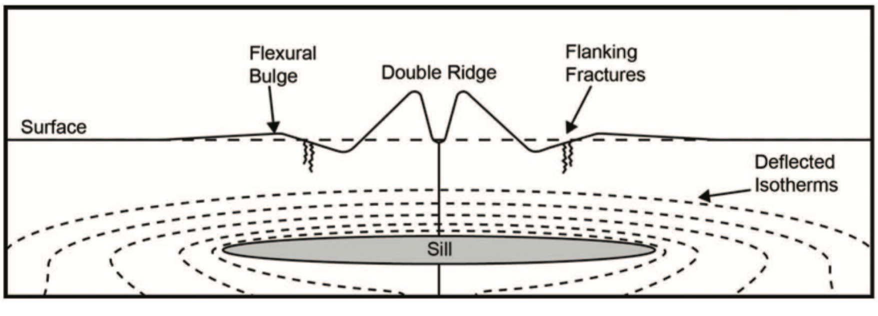

Figure 2.2: Figure from Dombard et al. (2013) presenting the formation of double ridge through a cryomagmatic sill model.

The second one is a *chaotic terrain*, which is a region of crustal disruption or disaggregation. Schmidt et al. (2011) suppose the presence of subsurface meltwater when suggesting the formation of the chaotic terrain by the collapse of liquid water lens. First, the rising thermal plume reaches the pressure-melting eutectic point of the overlying ice while the surface subsides due to melting, and the hydraulic flow forms tensile cracks. The ice blocks are formed by the hydrofractures from the melt lens and the matrix by the brine infiltration. In the end, the melt lens and matrix refreeze, ascending the chaos feature above the surroundings.

To produce the subsurface meltwater, two major mechanisms have been proposed: (i) increased tidal bulk dissipation in the top warm and low-viscosity parts of rising hot plumes and (ii) melting through frictional heating and dissipation in the surroundings of a strike-slip fault.

The possibility of generating larger water lenses associated with the first scenario was ruled out by Kalousová et al. (2014), where the generated meltwater was rapidly transported downwards by the porous flow. The second scenario, studied numerically for the first time by Nimmo and Gaidos (2002), was in Kalousová et al. (2014) considered as more plausible; however, later Kalousová et al. (2016) showed that even in this case, the longevity of the subsurface water reservoirs would be limited by a formation time of the Rayleigh-Taylor instabilities. In Section 2.1, we will study the process of frictional heating associated with strike-slip faults and related meltwater generation and its transport by means of numerical modeling.

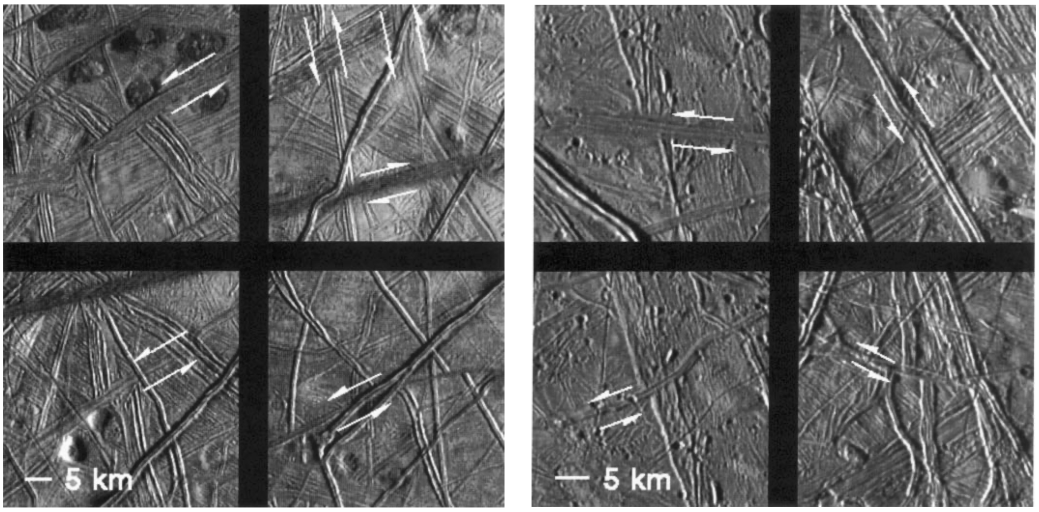

Figure 2.3: Examples of left-lateral offset from Hoppa et al. (1999a): from the northern bright plains region (left), from the Tyre region (right).

A surface lateral offset of up to a few kilometers has been identified on a number of locations on Europa; see Figure 2.3 and Section 1.1.2 for more information, indicating that strike-slip motion appeared on Europa's surface. On Earth, strike-slip motion occurs either through a primary shear failure if the intermediate compressive principal stress is vertical and the horizontal differential stress exceeds the frictional strength or through reactivation of the pre-existing faults and fractures due to temporal changes in the stress field (Anderson, 1905). While it is not clear if the primary shear failure could produce lineaments on a global scale (Kattenhorn et al., 2009), there is a convincing evidence for the shear fracture reactivation (Hoppa et al., 1999a; Sarid et al., 2002; Kattenhorn, 2004; Rhoden et al., 2012). It was suggested that the reactivation might be induced by tidal forcing through a process nicknamed "tidal walking" (Hoppa et al., 1999a), see Section 2.2.

2.1 Heat and meltwater production on strike-slip faults on Europa

To numerically test the hypothesis of producing meltwater on and in the vicinity of Europa's strike-slip fault through frictional heating and viscous dissipation, we study the mechanical and thermal evolution of a part of Europa's ice shell with reactivated planar fault, see Figure 2.4. In Kalousová et al. (2016), the generation of meltwater in the vicinity of strike-slip faults on Europa and its transport within the ice crust was modeled with a parameterized heating source. Here, we test the hypothesis of producing meltwater on strike-slip faults of Europa by including a more realistic description of the strike-slip fault and the heating sources. By computing strike-slip motions, we can numerically evaluate the friction at the fault and mechanical dissipation in the neighboring bulk. With such a model, we can assess whether the associated heating can be sustained long enough for the development and sustenance of the meltwater (Schmidt et al., 2011; Dombard et al., 2013). The model combines and improves the two mentioned approaches (Kalousová et al., 2016; Nimmo and Gaidos, 2002) in order to produce a 2D model of a thermal and mechanical evolution of europan strike-slip fault and its surroundings, including water production.

2.1.1 Model components

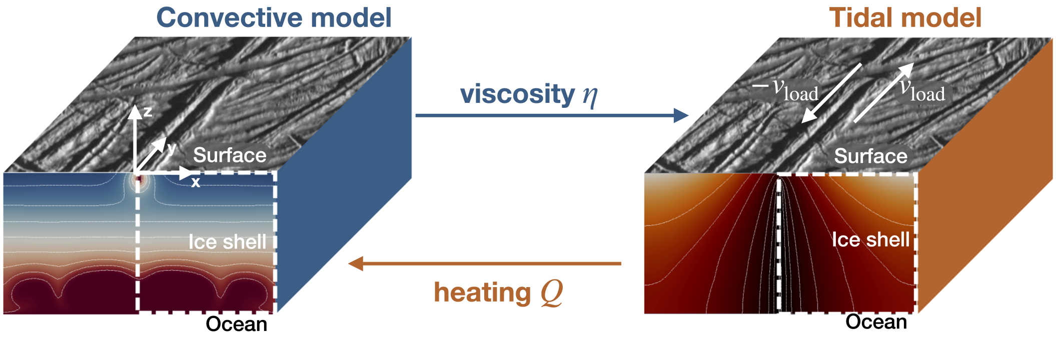

Figure 2.4: The thermo-mechanical model is composed of the tidal model (diurnal timescale) and the convective one (thousands of years timescale). The two parts exchange data regularly; viscosity η is provided from convective to the tidal model, whereas heating Q is passed the other way; see Figure 2.5 for a detailed description of the computational flow.

Since we consider the strike-slip fault to be activated by diurnal tides (Europa's orbit $\sim$ 3.55 days), and since it can take millions of years for thermal convection to reach a (statistical) steady state (Kalousová et al., 2016), the mechanical and thermal evolution model needs to involve two different timescales.

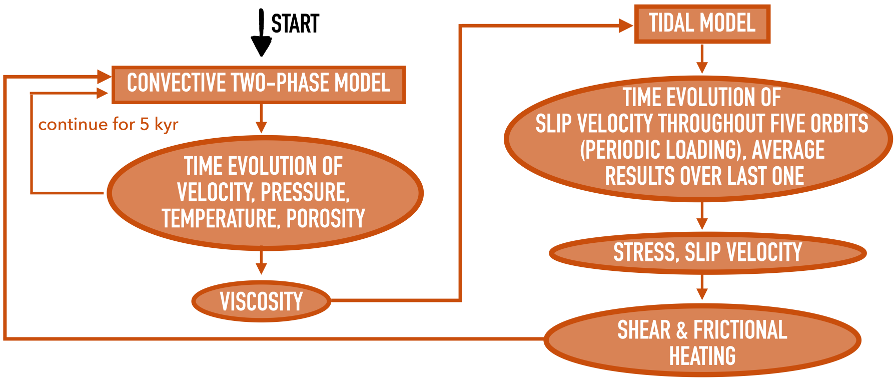

Figure 2.5: A flow chart describing the structure of the thermo-mechanical model with the regular exchange of data between the two parts: the convective two-phase model and the tidal model.

Hence, we decompose the thermo-mechanical problem into two: a tidal (mechanical) one acting on the diurnal timescale and the convective (thermal) one acting on geological timescale, while ensuring coupling between the two modules, see Figures 2.4 and 2.5.

Let us describe the computational order as shown in the flowchart in Figure 2.5: First, the convective two-phase model, based on Kalousová et al. (2016), is run for five thousand years, calculating the time evolution of velocity, pressure, temperature, and porosity (water content). At the end of this period, the viscosity η is exported (based on the state of the convective model) and used to parameterize mechanical properties in the tidal model (a viscoelastic mechanical model). The tidal model evolves slip velocity over five europan orbits to suppress the influence of initial conditions. Then, based on the averages of stress and slip velocity throughout the last calculated orbit, the shear and frictional heating are computed and provided as energy sources to the convective model. Then, another five thousand years of thermal convection is modeled, etc ... The model runs until a statistical steady state is reached. Both models are described in more detail in the following sections.

2.1.2 Tidal model - viscoleastic tidal deformation of the ice shell with an embedded strike-slip fault

The tidal part of our model resolves the mechanical response of part of Europa's ice shell with embedded strike-slip fault subjected to diurnal tides while providing calculation of the heating production for the convective model.

We solve the equation of continuity (derived from the balance of mass) and the equation of motion (derived from the balance of linear momentum). As a step towards a more realistic model (compared to Nimmo and Gaidos (2002)) we impose an incompressible Maxwell rheology (in small-strain approximation) in the whole domain. The model equations read

$$\nabla \cdot \mathbf{v} = 0, \tag{2.1a}$$

$$-\nabla \mathrm{p} + \nabla \cdot \mathbb{S} + \varrho_i \mathbf{f} = \mathbf{0}, \tag{2.1b}$$

$$\dot{\mathbb{S}} = 2\mu \mathbb{D}^d(\mathbf{v}) - \frac{\mu}{\eta}\mathbb{S}. \tag{2.1c}$$

Here $\mathbf{v}$ is the (tidal) velocity, p denotes the pressure, $\mathbb{S}$ is the deviatoric part of the Cauchy stress tensor, ϱ_i is the density of the ice, $\mathbf{f}$ is the body force, μ is the shear modulus of ice, $\mathbb{D}^d(\mathbf{v})$ is the deviatoric symmetric velocity gradient, η is the viscosity specified below in the convection model part of the Section 2.1.3, and dot denotes the partial time derivative. For the values of all parameters, see Table 2.2.

We solve the system (2.1) in a part of Europa's ice shell containing an embedded strike-slip fault, cf. right part of Figure 2.4. In order to model the tidal forcing, one should (i) take the body force $\mathbf{f}$ in (2.1b) of the form $\mathbf{f}=\mathbf{g}+\nabla V_{\text{tidal}}$, where $\mathbf{g}$ is the gravity acceleration, and V_{tidal} is the tidal potential, and (ii) impose suitable kinematic or dynamic boundary conditions.

For simplicity, and also led by simple scaling arguments, we neglect the tidal contribution to the body force, i.e., we consider

$$\mathbf{f} = \mathbf{g} = (0, 0, -g), \tag{2.2}$$

where g is the magnitude of gravity acceleration, and we mimic the effect of tidal forcing entirely through the boundary conditions. In particular, we do so by prescribing the surface velocity in the y-direction (along the fault) on the top boundary; see section Boundary and Initial conditions below.

Time discretization

The only equation involving time is the rheology formula (2.1c). We approximate it using a one-step implicit (Euler) method as follows

$$\frac{\mathbb{S}^{k+1} - \mathbb{S}^k}{\mathrm{dt}} = 2\mu\mathbb{D}^d(\mathbf{v}^{k+1}) - \frac{\mu}{\eta}\mathbb{S}^{k+1}, \tag{2.3}$$

where $k+1, k$ distinguish variables from the current and previous time steps, respectively. Multiplying the equation by the time step dt and performing several adjustments:

$$\left(1 + \frac{\mu\ \mathrm{dt}}{\eta}\right)\mathbb{S}^{k+1} = \mathbb{S}^k + 2\mu\ \mathrm{dt}\,\mathbb{D}^d(\mathbf{v}^{k+1}),$$

and defining the Maxwell time as

$$\tau_M = \eta/\mu\,, \tag{2.4}$$

we obtain the approximation

$$\mathbb{S}^{k+1} = \frac{1}{1 + \frac{\mathrm{dt}}{\tau_M}}\mathbb{S}^k + \frac{2\mu\ \mathrm{dt}}{1 + \frac{\mathrm{dt}}{\tau_M}}\mathbb{D}^d(\mathbf{v}^{k+1}). \tag{2.5}$$

Alternatively, by extending the right-hand side by τ_M/τ_M, one arrives at

$$\mathbb{S}^{k+1} = \frac{\tau_M}{\tau_M + \ \mathrm{dt}}\mathbb{S}^k + \frac{2\eta\ \mathrm{dt}}{\tau_M + \ \mathrm{dt}}\mathbb{D}^d(\mathbf{v}^{k+1}). \tag{2.6}$$

The former expression is particularly useful for obtaining the elastic limit of the model, corresponding to $\eta \to \infty$, or, equivalently $\tau_M \to \infty$:

$$\lim_{\eta\to\infty} \mathbb{S}^{k+1} = \lim_{\eta\to\infty}\left\{\frac{1}{1 + \frac{\mathrm{dt}}{\tau_M}}\mathbb{S}^k + \frac{2\mu\ \mathrm{dt}}{1 + \frac{\mathrm{dt}}{\tau_M}}\mathbb{D}^d(\mathbf{v}^{k+1})\right\} = \mathbb{S}^k + 2\mu\ \mathrm{dt}\,\mathbb{D}^d(\mathbf{v}^{k+1}),$$

which is equivalent to $(\mathbb{S}^{k+1} - \mathbb{S}^k)/\,\mathrm{dt} = 2\mu\mathbb{D}^d(\mathbf{v}^{k+1})$. And that is the discretized form of $\dot{\mathbb{S}} = 2\mu\mathbb{D}(\mathbf{v}) = 2\mu\dot{\mathbb{D}}(\mathbf{u})$, i.e. time derivative of elastic rheology.

On the other hand, the second expression (eq. 2.6) is suitable for the application of the viscous limit, defined as $\mu \to \infty$, or, equivalently, $\tau_M \to 0$:

$$\lim_{\eta\to\infty} \mathbb{S}^{k+1} = \lim_{\eta\to\infty} \left\{ \frac{\tau_M}{\tau_M + \mathrm{dt}}\mathbb{S}^k + \frac{2\eta\,\mathrm{dt}}{\tau_M + \mathrm{dt}}\mathbb{D}(\mathbf{v}^{k+1}) \right\} = 0 + 2\eta\mathbb{D}(\mathbf{v}^{k+1}).$$

Hence,

$$\mathbb{S}^{k+1} = 2\eta\mathbb{D}(\mathbf{v}^{k+1}),$$

which is rheology for viscous material in the current $k+1$ time step.

We rewrite the two formulas using a shorthand notation

$$\mathbb{S}^{k+1} = \mathcal{K}^{k+1}\mathbb{S}^k + 2\,\mathcal{L}^{k+1}\mathbb{D}^d(\mathbf{v}^{k+1}), \tag{2.7a}$$

where either (useful for viscous limit):

$$\mathcal{K}^{k+1} = \frac{\tau_M}{\tau_M + \mathrm{dt}}, \quad \mathcal{L}^{k+1} = \frac{\eta\,\mathrm{dt}}{\tau_M + \mathrm{dt}}, \tag{2.7b}$$

or, equivalently, (useful for the elastic limit):

$$\mathcal{K}^{k+1} = \frac{1}{1 + \frac{dt}{\tau_M}}, \quad \mathcal{L}^{k+1} = \mu\,\mathrm{dt}\,\mathcal{K}^{k+1}. \tag{2.7c}$$

Dimensional reduction

We present further assumptions that allow us to reduce the three dimensional problem (modeling a part of Europa's ice shell with a preexisting fault in the middle, see Figure 2.4) into a two dimensional one, formulated in the cross-section perpendicular to the fault. In particular, we shall assume that the variations of velocity and physical properties along the fault (in the y-direction) are negligible and that the velocity depends spatially on x and z coordinates only:

$$\mathbf{v} = (0, \mathrm{v}(t, x, z), 0), \tag{2.8}$$

where t is time.

Such an assumption allows us to reduce the computational domain into a two-dimensional cross-section perpendicular to the fault. Taking into account the antisymmetry of the problem (assuming strike-slip motion), we can, therefore, approximate the surroundings of the fault just by one half of the two-dimensional cross-section; see square bounded by the white dashed line in Figure 2.4 and the final computational domain on Figure 2.6. In such representation, the top boundary of the computational domain represents the upper free surface, the bottom boundary stands for the shell-ocean boundary, the left side represents the fault plane, and the right side represents an interior surface within the ice shell.

Let us now inspect the implications of the above dimensional reduction on the governing equations 2.1. First, the symmetric velocity gradient for velocity defined as 2.8 becomes:

$$\mathbb{D}(\mathbf{v}) = \frac{1}{2}\begin{bmatrix} 0 & \frac{\partial \mathrm{v}}{\partial x} & 0 \\ \frac{\partial \mathrm{v}}{\partial x} & 0 & \frac{\partial \mathrm{v}}{\partial z} \\ 0 & \frac{\partial \mathrm{v}}{\partial z} & 0 \end{bmatrix}.$$

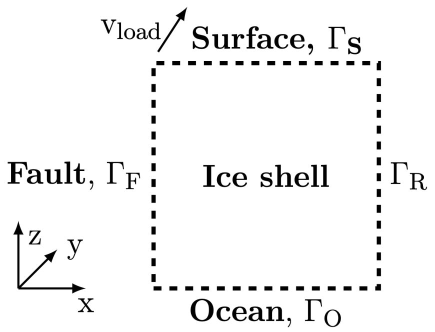

Figure 2.6: The computational domain for the numerical model of the vicinity of a strike-slip fault on Europa.

Note that the matrix is traceless (tr $\mathbb{D}(\mathbf{v}) = \nabla \cdot \mathbf{v} = 0$), consequently the symmetric gradient of velocity is equal to its deviatoric part: $\mathbb{D}^d = \mathbb{D}$. In addition, we have $\mathbb{D}_{xx} = \mathbb{D}_{yy} = \mathbb{D}_{zz} = \mathbb{D}_{xz} = \mathbb{D}_{zx} = 0$. Hence (see (2.7a)), if the initial deviatoric Cauchy stress tensor's diagonal elements $\mathbb{S}^0_{ii}$ are zero, then all the above-mentioned components of the deviatoric part of the stress tensor, i.e., the xx, yy, zz, xz and zx components, will remain zero throughout the whole time evolution. Therefore, defining the initial complete Cauchy stress tensor as $\mathbb{T}^0 = -p\mathbb{I} + \mathbb{S}^0$ and assuming $\mathbb{S}^0_{xx} = \mathbb{S}^0_{yy} = \mathbb{S}^0_{zz} = \mathbb{S}^0_{xz} = \mathbb{S}^0_{zx} = 0$, we get $\mathbb{S}^k_{xx} = \mathbb{S}^k_{yy} = \mathbb{S}^k_{zz} = \mathbb{S}^k_{xz} = \mathbb{S}^k_{zx} = 0$ for all time steps k.

Now, the continuity equation 2.1a is satisfied automatically, and we express the equation of motion 2.1b in index notation:

$$0 = -\frac{\partial \mathrm{p}}{\partial x} + \frac{\partial \mathbb{S}_{xx}}{\partial x} + \frac{\partial \mathbb{S}_{xy}}{\partial y} + \frac{\partial \mathbb{S}_{xz}}{\partial z} + f_x, \tag{2.9a}$$

$$0 = -\frac{\partial \mathrm{p}}{\partial y} + \frac{\partial \mathbb{S}_{xy}}{\partial x} + \frac{\partial \mathbb{S}_{yy}}{\partial y} + \frac{\partial \mathbb{S}_{yz}}{\partial z} + f_y, \tag{2.9b}$$

$$0 = -\frac{\partial \mathrm{p}}{\partial z} + \frac{\partial \mathbb{S}_{zx}}{\partial x} + \frac{\partial \mathbb{S}_{zy}}{\partial y} + \frac{\partial \mathbb{S}_{zz}}{\partial z} + f_z, \tag{2.9c}$$

We cross out the zero terms, i.e., $\mathbb{S}_{xx} = \mathbb{S}_{yy} = \mathbb{S}_{zz} = \mathbb{S}_{xz} = \mathbb{S}_{zx} = 0$ and also f_x and f_y, since we assume only gravitational force; see equation 2.2. Hence, using $f_z = -\varrho_i g f_z$ the system 2.1 reduces to

$$\frac{\partial \mathrm{p}}{\partial x} = 0,. \tag{2.10a}$$

$$\frac{\partial \mathbb{S}_{xy}}{\partial x} + \frac{\partial \mathbb{S}_{yz}}{\partial z} = 0, \tag{2.10b}$$

$$\frac{\partial \mathrm{p}}{\partial z} = -\varrho_i g. \tag{2.10c}$$

Equations 2.10a and 2.10c can be integrated and yield a hydrostatic pressure field. The only remaining non-trivial equation is 2.10b. Defining a stress vector $\mathbf{s} = (s_x, s_z) := (\mathbb{S}_{xy}, \mathbb{S}_{yz})$, we rewrite the equation 2.10b in the following vector form:

$$\mathrm{div}_{(x,z)}\mathbf{s} = 0. \tag{2.11}$$

Since all the components of the Cauchy stress tensor $\mathbb{S}$ except from xy, yz are zero, the Maxwell formula (eq. 2.1c) reduces to:

$$\dot{\mathbf{s}} = \mu \nabla_{(x,z)} \mathrm{v} - \frac{\mu}{\eta}\mathbf{s}. \tag{2.12}$$

Using the numerical approximation (eq. (2.7)) we get

$$\boxed{\mathbf{s}^{k+1} = \mathcal{K}^{k+1}\mathbf{s}^k + \mathcal{L}^{k+1}\nabla_{(x,z)}\mathrm{v}^{k+1}}. \tag{2.13}$$

Finally, we use the numerical approximation of vector $\mathbf{s}$ (eq. 2.13) to express the stress vector in equation 2.11

$$\begin{aligned} 0 &= \mathrm{div}_{(x,z)}\mathbf{s}^{k+1} \\ &= \frac{\partial}{\partial x}\left[\mathcal{K}^{k+1}s_x^k + \mathcal{L}^{k+1}\frac{\partial \mathrm{v}^{k+1}}{\partial x}\right] + \frac{\partial}{\partial z}\left[\mathcal{K}^{k+1}s_z^k + \mathcal{L}^{k+1}\frac{\partial \mathrm{v}^{k+1}}{\partial z}\right], \end{aligned} \tag{2.14}$$

and we omit the notation$_{(x,z)}$ assuming further on that all operators are in (x, z) coordinates only. Therefore the momentum balance reduces to the following scalar equation:

$$\boxed{\nabla \cdot \left(\mathcal{K}^{k+1}\mathbf{s}^k\right) + \nabla \cdot (\mathcal{L}^{k+1}\nabla \mathrm{v}^{k+1}) = 0.} \tag{2.15}$$

Fault description

We assume that the behavior of the fault (approximated through a boundary condition on the left side of the computational domain, cf. Figure 2.6) is governed by a relatively simple Mohr-Coulomb-type "stick-slip" friction criterion. However, ice-ice contact is known to exhibit more complex frictional properties, e.g., rate and state friction law, where the friction coefficient depends on both the slip velocity (rate) and an internal variable (state), that has its own evolution dynamics, see for example Fortt and Schulson (2009), Lishman et al. (2011) or Section 4.2.3 for a brief summary. In this part of the thesis, we use a constant value of the friction coefficient (μ_f=0.4 as a reference value), and we test the possible effect of a more complex description of fault behavior by considering the limiting cases (μ_f=0.1 and 0.8), see Section 2.1.6.

The Mohr-Coulomb criterion discriminates between the locked state (stick), which occurs in regions where the stress exerted on the fault is below the yield stress σ_Y, and the sliding regime (slip), which is activated when the friction force reaches this threshold. We introduce the slip velocity $\mathrm{v}_{\mathrm{slip}}$ as the tidal velocity (i.e., solution of eq. 2.15) at the fault:

$$\mathrm{v}_{\mathrm{slip}}(t, z) = \mathrm{v}(t, x{=}0, z). \tag{2.16}$$

The Mohr-Coulomb stick-slip friction criterion at the fault then reads:

$$\begin{aligned} \text{stick:} \quad \mathrm{v}_{\mathrm{slip}} = 0 \quad &\Leftrightarrow \quad |\mathrm{s}_x| < \sigma_Y, \\ \text{slip:} \quad \mathrm{v}_{\mathrm{slip}} \neq 0 \quad &\Leftrightarrow \quad |\mathrm{s}_x| = \sigma_Y. \end{aligned} \tag{2.17}$$

We approximate this behavior by a Navier-slip condition of the form:

$$\mathrm{s}_x = \beta_{\mathrm{eff}}\, \mathrm{v}_{\mathrm{slip}}, \tag{2.18a}$$

where β_{eff} is the effective sliding coefficient defined as:

$$\beta_{\text{eff}} = \frac{\beta^*}{\left[1 + \left(\frac{\beta^* |\mathrm{v}_{\text{slip}}|}{\sigma_Y}\right)^n\right]^{1/n}}, \tag{2.18b}$$

where β^* and n are real and integer parameters, respectively. The effective sliding coefficient β_{eff} prevents the shear stress s_x at the fault from exceeding the yield stress σ_Y and it corresponds to the stress-limiting viscosity in the fault zone approach explained in detail in the next chapter (see Section 3.1 for benchmarks and more details about the viscoelastic analogy for the contact problem).

Applying (2.18), the fault is always sliding even for an arbitrarily small applied stress. However, in regions with low applied stress with respect to σ_Y, the value of the effective sliding coefficient is $\beta_{\text{eff}} \simeq \beta^*$, where $\beta^* \gg 1\,\mathrm{Pa\,s\,m^{-1}}$, which implies that $|\mathrm{v}_{\text{slip}}| \ll 1$ and the fault in such locations is effectively locked. On the other hand, the value of β_{eff} can drop significantly whenever the yield stress σ_Y is approached. This, in turn, leads to a possibly very rapid sliding at the fault to ensure a sufficient stress drop for maintaining the stress at (or below) the threshold value σ_Y. Parameter n governs how fast the effective sliding coefficient switches from high friction below the yield stress to low friction when the yield stress is approached. The Mohr-Coulomb criterion corresponds to the limit $\beta^* \to \infty$ and $n \to \infty$, but in the simulations, we use $\beta^* = 10^{18}\,\mathrm{Pa\,s\,m^{-1}}$ and $n=2$.

We prescribe a Mohr-Coulomb-type form of the yield stress, which is given as a product of the coefficient of friction μ_f, the normal traction (positive for compression) and the reduction term, which reduces the coefficient of friction when meltwater is present on the fault (we suppose it works like a lubricant (Oksanen and Keinonen, 1982) and follow the viscosity reduction formula):

$$\sigma_Y = \mu_f \varrho_i g d \exp(-\gamma_f \Phi_s)\,, \tag{2.19}$$

where d is the depth measured from the surface downwards, γ_f is the yield stress reduction coefficient, and Φ_s is the regularized water content (volume fraction of water = porosity) defined in equation 2.25. Moreover, for numerical reasons, we replace the Mohr-Coulomb friction criterion (eq. 2.17) by its regularized version - the slip condition (eq. 2.18a) with an effective sliding coefficient (eq. 2.18b).

Boundary and Initial Conditions

We denote by Ω the computational domain and by $\partial\Omega$ its boundary, and we describe the top, bottom, right, and left boundary by $\Gamma_{\mathrm{S}}, \Gamma_{\mathrm{O}}, \Gamma_{\mathrm{R}}, \Gamma_{\mathrm{F}}$, respectively, see Figure 2.6. On the left boundary Γ_{F}, we prescribe the slip condition 2.18 mimicking the stick-slip behavior of the fault. In addition, we apply the free-slip condition on the bottom and the right boundary (Γ_{O} and Γ_{R} respectively), and on the top boundary (Γ_{S}), the loading velocity is prescribed through the Dirichlet boundary condition:

$$\mathrm{s}_z = 0 \text{ on } \Gamma_{\mathrm{O}}, \tag{2.20a}$$

$$\mathrm{s}_x = 0 \text{ on } \Gamma_{\mathrm{R}}, \tag{2.20b}$$

$$\mathrm{v} = \mathrm{v}_{\text{load}} = \frac{1}{2}\mathrm{v}^0_{\text{load}} \sin(\omega t) \text{ on } \Gamma_{\mathrm{S}}, \tag{2.20c}$$

where $\mathrm{v}_{\mathrm{load}}, \mathrm{v}_{\mathrm{load}}^0$ is the loading velocity and its amplitude and ω is the orbital frequency. Nimmo and Gaidos (2002) use the same approach for loading but with a constant loading velocity.

The tidal model is run from an undeformed stress-free state. In order to suppress the effect of initial conditions, five tidal periods are computed during each run of the tidal model.

Frictional and shear heating

As an output of the tidal model (that is used for coupling with the convection model), we need to evaluate the heating associated with the strike-slip motion at the fault and the resulting deformation of the shell in the fault's vicinity. We follow the approach of Nimmo and Gaidos (2002) and define the heating as composed of frictional heating Q_{fric} on the left boundary and shear heating Q_{shear} in the domain, averaged over the tidal (orbital) period P:

$$Q_{\mathrm{fric}} = \frac{1}{P}\int_0^P \sigma_Y |\mathrm{v}_{\mathrm{slip}}| \, \mathrm{dt}, \tag{2.21}$$

$$Q_{\mathrm{shear}} = \frac{1}{P}\int_0^P \frac{\mathbf{s}\cdot\mathbf{s}}{\eta} \, \mathrm{dt}. \tag{2.22}$$

2.1.3 The Convective Two-Phase Model

The convective model solves thermal convection in the ice shell on a geological timescale. Since it is taken from Kalousová et al. (2016), we do not go into details here. For more information, see the articles or Ph.D. thesis by Dr. Kalousová (`http://geo.mff.cuni.cz/~kalous/`), here we only summarize the model equations and later on, comment on the coupling with the tidal model.

Governing Equations

We present the governing equations of two-phase (water, ice) thermal convection, including the advection of water volume fraction (porosity), balances of mass, momentum, and energy. As in Kalousová et al. (2016), we consider a zero relative velocity between the phases; hence the liquid water is locked within and advected together with the deforming ice matrix (Tobie, 2003). Such an approach corresponds to the impermeable limit of the two-phase equations. The dimensional form of two-phase convection equations read as follows

$$\nabla\cdot\boldsymbol{v} = 0, \tag{2.23a}$$

$$\begin{aligned}\mathbf{0} &= -\nabla p - \Phi\Delta\varrho\mathbf{g} - (1-\Phi)\varrho_i\alpha\Delta T\mathbf{g} \\ &+ \nabla\left(\frac{(1-\Phi)\eta}{\Phi}(\nabla\cdot\boldsymbol{v})\right) \\ &+ \nabla\cdot\left((1-\Phi)\eta\Big[\nabla\boldsymbol{v} + (\nabla\boldsymbol{v})^T - \frac{2}{3}(\nabla\cdot\boldsymbol{v})\mathbb{I}\Big]\right),\end{aligned} \tag{2.23b}$$

$$\varrho_i c\left(\frac{\partial T}{\partial t} + \boldsymbol{v}\cdot\nabla T\right) + L_h r = \nabla\cdot(k(T)\nabla T) + Q, \tag{2.23c}$$

$$\frac{\partial \Phi}{\partial t} - \nabla \cdot \Big((1-\Phi)\boldsymbol{v} \Big) \;\; = \;\; \frac{r}{\varrho_i}. \tag{2.23d}$$

Here Φ is the porosity (volume fraction of water in the ice-water mixture), $\boldsymbol{v}$ is the ice matrix velocity, p is the excess water pressure with respect to the hydrostatic equilibrium pressure of pure ice, ϱ_w is the density of water, $\triangle\varrho = \varrho_i - \varrho_w$ is the density difference between the two phases, α is the ice thermal expansivity, T is the temperature, $\Delta T = T - T_\mathrm{m}$ is the temperature difference from the melting temperature, η is the ice shear viscosity, c is the specific heat of ice, L_h is the latent heat of melting of ice, r is the melt production rate (positive for melting), $k(T)$ is the temperature-dependent thermal conductivity (cf. below) and $Q = Q_\mathrm{shear}$ is the heating, taken as shear heating from the tidal model and defined in the tidal model part of Section 2.1.2.

Ice properties

Ice deforms by different mechanisms, with the prevalent one depending on the local thermo-mechanical conditions. In our model, we use a composite creep that combines volume and grain boundary diffusion, dislocation, basal slip, and grain-boundary sliding following Goldsby and Kohlstedt (2001). It can be characterized by a single effective viscosity defined as:

$$\eta = \left(\frac{1}{\eta^\mathrm{v}_\mathrm{diff}} + \frac{1}{\eta^\mathrm{b}_\mathrm{diff}} + \frac{1}{\eta_\mathrm{disl}} + \frac{1}{\eta_\mathrm{bs} + \eta_\mathrm{gbs}} \right)^{-1} \tag{2.24a}$$

where η_i denotes the viscosity of the particular mechanism that can, in general, depend on temperature, stress, and grain size as:

$$\eta_\mathrm{i} = \frac{1}{2} \frac{d_g^{m_i} T^{l_i}}{A_i \sigma_\mathrm{II}^{n_i - 1}} \exp\left(\frac{E_i}{RT} \right) , \tag{2.24b}$$

with d_g the grain size, σ_II the second invariant of the deviatoric stress tensor, and R the universal gas constant. The exponents m_i, n_i, and l_i, activation energy E_i and prefactor A_i are specific for each creep mechanism - we use values based on Goldsby and Kohlstedt (2001), which are summarized in Table 2.1. For both numerical and physical reasons, we impose a viscosity cut-off of at 10^{24}Pa s, which results in ten orders of magnitude viscosity contrast across the ice shell.

Table 2.1: Creep parameters of ice based on Goldsby and Kohlstedt (2001).

	T [K]	A_i [m^{m_i} Pa$^{-n_i}$ K^{l_i} s^{-1}]	n_i	m_i	l_i	E_i [kJ mol^{-1}]
$\eta^\mathrm{v}_\mathrm{diff}$		9.1×10^{-8}	1.0	2.0	1.0	59
$\eta^\mathrm{b}_\mathrm{diff}$		1.8×10^{-16}	1.0	3.0	1.0	49
η_disl	≤ 258	4.0×10^{-19}	4.0	0.0	0.0	60
	> 258	7.9×10^{5}	4.0	0.0	0.0	180
η_bs		2.2×10^{-7}	2.4	0.0	0.0	60
η_gbs	≤ 258	6.2×10^{-14}	1.8	1.4	0.0	49
	> 258	5.6×10^{15}	1.8	1.4	0.0	192

The presence of meltwater significantly reduces the viscosity of ice by attenuating the internal stress field in the ice crystals and thus promoting basal slip

(De La Chapelle et al., 1999). Following Tobie (2003), we include this effect by introducing a porosity-dependent factor into the formula for the effective ice viscosity.

However, in our particular case (and in contrast to Kalousová et al. (2016)), the porosity is concentrated in a relatively small area, and due to the representation by discontinuous elements (of zero degree, DG_0), substantial discontinuity can occur between the values on two adjacent elements. This leads to underestimating the viscosity reduction (and consequently of shear heating). Thus, we replace porosity with its regularized counterpart Φ_s (in the viscosity reduction term), obtained by the solution of:

$$-\epsilon_\Phi \triangle \Phi_s + \Phi_s = \Phi, \tag{2.25}$$

where ϵ_Φ is a smoothing parameter equal to 0.01. The resulting function Φ_s is represented by continuous Lagrange elements of the first degree (CG_1) and is used in the viscosity reduction as follows:

$$\eta = \eta_{\text{pure}} \exp(-\gamma \Phi_s), \tag{2.26}$$

with η_{pure} given by equation 2.24.

As in Kalousová et al. (2016), we choose $\gamma = 45$, which approximately corresponds to a reduction of viscosity by one order of magnitude with a 5% porosity increase, see De La Chapelle et al. (1999). The premelting effect, which results in an increase of activation energy near the melting point, is also taken into account (cf. Table 2.1).

The thermal conductivity of water ice is strongly dependent on temperature, and we employ the parameterization from Hobbs and Hobbs (1974):

$$k(T) = \frac{k_1}{T} + k_2\ . \tag{2.27}$$

The values of constants k_1 and k_2 are listed in Table 2.2 and lead to the conductivity of 2.28 $\mathrm{W\,m^{-1}\,K^{-1}}$ at the interface with the ocean and 5.35 $\mathrm{W\,m^{-1}\,K^{-1}}$ at Europa's surface.

Boundary and Initial Conditions

The governing equations (2.23) are supplemented with the following boundary conditions. The porosity equation (2.23d) does not require any boundary condition being hyperbolic and considering the absence of inflow boundaries. For the Stokes system (eqs. (2.23a), (2.23b)), free slip is applied on all boundaries, and the value of pressure is fixed in one corner of the computational domain:

$$\begin{aligned} \boldsymbol{v} \cdot \mathbf{n} &= 0\ , \qquad (2\eta \mathbb{D}(\boldsymbol{v})\mathbf{n})_\tau = 0 \qquad && \text{on } \partial\Omega, && (2.28a)\\ p &= p_0 && \text{(top left corner)}, && (2.28b) \end{aligned}$$

where $\mathbf{n}$ is the outer normal vector and the subscript τ denotes the tangential component of a vector. For the Laplace smoothening equation (2.25), we set the regularized porosity to be equal to the original one on all boundaries:

$$\Phi_s = \Phi \qquad \text{on } \partial\Omega. \tag{2.28c}$$

In the energy balance eq. (2.23c), we fix the temperature at the bottom (ice-ocean interface) at the melting point, and at the surface, we prescribe the value T_s:

$$T = T_\mathrm{m} \quad \text{on } \Gamma_\mathrm{O}, \qquad T = T_\mathrm{s} \quad \text{on } \Gamma_\mathrm{S}, \tag{2.28d}$$

see Table 2.2 for used values. On the left boundary (fault), we prescribe the normal heat flux corresponding to the frictional heating Q_fric based on the output of the tidal model (eq. 2.21):

$$-k\frac{\partial T}{\partial x} = Q_\mathrm{fric} \qquad \text{on } \Gamma_\mathrm{F}. \tag{2.28e}$$

Finally, the right boundary is considered thermally insulating:

$$k\frac{\partial T}{\partial x} = 0 \qquad \text{on } \Gamma_\mathrm{R}. \tag{2.28f}$$

Since this boundary is an interior surface within the ice shell, such a condition is somewhat artificial, albeit quite standard.

The convective model is initiated from a conductive/convective statistical steady-state (depending on the thickness of the ice shell).

2.1.4 Numerical scheme

The numerical solution is carried out using the open-source finite element software package FEniCS (`http://fenicsproject.org`; Logg et al., 2012; Alnaes et al., 2015).

Tidal model

To present the complete numerical approximation of the tidal model, we derive the weak form of model equations 2.15, multiplying it formally by a suitable test function v' and integrating over the computational domain Ω yields:

$$\int_\Omega \nabla \cdot (\mathcal{K}^{k+1}\mathbf{s}^k)\mathrm{v}' \;\mathrm{dx} \quad + \quad \int_\Omega \nabla \cdot (\mathcal{L}^{k+1}\nabla \mathrm{v}^{k+1})\mathrm{v}' \;\mathrm{dx} = 0. \tag{2.29}$$

Using the Gauss theorem, we get:

$$\begin{aligned} &- \int_\Omega \mathcal{K}^{k+1}\mathbf{s}^k \cdot \nabla\mathrm{v}' \;\mathrm{dx} + \underline{\textstyle\int_{\partial\Omega} \mathcal{K}^{k+1}\mathbf{s}^k \cdot (\mathrm{v}'\mathbf{n}) \;\mathrm{ds}} \\ &- \int_\Omega \mathcal{L}^{k+1}\nabla\mathrm{v}^{k+1} \cdot \nabla'\mathrm{v}' \;\mathrm{dx} + \underline{\textstyle\int_{\partial\Omega} \mathcal{L}^{k+1}\nabla\mathrm{v}^{k+1} \cdot (\mathrm{v}'\mathbf{n}) \;\mathrm{ds}} = 0, \end{aligned} \tag{2.30}$$

where $\mathbf{n} = (n_x, n_z)$. Using eq. 2.13 the terms underlined by blue color are equal to:

$$\underline{\textstyle\int_{\partial\Omega} \mathbf{s}^{k+1} \cdot (\mathrm{v}'\mathbf{n}) \;\mathrm{ds}} = \int_{\partial\Omega} (s_x^{k+1} n_x + s_z^{k+1} n_z)\mathrm{v}' \;\mathrm{ds}. \tag{2.31}$$

The surface integral on the right-hand side can be divided into four contributions over the four parts of the domain boundary. Due to the free slip conditions and the definition of $\mathbf{n}$ ($\mathbf{n} = (1, 0)$ on Γ_R and $\mathbf{n} = (0, 1)$ on Γ_O) the integrals over Γ_R and Γ_O are equal to zero. Since we prescribe the Dirichlet boundary condition for velocity on the top boundary, the integral is also zero there. Thus, equation

2.31 is reduced to the integral over the left boundary describing the fault, where the outer normal is equal to $\mathbf{n} = (-1, 0)$:

$$\int_{\partial\Omega} \mathbf{s}^{k+1} \cdot (\mathrm{v}'\mathbf{n})\ \mathrm{ds} = \int_{\Gamma_\mathrm{F}} (s_x^{k+1} n_x + s_z^{k+1} n_z)\mathrm{v}'\ \mathrm{ds} = -\int_{\Gamma_\mathrm{F}} s_x^{k+1}\mathrm{v}'\ \mathrm{ds}. \tag{2.32}$$

Furthermore, we use the Navier slip boundary condition (eq. 2.18) and the definition of slip velocity (eq. 2.16) to rewrite the integral over the left boundary Γ_F ($x = 0$):

$$\begin{aligned} -\int_{\Gamma_\mathrm{F}} s_x^{k+1}\mathrm{v}'\ \mathrm{ds} &\overset{\text{eq. 2.18}}{=} -\int_{\Gamma_\mathrm{F}} \beta_\mathrm{eff}\mathrm{v}_\mathrm{slip}^{k+1}\mathrm{v}'\ \mathrm{ds} \\ &= -\int_{\Gamma_\mathrm{F}} \frac{\beta^*}{\left[1 + \left(\frac{\beta^*\mathrm{v}_\mathrm{slip}}{\sigma_Y}\right)^n\right]^{1/n}} \mathrm{v}_\mathrm{slip}^{k+1}\mathrm{v}'\ \mathrm{ds}. \end{aligned} \tag{2.33}$$

Thus, the weak form of the governing tidal equation 2.15 is:

$$\boxed{\begin{aligned} \int_\Omega \mathcal{L}^{k+1}\nabla\mathrm{v}^{k+1} \cdot \nabla\mathrm{v}'\ \mathrm{dx} + \int_\Omega \mathcal{K}^{k+1}\mathbf{s}^k \cdot \nabla\mathrm{v}'\ \mathrm{dx} = \\ = -\int_{\partial\Gamma_\mathrm{F}} \frac{\beta^*}{\left[1 + \left(\frac{\beta^*\mathrm{v}_\mathrm{slip}^{k+1}}{\sigma_Y}\right)^n\right]^{1/n}} \mathrm{v}_\mathrm{slip}^{k+1}\mathrm{v}'\ \mathrm{ds}, \end{aligned}} \tag{2.34}$$

where the stress vector is updated as:

$$\mathbf{s}^k = \mathcal{K}^k\mathbf{s}^{k-1} + \mathcal{L}^k\nabla\mathrm{v}^k. \tag{2.35}$$

Equation 2.34 represents an elliptic problem in terms of the tidal velocity v and is discretized in space by CG_1 elements, i.e., piecewise continuous linear Lagrange elements. In each call of the tidal solver, five orbital periods with the time resolution of fifty time steps per period are computed.

Heating

The numerical approximation of the frictional and shear heating is obtained by averaging all the values calculated during the last run (orbital) period P as in eqs. 2.21 and 2.22. Several numerical problems arose during the development of the heating approximation.

First, to some extent, sliding always occurs on the fault, see Fault description in Section 2.1.2, the frictional heating is always nonzero, even in the effectively locked (inactive) parts of the fault. Hence, we define the fault activation depth d_a as the depth, where the $|\mathrm{v}_\mathrm{slip}|$ drops below ϵ^k equal to 2% of its maximal value, i.e., we compute

$$Q_\mathrm{fric} \sim \frac{1}{\mathrm{K}}\sum_{k=1}^{\mathrm{K}} Q_\mathrm{fric}^k, \tag{2.36a}$$

$$Q_\mathrm{fric}^k = \begin{cases} \sigma_Y^k|\mathrm{v}_\mathrm{slip}^k| & \text{if } |\mathrm{v}_\mathrm{slip}^k| > \epsilon^k, \\ 0 & \text{elsewhere,} \end{cases} \tag{2.36b}$$

$$\epsilon^k = 0.02 \max_{l=1,\ldots,k-1} |\mathrm{v}_\mathrm{slip}^l|, \tag{2.36c}$$

where k denotes the current time step and K denotes the total number of time steps (fifty).

Second, in some cases (typically in high-viscosity regions), evaluation of the shear heating as defined in eq. 2.22 becomes numerically unstable due to the multiplication of a very small number with a very large number (in situations corresponding to $\eta \gg 1$, hence $\frac{1}{\eta} \ll 1$, while $\mathbf{s} \cdot \mathbf{s} \gg 1$). Alternatively, one may consider (a formally equivalent) formula for viscous dissipation:

$$Q_{\text{shear}} = \frac{1}{P} \int_0^P \eta \Big(\nabla \mathrm{v} - \frac{\dot{\mathbf{s}}}{\mu} \Big) \cdot \Big(\nabla \mathrm{v} - \frac{\dot{\mathbf{s}}}{\mu} \Big) \, \mathrm{dt}, \tag{2.37}$$

where we subtract the elastic part of the deformation from the gradient of velocity in order to include the viscous deformation, only.

We have numerically confirmed that each of the two formulas (eqs. 2.22 and 2.37) for Q_{shear} leads to an overestimation of the value of shear heating in certain (differing) situations. Thus, as a partial remedy, we evaluate both equations and consider the minimum of these two values to be the correct one. Hence, shear heating passed to the convective model is defined as:

$$Q_{\text{shear}} = \min \Big\{ Q^1_{\text{shear}}, Q^2_{\text{shear}} \Big\} \tag{2.38a}$$

$$\text{where } Q^1_{\text{shear}} = \frac{1}{P} \int_0^P \frac{\mathbf{s} \cdot \mathbf{s}}{\eta} \, \mathrm{dt}, \tag{2.38b}$$

$$Q^2_{\text{shear}} = \frac{1}{P} \int_0^P \eta \Big(\nabla \mathrm{v} - \frac{\dot{\mathbf{s}}}{\mu} \Big) \cdot \Big(\nabla \mathrm{v} - \frac{\dot{\mathbf{s}}}{\mu} \Big) \, \mathrm{dt}\,, \tag{2.38c}$$

which is numerically approximated as follows:

$$Q_{\text{shear}} \sim Q^k_{\text{shear}} = \min \Big\{ Q^{1,k}_{\text{shear}}, Q^{2,k}_{\text{shear}} \Big\} \tag{2.38d}$$

$$Q^{1,k}_{\text{shear}} = \frac{1}{\eta^l} \frac{1}{\mathrm{K}} \sum_{k=1}^{\mathrm{K}} \mathbf{s}^k \cdot \mathbf{s}^k, \tag{2.38e}$$

$$Q^{2,k}_{\text{shear}} = \frac{\eta^l}{\mathrm{K}} \sum_{k=1}^{\mathrm{K}} \Big(\nabla \mathrm{v}^k - \frac{\mathbf{s}^k - \mathbf{s}^{k-1}}{\mu \ \mathrm{dt}} \Big) \cdot \Big(\nabla \mathrm{v}^k - \frac{\mathbf{s}^k - \mathbf{s}^{k-1}}{\mu \ \mathrm{dt}} \Big) \Big\}, \tag{2.38f}$$

where indices $k, k-1$ denote the approximations of variables in the current and previous time step in the tidal model, respectively, whereas l denotes the current time step in the convective model.

Finally, in the case of extensive heating, the usual frequency of running the tidal model (once per five thousand years in the convective model, see the flow chart on Figure 2.5), might not be sufficient. When the heating is high enough to produce a quick increase in porosity, a lack of feedback between the viscosity and porosity leads to an overestimation of the heating since the porosity reduces the viscosity and is not updated often enough. As the calculation of the tidal model in every time step of the convective model is impossible due to computational reasons, we introduce a reduction of the heating production with porosity in every convectional time step and recompute the tidal model every five thousand years.

The shear heating is lowered in a similar way as the viscosity, and the frictional heating as the coefficient of friction, which is reasonable since both are linearly dependent on these variables. We denote $\Delta\Phi_s = \Phi_s^l - \Phi_s^{lt}$ the difference in porosity in the current time step (denoted by l) and the time step, when the tidal model was run for the last time (lt):

$$
\begin{aligned}
Q_{\text{shear}}^{l+1} &= \exp[-\gamma(\Delta\Phi_s)]\, Q_{\text{shear}}^{lt}, && (2.39)\\
Q_{\text{fric}}^{l+1} &= \exp[-\gamma_f(\Delta\Phi_s)]\, Q_{\text{fric}}^{lt}. && (2.40)
\end{aligned}
$$

Summary of all discretized equations

We search for v^{k+1} in:

$$
\begin{aligned}
&\int_\Omega \mathcal{L}^{k+1} \nabla \mathrm{v}^{k+1} \cdot \nabla \mathrm{v}' \ \mathrm{dx} + \int_\Omega \mathcal{K}^{k+1} \mathbf{s}^k \cdot \nabla \mathrm{v}' \ \mathrm{dx} = \\
&\qquad = -\int_{\Gamma_{\mathrm{F}}} \frac{\beta^*}{\left[1 + \left(\frac{\beta^* \mathrm{v}_{\text{slip}}^{k+1}}{\sigma_Y}\right)^n\right]^{1/n}} \mathrm{v}^{k+1} \mathrm{v}' \ \mathrm{ds}, \qquad (2.41\text{a})
\end{aligned}
$$

where the yield stress and slip velocity are defined as follows:

$$
\begin{aligned}
\sigma_Y &= \mu_f \varrho_i g d \exp(-\gamma_f \Phi_s), && (2.41\text{b})\\
\mathrm{v}_{\text{slip}}(t,z) &= \mathrm{v}(t, x{=}0, z). && (2.41\text{c})
\end{aligned}
$$

The stress vector is updated as:

$$
\mathbf{s}^k = \mathcal{K}^k \mathbf{s}^{k-1} + \mathcal{L}^k \nabla \mathrm{v}^k, \qquad (2.41\text{d})
$$

with the coefficients defined as either (useful for viscous limit):

$$
\mathcal{K}^{k+1} = \frac{\tau_M}{\tau_M + \ \mathrm{dt}}, \quad \mathcal{L}^{k+1} = \frac{\eta \ \mathrm{dt}}{\tau_M + \ \mathrm{dt}}, \qquad (2.41\text{e})
$$

or, equivalently, (useful for the elastic limit):

$$
\mathcal{K}^{k+1} = \frac{1}{1 + \frac{dt}{\tau_M}}, \quad \mathcal{L}^{k+1} = \mu \ \mathrm{dt}\, \mathcal{K}^{k+1}. \qquad (2.41\text{f})
$$

Convective model

The convective model is the two-phase convection model developed by Kalousová et al. (2016). System (2.23) is the classical incompressible Stokes-Fourier system: we use CG_1-CG_2 Taylor-Hood elements for the pressure p and velocity $\boldsymbol{v}$, CG_2 elements for the temperature T and DG_0 discontinuous Lagrange elements for porosity (CG_1 Lagrange elements for regularized porosity). The time discretization of the energy balance (2.23c) is carried out through the traditional Crank-Nicolson scheme. The time step is constrained by a local CFL condition and adaptively controlled such that the maximal temperature change between two subsequent time steps does not exceed 0.5 K.

2.1.5 Benchmarks

Here, we present benchmarks obtained by the model described in the previous section.

Model of Nimmo and Gaidos (2002)

First, we briefly introduce the model of Nimmo and Gaidos (2002), which describes thermo-mechanical evolution of a strike-slip fault and its vicinity. The model determines velocity and temperature field in a 2D cartesian domain - a cross-section perpendicular to the fault plane. The model domain is divided into an upper brittle part underlain by a ductile part; see Figure 2.7. The fault plane intersects the model domain in half.

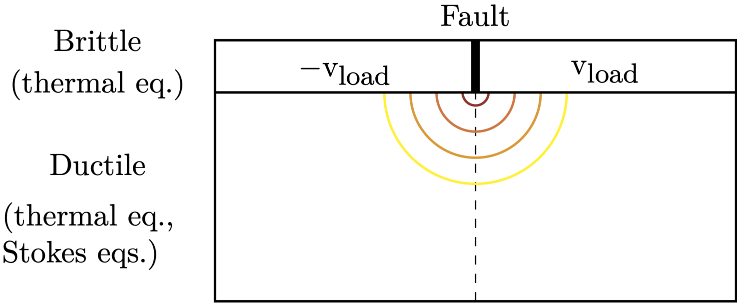

Figure 2.7: Sketch of the model of europan strike-slip fault and its vicinity according to Nimmo and Gaidos (2002). The colored lines show a sketch of the resulting steady-state distribution of temperature anomaly.

The left and right upper brittle blocks are mutually shearing in a strike-slip manner as rigid bodies with a prescribed velocity, dragging the viscous ductile material underneath. In the ductile part of the domain underlying the brittle one, the velocity field is sought as the solution of the Stokes equation with the imposed Dirichlet boundary condition at the top while being continuous across the fault plane. The thickness of the brittle layer thus specifies the depth of the strike-slip fault.

The temperature in the whole domain is searched for as the solution of the heat conduction equation with two internal heating sources: viscous dissipation (in the ductile domain) $Q_{\mathrm{shear}} = \mathbb{S} : \mathbb{D} = 2\eta\mathbb{D}(\mathrm{v}) : \mathbb{D}(\mathrm{v})$, and frictional heating at the fault (in the brittle zone) $Q_{\mathrm{fric}} = \mu_f \varrho_i g d |\mathrm{v}_{\mathrm{slip}}|$, where the notation is the same as in the previous section with $|\mathrm{v}_{\mathrm{slip}}|$ denoting the magnitude of slip velocity defined as the mutual movement of the fault's side, i.e., in this case, $2\mathrm{v}_{\mathrm{load}}$. The model seeks a steady state solution for temperature and velocity.

In a brief summary, from Nimmo and Gaidos (2002) we conclude that:

1. Since no strike-slip motion can (by definition) occur in the ductile part of the model, the velocity at the fault plane drops from the prescribed value $\mathrm{v}_{\mathrm{load}}$ to zero at the brittle-ductile boundary. Hence, the deformation rate and thus also the heating rate and temperature anomaly are the biggest there; see colored half circles sketched in Figure 2.7 simulating thermal and heating distribution or actual heat production in Figure 2.8.

2. The maximum temperature anomaly is about 66 K.

3. The highest heating rate is right below the fault, and it reaches peak values of $10^{-4}\,\mathrm{W\,m^{-3}}$ for the considered rheological and loading parameters.

4. Near surface melting, i.e., temperature exceeding the melting point, could occur for loading velocities greater than $10^{-6}\mathrm{m\,s^{-1}}$.

Benchmark - reproducing the results by Nimmo and Gaidos (2002)

First, in order to check our code's performance against the results of Nimmo and Gaidos (2002), we made several adjustments to the model presented in Sections 2.1.1 - 2.1.4 in order to mimic the setting by Nimmo and Gaidos (2002):

1. We employ purely viscous ice rheology, i.e., we set $\mathcal{K} = 0\,\forall k$ in eqs. 2.41a and 2.41d;

2. We solve the Stokes equations 2.41a in the ductile part of the domain, only, while prescribing the velocity (as a bulk Dirichlet boundary condition) in the brittle part of the domain $\mathrm{v} = \mathrm{v}_{\mathrm{load}} = 6 \times 10^{-7}\mathrm{m\,s^{-1}}$;

3. We define the viscosity as

$$\eta = \frac{|T|}{2B_N} \exp\left(\frac{E}{R|T|}\right), \tag{2.42}$$

   where B_N=$1.88626 \times 10^{-8}\,\mathrm{K\,Pa^{-1}\,s^{-1}}$, E=$20\,\mathrm{kJ\,mol^{-1}}$ is the activation energy (Nimmo and Gaidos, 2002).

4. We prescribe the motion at the fault plane as in Nimmo and Gaidos (2002), i.e., strike-slip motion in the upper brittle part and zero slip in the bottom ductile part.

5. The computational domain is prescribed consistently with Nimmo and Gaidos (2002): fifteen kilometers wide and twenty kilometers high ($D = 20$km).

The coefficient of friction (required only for the evaluation of frictional heating) is taken as μ_f=0.1. The density of ice is taken as ϱ_i=$1000\,\mathrm{kgm^{-3}}$, the amplitude of gravity acceleration g is equal to $1.3\,\mathrm{m\,s^{-2}}$ and the surface temperature T_S is 120K. The gas constant R, the melting (bottom) temperature T_{m}, and the specific heat c remain the same as in Table 2.2.

The shear heating is computed in the ductile part of the domain only, and it is set to zero in the brittle part. In contrast, the frictional heating is zero in the ductile part since there is no slip, and it is effectively prescribed in the brittle part as the velocity is defined there:

$$Q_{\mathrm{fric}} = \frac{1}{2}\mathrm{v}_{\mathrm{load}}\mu_f \varrho_i g d. \tag{2.43}$$

We compute the steady states of velocity and temperature fields and show the comparison of the velocity isolines (cf. Figure 2.8 a) and heat production (cf. Figure 2.8 b) obtained by our code (the right half of each subfigure) and published in Nimmo and Gaidos (2002) (the left half of each subfigure). The fit of the results is satisfactory, giving us confidence that in this setting, our model is working well.

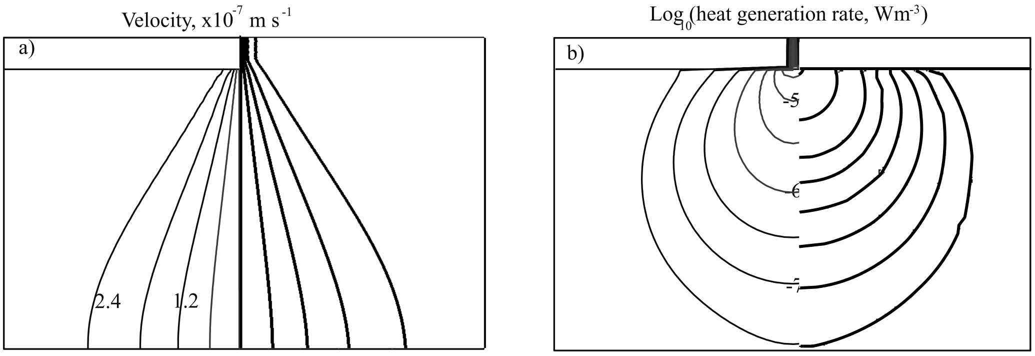

Figure 2.8: The comparison of steady state velocity (a) and heat production in logarithmic scale (b). Our results are plotted in the right half of each plot, in the left part we show the results of Nimmo and Gaidos (2002).

Benchmark with Comsol Multiphysics

In this benchmark, we test whether the tidal model works correctly with periodic velocity loading by comparing our results with the results obtained by Comsol Multiphysics®(COMSOL Multiphysics, 1998); specifically, we model the mechanical part of the problem, only. We solve the viscoelastic tidal deformation with a fault activating according to the Coulomb-type criterion with the deformation induced by strike-slip motion prescribed through velocity on the top of the domain. In Comsol Multiphysics, the problem was implemented in the general PDE module.

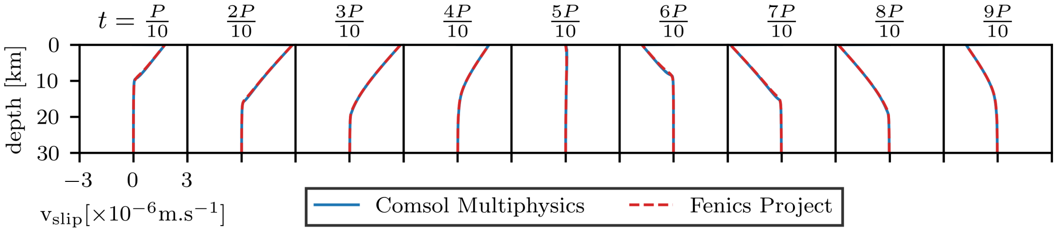

Figure 2.9: The slip velocity on the fault captured in every tenth of the period, blue full line denotes results calculated by Comsol Multiphysics, red dashed line stands for our calculations computed by Fenics Project.

On Figure 2.9, we compare the time evolution of slip velocity throughout one tidal period, calculated by the two different softwares: results calculated by the above-presented model in FEniCS Software are plotted by red dashed line while results computed by Comsol Multiphysics are denoted by blue full line. Note that the values of the slip velocity correspond well throughout the period. In addition, we also concentrate on the development of the fault's activation depth, which is for this purpose defined as the depth, where the $|v_{slip}|$ drops to 2% of its maximal value, so visually the minimal depth, where the slip velocity is approximately zero. We observe that the penetration depth is the same for both codes in all presented instants.

To summarize, in the viscoelastic regime, and with an evolving depth of the active part of the fault according to the Coulomb-type activation criterion, the model performs well. As a consequence, we have confidence that the code provides reliable estimates of the shear heating in bulk. The same holds for the slip velocity and activation depth (i.e., sliding part of the fault), implying reliable estimates of the frictional heating.

2.1.6 Results: Heat and meltwater production on strike-slip faults of Europa

Several indications point at the possibility of the near-surface meltwater presence on Europa, (Dombard et al., 2013; Schmidt et al., 2011), also the calculations of Nimmo and Gaidos (2002) hinted at the prospect of near-surface melting at strike-slip faults for high enough surface/loading velocities. In addition, the strike-slip faults were also identified by Kalousová et al. (2016) as one of the most favorable scenarios for producing water. Therefore, we have tried to overcome the main limitations of the model published by Nimmo and Gaidos (2002) - simplified viscous ice rheology and an a priori prescribed motion and depth of the active fault - and, using our novel model, we have tried to evaluate the magnitude of heating and meltwater production induced by strike-slip movements on the faults. Below, we summarize the results obtained with our 2D thermo-mechanical model of the strike-slip fault and its vicinity. The results turned out to be negative in the sense that only a limited amount of subsurface stable melt can probably be produced by such a mechanism. Consequently, these results turned out to have low publication potential, and they were not published in dedicated manuscripts, and were only presented at seminars and conference talks.

With the goal to address the question of heat and meltwater generation at strike-slip faults, we have changed the setting compared to Nimmo and Gaidos (2002) towards a more realistic description of the fault and its behavior:

- We simulate the diurnal tides (reactivating the old faults) by introducing the periodic velocity loading on the top boundary, see eq. 2.20c.
- In our model, the depth of the fault can develop self-consistently since we introduce the Mohr-Coulomb stick-slip friction criterion through the effective sliding coefficient and yield stress (the stress on the fault must exceed the friction force holding the fault together).
- We impose Maxwell viscoelastic rather than viscous rheology in the tidal model, which is much more appropriate for the periodic tidal forcing. As a consequence, we also do not need to define the brittle-ductile transition.
- In order to address the meltwater generation and transport on the convection timescale, we employ a two-phase convection model with a realistic temperature and stress-dependent viscous rheology that involves all known deformation mechanisms.

Results - setting analogous to Nimmo and Gaidos (2002)

First, we try to compare the results of our model in a setting analogous to that of Nimmo and Gaidos (2002). In particular, we use the model presented in Sections 2.1.1 - 2.1.4 and we use the domain size and viscosity law (in our Maxwell viscoelastic model for tidal deformation) as presented in Nimmo and Gaidos (2002). We keep the periodic strike-slip loading.

Taking the amplitude of the periodic velocity forcing equal to the (constant) loading velocity of Nimmo and Gaidos (2002), our results show that the frictional heating is much bigger than the viscous dissipation; the values of viscous dissipation presented in Nimmo and Gaidos (2002) has not been reached, and no significant heating of the ice is observed, see Figure 2.10.

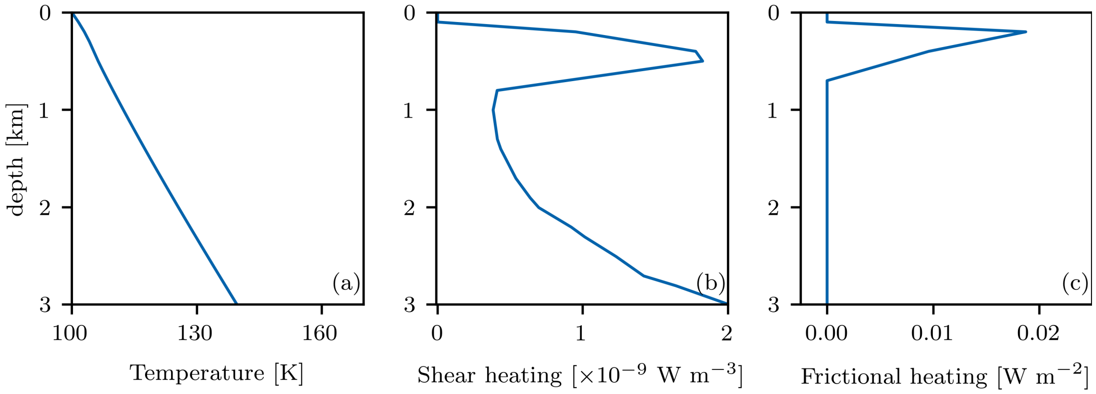

Figure 2.10: We plot the steady state variables on the fault (top three kilometers of the ice shell) of a run calculated with our model and viscosity according to Nimmo and Gaidos (2002). From the left, we show a) temperature, b) shear heating, and c) frictional heating.

There are several reasons for which the heating does not reach the values presented in Nimmo and Gaidos (2002), some of them might be manifested by steady-state temperature fields obtained with different boundary conditions for velocity, i.e., different velocity loading, see Figure 2.11:

1. As we are employing visco-elastic rheology of ice in the tidal model, most of the deformation in the bulk is reversible and does not contribute to dissipative shear heating (viscous dissipation). This contribution, on the other hand, is a substantial source in Nimmo and Gaidos (2002), and we argue that their estimate is, from this point of view, highly overestimated.

2. Since we consider a self-evolving fault by actually computing the activation depth based on a Coulomb criterion, the fault in our simulations does not propagate deep enough to produce substantial frictional heating (the activation depth is 2 km in Nimmo and Gaidos (2002)), in our model the typical value is around 0.5 km), compare a) and b) thermal fields in Figure 2.11.

3. In our model, the slip velocity at the fault plane decreases to zero smoothly, whereas in Nimmo and Gaidos (2002), abrupt drop is prescribed at the brittle-ductile transition (from loading velocity to zero); thus, in our case, the viscous dissipation is much smaller - compare b) and c) thermal fields in Figure 2.11.

Results with revised parameters

In this subsection, we revise the parameters chosen by Nimmo and Gaidos (2002) based on the observations of lateral offset on Europa; see Table 2.2. According to

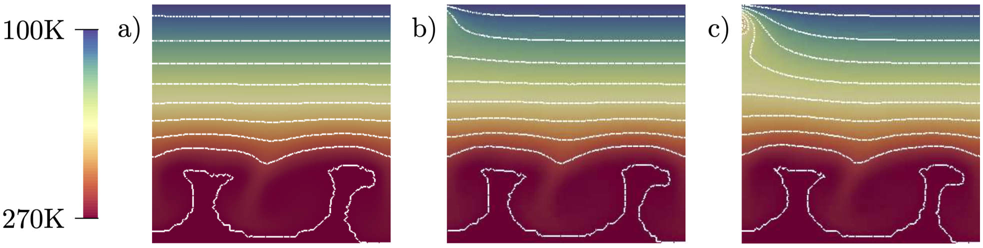

Figure 2.11: Steady state temperature fields for different velocity boundary conditions: a) the velocity is prescribed on the top and on the left boundary up to half kilometer depth, no visible effect on the thermal field, b) the velocity is prescribed on the top and on the left boundary linearly decreasing up to three kilometers depth, small effect on the thermal field, c) the velocity is prescribed on the top and the left boundary up to three kilometers depth with an abrupt drop from $\frac{1}{2}\mathrm{v}^0_{\mathrm{load}}$ to zero in the three kilometers.

Table 2.2: Model parameters

Symbol	Variable	Value	Unit
D	ice shell thickness	30	km
g	surface gravity magnitude	1.315	$\mathrm{m\,s^{-2}}$
ϱ_w	density of water	1000	$\mathrm{kg\,m^{-3}}$
ϱ_i	density of ice	920	$\mathrm{kg\,m^{-3}}$
Tidal model parameters			
β^*	background value of the effective sliding coefficient	10^{18}	$\mathrm{Pa\,s\,m^{-1}}$
n	sliding law exponent	2	-
μ	shear modulus of ice	3.3	GPa
μ_f $^\bullet$	ice friction coefficient	0.1, 0.4, 0.8	-
$\mathrm{v}^0_{\mathrm{load}}$ $^\bullet$	amplitude of loading velocity	1	$10^{-5}\mathrm{m\,s^{-1}}$
ω	orbital frequency	2.05×10^{-5}	$\mathrm{s^{-1}}$
P	tidal period	3.55	day
Convective model parameters			
α	thermal expansivity	1.6×10^{-4}	$\mathrm{K^{-1}}$
c	specific heat of ice	2100	$\mathrm{J\,kg^{-1}\,K^{-1}}$
d_g	grain size	0.7	mm
γ	viscosity reduction parameter	45	-
γ_f	frictional heating reduction parameter	45	-
η_{cut}	viscosity cut-off	1e24	$\mathrm{Pa\,s}$
R	universal gas constant	8.314	$\mathrm{J\,K^{-1}\,mol^{-1}}$
k_1	constant in eq. 2.27	488.12	$\mathrm{W\,m^{-1}}$
k_2	constant in eq. 2.27	0.4685	$\mathrm{W\,m^{-1}\,K^{-1}}$
T_{m}	melting temperature	270	K
T_{s}	surface temperature	100	K

The $^\bullet$ symbol indicates the model parameters varied in the parametric study.

Greenberg et al. (1998) a displacement of roughly one meter per orbit is plausible on Astypalaea Linea, a 810 km strike-slip fault, located near the south pole of Europa (Tufts et al., 1999). To produce a meter per orbit through a periodic loading velocity, the amplitude of $\mathrm{v}_{\mathrm{load}}^0 = \frac{\pi}{P} \sim 10^{-5}\mathrm{m\,s^{-1}}$ is necessary, since:

$$\delta = \int_0^{P/2} \frac{1}{2}\mathrm{v}_{\mathrm{load}}^0 \sin(\omega t) = \mathrm{v}_{\mathrm{load}}^0 \frac{P}{2\pi},$$

where displacement $\delta \sim 0.5$m (half a meter of displacement on one side of the fault by half period). Therefore, we use the value of 10^{-5} $\mathrm{ms^{-1}}$ as a reference one. Moreover, we choose the mean value from Fortt and Schulson (2009) for the coefficient of friction: μ_f=0.4.

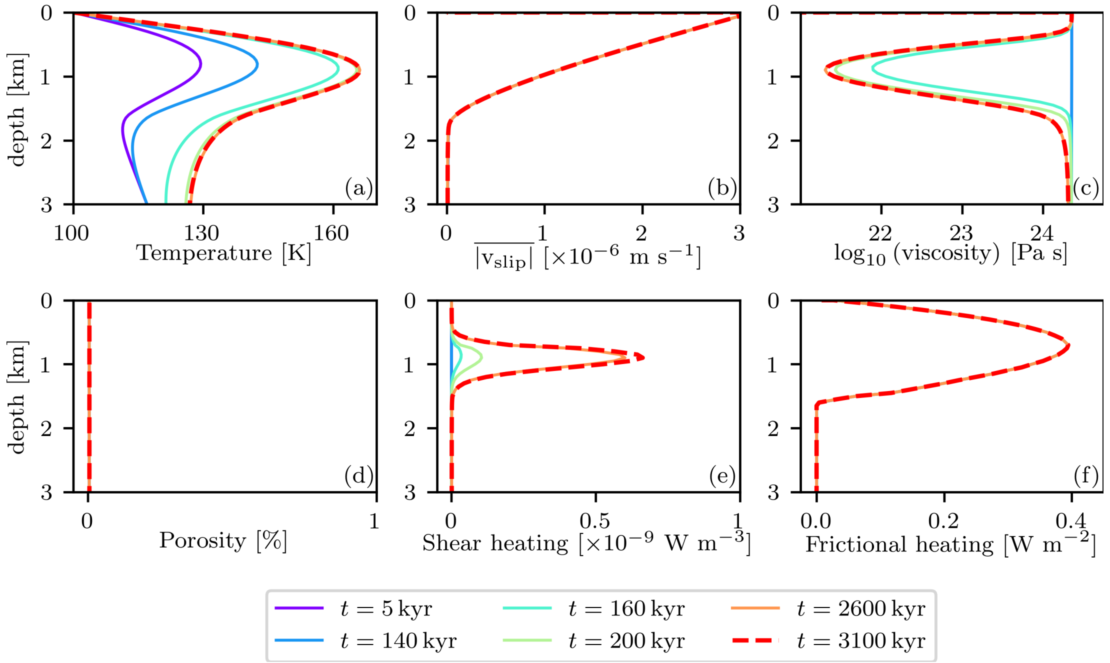

Figure 2.12: We plot the time evolution (colors) of reference run variables on the fault (top three kilometers of the ice shell) until the steady state is reached (red dashed line - 3100 kyr after the start of the calculation). From the top left to the bottom right, we show: a) temperature, b) the average (over the period) of the absolute slip velocity, c) viscosity (in logarithmic scale), d) porosity, e) shear heating, and f) frictional heating.

First, we present the time evolution of the reference run, where we plot the temperature, an average (over the tidal period) of the absolute value of slip velocity, viscosity, porosity, and shear and frictional heating in the top three kilometers of the fault (represented by the left boundary Γ_F), see Figure 2.12. We start the calculation from a thermal steady state (convection). Immediately after the start of the calculation (purple line), the frictional heating (panel f) starts to warm up the fault, thus reducing the viscosity (panel c). Since frictional heating is a surface source, only the fault is substantially heated, while its vicinity is slowly warmed up by thermal conduction. Once the viscosity drops enough (panel c, 160 kyr, turquoise color) the shear heating (panel e) starts to grow. Nevertheless, it never reaches substantial values to promote significant heating of ice. Finally, after approximately three thousand years (red dashed line), a (statistical) steady state is reached with a thermal anomaly of approximately 40 K (panel a) and no porosity (volume fraction of water) present (panel d).

Let us now present the results of a simple parametric study to infer the influence of the main model parameters: the coefficient of friction and the amplitude of the loading velocity.

Dependence on the coefficient of friction

Here, we present the steady state results for different values of the coefficient of friction, see Figure 2.13, minimal (0.1) and maximal (0.8) values were chosen according to Fortt and Schulson (2009).

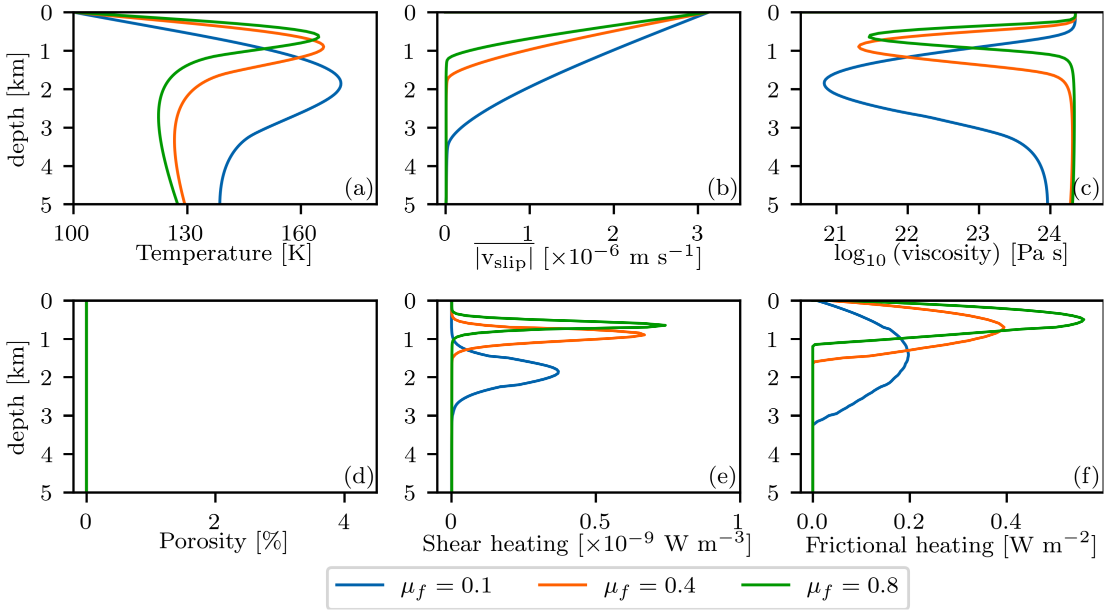

Figure 2.13: The comparison of the steady state variables plotted in the top five kilometers of the fault for three different values of the coefficient of friction (colors).

The choice of coefficient of friction directly affects the activation depth of the fault, see panel b, where the average of absolute slip velocity is plotted. The activation depth of the fault (defined as the minimal depth, where $\overline{|\mathrm{v_{slip}}|}$ is equal to 2% of its maximal value) is approximately proportional to the inverse value of the coefficient of friction, e.g., the fault penetrates much deeper for the coefficient of friction μ_f=0.1 (blue color) than for the reference run (μ_f=0.4, orange color). Since the frictional heating (panel f) is linearly dependent on the coefficient of friction, its maximal value is the smallest for the smallest coefficient of friction; however, as the fault penetrates deeper, the nonzero frictional heating covers a bigger surface. Thus surprisingly, the run with the smallest coefficient of friction produces the highest thermal anomaly (blue line, panel a), even though the shear heating (panel e) is not high enough to warm up the ice. The only difference remains in the depth of the shear heating maxima, which depends on the location of viscosity minimum (panel c), approximately one kilometer above the activation depth of the fault.

To summarize, the coefficient of friction has a substantial influence on the activation depth, which in return affects other properties; however, even the smallest coefficient of friction is not small enough for the penetration depth to reach the low viscosity zone; thus, the shear heating is negligible, and no porosity (panel d) is produced.

Dependence on the loading velocity amplitude

Here, we present the steady state results for different loading velocity amplitudes, varying the reference value by ± 50%.

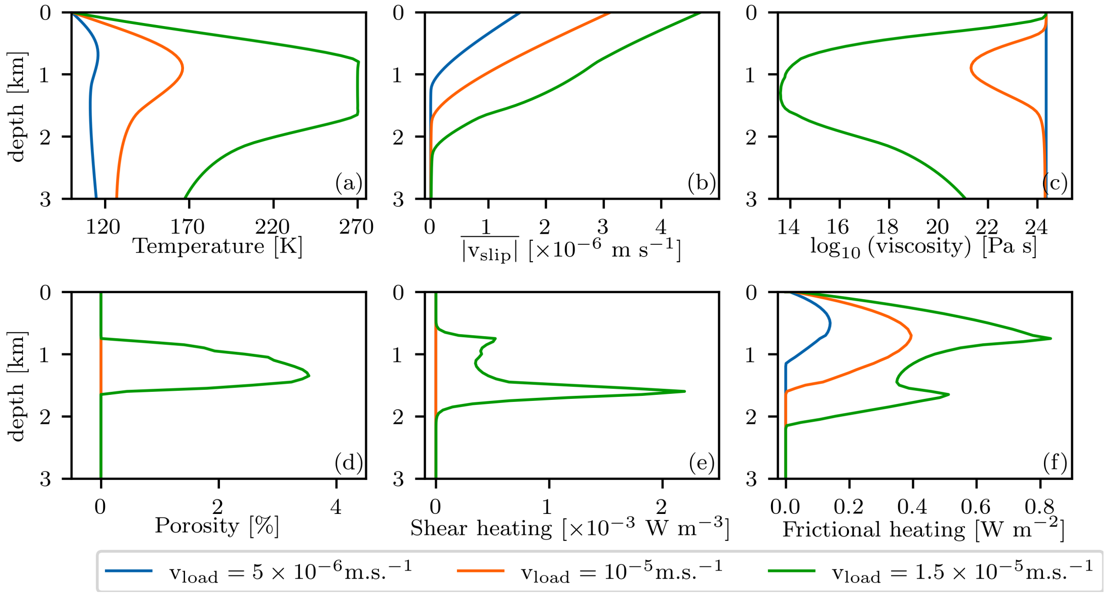

Figure 2.14: The comparison of the steady state variables plotted in the top three kilometers of the fault for three different values of the loading velocity amplitude (colors).

The loading velocity amplitude has a substantial influence on the results; increasing the reference loading velocity amplitude by 50% (green lines in Figure 2.14) results in more than 100K difference in the temperature on the fault (panel a) and leads to the generation of a small amount of porosity (panel d). With higher loading velocity the fault is activated deeper (panel b), enhancing the frictional heating (panel f) on a bigger surface area (reaching up to the surface), which in return leads to a substantial lowering of the viscosity (panel c, down to $\sim 10^{14}$Pa s) producing extensive shear heating (with the amplitude of 10^{-3}W m^{-3}, panel e).

On the other hand, if we reduce the velocity loading by 50% (blue lines on Figure 2.14), the temperature remains almost the same (panel a), making this run essentially indistinguishable from the case without any strike slip fault.

To summarize the results, for increased velocity (green lines on Figure 2.14), the fault activation depth reaches the depth of the brittle-ductile zone defined by Nimmo and Gaidos (2002) and even though we reduce the values of both shear and frictional heating by porosity (shear heating through viscosity and frictional heating by reducing the coefficient of friction - the cut-off parts of the green line on panels e and f corresponding to nonzero porosity), we obtain higher amplitudes of the shear heating than Nimmo and Gaidos (2002). The choice of loading velocity amplitude is thus a crucial one, and it is probably determining whether some porosity can be produced on strike-slip faults on Europa or not. However, even with our highest loading amplitudes, the reached melt volume fraction (porosity) is less than 4% and is nonzero just precisely at the fault. Therefore, no extensive subsurface water reservoirs seem to be produced by a mechanism of strike-slip motion with loading in the investigated range of amplitudes.

More realistic boundary conditions for temperature at the surface

Based on the previous results, we know that velocity loading amplitude is a crucial parameter, mainly because it directly affects the fault penetration depth. If the fault is not deep enough, then the frictional heating is not high enough to develop low viscosity zones. These, in turn, are required for magnifying the shear heating to a substantial level necessary for meltwater generation. From this perspective, a similarly important feature is the thermal structure within the ice layer. In order to test the robustness of our results, we have thus tried to replace the surface conditions used in our study with more realistic ones that take into account (i) heat radiation and (ii) the possible insulating effect of a regolith layer.

First, we simulate the radiation from the surface instead of directly prescribing the surface temperature:

$$q = -k\nabla T \cdot \mathbf{n} = \epsilon_{rad}\sigma_{rad}(T^4 - T_e^4) \text{ on } \Gamma_S, \tag{2.44}$$

where q is the normal conductive heat flux, $\mathbf{n}$ is the outer unit normal vector, ϵ_{rad} is the emissivity of Europa set to 0.33 and σ_{rad} is the Stefan-Boltzman constant equal to $5.670367 \times 10^{-8}\mathrm{kg\,s^{-3}\,K^{-4}}$, T is the temperature (on the surface) and T_e is the external (insolation) temperature (for Europa we consider $T_e = 100\mathrm{K}$). The introduction of this boundary condition does hardly influence the results, since the maximum of the steady state thermal field is even lower than for the reference run, reaching $\sim 153\mathrm{K}$, see Figure 2.15.

Second, according to Carlson et al. (2009) a layer of regolith might be present on Europa's surface, such a layer has a lowered thermal conductivity of k_{rego}=0.1 $\mathrm{W\,m^{-1}K^{-1}}$, cf. Mellon et al. (2018). Thus we introduce an isolating boundary condition by approximating a 100 meters thick layer of regolith on the surface. We assume that the heat transfers by conduction in the regolith:

$$q = -k\nabla T \cdot \mathbf{n} \sim -k_{rego}\frac{T_e - T}{d_{rego}} \text{ on } \Gamma_S, \tag{2.45}$$

where d_{rego}=100 m is the thickness of the regolith layer and T is the temperature just below the regolith layer. In the numerical solution, we deal with the regolith layer by the Neumann boundary condition on the surface.

Such a condition has a substantial influence - the isolating lid atop the ice layer leads to an increase in temperature within the layer. This results in enhanced heating on a larger portion of the fault plane (cf. Figure 2.15 panel a), reducing the viscosity (panel c) enough to allow for substantial shear heating (panel e) and a small amount of porosity (almost 4% locally, panel d). Summarizing, the regolith has a similar influence as the velocity loading amplitude; however, it still does not create conditions favorable enough for substantial production of meltwater.

Conclusions

To conclude, the reference run with parameters corresponding to a meter displacement per period at the strike-slip fault does not result in any meltwater

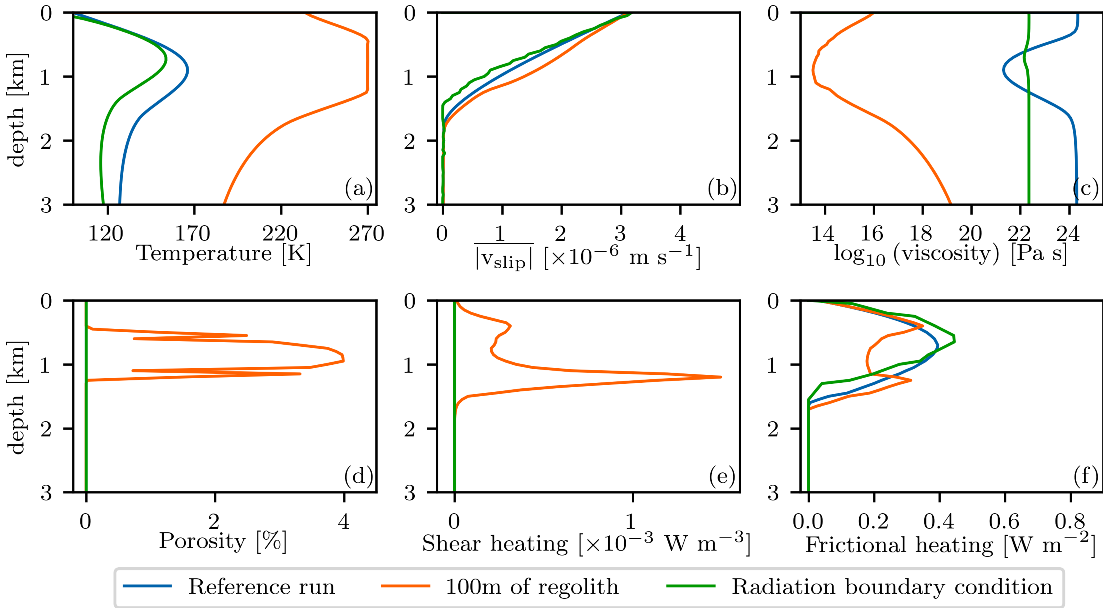

Figure 2.15: The comparison of steady states of the reference run (blue) and two runs with different boundary conditions for temperature: a run with one hundred meters of regolith on the top of the ice shell (orange) and radiation boundary condition (green). Variables are plotted in the top three kilometers on the fault.

generation. The velocity loading amplitude and the presence of the regolith layer have a substantial influence on the results. Increasing the loading velocity by 50% produces a little more than 3% of porosity right at the fault; however, no significant amount of melt is present in the fault's vicinity. Introducing a hundred meters thick layer of regolith at the surface of the ice shell produces 4% of porosity right at the fault. The choice of coefficient of friction (in the range from 0.1 to 0.8) is not an important one, as it influences only the activation depth of the fault.

We also tested changes in other parameters, such as the viscous contrast, given by viscosity cut-off (no influence), the grain size (0.7mm - 3mm - no influence), artificial softening of the material in the faults surroundings (due to repeated straining, no influence). Thus, the main negative conclusion stands: producing a substantial amount of meltwater is highly unlikely with the presented mechanism - strike-slip motion - and associated frictional and shear heating.

The reasons for not producing more meltwater, and elsewhere than right at the fault are the following: First and foremost, the main heating source (frictional heating) is only a surface one. Furthermore, the second heating source (viscous dissipation/shear heating) is not so intensive as the slip velocity drops to zero continuously and since most of the deformation happens in an elastic regime. In addition, the fault activation depth is usually relatively small compared to the results in Nimmo and Gaidos (2002). Also, the latent heat used to change ice into water consumes part of the produced heating. Finally, already produced porosity has a negative feedback on successive water production, as the non-zero porosity lowers both the coefficient of friction and viscosity, thus reducing both types of heating.

2.2 Tidal Walking on Europa's Strike-Slip Faults — Insight From Numerical Modeling (Sládková et al., 2020)

On some europan landforms, lateral offset has been observed, see Sections 1.1.2 and 2.1, indicating that strike-slip motion has occurred. Hoppa et al. (1999a) proposed a theoretical model (called "tidal walking") for producing such a lateral offset by reactivating existing faults via tidal stresses.

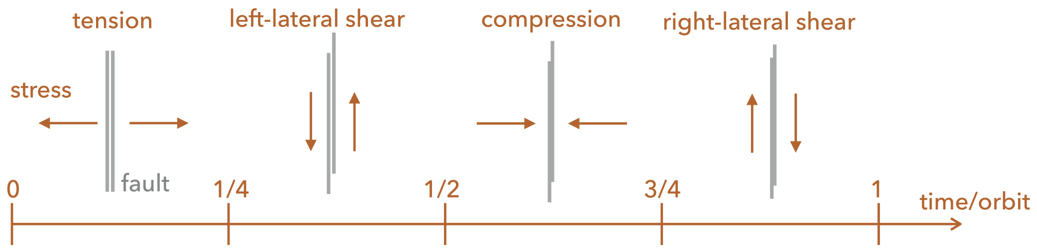

Figure 2.16: A simplistic sketch of tidal walking model in the most simple form (with phase shift equal to π): the tension opens the existing fault during the first quarter of the orbit, followed by the left-lateral shear producing an offset (enabled by the opened fault). In the third quarter of the orbital period, the compression closes the fault preventing or diminishing the right-lateral offset. In this case, all processes result in a small left-lateral offset. The specific tidal forces and final (if any) offset are dependent on the orientation and position of the fault on Europa's surface.

The "tidal walking" process is ought to work as follows: diurnal tides exert periodic normal and shear forces on the fault plane with a phase shift depending on the fault's location and azimuth. In the simplest setting, if the phase shift is π, the fault is opened by the tensional stresses during the first half of the tidal period facilitating the left-lateral motion due to shear forcing, see two windows on the left of Figure 2.16. During the second half of the period (two windows on the right of Figure 2.16), compression closes the fault suppressing the right-lateral motion in the reverse direction. Consequently, in this case, after each tidal period, a small amount of left-lateral offset is accumulated along the fault. For the phase shift equal to zero (shear and normal stress in phase), the situation is antisymmetric, producing the same amplitude of the offset as for the previous case but in the right-lateral direction. On the other hand, for phase shifts $\pi/2$ and $3\pi/2$, no accumulated offset is expected. For other values of phase shift, the process is more complex; however, the principle remains the same.

Hoppa et al. (1999a) considered a thin elastic ice shell overlying a liquid layer and tested their model by comparing the patterns of the predicted tidal stresses with the observed strike-slip offsets on Europa's surface. Using the normal and shear stresses corresponding to the fault's location and azimuth, they calculated the expected fraction of faults with right- and left- lateral offsets in the chosen regions on Europa's surface and compared the values with the data obtained from Voyager and Galileo images. To correctly predict the number of faults with a particular lateral offset, they concluded that most of the faults formed 60° to

90° west of their current location, shifted by the nonsynchronous rotation of the ice shell. However, Hoppa et al. (1999a) did not model the shear motions using frictional failure criteria; thus, their tidal walking model is rather a conceptual one.

A numerical study of the tidal walking mechanism was performed by Preblich et al. (2007) with a finite element code Tekton. The model employed viscoelastic ice rheology and simulated the evolution of an offset for different predefined temperature fields and ice shell properties. They concluded that except for a very special setting, penetration of the fault all the way to the underlying ocean is required to produce the strike-slip offset rates consistent with the observations. The model produced such offset rates only for a very short period of time (several tens of orbital cycles) before the stress that accumulated in the cold elastic part of the domain slowed down the process significantly. An additional independent stress release mechanism was suggested to be active, which was, however, not modeled in the study. Dissipation and the associated thermal effects were claimed to be unimportant for the tidal walking process.

Rhoden et al. (2012) studied Europa's strike-slip faults by a numerical model that extended the original approach of Smith-Konter and Pappalardo (2008) developed for Enceladus' tiger stripes. In their purely mechanical model, they took into account the effect of overburden pressure and employed the Mohr-Coulomb failure criterion to determine the frictional response at the fault. With a simplified treatment of viscoelasticity, the authors obtained the net offset for a large number of fault positions and azimuths and reproduced the global pattern observed on Europa's surface.

Most of the numerical models of strike-slip faults on Europa did not consider thermal effects to be important, with the exception of Nimmo and Gaidos (2002), see Section 2.1.5 for a summary of the article. In their model, however, the fault depth was fixed, and the strike-slip motion of the brittle layer was prescribed.

In this part of the thesis, we simplify the convective model from the previous section (Section 2.1.1) and extend the tidal model to test the tidal walking hypothesis and quantify the surface offset by numerical modeling of the thermomechanical evolution of a strike-slip fault and its vicinity. We also obtain estimates of surface thermal signature produced by the processes at and nearby the fault.

2.2.1 Numerical Model

We investigate the mechanical and thermal evolution of a part of Europa's ice shell in the fault's vicinity subjected to forcing by diurnal tidal stresses. We use the model defined in the previous section with several modifications, i.e., we consider a pre-existing planar fault perpendicular to the surface which penetrates the whole shell. We focus on the fault's reactivation by tides, i.e., we compute the evolution of the slip within the fault plane and the fault activation depth, but we do not model the initiation of the fault, i.e., the process of ice shell fracturing. As in the first section, the process of tidal walking involves two different timescales – the forcing takes place on the tidal period (~ 3.55 Earth's days), while the overall offset accumulates over the period of tens of thousands of years (Kattenhorn et al., 2009); see Section 1.1.2. The two-scale nature of the problem is reflected in the design of the numerical model, cf. Figure 2.4. The main properties of the model thus remain the same; however, there are important differences, which are described further.

Convective Model

The convective model solves thermal convection in the ice shell on a geological timescale. However, due to the more complex loading of the system, see Tidal model section and equation 2.48b, and the necessity of calculating long runs, the two-phase model of Kalousová et al. (2016), presented in the Section 2.1.1, had to be reduced to one phase only and we shortly present it once more.

Governing Equations

We solve balances of mass, momentum, and energy for a viscous non-Newtonian incompressible fluid in a two-dimensional Cartesian geometry using Boussinesq approximation:

$$\nabla \cdot \boldsymbol{v} = 0, \tag{2.46a}$$

$$-\nabla p + \nabla \cdot \eta \left(\nabla \boldsymbol{v} + (\nabla \boldsymbol{v})^T \right) - \varrho_i \mathbf{g} \alpha (T - T_0) = 0, \tag{2.46b}$$

$$\varrho_i c \left(\frac{\partial T}{\partial t} + \boldsymbol{v} \cdot \nabla T \right) = \nabla \cdot (k(T) \nabla T) + Q, \tag{2.46c}$$

where the notation remains the same as in Section 2.1.1, cf. also List of Symbols on page 138 at the end of the thesis. The values of all parameters are summarized in Tables 2.2 and 2.3. For the viscosity, we use a composite creep that combines volume and grain boundary diffusion, dislocation, basal slip, and grain-boundary sliding following Goldsby and Kohlstedt (2001), see formula 2.24. Since the porosity is not included and is therefore considered zero, the equation 2.26 for viscosity reduction is not used. For both numerical and physical reasons, we impose a viscosity cut-off of at 10^{22} Pa s, which results in eight orders of magnitude viscosity contrast across the ice shell.

The thermal conductivity of water ice is strongly dependent on temperature and we employ the parameterization from Hobbs and Hobbs (1974), cf. equation 2.27.

Boundary and Initial Conditions

The governing equations (2.46) are supplemented with the same boundary conditions as in the Section 2.1.1, cf. equation 2.28. Concerning the Stokes system, free slip is applied on all boundaries, and the value of pressure is fixed in one corner of the computational domain. As for the energy balance, we fix the temperature at the bottom (ice-ocean interface) at the melting point, and at the surface, we prescribe the value T_s. On the left boundary (fault), we prescribe the frictional heating Q_fric based on the output of the tidal model (eq. 2.36). Finally, the right boundary is considered thermally insulating. The convective model is initiated from a conductive/convective statistical steady-state (depending on the thickness of the ice shell). In addition to these boundary conditions, and since the porosity is not calculated, we cut the temperature at the melting value of $T_\mathrm{m} = 270$K everywhere in the domain.

Tidal Model

On the tidal timescale, we solve for the slip along the fault and the associated viscoelastic deformation of ice in the fault's vicinity; see Figure 2.17. For a given thermal and viscosity structure of the ice shell and for the particular regime and amplitude of forcing, the tidal model predicts the offset development and also provides the amplitudes of frictional heating at the fault plane and the shear heating in the surrounding bulk. These quantities are then used as inputs for the convective model; see Section 2.2.1.

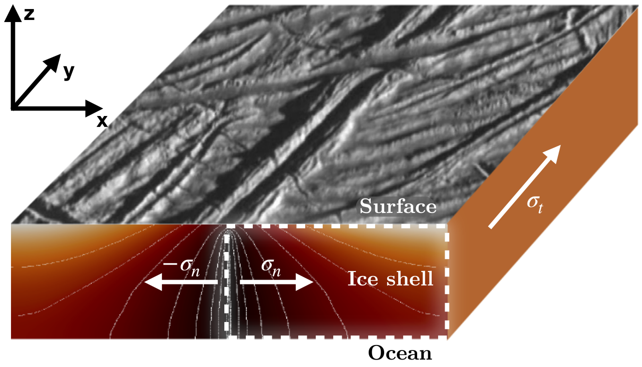

Figure 2.17: The sketch of the tidal model part of the tidal walking model.

Governing Equations - Bulk

The governing equations in the bulk comprise the mass and momentum balances for an incompressible Maxwell viscoelastic continuum and follow the same assumptions as in the Section 2.1.1; thus, they are reduced into a 2D form of equation 2.15. However, here we mimic the diurnal tides by prescribing the surface traction in the y-direction (along the fault) on the right boundary, and we pick the position of the right boundary such that the height-length aspect ratio is two for all simulations, see Figure 2.17 and also discussion in Section 2.2.3. The fault is still represented by the left boundary of the computational domain, the top boundary is Europa's surface, and the bottom boundary is the interface between the ice shell and the internal ocean. Note that since eq. 2.15 represents only the y-component (along the fault) of the momentum balance, it does not contain gravity. Consequently, the effect of overburden pressure only appears in the boundary conditions via the yield stress; see eq. (2.47a) below.

Governing Equations - Fault

We use the same description of the fault's behavior as above, see Section 2.1.1. However, in the Mohr-Coulomb-type form of the yield stress, which is given as a product of the coefficient of friction μ_f and the normal traction (taken positive for compression), we add the normal part of the diurnal tides enabling opening and closing of the fault by reducing and increasing the yield stress on the fault:

$$\widetilde{\sigma_Y} = \mu_f(\sigma_n + \varrho_i g d). \tag{2.47a}$$

The normal traction is a sum of the overburden (hydrostatic) pressure $\varrho_i g d$ (as before), and the normal part of the diurnal stress σ_n, which is changing in time as:

$$\sigma_n = \sigma_0[\sin(\omega t - \varphi)]. \tag{2.47b}$$

Here φ is the phase shift between the normal and shear stress, σ_0 is the stress magnitude, and ω denotes the tidal angular frequency. Finally, the coefficient of friction μ_f is kept constant.

The yield stress σ_Y is taken as the non-negative part of $\widetilde{\sigma_Y}$, which may become negative as a result of a negative σ_n in the tensional part of the loading cycle, i.e., we set:

$$\sigma_Y = \max(0, \widetilde{\sigma_Y}) \; . \tag{2.47c}$$

Boundary and Initial Conditions

On the left boundary, we prescribe the slip condition (2.18) mimicking the stick-slip behavior of the fault. We apply the free-slip condition on the bottom and the top boundary:

$$\mathrm{s}_z = 0 \quad \text{(top, bottom)}. \tag{2.48a}$$

On the right boundary, we specify the tangential stress in the direction along the fault - a condition that mimics the shear part of the diurnal tidal stress:

$$\mathrm{s}_x = \sigma_t, \text{ where } \sigma_t = \sigma_0 \sin(\omega t) \quad \text{(right)} \; . \tag{2.48b}$$

Note that for the sake of conciseness, we assume that the amplitudes of loading shear and normal stresses are both equal to σ_0, which may not hold in general. We discuss the effect of differing shear and normal stress amplitudes in Section 2.2.3. This type of forcing differs from both the one used by Preblich et al. (2007) or Nimmo and Gaidos (2002). The former study prescribes the strain rate on the right boundary, while the second study directly imposes displacement on the top. The tidal model is initiated from an undeformed stress-free state.

Table 2.3: Model parameters differing from the parameters used in the previous model, cf. Table 2.2. The $^{\bullet}$ symbol indicates the model parameters varied in the parametric study.

Symbol	Variable	Value	Unit
$D^{\bullet}$	ice shell thickness	$1, 5, 10, 30$	km
a'	domain aspect ratio	2	-
Tidal model parameters			
$\sigma_0{}^{\bullet}$	amplitude of forcing stresses	$0.6, 2, 4, 6$	10^5Pa
ω	orbital frequency	2.05×10^{-5}	s^{-1}
$\varphi^{\bullet}$	phase shift	$k\frac{\pi}{4}, \quad k{=}0, 1, \ldots, 8$	-
Convective model parameters			
η_{cut}	viscosity cut-off	1e22	Pa s

Coupling of the Models

The two models exchange information (viscosity and heating production) in the same manner as explained in the previous section; see the flow chart in Figure 2.5.

However, in this case, the exchange takes place every convectional time step. The tidal model computes five periods except for the first run, where one hundred periods are calculated to suppress the role of the initial conditions.

2.2.2 Results

We study the thermo-mechanical evolution of a tidally deformed viscoelastic ice shell in the vicinity of Europa's strike-slip fault. The main model parameters are the amplitude of the shear and normal stresses σ_0, their mutual phase shift φ, the thickness of the ice shell D, and the coefficient of friction μ_f. We focus on two potentially observable quantities: the accumulated surface offset δ_{s} at the fault, i.e., the irreversible mutual displacement of the two sides of the fault, and the heat flux anomaly Δq on the surface in the fault's vicinity.

The observed offset on the strike-slip faults on Europa is usually a few kilometers (the measured maximum being 83 km, e.g. Kattenhorn, 2004) and the time of formation considered by previous studies is several tens of thousands of years (e.g. Greenberg et al., 1998; Kattenhorn et al., 2009; Preblich et al., 2007). In this regard, we want to identify the range of parameters for which the offset accumulated within less than 100 kyr would be of the order of 10^3–10^4 m.

Greenberg et al. (1998) and Hoppa et al. (1999a) computed the amplitudes of diurnal tidal stresses (proportional to eccentricity, see e.g., Wahr et al., 2009; Sotin et al., 2009) assuming a thin elastic ice shell overlying a fluid layer. They chose an eccentricity of 0.01 and obtained the stress amplitudes of $\sim 10^5$ Pa. Since the eccentricity probably varied significantly during Europa's history and could have been up to one order of magnitude higher (e.g. Hussmann and Spohn, 2004), we consider the amplitudes of forcing stresses from 6×10^4 Pa to 6×10^5 Pa. The estimates of ice shell thickness vary between a few and a few tens of kilometers (e.g. Billings and Kattenhorn, 2005). In this part of the thesis, we thus investigate the values of 1, 5, 10, and 30 km (cf. Table 2.3). We consider the coefficient of friction μ_f=0.4 as a reference value, which is a conservative mean value of the published results, cf. Schulson and Fortt (2012).

In describing the results, we proceed in two steps. First, we investigate the model response in a simplified purely mechanical setting in which we demonstrate the basic characteristics of the tidal walking mechanism. Then, we present the results of a more realistic thermo-mechanically coupled model where we also look for the surface thermal signatures of Europa's internal processes. For conciseness, all results are plotted only in a part of the domain even though all computations are done in a domain with aspect ratio two. This is in order to subdue the effect of a somewhat artificial boundary condition on the right boundary.

Mechanical Model

In this section, we focus only on the mechanical part of the problem and do not take into account the thermal coupling – therefore, only the tidal model is used assuming constant (in time and space) viscosity. First, we describe in detail the time evolution of processes that occur at the fault plane during one orbital period. Then we evaluate the maximal depth at which sliding occurs and how it depends on the model forcing and material parameters. We also provide an analytical estimate for the maximal activation depth of the fault and compare it with the numerical results. Based on the fault activation depth, we then discuss two cases that may occur: (i) a partially locked fault for which the maximal activation depth does not reach the bottom of the shell, and (ii) the whole-fault sliding when the activation depth equals the shell thickness. We conclude this section by showing how the accumulated surface offset for these two cases depends on the ice viscosity and the phase shift between the applied normal and shear stresses. In particular, we demonstrate the critical effect of viscosity in the partially-locked case.

Time Evolution at the Fault

For the reference simulation, we consider a 10 km thick shell forced by normal

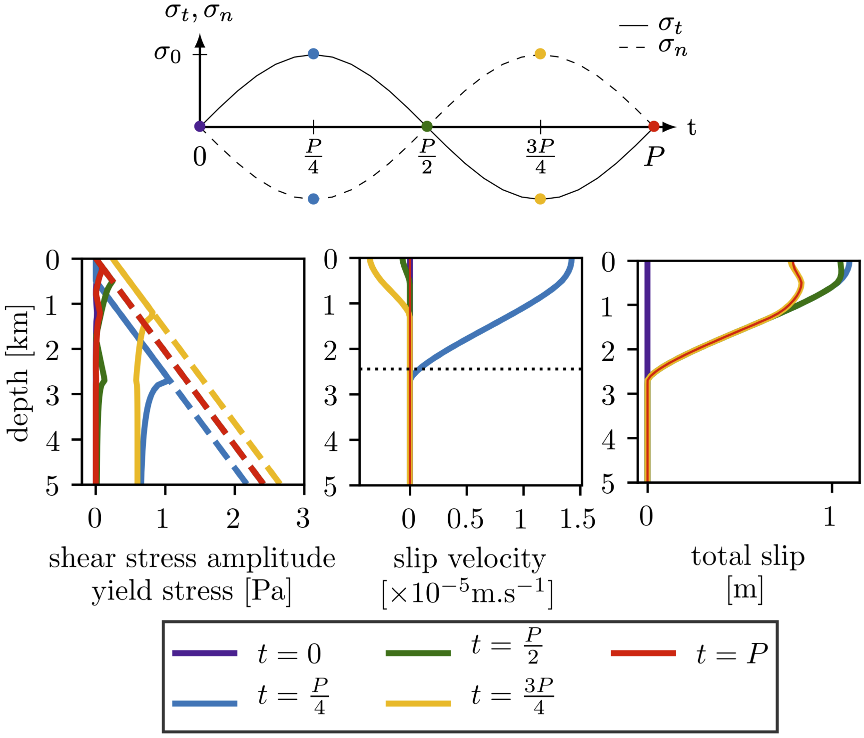

Figure 2.18: Results of the reference simulation computed with constant viscosity 10^{14} Pa s, phase shift π, shell thickness 10 km, loading force amplitude 6×10^5 Pa and friction coefficient 0.4. *Top*: Time evolution of the applied normal (dashed line) stress on the left boundary and of the tangential (full line) stress on the right boundary. *Bottom*: Time evolution of quantities at the fault, only top 5 km are shown. The colors correspond to time instants highlighted by dots in the top panel. Left: Shear stress amplitude $|\mathrm{s}_x|$ (solid lines) and yield stress σ_Y (dashed lines). Middle: Slip velocity $\mathrm{v}_{\mathrm{slip}}$. The dotted line denotes the activation depth d_a (cf. text for more details). Right: Accumulated slip $\mathrm{u}_{\mathrm{slip}}$.

and shear stresses with amplitude of 6×10^5 Pa and phase shift π. As we shall see later, such phase shift results in the largest possible (left-lateral) offset. Viscosity is constant equal to 10^{14} Pa s, and we use the reference value of the friction coefficient (μ_f=0.4).

The top panel of Figure 2.18 shows the time evolution of loading normal (dashed line) and tangential (full line) stresses. In the following text, we use the colors corresponding to the selected time instants during one period (cf. the colored points). In the bottom row of Figure 2.18, we plot (from left to right): the shear stress amplitude $|\mathrm{s}_x|$ at the fault (left panel, solid line) together with the yield stress σ_Y (left panel, dashed line), the slip velocity $\mathrm{v}_{\mathrm{slip}}$ (middle panel), and the total slip $\mathrm{u}_{\mathrm{slip}}$ (time-integrated slip velocity, right panel) that expresses the displacement of the fault block with respect to the fault plain – the mutual offset δ between the two blocks is then twice as much.

At the beginning of the period (t=0, violet), the fault is unloaded both in the normal and tangential direction, and the slip velocity, as well as the accumulated slip, are zero. During the first quarter of the period, the fault is gradually opening which is caused by the applied negative σ_n that partially counteracts the overburden hydrostatic pressure and thus decreases the yield stress. Simultaneously, the applied tangential stress increases. At $t=\frac{P}{4}$ (blue), the applied tangential stress σ_t is maximal and the yield stress is minimal due to maximal negative σ_n. Note that in the top $\sim$2.5 km, $|\mathrm{s}_x|=\sigma_Y$ (blue line, bottom row, left panel) – this part of the fault is sliding and at this time, slip velocity is maximal (blue line, bottom middle panel). Consequently, a positive (left-lateral) slip appears on the fault (blue line, bottom right panel). In the second quarter of the period, the amplitudes of tangential and normal loading both decrease and after $t=\frac{P}{2}$ (green), the fault starts to close because σ_n becomes positive thus increasing the yield stress.

In the second half of the period, σ_t changes sign (leading to right-lateral movement) and reaches the negative maximum at $t=\frac{3P}{4}$ (yellow). Since the backward motion is significantly suppressed by the build-up of positive normal stress, which is closing the fault, the depth profiles of shear stress amplitude and slip velocity are not symmetric – at $t=\frac{3P}{4}$ (yellow), the fault is only activated in the top $\sim$1 km, and the maximal negative slip velocity is approximately 4 times smaller compared to the maximal positive value at $t=\frac{P}{4}$ (blue). Consequently, the accumulated negative (right-lateral) slip does not cancel out but only reduces the accumulated positive slip. Therefore, at the end of the period (red), the total accumulated slip $\mathrm{u}_{\mathrm{slip}}$ is positive, i.e., left-lateral – cf. the red line in the bottom right panel.

The left bottom panel of Figure 2.18 shows how the depth of the activated (sliding) part of the fault where the shear stress follows the yield stress changes throughout the period. The activation depth d_a is defined as above, i.e., it is the depth, where the average (over the period) of $|\mathrm{v}_{\mathrm{slip}}|$ drops to 2% of the maximal (over the period) value. This depth is denoted by the black dotted line in the bottom middle panel of Figure 2.18. Note that it roughly corresponds to the maximal depth of the activated part of the fault during one period (blue line).

Fault Activation Depth

We now investigate how the fault activation depth depends on the model parameters. In Figure 2.19, we plot the activation depth for three values of friction coefficient, μ_f=0.1, 0.4, 0.8 (colors), as a function of the applied stress amplitude σ_0. We consider two ice shell thicknesses, D=10 and 30 km, and two values of ice viscosity $\eta=10^{14}$ and 10^{22} Pa s. The left panel illustrates the effect of ice shell thickness D=10 km (dotted lines) and D=30 km (dashed lines) while viscosity is fixed at 10^{14} Pa s. The right panel shows the effect of ice viscosity $\eta=10^{14}$ Pa s (dotted lines) and $\eta=10^{22}$ Pa s (dashed lines) while the shell thickness is fixed at 30 km. The solid lines represent an analytical estimate of the fault activation depth:

$$d_{\max} = \frac{\sigma_0}{\varrho_i g} \frac{1+\mu_f+\sqrt{1+2\mu_f}}{\mu_f} \;, \tag{2.49}$$

which corresponds to the considered setting (equal amplitudes of applied σ_n and σ_t and phase shift $\varphi{=}\pi$). A more general estimate and derivation are presented in the Appendix 2.2.5.

Figure 2.19 confirms the expected linear dependence of activation depth on loading stresses amplitude with the slope increasing with decreasing coefficient of friction. In the left panel, we see that for the middle (0.4) to large (0.8) value of μ_f (yellow and red lines), the fault activation depth is significantly smaller than the shell thickness, $d_a{\ll}D$, in which case the dependence of the activation depth on the ice shell thickness is insignificant. On the other hand, the small value of friction coefficient ($\mu_f{=}0.1$, green lines), significantly increases the activation depth, which can then approach the shell thickness, $d_a{\sim}D$, corresponding to the whole-fault activation. In such a case, we observe that for the same values of σ_0, μ_f, and η, the fault activation depth becomes larger for shells with smaller thicknesses. Simultaneously, for the fully activated fault (green square), the analytical estimate $d_{\max}$ (eq. 2.49) becomes more accurate, while for thicker shells, it only provides an upper bound. Finally, in the right panel of Figure 2.19, we observe that the role of viscosity is relatively minor for all considered cases, although it increases for larger values of μ_f.

Partial Locking vs. Whole-fault Activation

We have seen that under favorable conditions, the fault activation depth d_a may

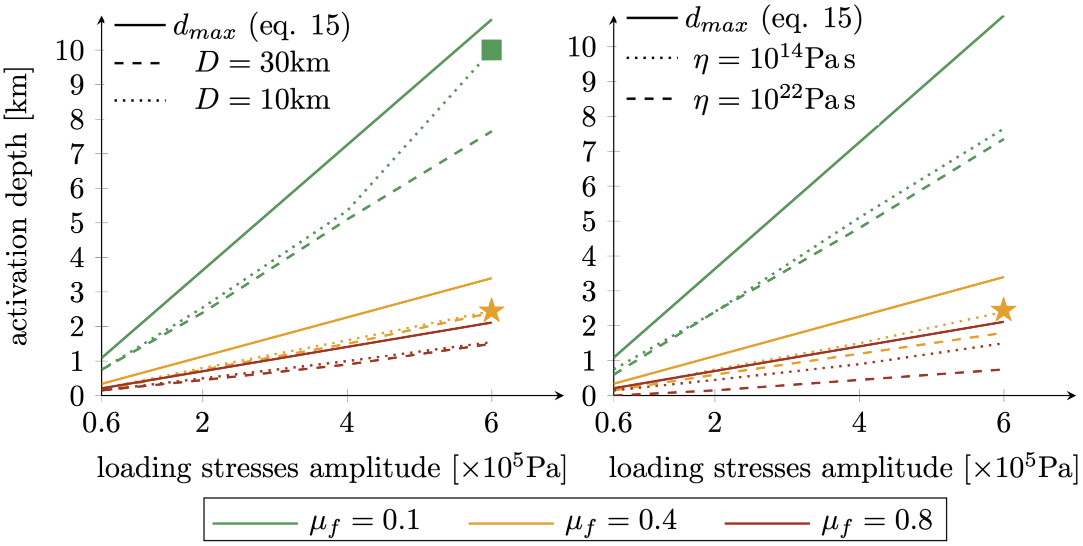

Figure 2.19: Fault activation depth d_a as a function of the loading stresses amplitude. Colors indicate different values of the friction coefficient μ_f. The full lines show the analytical estimate $d_{\max}$ given by eq. 2.49. *Left*: Effect of the ice shell thickness D for fixed viscosity 10^{14}Pa s. *Right*: Effect of the ice viscosity η for fixed ice shell thickness of 30 km. In both panels, the yellow star corresponds to the reference simulation from Figure 2.18. In the left panel, the green square indicates the setting in which the fault is activated across the whole shell: $d_a{=}D$.

reach the base of the shell, in which case the whole fault becomes activated. Let us investigate in more detail the differences between the partially locked case and the whole-fault activation. For this purpose, we compare the results of the reference simulation from Figure 2.18 (cf. also yellow star in Figure 2.19) with the results of a simulation with a smaller friction coefficient that leads to the whole-fault activation (cf. green square in Figure 2.19). Namely, we consider a 10 km thick shell, constant viscosity 10^{14} Pa s, phase shift π, forcing amplitude 6×10^5 Pa and two values of friction coefficient: μ_f=0.4 (Case 1) and μ_f=0.1 (Case 2). We plot the amplitude of shear stress $|\mathrm{s}_x|$ at the fault and the slip velocity $\mathrm{v}_{\mathrm{slip}}$ during one tidal period for both cases in Figure 2.20 (Case 1 – the top two rows, Case 2 – the bottom two rows).

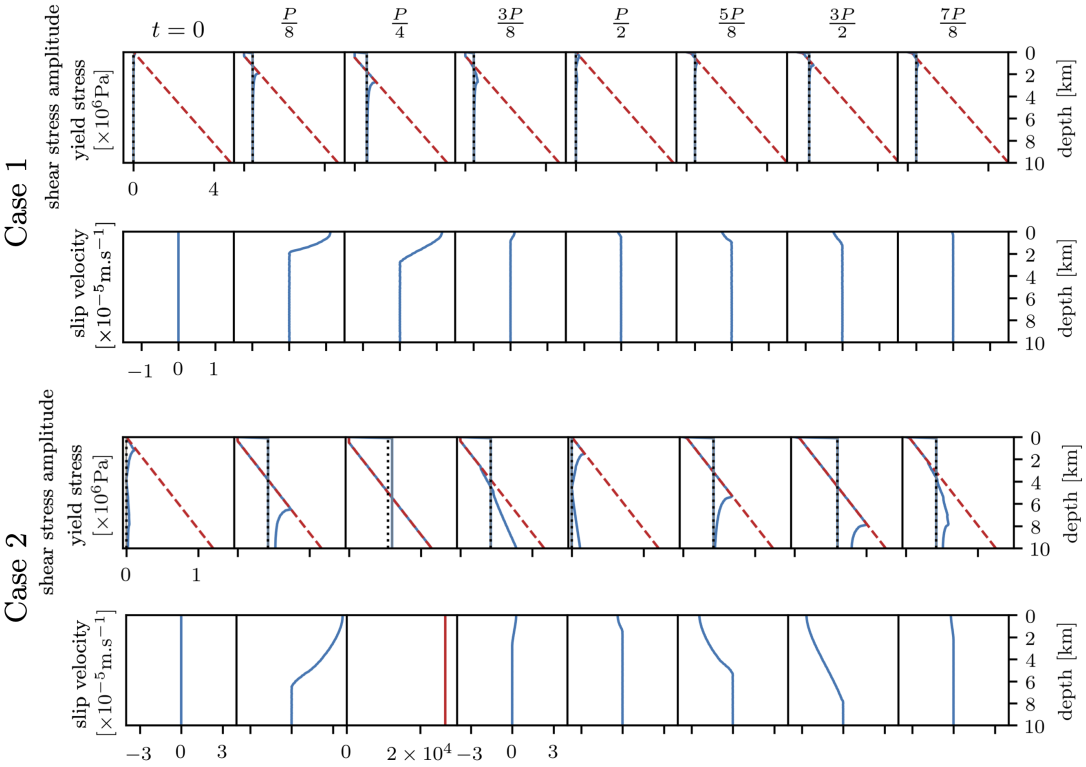

Figure 2.20: Time evolution of shear stress and slip velocity during one tidal period for Case 1 (μ_f=0.4, top two rows) and Case 2 (μ_f=0.1, bottom two rows). In Case 2, the value of the stabilization parameter γ_s is 10 kg m^{-3} s^{-1} (cf. text for more details). *Odd rows*: shear stress amplitude $|\mathrm{s}_x|$ at the fault (blue line), yield stress σ_Y (red dashed line), loading stress amplitude at the right boundary σ_t (grey line), and average (integral over whole fault) shear stress at the fault (black dotted line). *Even rows*: slip velocity $\mathrm{v}_{\mathrm{slip}}$ at the fault (blue line). Note that for Case 2 and $t=\frac{P}{4}$, the $\mathrm{v}_{\mathrm{slip}}$ range is different from the other panels in the same row (highlighted by the red line).

In Case 1, we can see that the shear stress at the fault (Figure 2.20, top row, blue lines) remains below yield stress (red dashed lines) in a significant part of the fault. Sliding takes place only in the uppermost ~2.5 km (at $t=\frac{P}{4}$), but most of the fault is locked throughout the tidal period. The combination of sliding in the upper part of the fault and effective no-slip below the activation depth results in the strain-rate maximum just below the tip of the activated part of the fault. Note that, locally, the shear stress at the fault (blue line) may exceed the loading stress amplitude at the right boundary (grey line, cf. $t{=}\frac{P}{4}$), but the average shear stress at the fault (black dotted lines) matches the loading stress at each time step, which expresses the global (tangent) force equilibrium. Indeed, by considering the free-slip boundary conditions both at the top and bottom boundary (see eq. 2.48a), integration of the momentum balance (2.11) over the whole domain yields equality between the tangent loading force on the right boundary and integral of the shear stress at the fault (left boundary).

In Case 2, the yield stress is smaller due to the smaller value of μ_f and, at some time during the opening phase of the period ($\sigma_n{<}0$), the stress at the fault (blue lines) reaches the yield stress (red dashed lines) across the whole shell - cf. Figure 2.20, third row, $t{=}\frac{P}{4}$. Therefore, the fault activation depth reaches the base of the shell, and the fault starts sliding rapidly as one block (bottom row, $t{=}\frac{P}{4}$). This lasts until the stress drops below the yield stress again (third row, $t{=}\frac{3P}{8}$), which leads to an abrupt decrease in the slip velocity (bottom row, $t{=}\frac{3P}{8}$). In the second half of the period, the fault remains partially locked ($d_a{<}D$). Let us note here that, as long as the whole domain slides (around $t{=}\frac{P}{4}$), the slip velocity is effectively unconstrained. For numerical reasons, we add a stabilizing term in the form of a volume force acting along the fault, which is negatively proportional to the tidal velocity, i.e., we augment $\mathbf{f}$ in eq. (2.1b) by $-\gamma_s\mathbf{v}$ with $\gamma_s{=}10\,\mathrm{kg\,m^{-3}\,s^{-1}}$, which transforms eq. (2.11) into

$$\nabla \cdot \mathbf{s} = \gamma_s \mathrm{v}. \tag{2.50}$$

To some extent, one could try to interpret this term physically as a simple parameterization of the “far-field” effects due to the finiteness of the fault. Note that in reality, the slip should be limited by the change in the shape of the equilibrium tidal figure, which provides another constraint on the sliding in the case of whole-fault activation. We restrain ourselves from any deeper physical interpretation and consider the $-\gamma_s\mathbf{v}$ term solely as a stabilization. Note also that while this stabilization has some effect on the slip velocities, the force balance is satisfied for all times except $t{=}\frac{P}{4}$ where the average stress at the fault (black dotted line) is smaller than the loading force (grey line) due to the stabilization.

Accumulated Surface Offset

We now compare the two cases introduced above in terms of the surface offset δ_s ($2{\times}\mathrm{u_{slip}}$ at the surface) accumulated during one period. In Figure 2.21, we vary the phase shift between the normal and the shear stress (so far taken as $\varphi{=}\pi$) over the whole range from 0 to 2π with a step of $\pi/4$. We also study the effect of ice viscosity η. Since for Case 2, the results quantitatively depend on the unconstrained value of stabilization parameter γ_s, we normalize the obtained offsets by their maximal computed value (for each Case separately), and thus, in Figure 2.21, we plot this normalized surface offset $\tilde{\delta}_\mathrm{s}$. Consequently, these results are insensitive to the choice of γ_s.

We can see that for both cases, the surface offset depends strongly on φ. The maximum is reached around $\varphi{=}0$ (right-lateral offset), and $\varphi{=}\pi$ (left-lateral offset), the minima corresponding to zero offset are attained around $\varphi{=}\frac{\pi}{2}$ or $\varphi{=}\frac{3\pi}{2}$. This observation is in good agreement with the conceptual model of tidal walking as proposed by Hoppa et al. (1999a): maximum offset is expected if

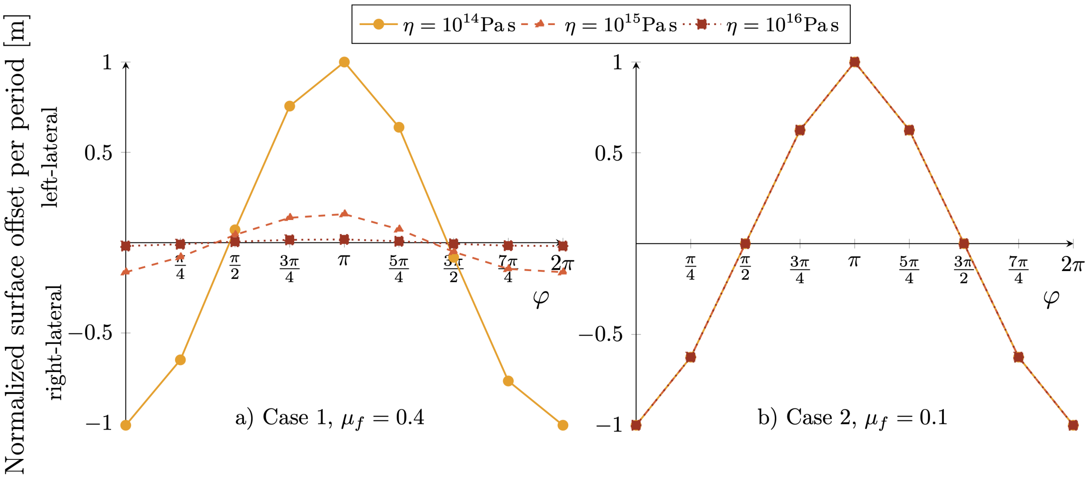

Figure 2.21: The normalized surface offset per period $\tilde{\delta}_s$ as a function of the phase shift φ between the normal and shear loading stress and the viscosity η (colors). For each Case, the results are normalized by the corresponding maximal value (cf. text for details). *Left*: Case 1 – the fault is only partially activated. *Right*: Case 2 – whole fault is activated.

the maximum of lateral stresses (left or right) occurs simultaneously with the minimum of normal stress.

For Case 1, we observe a very strong dependence on the ice viscosity – the surface offset is maximal for the lowermost considered value of ice viscosity (η=10^{14}Pa s) and rapidly decreases for higher values. The reason for this behavior is that in this setting, the offset accumulates mainly due to the viscoelastic relaxation of the strongly deformed ice in the fault's vicinity, which becomes more efficient with smaller viscosity. One can hypothesize that thermal effects might facilitate weakening in some situations, see the part Thermal Activation of Tidal walking lower on page 58. Note that the viscoelastic behavior is also responsible for the slight asymmetry with respect to φ.

In contrast to Case 1, the offset in Case 2 is completely insensitive to the viscosity value. This is due to the fact that when sliding, the parts of the shell right and left of the fault move essentially as uniform blocks with negligible viscous deformation (see bottom row of Figure 2.20, t=$\frac{P}{4}$). The surface offset then results from the combination of the opening and locking of the fault and the "far-field" response characterized by γ_s. For different values of γ_s, different values of the offset would be obtained, but ice viscosity does not affect the process at all.

Thermo-mechanically Coupled Model

In this section, we take into account also thermal effects and present the results of the thermo-mechanically coupled model as described in Section 2.2.1. We vary the main model parameters: shell thickness D, forcing amplitude σ_0, and the coefficient of friction μ_f, in order to determine for which structural and loading parameters could Europa's fault produce observable offset by the process of tidal walking. We again consider a fixed value of the phase shift φ=π, which is the most favorable for producing observable offset (see Fig. 2.21 and discussion in the previous section).

We quantify the accumulated surface offset δ_s at the fault, and simultaneously, we attempt to quantify the possible thermal signatures of the strike-slip motions since these may serve as indicators of active faults for future missions to Europa. Let us recall that these thermal signatures are due to the two heating sources described in detail in the previous section 2.1.4 – the frictional heating at the fault and the mechanical dissipation in the bulk.

Results of our parametric study for the reference value of μ_f=0.4 are summarized in the left panel of Figure 2.22, where we vary the ice shell thickness (columns) and the amplitude of the loading stress (rows). The presence or the absence of an observable offset (defined as >100 m produced in 100 kyr) at the fault is indicated by walking and standing figures, respectively. The magnitude of the heat flux anomaly Δq, defined as the difference between the produced surface heat flux above the fault and the heat flux value at this point in the initial state, i.e., before the fault activation, is coded by color: blue corresponds to a negligible anomaly ($\Delta q \leq 10^{-2}$ W m^{-2}) while red indicates values greater than 1 W m^{-2}. The grey color is used for cases where the stabilization had to be used due to the fact, that the fault is activated across the whole shell. This makes the results quantitatively biased by the choice of the stabilizing parameter γ_s.

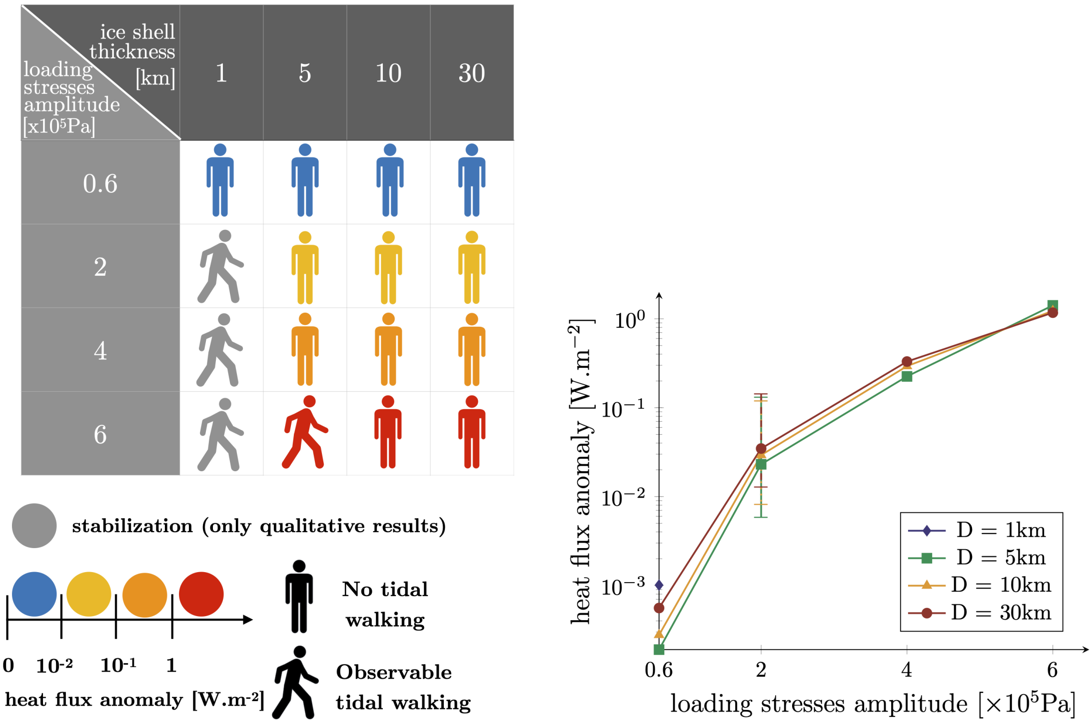

Figure 2.22: *Left*: Table summarizing the results of the thermo-mechanical model for various ice shell thicknesses (columns) and the loading stresses amplitudes (rows). The walking/standing figure corresponds to the model that produces visible offset or not respectively. Color from blue to red represents the value of the heat flux anomaly Δq on the fault, grey color describes the simulations for which stabilization was used, and thus only qualitative results were obtained. *Right*: Heat flux anomaly Δq for different ice shell thicknesses D (colors) and different loading stresses σ_0 (x-axis). The error bars for σ_0=2×10^{5}Pa denote the variations of Δq with the coefficient of friction (lower values obtained for μ_f=0.8, higher values for μ_f=0.1).

The high percentage of standing figures in Figure 2.22 reflects the fact that in the applied setting and for the considered range of model parameters, it is rather challenging to produce an observable offset. Except for the thermally activated simulation (σ_0=6 × 10^5 Pa and D=5 km, explained below), the shell would have to be extremely thin ($<$ 5 km). In addition, the forcing amplitudes would have to exceed the present day amplitude of the diurnal stress ($\sim 6{\times}10^4$ Pa, Greenberg et al., 1998) to produce an observable offset within the considered time span of 100 kyr. In these cases (i.e., for $\sigma_0 > 6{\times}10^4$ Pa and D=1 km), the loading stress is high enough to facilitate fault activation across the whole shell. Then, in accord with our findings from the purely mechanical case (part Mechanical Model on page 50), we obtain extremely high slip velocities and accumulated surface offsets per period. The frictional heating for these cases can be high enough to induce partial melting across the whole fault. Consequently, the surface thermal signature, in this case, can be very high. Quantitative prediction of both δ_s and Δq is, however, biased by the use of the stabilization parameter γ_s.

The heat flux anomaly resulting from the strike-slip motions at the fault for the subcritical cases (only partial fault activation) is plotted in the right panel of Figure 2.22 as a function of the loading stresses amplitude σ_0 for different ice shell thicknesses (color). Note that in some cases ($\sigma_0 \geq 2{\times}10^5$ Pa), a significant heat flux anomaly can be produced while generated offset is negligible. The overall trend is intuitive – the higher the loading force, the higher the heat flux anomaly. The error bars (shown only for σ_0=2×10^5 Pa) indicate the quantitative effect of the friction coefficient μ_f on heat flux anomaly, the higher values corresponding to μ_f=0.1 and the lower to μ_f=0.8. While the effect of the friction coefficient is rather pronounced, the forcing amplitude σ_0 is of greater importance. For the lower values of σ_0, the anomaly would be probably undetectable (units of $\mathrm{mWm^{-2}}$), whereas for the higher loading stresses (σ_0=6 × 10^5 Pa), we obtain the heat flux anomaly of up to 1 $\mathrm{Wm^{-2}}$. Interestingly, the ice shell thickness D does not significantly affect the heat flux anomaly. This is due to the fact that in the regime of partial fault activation, the mechanical response of the fault (in particular d_a and $\mathrm{v_{slip}}$) is rather insensitive to D.

Thermal Activation of Tidal Walking

Our parametric study has revealed an interesting case (corresponding to the loading force σ_0=6×10^5Pa and shell thickness D=5km), where a significant offset accumulates even though the activation depth does not reach the bottom of the shell. Let us demonstrate that this is, in fact, due to thermo-mechanical coupling.

In Figure 2.23, we plot snapshots from the time evolution over 100 kyr for this simulation. In the top row, we show depth profiles of the absolute value of the slip velocity at the fault averaged over one period ($\overline{|\mathrm{v_{slip}}|}$, panel a), the accumulated offset per period δ at the fault (panel b), and the temperature T at the fault (panel c). In the bottom row, we depict the surface offset per period (δ_s, panel d) and the heat flux anomaly (Δq, panel e) as functions of the distance from the fault x. The initial state (violet) is characterized by a zero offset, a conductive temperature profile, and a negligible heat flux anomaly. Throughout the simulation, the activation depth d_a varies between 2 and 3 km; thus the active part of the fault never penetrates the whole shell (panel a). The slip velocity is high enough to produce significant frictional heating at the fault, which leads to

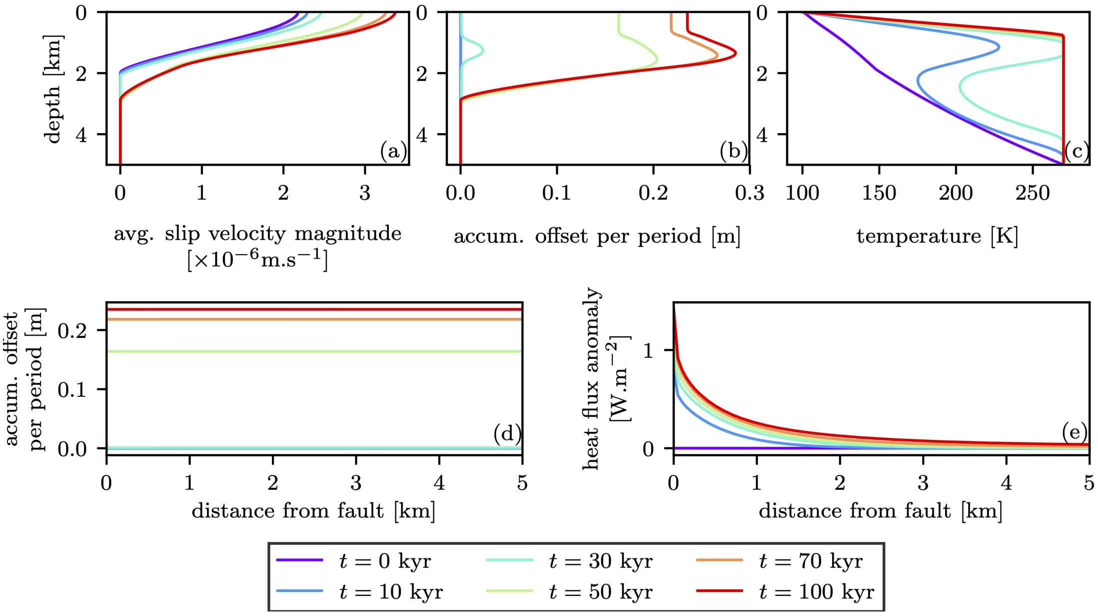

Figure 2.23: Time evolution of the thermally activated simulation, where the surface observable offset is obtained without the whole shell penetration (σ_0=6×10^5 Pa, D=5 km, φ=π, μ_f=0.4). *Top*: Depth profiles of quantities at the fault: (a) absolute value of the slip velocity averaged over one period $\overline{|\mathrm{v}_{\mathrm{slip}}|}$, (b) accumulated offset per period δ, (c) temperature T. *Bottom*: Surface quantities as a function of distance from the fault x: (d) accumulated surface offset per period δ_{s}, (e) heat flux anomaly Δq.

a gradual increase of the temperature at the fault (panel c) and in its vicinity. This eventually leads to the development of a rising plume-like structure underneath the fault, cf. Fig. 2.24, with a very high temperature and, consequently, the viscosity as low as $\sim 10^{14}$ Pa s. At this time (approximately after 50 kyr since the beginning of the simulation), the region of the shell underneath the active part of the fault is mechanically so weak that the deformation regime switches effectively to the low-viscosity Case 1 situation shown in Section 2.2.2 part Mechanical Model (see Figures 2.20 top and 2.21 left). This leads to a production of surface offset as high as $\sim$ 0.2 m per period (cf. Fig. 2.23 b, d), corresponding to the accumulated offset $\delta_{\mathrm{s}} \sim$ 20 m in one year or 1 km within 100 kyr (including the 50 kyr "initiation" phase). Note that already after 30 kyr, part of the fault is at the melting temperature (at the depth between ∼1 and 2 km, Fig. 2.23c), and gradually, this zone grows until ∼50 kyr, when it reaches all the way to the bottom of the shell. Consequently, a very strong temperature gradient is established in the near subsurface (approximately the first 1 km), leading to the surface heat flux anomaly reaching up to $\sim$ 1.5 W m^{-2} right above the fault, cf. Fig. 2.23e). For numerical reasons, we do not solve for the production of melt and its transport as in Kalousová et al. (2016) and Section 2.1, and thus the temperature field is simply truncated at the melting temperature. According to results of Kalousová et al. (2014), any melt above an ice column that is at the melting temperature would be extracted into the ocean within a few to a few tens of kyr, depending on the ice permeability.

Despite the fact that the considered conditions are probably irrelevant for

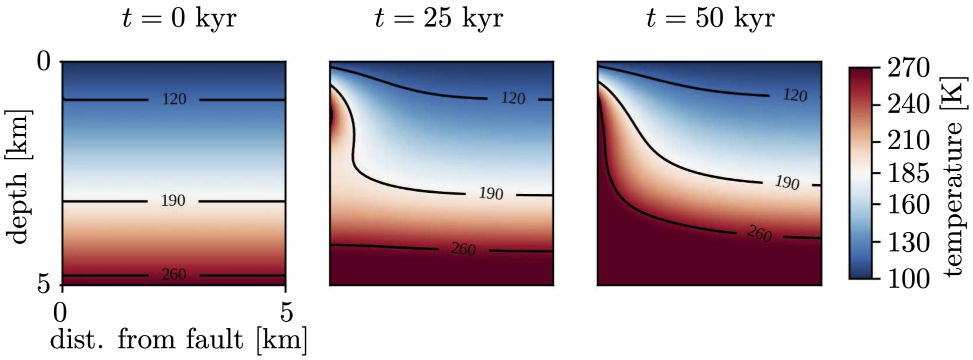

Figure 2.24: Time evolution of the temperature field in the thermally activated simulation (σ_0=6×10^5Pa, D=5km, φ=π, μ_f=0.4), the contours indicate temperatures of 120, 190 and 260 K.

the current state of Europa's shell (the stress amplitude is significantly smaller and the shell probably thicker), this case clearly shows the importance of thermo-mechanical coupling for the evolution of strike-slip faults on Europa. While earlier studies have either neglected the thermal effects (e.g. Rhoden et al., 2012) or considered them unimportant (e.g. Preblich et al., 2007), we have demonstrated that the thermo-mechanical coupling may, under favorable conditions, govern the deformation regime on the strike-slip faults and should, therefore, be taken into account.

2.2.3 Discussion

In this section, we first describe another setting in which a visible offset can be produced by the tidal walking model – partial flooding of the fault zone by liquid water from the ocean. Then we investigate the possible effect of a more general stress field than considered in this part of the thesis. We also discuss the key assumptions adopted here; in particular, we address the description of the fault behavior, the design of the tidal model in terms of the prescribed boundary conditions (parameterization of the tidal forcing), and the effect of different near subsurface material properties. We also consider the limitations of the convective model in terms of the employed ice rheology and single-phase formalism or the effect of the computational domain aspect ratio.

Water Filled Cracks

In the previous section, we assumed that yield stress at the fault increases gradually with depth due to the increase of the overburden pressure. This is true if the contact between the fault walls is dry. However, a water column rising from the ocean can lubricate the contact and simultaneously counteract the overburden pressure in the shell, as suggested by Greenberg et al. (1998). Let us now briefly discuss the results for such a setting with which an observable offset can be produced even for today's diurnal stress amplitudes and range of ice shell thicknesses.

The majority of Europa's faults are assumed to be of extensional origin (Kattenhorn et al., 2009). If the original crack forming the fault reached all the way to the internal ocean, the water column would rise to approximately nine-tenths ($\sim \frac{\varrho_i}{\varrho_w}$) of the shell thickness, thus, partially compensating the overburden pressure within the shell. In order to take this possibility into account, we consider the following extension of (2.47a):

$$\widetilde{\sigma_Y} = \begin{cases} \mu_f(\sigma_n + \varrho_i g(D-z)) \ , & \text{if } z \in \langle \frac{\varrho_i}{\varrho_w} D, D \rangle \\ \mu_f^{\mathrm{w}}(\sigma_n + (\varrho_{\mathrm{w}} - \varrho_i) g z), & \text{if } z \in \langle 0, \frac{\varrho_i}{\varrho_{\mathrm{w}}} D) \end{cases} , \tag{2.51}$$

where z is the vertical coordinate (z=0 at the ice-ocean interface). In this formula, the static normal stress at the fault increases as before down to a depth of $\left(1-\frac{\varrho_i}{\varrho_w}\right)D \sim 0.1D$, where the water column starts to counteract the overburden pressure in the ice, cf. panel (b) on Figure 2.25. At the bottom boundary (z=0), the difference between the two competing pressures is zero, i.e., we assume that the shell is in hydrostatic equilibrium. In the part of the fault, that is filled with water, the friction coefficient changes to $\mu_f^{\mathrm{w}} = 0.1\mu_f$ to mimic the lubrication effect of water (Oksanen and Keinonen, 1982).

For the parameterization of the yield stress given by (2.51), we calculate the thermo-mechanical response as in the previous section - i.e., varying the shell thickness and the stress forcing amplitude. The main difference is that now the yield stress reaches the maximum value at d~$0.1D$, cf. panel (b) on Figure 2.25, which means that the effective mechanical strength of such fault zones is reduced by order of magnitude compared to the case without water column filling the crack.

As a result, we observe accumulation of a substantial surface offset and significant heat generation also for D between 1 km and 10 km and $\sigma_0 = 6 \times 10^4$ Pa. Such forcing corresponds to the activation depth of a few hundred meters (depending on μ_f), which is comparable or larger than one-tenth of the considered thickness. In all these cases, we thus observe activation of the whole fault, and as before, a stabilizing term had to be added (cf. Section 2.2.2), which makes our results only qualitative. However, for the thickest assumed ice shell, the lowest loading stress amplitude is not enough to penetrate the whole ice shell, see Figure 2.25 and the fault is activated in the lower part only, see panel (a) on Figure 2.25. Substantial heating can be then produced to heat the fault up to melting point (panel (c) on Figure 2.25). However, there is no observable offset on the surface, cf. panel (d) on Figure 2.25.

In conclusion, we find that the presence of a water column in the fault zone significantly changes the response of the fault. For the cracks that are filled with water, tidal walking could be an efficient mechanism producing the surface offset even for the present day estimates of the tidal stress and for moderate estimates of the ice shell thickness ($\leq$ 10 km).

Stresses in the Shell

In all simulations, the amplitudes of the loading tangential and normal stresses were taken equal. We also considered their mutual phase shift to be $\varphi = \pi$ (except for results in Figure 2.21), which leads to the largest possible (left-lateral) offset. In reality, both stresses consist of several modes on different timescales, and can differ in amplitudes depending on the position and orientation of the fault. In

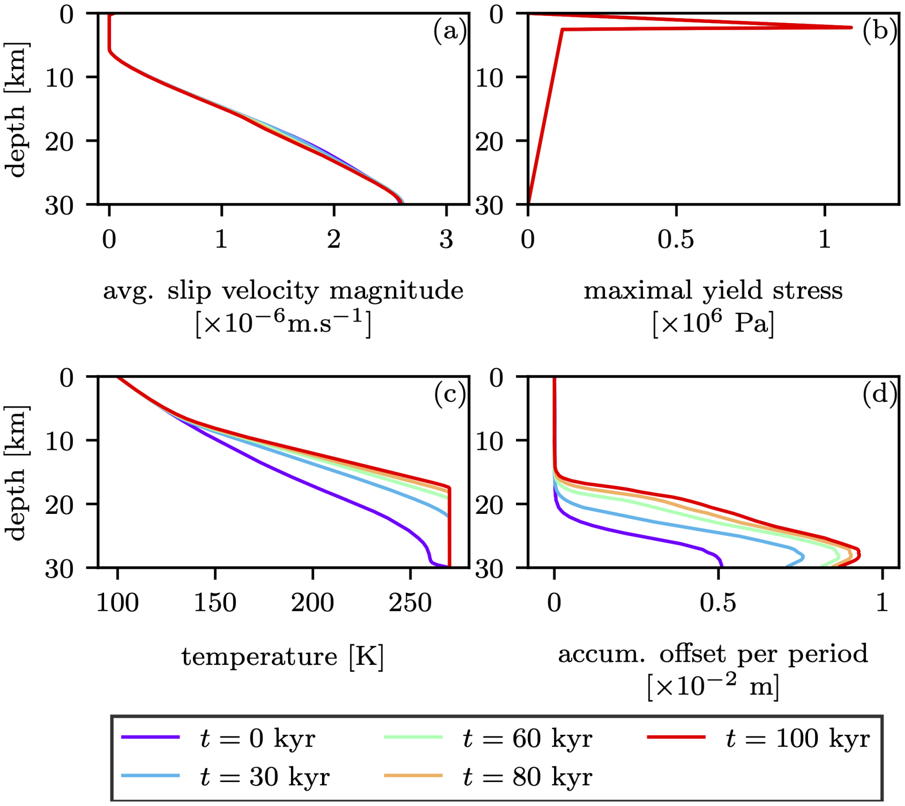

Figure 2.25: Time evolution of a simulation with water filled cracks (σ_0=6×10^4 Pa, D=30 km, $\varphi = \pi$, μ_f=0.4). *Top*: Depth profiles of quantities at the fault: (a) absolute value of the slip velocity averaged over one period $\overline{|\mathrm{v}_{\mathrm{slip}}|}$, (b) maximal yield stress (with $\sigma_n = 6 \times 10^4$ Pa), *Bottom*: (c) temperature T, (d) accumulated offset per period at the fault.

general, the tangential and normal loading stresses at a given point and for a given orientation can be expressed as follows

$$\sigma_t(t) = \sigma_t^{\mathrm{BG}}(t) + \sigma_{0,t}\sin(\omega t) \ , \tag{2.52a}$$
$$\sigma_n(t) = \sigma_n^{\mathrm{BG}}(t) + \sigma_{0,n}\sin(\omega t + \varphi) \ , \tag{2.52b}$$

where $\sigma_{0,\bullet}$ are the amplitudes of stresses induced on diurnal timescale and $\sigma_\bullet^{\mathrm{BG}}$ are stresses induced on longer timescales. The diurnal stresses include eccentricity tides and possibly also obliquity tides as well as the contribution from physical libration. Their magnitudes are probably comparable with values of about 100 kPa (e.g. Nimmo et al., 2009; Bills et al., 2009; Rhoden et al., 2010), which are consistent with the range considered here. The other known stress-inducing mechanisms comprise the non-synchronous rotation and polar wander (amplitudes of up to several MPa), thermal and compositional convection (<1 MPa), or tensile stress due to the ice shell thickening (several MPa) (Nimmo et al., 2009; Sotin et al., 2009). These mechanisms act on considerably longer than diurnal periods and can thus be considered as a constant-in-time stress background within each diurnal tidal period.

In this study, we did not consider any difference between the tangential and normal diurnal stress amplitudes nor the presence of any long-period stress background. Their importance can be, in a simplified manner, assessed through the methodology for estimating the upper limit on fault activation depth $d_{\max}$, derived in Appendix 2.2.5. Investigating $d_{\max}$ can then be used as a guide for assessing the impact of variables, which we were not able to investigate in detail by the presented model due to computational consideration.

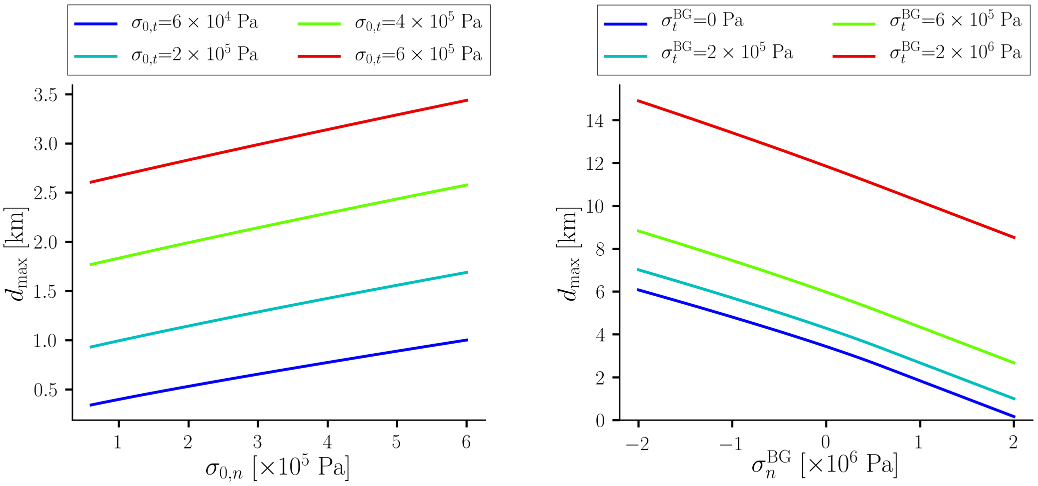

Figure 2.26: Maximum fault activation depth $d_{\max}$ during one cycle. *Left*: effect of variations of the normal $\sigma_{0,n}$ (x-axis) and tangential $\sigma_{0,t}$ (color) stress amplitudes with no background stress. *Right*: effect of the background stresses σ_t^{BG} (color) and σ_n^{BG} (x-axis) for fixed diurnal amplitudes $\sigma_{0,t}$=$\sigma_{0,n}$=6×10^5 Pa. Friction coefficient μ_f=0.4 and phase shift φ=π were used in both cases.

Figure 2.26 (left) illustrates the effect of the normal and tangential stress amplitudes on the maximum fault activation depth $d_{\max}$, given by the following formula assuming φ=π (see eq. 2.67):

$$d_{\max} = \frac{\sigma_{0,t}}{\varrho_i g} \frac{1{+}\mu_f \left(\frac{\sigma_{0,n}}{\sigma_{0,t}}\right) + \sqrt{1 + 2\mu_f \left(\frac{\sigma_{0,n}}{\sigma_{0,t}}\right)}}{\mu_f} = \frac{\sigma_{0,t}{+}\mu_f\sigma_{0,n} + \sigma_{0,t}\sqrt{1{+}2\mu_f \left(\frac{\sigma_{0,n}}{\sigma_{0,t}}\right)}}{\varrho_i g \mu_f} . \tag{2.53}$$

The depth $d_{\max}$ is a monotone increasing function of both $\sigma_{0,n}$ and $\sigma_{0,t}$. The numerator in the second expression shows that the dependence (of the leading order terms) differs by a factor μ_f (<1), and therefore, $d_{\max}$ is more sensitive to variations of $\sigma_{0,t}$ than $\sigma_{0,n}$. We can also see from the first expression in eq. (2.53) that especially for lower values of μ_f, the ratio between the stresses $\frac{\sigma_{0,n}}{\sigma_{0,t}}$ can be considered as a secondary parameter (compared to the magnitude of the tangential stress and the friction coefficient). This justifies the simplifying assumption $\sigma_{0,n}{\sim}\sigma_{0,t}$, that we use.

The amplitudes of long-period stresses can exceed those of diurnal stresses by orders of magnitude and can be comparable to the hydrostatic pressure. In Figure 2.26 (right), we show the behavior of $d_{\max}$ (computed in this case as a numerical maximum of expressions 2.59 and 2.62 in the Appendix 2.2.5, see the discussion at the end of the Appendix 2.2.5 for a range of background stresses). We observe that large background tensile (negative in our notation) normal stress, as well as large tangential stress, result in larger $d_{\max}$, while large compressive normal stress reduces it. The latter effect can be, to some extent, compensated by an increased tangential stress. Note also that the effect of normal stress is again scaled by the friction coefficient: for $\mu_f<1$, the effect of the tangential stress is more pronounced than the effect of the normal stress. Unless the background compressive normal stress is significantly larger than the tangential stress, the magnitude of several MPa can help to increase the activation depth from a few kilometers to $\sim$10 km even for the current value of eccentricity. As a consequence, the background stress can help to facilitate the process of tidal walking or modulate it on the characteristic timescale of the associated long-period mechanism.

Fault Description

The description of the fault employed in this study is based on a relatively simple Mohr-Coulomb-like criterion. However, ice-ice contact is known to exhibit more complex frictional properties. It has been described, for instance, by the so-called rate and state friction law (e.g., Fortt and Schulson, 2009; Lishman et al., 2011), where the friction coefficient depends on both the slip velocity (rate) and an internal variable (state), that has its own evolution dynamics, see Section 4.2.3. Even though we use a constant value of the friction coefficient (μ_f=0.4 as a reference value), we tested the possible effect of this more complex description of fault behavior by considering the limiting cases (μ_f=0.1 and 0.8). The effect is significant, both in terms of the activation depth and in terms of the produced heat flux anomaly; see Figs. 2.19 and 2.22 right. Better estimates of the frictional properties of ice-ice contact in icy-worlds conditions are therefore necessary for constraining the quantitative predictions; however, all the qualitative results of our study remain unaffected by the choice of μ_f.

Moreover, for numerical reasons, we replace the Mohr-Coulomb friction criterion (2.17) by its regularized version, i.e., by the slip condition (2.18a) with an effective sliding coefficient (2.18b). The parameterization contains two parameters, β^* and n. The first parameter is the sliding coefficient in the "locked case" (i.e., $\beta^*\gg1$ Pa s m^{-1}), the second parameter n governs how fast the effective sliding law switches from high-friction below the yield stress to low-friction when the yield stress is approached. The Mohr-Coulomb criterion corresponds to the limit $\beta^*\to\infty$ and $n\to\infty$, but in the simulations, we used $\beta^*=10^{18}$ Pa s m^{-1} and n=2. The former value does not have any particular significance, and changing it by orders of magnitude did not affect the results. The latter choice for parameter n was motivated by numerical reasons - having lower n improved the convergence of the Newton solver. We verified that using larger exponents did not have any significant effect on the simulations.

In this part of the thesis, we do not consider the effect of melting at the fault since our convective model does not allow us to quantify the amount of meltwater (cf. discussion below) and simply cuts-off the temperature at the melting point. The presence of liquid lubricant on a frictional contact may reduce the friction coefficient by more than one order of magnitude (Oksanen and Keinonen, 1982); hence it would probably affect the quantitative response of the model. Based on numerical experiments with the model from the previous section (coupled tidal and a two-phase convective model), we can hypothesize that after melt appears at the fault, the sliding process becomes very complex. Namely, the reduction of the friction coefficient with melt (exponential decrease in Kalousová et al.

(2016) and in Section 2.1.1) leads to a very fast and localized switch-off of the frictional heating followed by rapid melt refreezing, and consequently, the heat production increases again. This feedback mechanism adds a lot of complexity to the fault behavior, which can be resolved only under extreme spatial and temporal resolutions. Since we are primarily interested in the depth- and time-averaged quantities at the surface, all of which are quite insensitive to most of these subtleties, we restrained ourselves to the simpler approach.

Forcing of the Tidal Model

Let us also comment on the delicate choice of the boundary conditions for the tidal model, i.e., on its forcing. We prescribe the value of the shear stress (time-variable but constant in space) on the right boundary and keep the top and bottom boundaries frictionless. The latter assumption is quite natural since the bottom boundary is an ice-ocean contact and the top boundary represents the surface. The former assumption is, however, more questionable since the right boundary of the computational domain is artificial – in reality, it is an internal surface within the ice shell. Our aim was to prescribe such a forcing, which would result in internal shear stresses compatible with the tidal stress amplitudes inferred from an independent tidal deformation simulation by e.g., widely used SatStress code (Crawford et al., 2007; Wahr et al., 2009; Kay and Kattenhorn, 2010). While in reality, the internal stresses are induced by the global tidal deformation of the three-dimensional planetary shell, in the simplified two-dimensional model, this forcing could be reasonably reproduced through the adopted stress boundary condition. An alternative forcing was used in Preblich et al. (2007), who imposed the tidal strain rate instead of stress, which, however, prevented their model from accumulating any irreversible offset at the right boundary. Nimmo and Gaidos (2002) forced their model also kinematically by prescribing the displacement at the surface. This choice again does not allow to obtain the surface offset as a model output.

Near-subsurface Mechanical and Thermal Properties

Flexural model of fault-related topography in Nimmo and Schenk (2006) suggests a reduction of the near-surface shear modulus of Europa's ice shell by order of magnitude as a consequence of large porosity or near-surface fracturing (Nimmo et al., 2003). Similarly, either high porosity or the possible presence of clathrate hydrates at the surface are expected to lead to a decrease of thermal conductivity in the uppermost part of the shell (Nimmo and Giese, 2005). We attempted to estimate the effect of both phenomena on our results numerically.

Reduction of the near-surface shear modulus, i.e., weakening of the uppermost part of the shell, leads to a partial reduction of the stresses transmitted at the fault. One order of magnitude reduction in shear modulus in the topmost one kilometer of a 10km shell leads in the setting of Case 1 from Section 2.2.2 to a reduction of the surface offset δ_{s} by 30-40% depending on the viscosity and details of the shear modulus depth dependence.

A near-surface reduction of thermal conductivity as in Nimmo and Giese (2005) (reduction of k by a factor of 20 near the surface) in the thermally coupled models does not have a significant impact on the surface accumulated offset δ_{s}, but leads to a reduction of the thermal signature Δq. For the thermally-activated case described in Section 2.2.2, the amplitude of the surface heat flux anomaly was reduced by approximately 20%.

Convective Model

The convective model used in this study is based on the two-phase model of Kalousová et al. (2016), where we suppressed the two-phase formalism and reduced the system of governing equations to the standard single-component incompressible Stokes-Fourier system (2.46). The reason for this choice, that has already been mentioned in the previous section, was the additional complexity. When melting was included, it led to an extreme increase of resolution requirements both in space and time, while it did not seem to affect the main conclusions of this study. Hence, we opted for the simpler choice, which allowed us to compute more and longer coupled simulations.

The convective model describes the ice as a non-Newtonian viscous fluid with viscosity given by (2.24). The temperature dependence of this empirical law leads to unrealistically high viscosities larger than 10^{30} Pa s in the very low temperature zone near the surface. Such high values of viscosity can lead to stresses inconsistent with the mechanical strength of ice. Ideally, this should be avoided by replacing the viscous rheology with some form of visco-plastic law (e.g. Showman and Han, 2005; Bland and McKinnon, 2012; Howell and Pappalardo, 2018), or, one can circumvent the problem by adopting a viscosity cut-off which imposes an upper bound on the viscosity value. In this study, we use the value of 10^{22}Pa s, and viscosity is thus reduced only in the coldest part of the shell that deforms elastically. For that reason, the viscosity cut-off does not affect the viscous dissipation. Similarly, also the frictional heating at the fault is insensitive to the choice of viscosity cut-off.

Aspect Ratio

Since the right boundary of our computational domain is artificial (internal surface within the shell), a natural question arises as to what amount are the results affected by the chosen aspect ratio. Although we plot the results on a domain with aspect ratio 1, the computations were done on a domain with aspect ratio 2. We have investigated the effects of different aspect ratios (1 and 4) but found the differences in the results insignificant.

2.2.4 Conclusions

In this part of the thesis, we have numerically tested the tidal walking hypothesis proposed by Hoppa et al. (1999a) to explain the observed lateral offset on some of the strike-slip faults on Europa's surface. Our numerical model combines two building blocks: (i) a viscoelastic tidal model that evaluates the slip on the fault, which is characterized by the Mohr-Coulomb failure criterion, and the deformation of the surrounding ice, and (ii) a viscous convective model solving the long-term thermal evolution of the shell.

We have modeled the thermo-mechanical evolution of a shell containing a predefined fault zone considering the range of ice shell thickness between 1 km and

30 km, and for the tidal stress amplitudes between the present-day estimate of 6×10^4 Pa and 6×10^5 Pa corresponding to a possible high eccentricity epoch in Europa's history. We studied the development of an offset between the two sides of the strike-slip fault at the surface within a period of 100 kyr, estimated as a time span for fault's activity.

Our results confirm the conclusions of an earlier numerical study by Preblich et al. (2007) that a significant lateral offset at the strike-slip faults can be produced if the active part of the fault reaches either the bottom of the shell or penetrates to a very low viscosity zone. The whole-shell penetration appears to be quite improbable since it requires the shell to be very thin (≤ 1 km) and, simultaneously, the acting tidal stresses to be larger than the present-day values. We demonstrate, however, that the second scenario – i.e., penetration of the active fault zone to a low-viscosity zone, could have been facilitated by a mechanism of thermo-mechanical coupling. For ice shell thickness of 5 km and the tidal stress amplitude of 6×10^5 Pa, the frictional heating at the fault and mechanical dissipation in its vicinity lead to a sufficient thermal weakening of the ice near and underneath the fault, that an offset of 1 km is produced within 100 kyr. Finally, a third option, which allows producing a significant offset even for the present-date estimates of the tidal forcing amplitudes and ice-shell thickness of less or equal to ten kilometers, requires that the crack forming the fault is partially filled with liquid water from the underlying ocean. The resulting compensation of the ice overburden pressure by the water column reduces the effective strength of the shell by an order of magnitude, thus promoting the slip and offset accumulation even for the current tidal stress forcing. In this setting, the tidal walking mechanism seems to be very efficient. Still, for this case, our model loses quantitative predictability since stabilization of the motion along the fault must be added.

For all cases, we have also studied the corresponding thermal signatures of the strike-slip motions at the fault. We show that moderate surface heat flux anomaly Δq between 10^{-2} and $10^{-1}\,\mathrm{W\,m^{-2}}$ can be obtained even for cases when the accumulated offset is negligible ($D{>}1$ km, $\sigma_0{=}2\times10^5$ Pa). From this point of view, measuring heat flux anomalies could serve as a tool for identifying active strike-slip faults on Europa even for faults without any significant offset. If the fault activation depth reaches the bottom of the shell, the mechanical dissipation by frictional heating at the fault combined with the bulk dissipation in the visco-elastically deforming ice is often enough to drive a significant temperature increase, possibly accompanied by partial melting in the fault zone. In these cases, the thermal signatures at the surface are expected to be very significant. Since partial melting in the fault zone has been suggested to affect the surface morphology (e.g., formation of double ridges, Nimmo and Gaidos, 2002), one could hypothesize that the presence of such surface features could be interpreted as the witness of a period of (earlier) vigorous strike-slip activity.

2.2.5 Appendix A: Analytical estimate of the fault activation depth

We now derive the approximate formula for the fault activation depth (eq. 2.49). Figure 2.27 shows an illustrative snapshot of the shear stress amplitude at the fault $|\mathrm{s}_x|$ at some instant during the opening phase, i.e., for $\sigma_n(t){<}0$ (left), and during the closing phase, i.e., for $\sigma_n(t)>0$ (right).

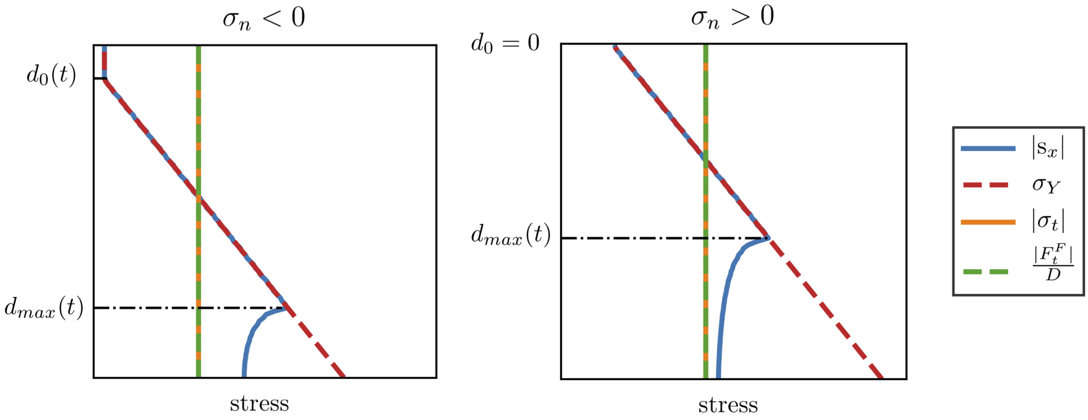

Figure 2.27: Shear stress amplitude at the fault $|\mathrm{s}_x|$ (blue line) as a function of depth in the opening ($\sigma_n<0$, left panel) and closing ($\sigma_n>0$, right panel) phase. The red dashed line represents the yield stress σ_Y and the two vertical lines represent the (absolute values of) the average tangential stress $|F_t^F(t)|/D$ at the fault (green dashed line) and of the average tangential stress $|F_t^R(t)/D|=|\sigma_t|$ at the right boundary (orange line), respectively.

During the opening phase (Figure 2.27 left), the fault is divided into three parts: (i) top ($d\in\langle 0, d_0(t)\rangle$), where the fault is stress free in the tangential direction due to negative σ_n exceeding the overburden pressure, i.e., $\mathrm{s}_x=0$, (ii) middle ($d\in\langle d_0(t), d_{\max}(t)\rangle$), where the amplitude of shear stress equals the yield stress, $|\mathrm{s}_x| = \sigma_Y$, and (iii) bottom ($d\in\langle d_{\max}(t), D\rangle$), where the shear stress is below the yield stress, $|\mathrm{s}_x|<\sigma_Y$. During the closing phase, the top part is missing, i.e., $d_0=0$, since σ_n is in the compressive regime, $\sigma_n>0$. For both cases, the bottom part is absent if the fault is activated across the whole shell. Let us now investigate these two cases separately.

Opening phase ($\sigma_n(t)<0$)

The total tangential force exerted at the fault in the opening phase reads

$$F_t^F(t) = \mathrm{sgn}(\sigma_t(t)) \int_{d_0(t)}^{d_{\max}(t)} \mu_f(\sigma_n(t) + \varrho_i g\xi) d\xi + \int_{d_{\max}(t)}^{D} \mathrm{s}_x(t,\xi)\, d\xi, \tag{2.54}$$

where $d_0(t){=}-\frac{\sigma_n(t)}{\varrho_i g}$ is the depth at which the yield stress given by formula (2.47) becomes positive and $d_{\max}(t)$ is the maximum activation depth at a given time. In the following derivation, we will implicitly assume that $d_{\max}\leq D$. We obtain

$$F_t^F(t) = \frac{\mu_f}{2\varrho_i g} \mathrm{sgn}(\sigma_t(t)) \Big(\sigma_n(t) + \varrho_i g d_{\max}(t)\Big)^2 + \int_{d_{\max}(t)}^{D} \mathrm{s}_x(t,\xi)\, d\xi. \tag{2.55}$$

In the absence of stabilization or any other body forces, cf. (2.11), and because of free-slip boundary conditions at the top and bottom boundaries, this force must be balanced by the tangent force acting on the right boundary:

$$F_t^R(t) = \sigma_t(t) D, \tag{2.56}$$

where $\sigma_t(t)$ is the shear stress prescribed at the right boundary (see eq. 2.48b) which is constant in space. The tangential force balance $F_t^R(t) = F_t^F(t)$ can be recast into

$$\frac{\mu_f}{2\varrho_i g}\Big(\sigma_n(t) + \varrho_i g d_{\max}(t)\Big)^2 - |\sigma_t(t)| d_{\max}(t) = \operatorname{sgn}(\sigma_t(t)) \int_{d_{\max}(t)}^{D} \Big(\sigma_t(t) - \mathrm{s}_x(t,\xi)\Big)\, d\xi. \tag{2.57}$$

Based on the stress snapshot in Figure 2.27 (left), it appears that the right-hand side of (2.57) is non-positive (in the picture it holds $|\mathrm{s}_x(t,\xi)| \geq |\sigma_t(t)|$, for all $\xi \geq d_{\max}(t)$), however, the non-positivity cannot be guaranteed in general. Taking it as an assumption of the derivation (see discussion further) yields a quadratic inequality for $d_{\max}(t)$:

$$\frac{\mu_f}{2\varrho_i g}\Big(\sigma_n(t) + \varrho_i g d_{\max}(t)\Big)^2 - |\sigma_t(t)| d_{\max}(t) \leq 0. \tag{2.58}$$

Search for the maximum $d_{\max}(t)$ satisfying (2.58) yields

$$d_{\max}(t) = \frac{|\sigma_t(t)| - \sigma_n(t)\mu_f}{\mu_f \varrho_i g} + \frac{1}{\mu_f \varrho_i g}\sqrt{(\sigma_t(t))^2 - 2\mu_f |\sigma_t(t)| \sigma_n(t)}\,. \tag{2.59}$$

Closing phase ($\sigma_n(t)>0$)

Here, the situation is simpler since $d_0=0$ during the closing phase. The total tangential force exerted at the fault in the closing phase reads

$$\begin{aligned} F_t^F(t) &= \operatorname{sgn}\Big(\sigma_t(t)\Big) \int_0^{d_{\max}(t)} \mu_f \Big(\sigma_n(t) + \varrho_i g \xi\Big) d\xi + \int_{d_{\max}(t)}^{D} \mathrm{s}_x(t,\xi)\, d\xi, \\ &= \operatorname{sgn}\Big(\sigma_t(t)\Big) \left(\mu_f \sigma_n(t) d_{\max}(t) + \mu_f \varrho_i g \frac{d_{\max}^2}{2}\right) + \int_{d_{\max}(t)}^{D} \mathrm{s}_x(t,\xi)\, d\xi. \end{aligned} \tag{2.60}$$

Comparing this force again with the tangent force acting on the right boundary (2.56), we obtain the following analogy of (2.58):

$$d_{\max}(t)\left(d_{\max}(t) - \frac{2}{\mu_f \varrho_i g}\Big(|\sigma_t(t)| - \mu_f \sigma_n(t)\Big)\right) \leq 0, \tag{2.61}$$

under the same assumptions on the term which appears on the right-hand side of (2.57). Looking for maximum non-negative $d_{\max}(t)$ satisfying (2.61), we get

$$d_{\max}(t) = \max\left(0, \frac{2}{\mu_f \varrho_i g}\Big(|\sigma_t(t)| - \mu_f \sigma_n(t)\Big)\right). \tag{2.62}$$

Special case $\varphi=\pi$

Considering now the special case used in the manuscript, i.e., taking the phase shift between the normal and tangential applied stress to be $\varphi=\pi$:

$$\sigma_t(t) = \sigma_{0,t} \sin(\omega t), \tag{2.63}$$
$$\sigma_n(t) = -\sigma_{0,n} \sin(\omega t), \tag{2.64}$$

we obtain

$$d_{\max}(t) = \frac{\sigma_{0,t}}{\varrho_i g} \frac{1{+}\mu_f\left(\frac{\sigma_{0,n}}{\sigma_{0,t}}\right) + \sqrt{1 + 2\mu_f\left(\frac{\sigma_{0,n}}{\sigma_{0,t}}\right)}}{\mu_f} \sin(\omega t) \quad \text{if} \quad t \in \langle 0, P/2 \rangle\,, \tag{2.65}$$

$$d_{\max}(t) = \max\left(0, \frac{2}{\mu_f \varrho_i g}(\mu_f \sigma_{n,0} - \sigma_{t,0}) \sin(\omega t)\right) \quad \text{if} \quad t \in \langle P/2, P \rangle\,, \tag{2.66}$$

which has a global maximum at $t{=}\frac{\pi}{2\omega}{=}\frac{P}{4}$:

$$d_{\max} = \frac{\sigma_{0,t}}{\varrho_i g} \frac{1{+}\mu_f\left(\frac{\sigma_{0,n}}{\sigma_{0,t}}\right) + \sqrt{1 + 2\mu_f\left(\frac{\sigma_{0,n}}{\sigma_{0,t}}\right)}}{\mu_f}. \tag{2.67}$$

Analogously, we would get the same expression if we took $\varphi{=}0$, i.e., for normal and tangential loading stresses in phase, the maximum (2.67) would be attained at $t{=}\frac{3P}{2}$. Considering the same amplitudes of the forcing normal and tangential stress, i.e., setting $\sigma_{0,t} = \sigma_{0,n}{=}\sigma_0$, yields formula (2.49) from the main text.

During the derivation, we assumed the non-positivity of the term

$$\operatorname{sgn}(\sigma_t(t)) \int_{d_{\max}(t)}^{D} \Big(\sigma_t(t) - \mathrm{s}_x(t,\xi)\Big) d\xi,$$

which cannot be guaranteed by analytical arguments for all times during the period, but in numerical experiments, it holds at the instant corresponding to the maximal depth of fault activation. The justification of the assumption is also supported by the fact that the analytical estimate provides an upper bound for numerically obtained values of fault activation depths – see Figure 2.19. Finally, note that the validity of the assumption is ensured if the integral vanishes thanks to $d_{\max}(t){=}D$, that is if the fault activation depth equals the thickness of the shell. The estimate (2.67) is, therefore, most accurate in the regime when the fault activation depth $d_{\max}$ approaches the shell thickness D and the sliding switches from the partially-locked regime to the whole-fault sliding. This best corresponds to the simulation with whole-fault activation (cf. the green square in the left panel of Figure 2.19).

Let us note, that we derived the final formula (2.67) under the assumption that $\varphi{=}\pi$ (or $\varphi{=}0$). For other values of the phase shift, one would have to seek a numerical maximum over the period of the function defined by expression (2.59) for $\sigma_n(t){<}0$ and by (2.62) for $\sigma_n(t){>}0$.

3. Modelling “tiger stripes” on Enceladus

Despite its small size, Enceladus is one of the most active Solar System bodies with a unique cryovolcanic activity feeding Saturn’s E-ring (Kempf et al., 2010). Enceladus is differentiated into a (probably) porous core, global ocean, and an ice shell with variable thickness reaching its minimum in the south polar terrain (SPT); see Section 1.2 for more information. The most prominent features in the SPT are the “tiger stripes” (Damascus, Baghdad, Cairo, and Alexandria) correlating with the position of Enceladus’ jet plumes (Porco et al., 2006). The activity of the jet plumes varies significantly depending on the position of Enceladus in its orbit, indicating a relation to periodic variations in tidal stress (Hurford et al., 2007; Hedman et al., 2013; Nimmo et al., 2014; Ingersoll et al., 2020).

The nature of the tiger stripes remains a subject of debate. Given their appearance and ability to transfer heat and mass through the ice shell, the tiger stripes are likely to be a combination of tectonic faults and fissures. Models of tidal deformation usually assume that the displacement field is continuous and that the stress in the SPT is not affected by the presence of faults (Hurford et al., 2007; Smith-Konter and Pappalardo, 2008; Hurford et al., 2009, 2012; Nimmo et al., 2014; Běhounková et al., 2015; Beuthe, 2018, 2019; Patthoff et al., 2019; Rhoden et al., 2020). Then spatial and temporal changes in the normal stress on the fault planes can be evaluated using spectral methods and compared with the observed variations in the plume activity.

This approach was challenged by Souček et al. (2016), who developed a finite element model in which the tiger stripes are treated as frictionless water-filled cracks, cf. Kite and Rubin (2016). The model was later modified to include lateral variations in ice shell thickness (Běhounková et al., 2017), and a viscoelastic ice rheology (Souček et al., 2019). Although the model of Souček and co-workers is undoubtedly a step towards a better understanding of the role played by the tiger stripes in Enceladus thermal evolution, it has a major weakness: it does not take into account the friction force acting on the fault planes. As a consequence, the model overestimates the stress near the tips of the faults and predicts zero dissipation between the fault walls.

In this chapter, we present a new 3D finite-element model of Enceladus’ ice shell with the friction inside the fault zone of tiger stripes approximated by a Mohr-Coulomb-type yield criterion similar to Chapter 2 and Sládková et al. (2020).

3.1 Test case - planar fault zone geometry

In the second chapter, we modeled a behavior of a strike-slip fault and its surroundings using a 2D model where the fault was represented by a boundary condition using the Mohr-Coulomb type yield criterion. In this chapter, we want to employ the same type of contact condition but represented by a specific stress-dependent rheology within a narrow fault zone in order to be able to model the tiger stripes (and not just one fault) within the 3D model of the Enceladus ice

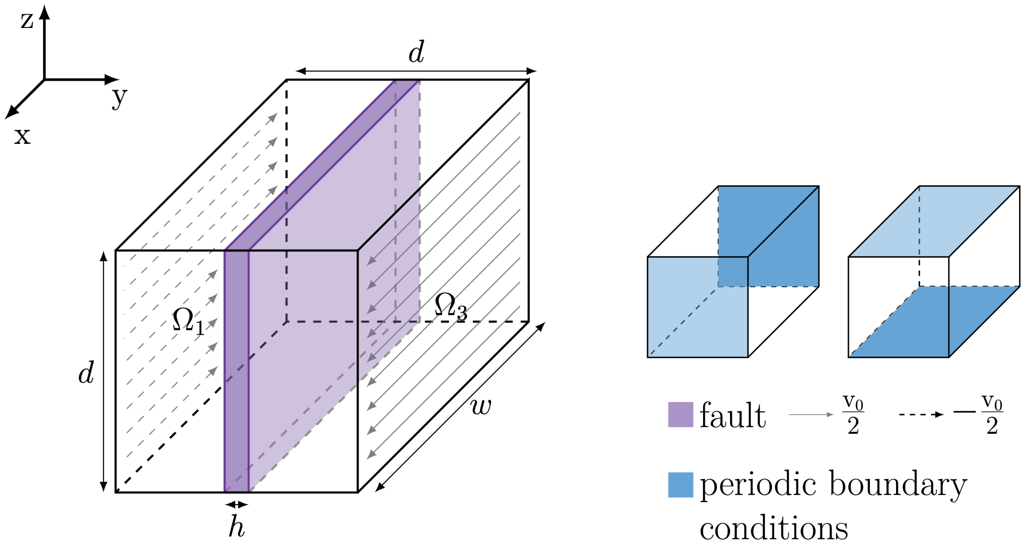

Figure 3.1: A computational domain Ω with a prescribed fault zone in the middle (purple). The Dirichlet boundary conditions for velocity are depicted by arrows; on the rest of the boundaries, periodic boundary conditions are used, providing an effectively infinite domain in the x and z direction. The periodic boundary conditions are illustrated by the blue color: darker color indicates the side from which the velocity is copied, and lighter denotes the destination.

shell (Souček et al., 2019).

We start with a problem in simplified geometry - considering a box-shaped ice domain with a preexisting "planar" fault zone in the center, see Figure 3.1, and we subject it to velocity strike-slip forcing at the sides in order to test and benchmark our approach and the employed approximations. The behavior of the ice is simulated by viscoelastic Maxwell-type rheology, where the fault zone is described as a weaker region with effectively plastic behavior (through effective stress-dependent viscosity), while the surrounding of the fault is set to be effectively elastic (having high constant viscosity).

3.1.1 Governing equations

We solve the equation of motion for a compressible Maxwell viscoelastic body (in the small displacement approximation) in a computational domain Ω, assuming a quasi-static setting relevant for the tidal loading in planetary applications, i.e., we ignore the inertial forces:

$$\operatorname{div} \mathbb{T} = \mathbf{0}, \tag{3.1a}$$

$$\mathbb{T} = K(\nabla \cdot \mathbf{u})\mathbb{I} + \mu\Big[\nabla\mathbf{u} + \big(\nabla\mathbf{u}\big)^T - \frac{2}{3}(\nabla \cdot \mathbf{u})\mathbb{I}\Big] - \frac{\mu}{\eta}\int_0^t \mathbb{S}(t')\mathrm{d}t', \tag{3.1b}$$

where $\mathbb{T}$ is the Cauchy stress tensor, K and μ are the bulk and shear moduli, $\mathbf{u}$ is the displacement, $\mathbb{I}$ is the identity tensor, η is the viscosity, $\mathbb{S}$ is the deviatoric part of the stress tensor and t is time.

3.1.2 Finite-width fault zone analogue of a frictional contact

In order to approximate the friction on a contact plane by deformation in a narrow fault zone, see Figure 3.1, we need to translate the contact problem into the terms of continuum mechanics. As in Section 2.1.2, we assume that the behavior of the fault, which we wish to approximate, is governed by a Mohr-Coulomb-type “stick-slip” friction criterion. This criterion discriminates between the locked state (“stick”), which occurs in regions where the stress exerted on the fault is below the yield stress σ_Y, and the sliding regime (“slip”), which is activated when the friction force reaches this threshold.

To approximate the stick-slip behavior in the fault zone, we will introduce an approximation of plasticity through a stress-limiting viscosity; see Tosi et al. (2015). The stress-limiting viscosity η_{eff} will allow us to mimic the effective sliding coefficient in the fault zone in the sense of preventing the stress in the fault zone from exceeding the yield stress σ_Y. Since we want to describe the rest of the domain elastically, we shall employ a visco-elastic Maxwell rheology in the whole domain and distinguish between two regions - the fault and its surrounding - by different viscosities. In the fault zone, we use the stress limiting viscosity η_{eff}, while in the complement of the fault zone, we employ a very high constant viscosity value η_{Max}, thus making the material there effectively elastic.

1D mechanical analogues

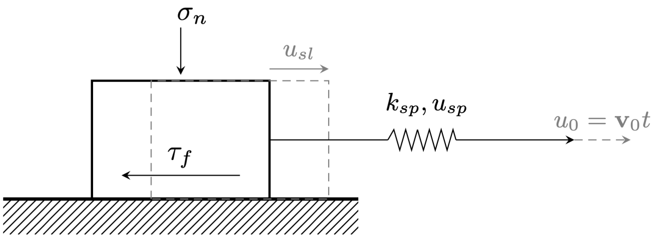

Figure 3.2: A mechanical analogue for a contact frictional problem: the spring slider, where u_{sp}, u_{sl} denote the displacement of the spring and the slider, respectively, k_{sp} is the stiffness of the spring, and the frictional force τ_f is given by the multiplication of the coefficient of friction μ_f and the normal stress σ_n applied on the pad.

To better understand the correspondence between a contact frictional problem and the visco-elastic model with stress-limiting viscosity, we first concentrate on 1D mechanical analogues. The frictional contact can be simulated through a spring slider, see Figure 3.2, where (in our case) the spring is pulled with a constant velocity v_0. Once the frictional force (given by the product of the coefficient of friction and normal stress applied on the pad) between the slider and the pad is overcome, the slider starts sliding.

The Maxwell rheology with stress-limiting viscosity, which we want to use to mimic the spring-slider (see Figure 3.3), is represented by a spring with stiffness

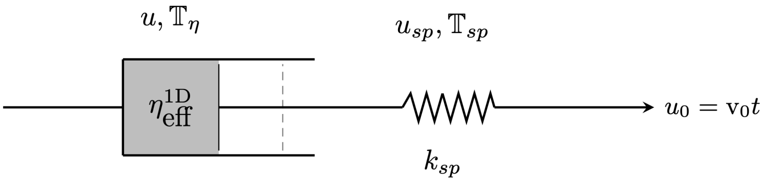

Figure 3.3: Mechanical analogue for the Maxwell model: a dashpot with viscosity $\eta_{\text{eff}}^{\text{1D}}$ connected to a spring with stiffness k_{sp} pulled by constant velocity v_0.

k_{sp} in series with a dashpot with effective viscosity $\eta_{\text{eff}}^{\text{1D}}$ defined as

$$\eta_{\text{eff}}^{\text{1D}} = \frac{\eta_{\text{Max}}}{\left\{1 + \left(\frac{\eta_{\text{Max}}\text{v}_{\text{slip}}}{\sigma_Y}\right)^n\right\}^{\frac{1}{n}}}. \tag{3.2}$$

When the spring is pulled by a constant velocity, the stress in the dashpot has to overcome the yield stress σ_Y in order for the dashpot to start deforming. Here the symbol σ_Y is a yield stress, characterizing the maximal force, η_{Max} is a large auxiliary number, and n is an exponent characterizing the transition between the "stick" and "slip" regimes. In Figure 3.4, we plot the characteristic behavior of the Maxwell model with effective viscosity $\eta_{\text{eff}}^{\text{1D}}$. On the x axis, we move the slip velocity v_{slip} corresponding to the rate of deformation of the dashpot and defined here as the ratio of the stress magnitude and the viscosity. On the left y axis, we have the effective viscosity (blue) expressed in fractions of background viscosity (η_{Max}), and on the right y axis, we have the stress (purple) plotted in fractions of the yield stress σ_Y.

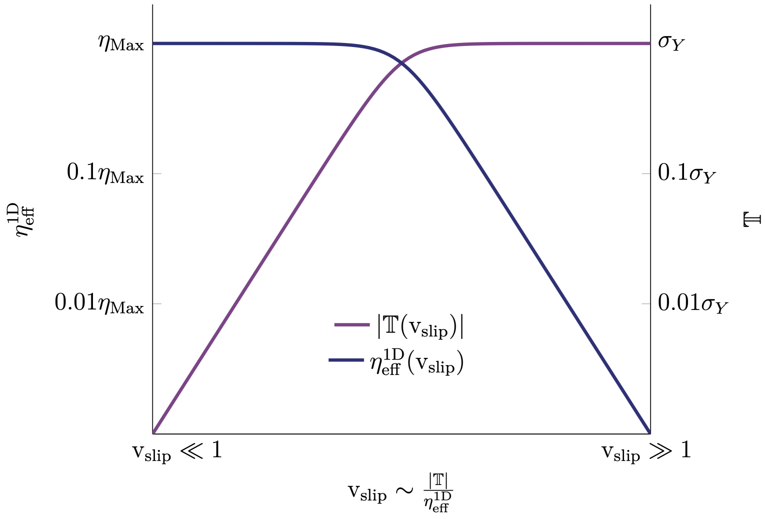

Figure 3.4: The dependence of the effective pseudoplastic stress-limiting viscosity η_{eff} (blue line) and stress $\mathbb{T}$ (purple line) on the slip velocity v_{slip} (logarithmic scale is used).

In Figure 3.4, we can see how the response of such a system corresponds to the spring slider. For low slip velocity $\text{v}_{\text{slip}} \ll 1$, corresponding to the "stick" state (left part of Figure 3.4), the viscosity is very high, $\eta_{\text{eff}}^{\text{1D}} \sim \eta_{\text{Max}}$ (making the "fault zone" represented by the dashpot very stiff). For states with higher slip velocity ("slip" state), the viscosity is decreasing (effectively weakening the “fault zone”), so that it ensures that the stress does not exceed the yield stress σ_Y ($|\mathbb{T}| \sim \eta^{1D}_{\mathrm{eff}} \mathrm{v}_{\mathrm{slip}} \leq \sigma_Y$). This is the reason why we talk about “stress-limiting viscosity”; see the right y axis on Figure 3.4.

3D fault zone - approximating slip velocity

In contrast with the contact problem (as in Chapter 2), when considering the finite fault zone, we must first deal with the fact that the very definition of the slip velocity is not straightforward. In the contact problem (e.g., the spring slider), the slip velocity is perfectly defined as the velocity of the slider. In the 1D Maxwell mechanical analogue, we can define it as the rate of deformation of the dashpot. For a finite-width fault zone, we still wish to define slip velocity as the mutual velocity of the opposite sides of the fault, see Figure 3.5 a); however, for further calculations, and, in particular, for the numerical implementation, an approximation of the slip velocity, which can be expressed locally in every point of the fault zone, is necessary.

In the 3D test case, we assume a cuboidal viscoelastic fault zone, which is loaded by velocity on the sides (transferred through the effectively elastic rest of the domain); see purple zone on Figure 3.1. Since in the “slip state” (non-zero velocity), the viscosity in the fault zone is small; the viscous regime prevails in the Maxwell rheology; hence, let us consider for the moment just a purely viscous deformation in the fault zone. In addition, assuming uniformity in the z-direction (together with the imposed periodic boundary conditions), we can reduce the problem into two dimensions (a xy cross-section of the box, see Figure 3.1).

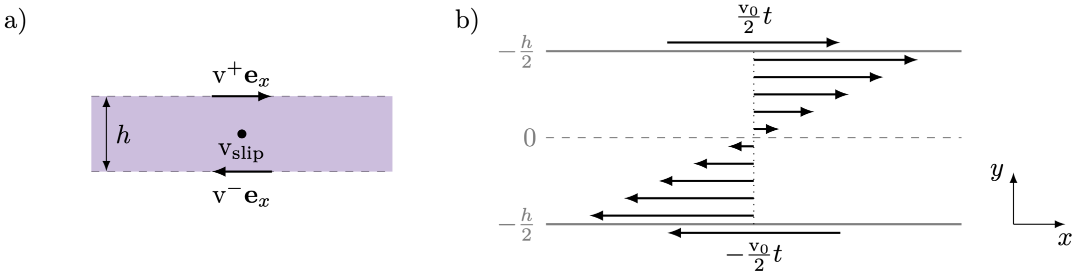

Figure 3.5: a) Sketch of the fault zone with marked velocity loading $\mathrm{v}^+\mathbf{e}_x$, $\mathrm{v}^-\mathbf{e}_x$ and slip velocity $\mathrm{v}_{\mathrm{slip}}$, b) derived displacement in the xy cut of the domain - simple shear deformation.

We are left with the following setup: a two-dimensional infinite rectangular viscous fault zone of height h loaded by velocities acting in opposite directions, specifically by $\mathrm{v}^+\mathbf{e}_x$ and $\mathrm{v}^-\mathbf{e}_x$, where $\mathrm{v}^+ > 0$ and $\mathrm{v}^- < 0$ and $\mathbf{e}_x$ is a unit vector in the direction of axis x, see Figure 3.5 a). In this case, a simple shear deformation develops in the fault zone; see the cross-section through the xy plain of the computational domain on Figure 3.5 b). Since the velocity needs to change the orientation (from positive $\mathrm{v}^+\mathbf{e}_x$ to negative $\mathrm{v}^-\mathbf{e}_x$) through the fault zone (i.e., along the y axis) and since we push in the x-direction only, one can show that for a wide class of viscosity functions, the resulting deformation is a simple shear, i.e., deformation depends on y-direction only and linearly.

According to the assumption of viscous rheology, it holds $\mathbb{S} = 2\eta\,\mathbb{D}(\mathbf{v})$, and we take the viscosity as a function of the symmetric velocity gradient $\eta = \eta\big(\mathbb{D}(\mathbf{v})\big)$. Now, we need to show that the deformation depends only on y and linearly, i.e., that $\mathbf{v} = (\mathrm{a}y + \mathrm{b}, 0)$, where a and b are constants. Due to the uniformity of the domain and the loading in the direction of x, the y-coordinate of velocity is zero, $\mathrm{v}_y = 0$. Since the domain is infinite in the x direction and the loading is equal everywhere along the x axis, one can neglect all derivatives with respect to the x coordinate, in particular, we assume $\frac{\partial \mathrm{v}_x}{\partial x} = 0$ and $\frac{\partial \mathbb{T}_{xx}}{\partial x} = 0$. The x-component of the equation 3.1a yields

$$\frac{\partial \mathbb{T}_{xy}}{\partial y} = 0. \tag{3.3}$$

Since also $\frac{\partial \mathbb{T}_{xy}}{\partial x} = 0$, this implies that $\mathbb{T}_{xy}$ is constant within the fault zone. Plugging in the viscous rheology yields

$$const. = \mathbb{T}_{xy} = 2\eta(\mathbb{D})\mathbb{D}_{xy} = \eta(\mathbb{D})\frac{\partial \mathrm{v}_x}{\partial y}.$$

Now, it remains to show that $\frac{\partial \mathrm{v}_x}{\partial y}$ is constant. Let's consider the viscosity to be either constant or depending on the symmetric velocity gradient:

1. $\eta = const.$
   Then,
   $$\frac{\partial \mathrm{v}_x}{\partial y} = \frac{\mathrm{c}}{\eta} \Rightarrow \mathrm{v}_x = \mathrm{v}_x(0) + \frac{\mathrm{c}}{\eta}y,$$
   and we choose $y = 0$ to be in the middle of our domain, thus $\mathrm{v}_x(0) = 0$. Therefore, $\mathbf{v} = (\frac{\mathrm{c}}{\eta}y, 0)$ and, consequently
   $$\mathbb{D} = \begin{bmatrix} \frac{\partial \mathrm{v}_x}{\partial x} & \frac{1}{2}\left(\frac{\partial \mathrm{v}_x}{\partial y} + \frac{\partial \mathrm{v}_y}{\partial x}\right) \\ \frac{1}{2}\left(\frac{\partial \mathrm{v}_x}{\partial y} + \frac{\partial \mathrm{v}_y}{\partial x}\right) & \frac{\partial \mathrm{v}_y}{\partial y} \end{bmatrix} = \begin{bmatrix} 0 & \frac{1}{2}\frac{\partial \mathrm{v}_x}{\partial y} \\ \frac{1}{2}\frac{\partial \mathrm{v}_x}{\partial y} & 0 \end{bmatrix}.$$
   Hence $\|\mathbb{D}\| = \frac{1}{2}\left|\frac{\partial \mathrm{v}_x}{\partial y}\right|$.

2. $\eta = \eta\big(\mathbb{D}(\mathbf{v})\big)$
   The only not zero coordinates of $\mathbb{D}$ are $\mathbb{D}_{xy}$ since v_y and $\frac{\partial \mathrm{v}_x}{\partial x}$ are zero, thus $\eta = \eta\Big(\frac{\partial \mathrm{v}_x}{\partial y}\Big)$. Plus, we have $const. = \mathbb{T}_{xy} = \eta\Big(\frac{\partial \mathrm{v}_x}{\partial y}\Big)\frac{\partial \mathrm{v}_x}{\partial y}$. If we, in addition, assume that viscosity is a monotone function of its argument, we get $\frac{\partial \mathrm{v}_x}{\partial y} = \widetilde{const.}$, so again, $\mathbf{v} = (\frac{\mathrm{c}}{\eta}y, 0)$ by the same argument as before.

To summarize, for viscosity, which is a monotone function of the symmetric velocity gradient and with the considered symmetries, we have $\mathbf{v} = (\mathrm{a}y + \mathrm{b}, 0)$, where b can be zero by the choice of the origin. Furthermore, we assume that the velocities on the opposite sides of the fault zones are equal in size: $|\mathrm{v}^+| = |\mathrm{v}^-| = \frac{\mathrm{v}_0}{2}$, hence the velocity in the fault zone is $\mathbf{v} = \frac{\mathrm{v}_0}{h}(y, 0, 0)$, see Figure 3.5 b). Thus the symmetric gradient of velocity has a simple form:

$$\mathbb{D}(\mathbf{v}) = \frac{1}{2}\begin{bmatrix} 0 & \frac{\mathrm{v}_0}{h} \\ \frac{\mathrm{v}_0}{h} & 0 \end{bmatrix}. \tag{3.4}$$

Since we have defined the slip velocity as the mutual motion of the fault boundaries (see Figure 3.5 a), we have $\mathrm{v}_{\mathrm{slip}} = |\mathrm{v}^{+} - \mathrm{v}^{-}|$. Therefore

$$\mathrm{v}_{\mathrm{slip}} = |\mathrm{v}^{+}\mathbf{e}_x - \mathrm{v}^{-}\mathbf{e}_x| = \frac{\mathrm{v}_0}{h}\left(\frac{h}{2} - \frac{-h}{2}\right) = \frac{\mathrm{v}_0}{h}h = \mathrm{v}_0 \tag{3.5}$$

Using equations 3.4 and 3.5, the slip velocity can be approximated by the symmetric velocity gradient $\mathrm{v}_{\mathrm{slip}} = \mathrm{v}_0 = 2h|\frac{1}{2}\frac{\mathrm{v}_0}{h}| = 2h\,|\mathbb{D}_{xy}(\mathbf{v})| = 2h\,\|\mathbb{D}(\mathbf{v})\|$. The same approximation can be made for arbitrary simple-shear configuration within the fault zone.

It is, however, necessary to employ only the part of the deformation field that corresponds to the irreversible slip since we are using Maxwell rheology for the description of the ice shell. Thus, we replace $\mathbb{D}$ in the above formulas with the viscous part of the symmetric gradient of velocity $\mathbb{D}_{\mathrm{visc}}(\mathbf{v})$ only, defined as the difference between the total and the elastic deformation rate. In particular, we employ the following approximation

$$\mathrm{v}_{\mathrm{slip}} \sim 2h\|\mathbb{D}_{\mathrm{visc}}(\mathbf{v})\| = 2h\Big\|\mathbb{D}(\mathbf{v}) - \mathbb{D}_{\mathrm{elast}}(\mathbf{v})\Big\| \tag{3.6}$$

$$= 2h\Big\|\mathbb{D}(\mathbf{v}) - \frac{\dot{\mathbb{S}}}{2\mu}\Big\|, \tag{3.7}$$

where $\mathbb{D}_{\mathrm{elast}}(\mathbf{v})$ denotes the elastic part of the symmetric gradient of velocity.

3D fault zone - effective viscosity

Going back to the 3D test case with finite fault zone, we define the viscosity of the material as the effective viscosity η_{eff} in the fault zone (by generalizing the above 1D analogy) and a background viscosity η_{Max} elsewhere as follows

$$\eta = \begin{cases} \eta_{\mathrm{eff}} \text{ in the fault zone,} \\ \eta_{\mathrm{Max}} \text{ elsewhere,} \end{cases} \tag{3.8a}$$

$$\eta_{\mathrm{eff}} = \frac{\eta_{\mathrm{Max}}}{\left\{1 + \left(\frac{2\eta_{\mathrm{Max}}\|\mathbb{D}_{\mathrm{visc}}\|}{\sigma_Y}\right)^n\right\}^{\frac{1}{n}}}. \tag{3.8b}$$

The effective viscosity defined in the above manner ensures that

$$\|\mathbb{T}\| = 2\eta_{\mathrm{eff}}\|\mathbb{D}_{\mathrm{visc}}\| \leq \sigma_Y,$$

which, in the simple shear setting of the test case problem (assuming, in addition, $\mathbb{T}_{xx} = 0$), implies that $|\mathbb{T}_{xy}| \leq \sigma_Y$, showing the relationship between the maximal tangent force and the yield stress.

Note that the correspondence between the 1D and 3D cases, i.e., between the formulas for $\eta_{\mathrm{eff}}^{\mathrm{1D}}$ and η_{eff} is not perfect as it holds

$$|\mathbb{T}^{\mathrm{1D}}| = \eta_{\mathrm{eff}}^{\mathrm{1D}}\mathrm{v}_{\mathrm{slip}} = \frac{2h\eta_{\mathrm{Max}}\|\mathbb{D}_{\mathrm{visc}}\|}{\left\{1 + \left(\frac{2h\eta_{\mathrm{Max}}\|\mathbb{D}_{\mathrm{visc}}\|}{\sigma_Y}\right)^n\right\}^{\frac{1}{n}}} = \frac{2\eta_{\mathrm{Max}}\|\mathbb{D}_{\mathrm{visc}}\|}{\left\{\left(\frac{1}{h}\right)^n + \left(\frac{2\eta_{\mathrm{Max}}\|\mathbb{D}_{\mathrm{visc}}\|}{\sigma_Y}\right)^n\right\}^{\frac{1}{n}}},$$

where we replaced $\mathrm{v}_{\mathrm{slip}}$ by $2h\|\mathbb{D}_{\mathrm{visc}}\|$. On the other hand, in the 3D case, we get

$$\|\mathbb{T}\| = 2\eta_{\mathrm{eff}}\|\mathbb{D}_{\mathrm{visc}}\| = \frac{2\eta_{\mathrm{Max}}\|\mathbb{D}_{\mathrm{visc}}\|}{\left\{1+\left(\frac{2\eta_{\mathrm{Max}}\|\mathbb{D}_{\mathrm{visc}}\|}{\sigma_Y}\right)^n\right\}^{\frac{1}{n}}}.$$

This means that the two formulas differ in the low-velocity ('stick') regime, where the effective (maximal) viscosity in the 1D analogue and the 3D analogue differ by a factor related to the fault zone thickness $2h$. As this value is auxiliary anyway, we have decided to use the formula (3.8b) in the following.

Definition of the fault zone

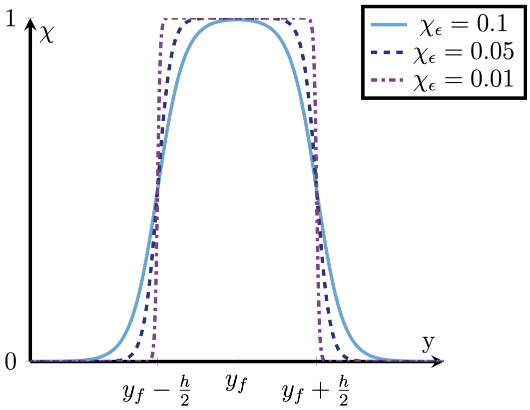

Figure 3.6: Characteristic function χ used to define the fault zone.

A precise definition of the fault zone is necessary for the definition of the viscosity, and for the box domain, the definition is straightforward:

$$\eta = \eta_{\mathrm{Max}}^{1-\chi}\,\eta_{\mathrm{eff}}^{\chi}, \tag{3.9}$$

where we define the characteristic function χ as:

$$\chi = \frac{1}{2}\left\{\tanh\left[\frac{y-y_f+\frac{h}{2}}{\chi_\epsilon/6}\right] - \tanh\left[\frac{y-y_f-\frac{h}{2}}{\chi_\epsilon/6}\right]\right\}, \tag{3.10}$$

where tanh is a hyperbolical tangent, y_f is a y coordinate of the center of the fault zone, and χ_ϵ is the thickness of the transient zone, which is a length over which the characteristic function drops from one to zero, see Figure 3.6. In the code, χ_ϵ corresponds to the minimal diameter of the elements and $y_f = 0.5d$.

3.1.3 Numerical scheme

The numerical solution is carried out using the open-source finite element software package FEniCS (`http://fenicsproject.org`; Alnaes et al., 2015; Logg et al., 2012).

Cauchy stress tensor

To approximate the equation of motion (eq. 3.1a), we start with the approximation of the Cauchy stress tensor $\mathbb{T}$ (eq. 3.1b). Before presenting in detail the final implementation, we first briefly summarize the unsuccessful attempts with the reasons why there were unfit for use.

Displacement formulation - integral approach
First, we tested an approximation of the Maxwell rheology (in terms of displacement) using its integral form as in (3.1b) - the integral was discretized in time and split into two parts: the known part (until the current time step t^k) and the new part (from the current step t^k to the next step t^{k+1}). The new part is estimated by the trapezoidal rule. Such an approach was able to reproduce the fault's behavior in the sense of mutual motion of two blocks with respect to each other; however, it turned out to lead to a gradual accumulation of numerical errors in the stress, leading to a loss of accuracy over time.

Displacement formulation - differential Euler scheme
As a second choice, we applied the time derivative to equation 3.1b, employing a simple one-step Euler scheme. Since the viscosity is strongly dependent on the slip velocity (see eq. 3.8), and a fully implicit approach would bring strong nonlinearity to the model, we used a fixed point iteration scheme instead. However, even this approach was not fully satisfactory as the results developed spatial oscillations; in addition, it turned out that the slip velocity was relatively poorly approximated. Moreover, the slip was concentrated just at the boundaries between the fault zone and the rest of the computational domain.

Displacement formulation - differential Euler scheme with auxiliary smoothing
We tried to regularize the previous method by attempting to defocus the slip zones (boundaries of the fault zone). To smear out the velocity gradient, we introduced an auxiliary variable evolving through a parabolic conduction-like problem with the source term dependent on slip velocity - in our approximation, represented by the symmetric velocity gradient, see Section 3.1.2. The time derivative was also dealt with by the Euler scheme. Two parameters controlled the amount of smoothing (in time and space) in the "conduction" equation, and we were not able to tune the parameters to regularize the gradient sufficiently. Either the slip velocity approximation was too "broad", or it grew too much on the fault boundary, and the slip of the fault was still focused there.

Velocity formulation
Finally, we use the time derivative of the equation 3.1b, but rewritten in velocity defined as the time derivative of the displacement $\mathbf{v} := \dot{\mathbf{u}}$ obtaining:

$$\dot{\mathbb{T}} \; = \; K(\nabla \cdot \mathbf{v})\mathbb{I} + \mu\Big[\nabla \mathbf{v} + \big(\nabla \mathbf{v}\big)^T - \frac{2}{3}(\nabla \cdot \mathbf{v})\mathbb{I}\Big] - \frac{\mu}{\eta}\mathbb{S}. \tag{3.11}$$

We apply the Euler scheme for the time derivative in stress:

$$\begin{aligned}\frac{\mathbb{T}^{k+1}-\mathbb{T}^{k}}{\mathrm{dt}} &= K(\nabla\cdot\mathbf{v}^{k+1})\mathbb{I}+\mu\Big[\nabla\mathbf{v}^{k+1}+\big(\nabla\mathbf{v}^{k+1}\big)^{T} \\ &- \frac{2}{3}(\nabla\cdot\mathbf{v}^{k+1})\mathbb{I}\Big]-\frac{\mu}{\eta^{k+1}}\mathbb{S}^{k+1}, \qquad (3.12)\end{aligned}$$

where $k+1$ denotes the time step to be computed, k is the current one, and dt is the time step.

To get the prescription for $\mathbb{T}^{k+1}$, several adjustments are necessary. First, we apply the trace operator on equation 3.12, and we express the deviatoric part of the stress tensor in the current time step $\mathbb{S}^{k+1}$:

$$\begin{aligned}\frac{\mathrm{tr}\mathbb{T}^{k+1}-\mathrm{tr}\mathbb{T}^{k}}{\mathrm{dt}} &= K(\nabla\cdot\mathbf{v}^{k+1})\mathrm{tr}\,\mathbb{I}, \qquad (3.13)\\ \mathbb{S}^{k+1} &= \mathbb{T}^{k+1}-\frac{1}{3}\mathrm{tr}\mathbb{T}^{k+1}\mathbb{I}, \qquad (3.14)\end{aligned}$$

from which:

$$\mathrm{tr}\mathbb{T}^{k+1}=3K(\nabla\cdot\mathbf{v}^{k+1})\ \mathrm{dt}+\mathrm{tr}\mathbb{T}^{k}. \qquad (3.15)$$

Applying eq. 3.15 in eq. 3.14 we get:

$$\mathbb{S}^{k+1} = \mathbb{T}^{k+1}-\ \mathrm{dt}\,K(\nabla\cdot\mathbf{v}^{k+1})\mathbb{I}-\frac{1}{3}\mathrm{tr}\mathbb{T}^{k}\mathbb{I}. \qquad (3.16)$$

Furthermore, using eq. 3.16 in eq. 3.12 we obtain:

$$\begin{aligned}\mathbb{T}^{k+1} &= \mathbb{T}^{k}+\ \mathrm{dt}\,K(\nabla\cdot\mathbf{v}^{k+1})\mathbb{I}+\ \mathrm{dt}\,\mu\Big[\nabla\mathbf{v}^{k+1}+(\nabla\mathbf{v}^{k+1})^{T}-\frac{2}{3}(\nabla\cdot\mathbf{v}^{k+1})\mathbb{I}\Big]\\ &- \frac{\mathrm{dt}\,\mu}{\eta^{k+1}}\Big(\mathbb{T}^{k+1}-\ \mathrm{dt}\,K(\nabla\cdot\mathbf{v}^{k+1})\mathbb{I}-\frac{1}{3}\mathrm{tr}\mathbb{T}^{k}\mathbb{I}\Big). \qquad (3.17)\end{aligned}$$

From that:

$$\begin{aligned}\Big(1+\frac{\mathrm{dt}\,\mu}{\eta^{k+1}}\Big)\mathbb{T}^{k+1} &= \mathbb{T}^{k}+\ \mathrm{dt}\,K(\nabla\cdot\mathbf{v}^{k+1})\mathbb{I}\\ &+ \ \mathrm{dt}\,\mu\Big[\nabla\mathbf{v}^{k+1}+(\nabla\mathbf{v}^{k+1})^{T}-\frac{2}{3}(\nabla\cdot\mathbf{v}^{k+1})\mathbb{I}\Big]\\ &+ \frac{\mathrm{dt}^{2}\,\mu K}{\eta^{k+1}}(\nabla\cdot\mathbf{v}^{k+1})\mathbb{I}+\frac{\mathrm{dt}\,\mu}{3\eta^{k+1}}\mathrm{tr}\mathbb{T}^{k}\mathbb{I}. \qquad (3.18)\end{aligned}$$

By multiplying the equation 3.18 by $\mathcal{K}^{k+1}:=\frac{\eta^{k+1}}{\eta^{k+1}+\ \mathrm{dt}\,\mu}$ we get the final formula for the approximation of the stress tensor:

$$\begin{aligned}\mathbb{T}^{k+1} &= \mathcal{K}^{k+1}\mathbb{T}^{k}+\mathcal{K}^{k+1}\ \mathrm{dt}\Big[K+\frac{\mathrm{dt}\,\mu K}{\eta^{k+1}}-\frac{2}{3}\mu\Big](\nabla\cdot\mathbf{v}^{k+1})\mathbb{I}\\ &+ \ \mathrm{dt}\,\mu\,\mathcal{K}^{k+1}\Big[\nabla\mathbf{v}^{k+1}+(\nabla\mathbf{v}^{k+1})^{T}\Big]+\frac{1-\mathcal{K}^{k+1}}{3}\mathrm{tr}\mathbb{T}^{k}\mathbb{I}. \qquad (3.19)\end{aligned}$$

Weak solution of the governing equations

We derive the weak solution for the equation of motion by multiplying eq. 3.1a by a test function $\mathbf{v}'$ and integrating over the computational domain Ω:

$$\int_\Omega \operatorname{div}\mathbb{T}\cdot\mathbf{v}'\ \mathrm{dx} = 0. \tag{3.20}$$

Moreover, we use the Gauss theorem to obtain the following:

$$-\int_\Omega \mathbb{T} : \nabla\mathbf{v}'\ \mathrm{dx} + \int_{\partial\Omega} (\mathbb{T}\cdot\mathbf{n})\cdot\mathbf{v}'\ \ \mathrm{ds} = 0, \tag{3.21}$$

where $\mathbf{n}$ is the outer normal vector. By using the Dirichlet (for setting the velocity) and periodic boundary conditions, we get:

$$\int_\Omega \mathbb{T} : \nabla\mathbf{v}'\ \mathrm{dx} = 0. \tag{3.22}$$

Continuous Lagrange elements of the first degree (CG_1) are used for the velocity and discontinuous Galerkin elements (DG_0) for the stress.

Summary of the numerical scheme

We solve the equation

$$\int_\Omega \mathbb{T}^{k+1} : \nabla\mathbf{v}'\ \mathrm{dx} = 0 \tag{3.23a}$$

in a computational domain Ω: a box with the dimensions $w\times d\times d$ and a fault zone of thickness h depicted by purple color in Figure 3.1.

The Cauchy stress tensor and the viscosity are approximated as follows:

$$\begin{aligned}
\mathbb{T}^{k+1} &\approx \mathcal{K}^{k+1}\mathbb{T}^k + \mathcal{K}^{k+1}\ \mathrm{dt}\left[K + \frac{\mathrm{dt}\,\mu K}{\eta^{k+1}} - \frac{2}{3}\mu\right](\nabla\cdot\mathbf{v}^{k+1})\mathbb{I} \\
&+ \ \mathrm{dt}\,\mu\,\mathcal{K}^{k+1}\Big[\nabla\mathbf{v}^{k+1} + (\nabla\mathbf{v}^{k+1})^T\Big] + \frac{1-\mathcal{K}^{k+1}}{3}\mathrm{tr}\mathbb{T}^k\mathbb{I},
\end{aligned} \tag{3.23b}$$

$$\mathcal{K}^{k+1} = \frac{\eta^{k+1}}{\eta^{k+1} +\ \mathrm{dt}\,\mu}, \tag{3.23c}$$

$$\eta^{k+1} = \eta_{\mathrm{Max}}^{1-\chi}\,\eta_{\mathrm{eff}}^{\chi,k+1}, \tag{3.23d}$$

$$\chi = \frac{1}{2}\left\{\tanh\left[\frac{y-y_f+\frac{h}{2}}{\chi_\epsilon/6}\right] - \tanh\left[\frac{y-y_f-\frac{h}{2}}{\chi_\epsilon/6}\right]\right\}, \tag{3.23e}$$

$$\eta_{\mathrm{eff}}^{k+1} \approx \frac{\eta_{\mathrm{Max}}}{\left\{1+\left(\frac{2\eta_{\mathrm{Max}}\|\mathbb{D}_{\mathrm{visc}}^\eta\|}{\sigma_Y}\right)^{2n}\right\}^{\frac{1}{2n}}}, \tag{3.23f}$$

$$\|\mathbb{D}_{\mathrm{visc}}^\eta\| = \sqrt{\frac{\mathbb{D}_{\mathrm{visc}}^\eta : \mathbb{D}_{\mathrm{visc}}^\eta}{2}}, \tag{3.23g}$$

$$\mathbb{D}_{\mathrm{visc}}^\eta = \mathbb{D}(\mathbf{v}_\eta^k) - \frac{\mathbb{T}_\eta^k - \mathbb{T}^{k-1}}{2\mu\ \mathrm{dt}}, \tag{3.23h}$$

$$\mathbb{D}(\mathbf{v}_\eta^k) = \frac{1}{2}\Big(\nabla\mathbf{v}_\eta^k + (\nabla\mathbf{v}_\eta^k)^T\Big), \tag{3.23i}$$

where $\mathbb{D}_{\mathrm{visc}}^{\eta}, \mathbf{v}_{\eta}^{k}$, $\mathbb{D}(\mathbf{v}_{\eta}^{k})$, $\mathbb{T}_{\eta}^{k}$ are auxiliary variables defined for the fixed point iterations. In the first step of the fixed point iterations loop, $\mathbb{T}^{k-1}$ is updated as $\mathbb{T}_{\eta}^{k}$, $\mathbb{T}_{\eta}^{k}$ as $\mathbb{T}^{k+1}$, $\mathbf{v}_{k}^{\eta}$ as $\mathbf{v}^{k+1}$, where $\mathbf{v}^{k+1}$ is the solution of (3.23a). The rest of the variables is calculated according to the above formulas. In the following steps of the fixed point iterations, only $\mathbb{T}_{\eta}^{k}$ and $\mathbf{v}_{\eta}^{k}$ are updated. The fixed point iteration loop is run until convergence or maximum iterations (usually 20) are reached.

The Dirichlet boundary conditions for velocity are implied on the sides parallel to the fault acting in opposite directions, which are supplemented with periodic boundary conditions on the remaining boundaries to mimic the infiniteness of the computational domain, see Figure 3.1. The periodic boundary conditions are prescribed through the copy of the velocity from the top and forward sides to the bottom and back sides, respectively; see Figure 3.1, i.e.,:

$$\mathbf{v}(w,y,z) = \mathbf{v}(0,y,z), \tag{3.24}$$

$$\mathbf{v}(x,y,d) = \mathbf{v}(x,y,0). \tag{3.25}$$

$$\mathbf{v} = \frac{\mathrm{v}_0}{2}\mathbf{e}_x \quad \text{for } y = d, \tag{3.26}$$

$$\mathbf{v} = -\frac{\mathrm{v}_0}{2}\mathbf{e}_x \quad \text{for } y = 0. \tag{3.27}$$

The computation is started from zero initial boundary conditions for stress and velocity.

3.2 Benchmark

Here, we test the viscoelastic analogy and the employed approximations through a comparison of the results for the finite fault zone test case and two 1D models: a spring-slider model and a 1D Maxwell model. The benchmark problem describes a frictional contact with a constant coefficient of friction μ_f=1 loaded by constant velocity v_0=$5 \times 10^{-5}\,\mathrm{m\,s^{-1}}$. The yield stress is set to σ_Y=10^7 Pa.

For the 1D models, the constant velocity loading is translated into loading by time-dependent displacement: u_0=$\mathrm{v}_0 t$. As for the 3D model, the results presented for the test case are calculated by a 2D model produced as a xy cross-section through the 3D model's domain. Since no force depends on z and the model is effectively infinite in the z direction, the xy cross-section corresponds perfectly to the whole 3D model. The correspondence was, in fact, also verified by independent, truly 3D numerical calculation. In order to perform the comparison with the simplified 1D models, we first need to establish the correspondence.

3.2.1 Spring slider model

A straightforward benchmark model for the verification of the viscoelastic analogy is the original mechanical analogue used for the description of friction: the spring slider - described in Section 3.1.2, see Figure 3.2, pulled by time-dependent displacement $\mathrm{v}_0 t$ and with a constant coefficient of friction.

As mentioned earlier, the friction force τ_f=$\mu_f \sigma_n$ is greater or equal to the pulling force τ_p=$k_{sp}(u_0 - u_{sl})$ (the equality holds when sliding occurs):

$$\mu_f \sigma_n \geq k_{sp}(u_0 - u_{sl}), \tag{3.28}$$

where $\mu_f \sigma_n$ corresponds to $\mu_f \sigma_Y$. Using $u_0 = \mathrm{v}_0 t$ we get:

$$\mu_f \sigma_Y \geq k_{sp}(\mathrm{v}_0 t - u_{sl}). \tag{3.29}$$

Hence, the slider is still until the pulling force (increasing with time) reaches the friction force, and then it starts to move. We approximate the stiffness of the spring as the bulk modulus of the Maxwell rheology model scaled with the size of the domain: $k_{sp} = \frac{K}{d-h} = \frac{K}{0.9}$, where $K = 3.3\,\mathrm{GPa}$, h is the thickness of the fault zone, and d is the height of the computational domain, see Figure 3.1.

The onset of the sliding can be calculated from the equality of forces as a point, where the slider displacement u_{sl} reaches values above zero, i.e.,:

$$u_{sl} \geq 0 \iff \mathrm{v}_0 t - \frac{\mu_f \sigma_Y}{k_{sp}} \geq 0 \iff \tag{3.30}$$

$$\iff t \geq t_s := \frac{\mu_f \sigma_Y}{k_{sp} \mathrm{v}_0} = \frac{\mu_f \sigma_Y (d-h)}{K \mathrm{v}_0} = 54.\overline{54}\mathrm{s} \tag{3.31}$$

Hence, the displacement is zero until the onset of sliding t_s, and then it grows linearly with the slider displacement (u_{sl}=$\mathrm{v}_0 t - \frac{\mu_f \sigma_Y (d-h)}{K}$), implying that velocity is also zero until the onset of sliding and then constant equal to the loading velocity v_0. The pulling force is equal to $\frac{K}{d-h}\mathrm{v}_0 t$ as long as it is smaller than the yield stress σ_Y (i.e., until t_s), then it's equal to σ_Y, see the full turquoise line on Figure 3.7 for results of the spring slider with a constant coefficient of friction.

3.2.2 1D Maxwell model

To verify the implementation of the viscoelastic analogy of the contact problem, we also approximate the compressible Maxwell rheology by a 1D mechanical analogue corresponding to a dashpot connected to a spring, see Figure 3.3.

The stress on the dashpot $\mathbb{T}_\eta$ is defined as $\mathbb{T}_\eta = \eta_{\mathrm{eff}}^{1\mathrm{D}}\, \dot{u}$, whereas for the stress on the spring $\mathbb{T}_{sp}$ it holds $\mathbb{T}_{sp} = k_{sp} u_{sp}$. The displacement of the spring equals the loading displacement subtracted by the dashpot displacement: $u_{sp} = \mathrm{v}_0 t - u$. Since the stress is equal everywhere in the mechanical analogue ($\mathbb{T}_\eta = \mathbb{T}_{sp}$), we have:

$$\eta_{\mathrm{eff}}^{1\mathrm{D}}\, \dot{u} = k_{sp}(\mathrm{v}_0 t - u) \tag{3.32}$$

as the governing equation for the 1D Maxwell model with viscosity as in eq. 3.2 and the slip velocity defined as the velocity of the dashpot $\mathrm{v}_{\mathrm{slip}} = \mathrm{v} = \dot{u}$.

Numerical model

To establish consistency between the 2D/3D models we approximate the equation 3.32 by the Euler method:

$$\eta_{\mathrm{eff}}^{1\mathrm{D},k+1} \frac{u^{k+1} - u^k}{\mathrm{dt}} = k_{sp}(\mathrm{v}_0 t - u^{k+1}), \tag{3.33}$$

from which

$$u^{k+1} = \frac{k_{sp}\,\mathrm{dt}}{\eta_{\mathrm{eff}}^{1\mathrm{D},k+1} + k_{sp}\,\mathrm{dt}} \mathrm{v}_0 t + \frac{\eta_{\mathrm{eff}}^{1\mathrm{D},k+1}}{\eta_{\mathrm{eff}}^{1\mathrm{D},k+1} + k_{sp}\,\mathrm{dt}} u^k, \tag{3.34a}$$

where $k_{sp} = \frac{K}{d-h} = \frac{K}{0.9}$ as in the spring slider model. Furthermore, we approximate the slip velocity (i.e., the velocity of the dashpot v) in the viscosity through the method of fixed point iterations:

$$\eta_{\text{eff}}^{1\text{D},k+1} = \frac{\eta_{\text{Max}}}{\left(1 + (\frac{\mathrm{v}^k \eta_{\text{Max}}}{\sigma_Y})^n\right)^{1/n}}, \tag{3.34b}$$

$$\mathrm{v}^k = \frac{u_\eta^k - u_\eta^{k-1}}{\mathrm{dt}}. \tag{3.34c}$$

The arbitrary displacement u_η^{k-1} is updated as u^k after the first step of internal iterations, while u_η^k is set to u^{k+1} every step of the internal iterations. The model is coded in Fortran 90. In each time step, a fixed number of iterations (100 for the blue dashed line in Figure 3.7) is calculated while updating the values of displacement, velocity and viscosity.

3.2.3 Results

In Figure 3.7, we plot the time evolution of magnitude of stress, displacement, and slip velocity for all three models with a constant coefficient of friction and constant velocity loading. Apart from a little lag in the onset of slip in the 2D Maxwell model, all three models show a very reasonable fit with each other. This demonstrates the basic viability of the effective rheology approach to mimic a contact frictional problem via the deformation of a fault zone. This approach is in the following section employed for extending an existing tidal deformation model of Enceladus's ice shell. In particular, we shall replace the previous implementation of the fault zones as effectively frictionless by zones corresponding to a frictional Coulomb-type contact.

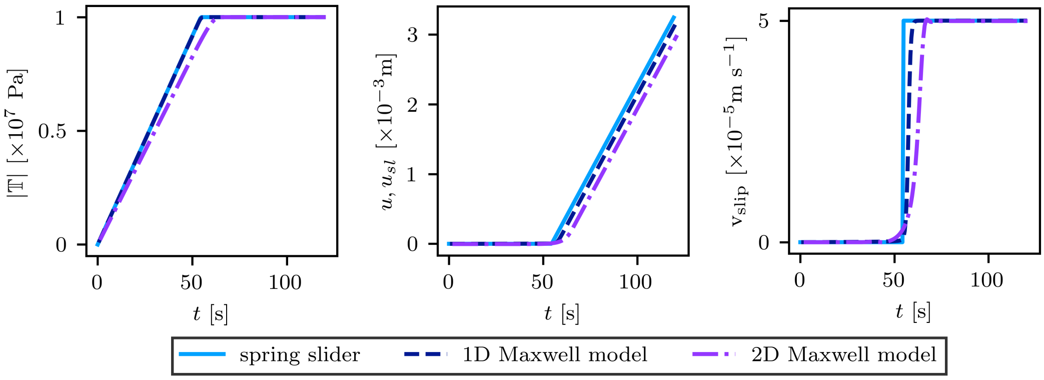

Figure 3.7: From left: time evolution of the stress magnitude/pulling force, displacement and slip velocity for the three models with a constant coefficient of friction and constant velocity loading. The full turquoise line denotes the analytical results of the spring slider model; the blue dashed line symbolizes the 1D Maxwell model computed with a Fortran code using finite differences; the purple cross-hatched line depicts the result of the 2D Maxwell model written in Fenics Project (Alnaes et al., 2015) using finite element method.

3.3 Enceladus’ tiger stripes as frictional faults: Effect on stress and heat production (Pleiner Sládková et al., 2021)

In this part of the thesis, we present a new 3D finite-element model of Enceladus’ ice shell where the friction is included in the approximation of the tiger stripes. The friction inside the fault zone is described by a Mohr-Coulomb-type yield criterion as presented in the previous part of this chapter, similar to Chapter 2 and Sládková et al. (2020). The model includes lateral variations in ice thickness derived from Cassini’s gravity and shape data (Čadek et al., 2019) and the observed geometry of the tiger stripes (Porco et al., 2014). The friction on the fault is represented by a single parameter, which contains information about the nature of the tiger stripes and can, in principle, be determined from observations of the displacement field and temporal variations in gravity (Vance et al., 2021). The model provides a first estimate of tidal heating produced on the faults and brings a new perspective on the tidally induced stresses in the SPT. All presented results were published in Pleiner Sládková et al. (2021).

3.3.1 Model description

We investigate the deformation of Enceladus’ ice shell caused by a periodic tidal forcing. The basic equations and the numerical method are based on Souček et al. (2019). The novelty of the present approach lies in the way the tiger stripes are integrated into the model.

We assume that the tiger stripes represent fault zones of finite width, filled with a mixture of water and broken ice. In the previous works (e.g., Souček et al., 2016), these zones were treated as idealized frictionless cracks and modeled as regions with significantly reduced elastic moduli. Here we present a more realistic model in which friction in the fault zones is implemented using a visco-elasto-plastic rheology, while the rest of the shell is modeled as an effectively elastic medium (for discussion of the role of viscous deformation in Enceladus’ tidal deformation, see Souček et al. (2019)). Both regions are treated in a unified manner using a Maxwell viscoelastic material model, which is characterized by a stress dependent viscosity, η_{eff}, in the fault zone and a constant viscosity, $\eta_{\mathrm{Max}}=10^{20}\,\mathrm{Pa\,s}$, in the rest of the ice shell. The viscosity η_{eff} is defined as follows (using the approximation of slip velocity directly):

$$\eta_{\mathrm{eff}} = \frac{\eta_{\mathrm{Max}}}{\left(1+\left(\frac{2\eta_{\mathrm{Max}}\|\mathbb{D}^{\mathrm{d}}_{\mathrm{visc}}\|_2}{\sigma_Y}\right)^{2n}\right)^{\frac{1}{2n}}}\,, \tag{3.35}$$

where $\mathbb{D}^{\mathrm{d}}_{\mathrm{visc}}$ is the deviatoric part of the viscous strain rate tensor (in the case of a deformation of an ice shell $\mathbb{D}$ does not have to be traceless), $\|\bullet\|_2$ denotes the second invariant of a tensor. Equation (3.35) ensures that the deviatoric stress in the fault zone is below the yield stress, and the viscosity goes to η_{Max} when the (deviatoric) stress is significantly smaller than σ_Y, for more information see Section 3.1.2. Note that similar (though not identical) constitutive equations were used in modelling the deformation of the lithosphere on Earth (e.g., Trompert and Hansen, 1998; Tosi et al., 2015; Herrendörfer et al., 2018).

The yield stress σ_Y is composed of a static part, corresponding to the mean effective pressure, and a dynamic (time-dependent) part, related to tidal deformation:

$$\sigma_Y = \begin{cases} \mu_f(\overline{p^{\text{eff}}} - \sigma_{\text{nn}}) & \text{if} \quad \overline{p^{\text{eff}}} \geq \sigma_{\text{nn}} \\ 0 & \text{otherwise} \end{cases} , \tag{3.36}$$

where $\overline{p^{\text{eff}}}$ is the effective pressure (ice overburden pressure minus liquid water pressure) averaged over the depth, and σ_{nn} is the normal component of the traction vector acting on the fault surface; for details, see Section 3.4.1 in Supporting information (further noted as SI, Section 3.4). Since the static part is relatively small ($\overline{p^{\text{eff}}} \sim 10^4$ Pa), the yield stress is mainly controlled by σ_{nn}. The coefficient of friction depends on a number of factors, such as slip velocity, temperature, the mechanical state of ice filling the fault zone, and the presence of a liquid phase (for a review, see Section 4.2, or e.g., Oksanen and Keinonen (1982) and Schulson and Fortt (2012)). Its value can range between 0.01 and 0.8, with the lower values corresponding to a fault zone lubricated by water. When μ_f=0, the fault behaves as a frictionless water-filled crack (cf. Souček et al., 2019), while $\mu_f \gg 1$ corresponds to a locked fracture with no impact on the stress field.

In the simulations, we look for periodic solutions for each given model setup. Let us note, however, that the behavior of frictional systems subjected to periodic loading is nontrivial, and the existence of a steady-state periodic solution that is independent of the initial conditions cannot be guaranteed a priori (e.g., Andersson et al., 2013). However, for the given set of physical parameters, the studied system converged to a unique periodic steady state within four tidal periods; for further details on the time discretization, see Section 3.4.2. The equations governing the tidal deformation have been expressed in an integral (so-called weak) form (Souček et al., 2019), and the model was implemented in the finite element software package FEniCS (`http://fenicsproject.org`; Logg et al., 2012; Alnaes et al., 2015). For a more detailed description of the numerical method, see Section 3.4.2.

3.3.2 Deformation of the ice shell

Figure 3.8 shows the surface displacement in the vicinity of the tiger stripes obtained for the model with μ_f=0.2. During one tidal cycle, the fault zones are compressed and stretched in the normal direction by tens of centimeters, and the relative displacement parallel to the faults exceeds 1 m. The maximum radial displacement between the fault zones is about 3 m, which is a factor of 2 less than for the model with frictionless faults (μ_f=0), but significantly more than for models where the faults are not included, or the relative motion across the faults is negligible ($\mu_f \gg 1$, see also Běhounková et al. (2017)). The differences between models with different friction coefficients suggest that parameter μ_f could, in principle, be determined from precise gravity and altimetry measurements (Vance et al., 2021).

It is worth remembering that the periodic tidal potential V_{tidal} satisfies the symmetry relation $V_{\text{tidal}}(t) = -V_{\text{tidal}}(t + P/2)$, where t is the time, and P is the rotation period. This implies that if μ_f=0 or $\mu_f \gg 1$, the displacement vectors at times t and $t + P/2$ have the same magnitude but opposite signs. Inspection of Figure 3.8 shows that this symmetry is broken when friction is included – the

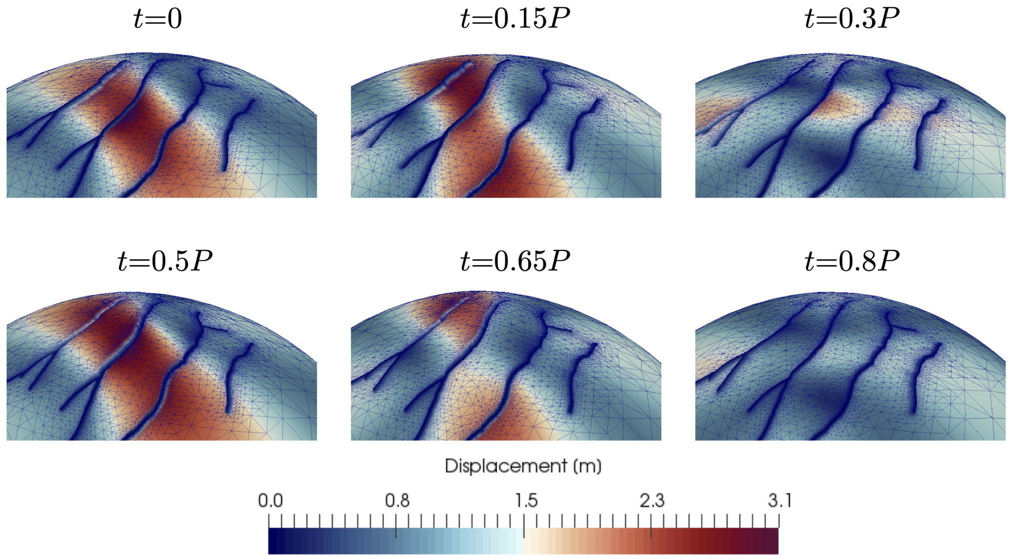

Figure 3.8: Periodic variations of the displacement field at the surface obtained for the model with μ_f=0.2. The displacement is shown for six different phases of the tidal cycle. The symbol P denotes the orbital period. Colors show the magnitude of the displacement while thin blue lines indicate the mesh used in the finite-element solver. The displacement is exaggerated by a factor of 3000 to emphasize the radial motion along the faults. For a video showing the displacement field over the whole rotational period, see Supporting Information on the web page `https://agupubs.onlinelibrary.wiley.com/doi/10.1029/2021GL094849`.

displacement in the time interval $(0, P/2)$ is considerably larger than that in the time interval $(P/2, P)$, with the difference exceeding 1 m.

The motion along the faults is continuous in time, which may seem surprising given that the deformation is controlled by a Coulomb-type yield criterion. The term “Coulomb friction” usually evokes a fault which is locked, and the stress builds up until it exceeds the strength threshold, resulting in motion along the fault. As will be shown later, this behavior is only found for models with a relatively high coefficient of friction. If $\mu_f \lesssim 0.5$, the slip velocity varies in a continuous manner because the tidal deformation of the ice shell is accommodated by plastic flow in the fault zone. To get a more comprehensive picture of the surface deformation in the SPT, see the video in the Supporting Information on the web page `https://agupubs.onlinelibrary.wiley.com/doi/10.1029/2021GL094849`.

The time variations of the deviatoric stress are shown in Figure 3.9. The deviatoric stress changes on the length scale of a few tens of kilometers and reaches a magnitude of up to 300 kPa. The distribution of stress differs significantly from that obtained for the frictionless model (μ_f=0), which is characterized by stress peaks (and also the maximum dissipation) at the fault tips (see Figure 3 in Souček et al. (2016)). In contrast, the model including friction suggests that the stress is maximum in the central parts of the faults, which is more consistent with observation (Spencer et al., 2018).

The complex behavior of the fault system demonstrated in Figures 3.8 and 3.9 results from the interplay between the dynamic part of the normal stress, σ_{nn}, controlling the yield stress (equation 3.36), and the viscous strain rate, $\mathbb{D}^{\mathrm{d}}_{\mathrm{visc}}$.

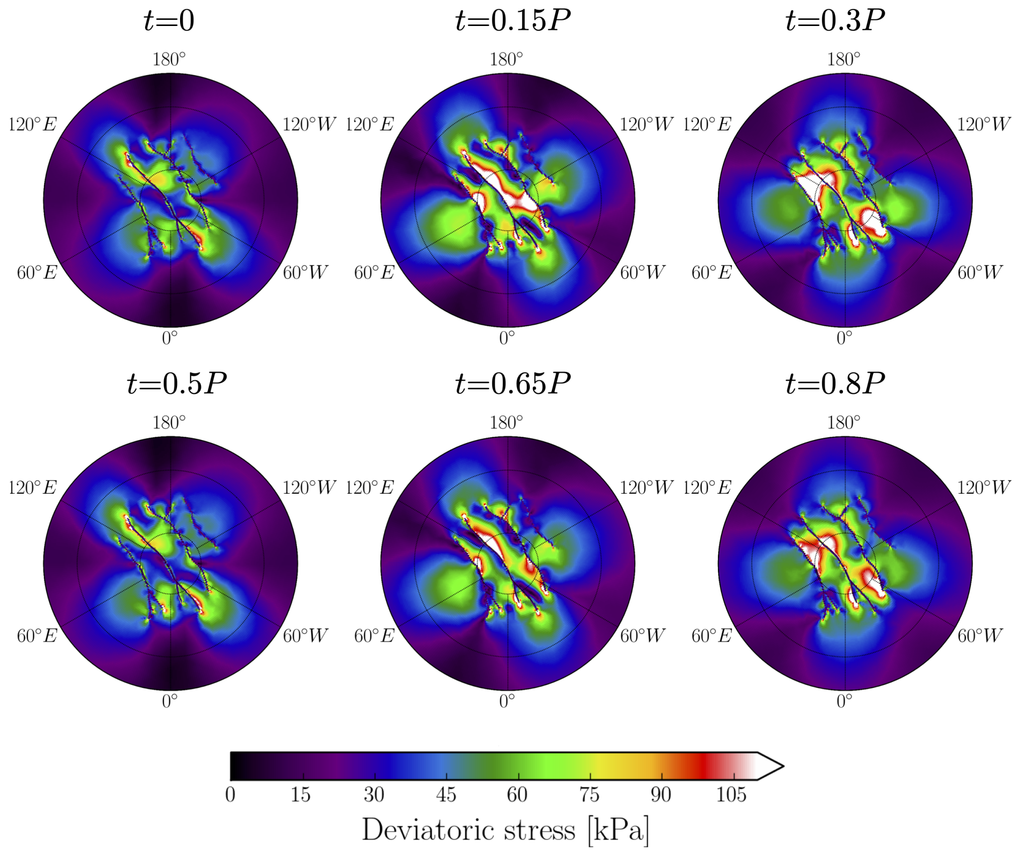

Figure 3.9: Periodic variations of the deviatoric stress at the surface calculated for the model with μ_f=0.2. The magnitude of the deviatoric stress, $|\mathbb{S}|=\sqrt{\mathbb{S}_{ij}\mathbb{S}_{ij}}$, is shown at the same times as in Figure 3.8.

Together, these two variables control the viscosity of the fault zones. In the course of one tidal period, the fault system is subjected to compression (σ_{nn}<0) and extension (σ_{nn}>0, see Figure 3.10 a). During the compression phase, the normal stress increases the yield stress, and the slip rate reduces. In the extension phase, the positive normal stress decreases the yield stress, thus facilitating the sliding of the faults. Since the geometry of the faults is complex and the faults interact with each other, the normal stress is not fully synchronized along faults, implying that parts of the faults may be under compression while the rest is subjected to extension. The resulting motion of the faults is continuous (Figures 3.10 b, c) and modulated by the interplay of the above processes. Note that the compression phase is significantly longer than the extension phase, and the average value of σ_{nn} is about $-50\,\mathrm{kPa}$ (and not zero as might be intuitively expected). This average value represents a static ("background") stress that occurs due to the asymmetry in the frictional response to normal loading (see Section 3.4.3). The static stress is not included in Figure 3.9 and will be discussed in the next section.

In Figures 3.10 b–e, we compare the kinematic characteristics of Enceladus' fault system calculated for the model without friction (μ_f=0) with those obtained for the models with μ_f=0.1, 0.2, 0.4, 0.8 and the model without any faults. Note that, for simplicity, we plot the magnitude of the slip rate because the slip vector has both horizontal and vertical components. The inclusion of friction

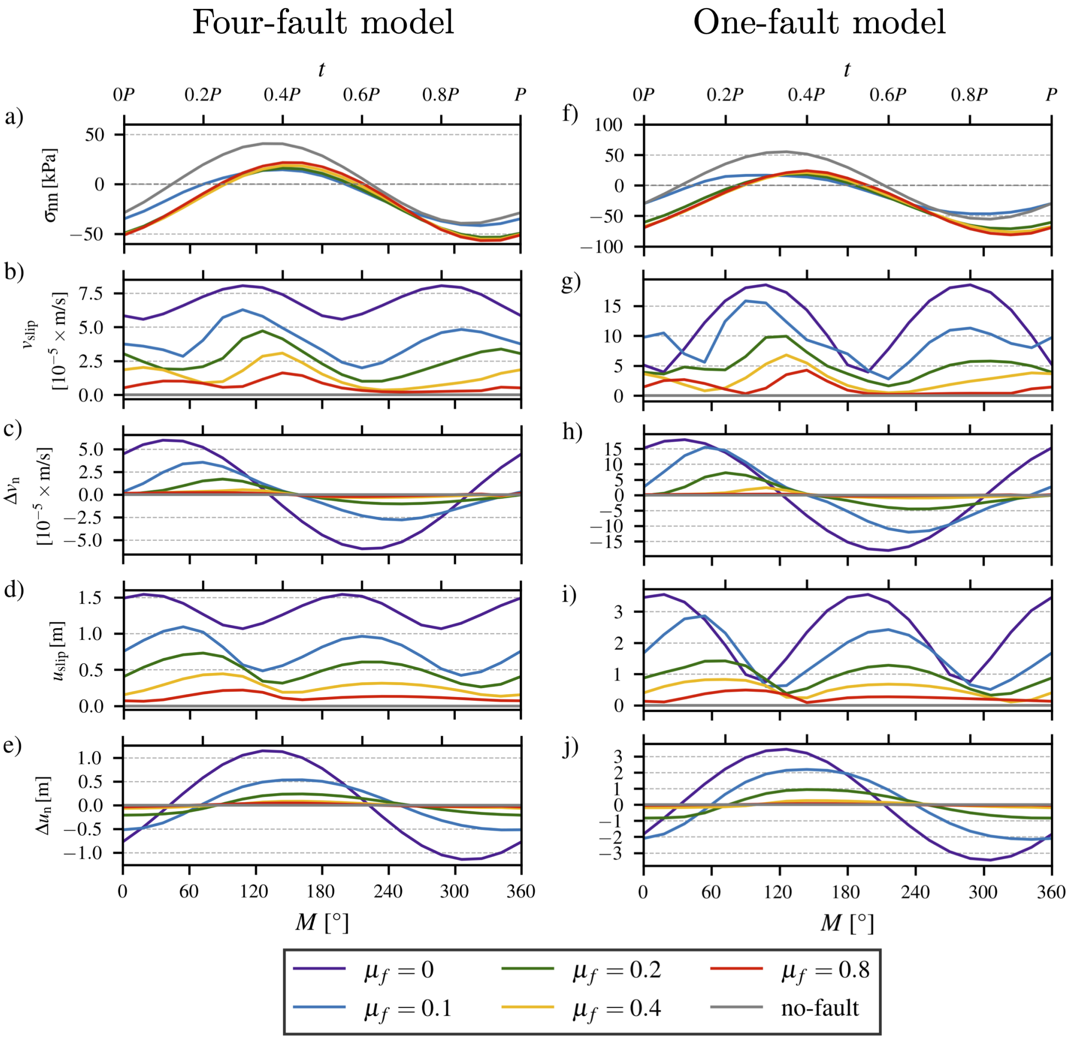

Figure 3.10: Left: Time variations of quantities characterizing the behavior of Enceladus fault system calculated for models with different μ_f and the no-fault model. All quantities are averaged along the faults and over the depth. Symbol $\sigma_{\rm nn}$ is the normal component of the traction vector acting on the fault surface (see equation 3.36), $v_{\rm slip}$ is the magnitude of the jump across the fault in the velocity component parallel to the fault, $\Delta v_{\rm n}$ is the jump in the velocity component normal to the fault ($\Delta v_{\rm n}$>0 corresponds to the opening phase), $u_{\rm slip}$ is the magnitude of the jump in the displacement component parallel to the fault, and $\Delta u_{\rm n}$ is the jump in the displacement component normal to the fault ($\Delta u_{\rm n}$>0 when the faults are open). We show only the periodic part of the displacement. Note that $v_{\rm slip}$ and $u_{\rm slip}$ include both horizontal and vertical components. Right: The same as on the left hand side but for models with only one fault (the main branch of Baghdad Sulcus).

(Figure 3.10 b, g) leads to a decrease of the slip rate and breaking of symmetry – the slip rate is larger in the extension than in the compression phase. A similar behavior is found for the extension rate, $\Delta v_{\rm n}$ (Figure 3.10 c). The contraction phase ($\Delta v_{\rm n}$<0) in the model with intermediate values of coefficient of friction (e.g., μ_f=0.2) is significantly longer than the dilation phase ($\Delta v_{\rm n}$>0), and the onset of the dilation phase is delayed by several hours compared to the frictionless model.

The average jump in displacement across the fault is shown in panels d and e. The normal components of the displacement jump, Δu_n, was used in the previous studies (Souček et al., 2016; Běhounková et al., 2017) to predict the temporal variations in Enceladus' plume activity. The choice of Δu_n was motivated by the assumption that the mass transfer across the ice shell is most efficient (the plume is brightest) when the tiger stripes are open (i.e., when Δu_n is maximum). However, the results of the present study do not support this assumption. Figure 3.10 e shows that the maximum of u_n is delayed by up to $0.1P$ for the models with friction compared to the frictionless model. However, the maxima of Δu_n for all the models are still several hours advanced with respect to the observed brightness maximum (occurring at $t \approx 0.55P$, Ingersoll et al. (2020)). It is noteworthy, however, that the brightness maximum coincides with the period when $\Delta u_\mathrm{n} > 0$ (the faults are "open") and occurs shortly before u_slip attains its (secondary) local maximum. This might indicate that the permeability (and thus activity) of the faults is related to the total strain experienced by the material filling the faults rather than to Δu_n.

The characteristics shown in panels a–e are affected by the interaction between the faults. Therefore, in order to isolate the effect of μ_f on the fault motion, we show the results obtained for a model containing only a single fault – the main branch of Baghdad Sulcus (Figure 3.10 f–j). Note that the reduced magnitude of all the variables for four-fault models is a consequence of the prominence of Baghdad Sulcus (see Figure 3.11 b) and spatial averaging over all the faults.

Unlike the normal stress (panel f), which is only weakly sensitive to the value of μ_f, the motion of the fault (panels g–j) is strongly influenced by the choice of the friction coefficient. As μ_f is increased, the amplitude of the curves decreases, and the phase lag increases. For $\mu_f = 0.8$ the results approach the no-fault model, i.e., $v_\mathrm{slip} \approx 0$ for almost half of the time, and the maximum normal displacement at the fault does not exceed a few centimeters.

3.3.3 Static stress and frictional heating

An elastic system with frictional interfaces subjected to periodic loading can produce a static stress field that forms a background on which oscillatory stress is superposed (for a simple example, see Section 3.4.3 and Figure 3.15; for a review, see Barber (2016)). The behavior of such a system and the distribution of the static stress depend on the value of the friction coefficient and the coupling between the relative tangential motion at the interface and the acting normal traction. The static part of the stress field obtained for the model with $\mu_f = 0.2$ is shown in Figure 3.11 a while the results obtained for different values of μ_f are presented in the Section 3.4.3 (see Figure 3.17).

Figure 3.11 a shows that the static stress field at the surface is characterized by horizontal compression in the direction perpendicular to the faults (cf. Figure 3.10 a) and tension in the direction parallel to the faults (see also Section 3.4.3 and Figure 3.11). This stress orientation is independent of the friction coefficient (see Figure 3.17) and is primarily determined by the orientation of the fault system relative to the tidal loading. Near the tips of the faults, the stress field is more heterogeneous and has no dominant direction. The static stress has

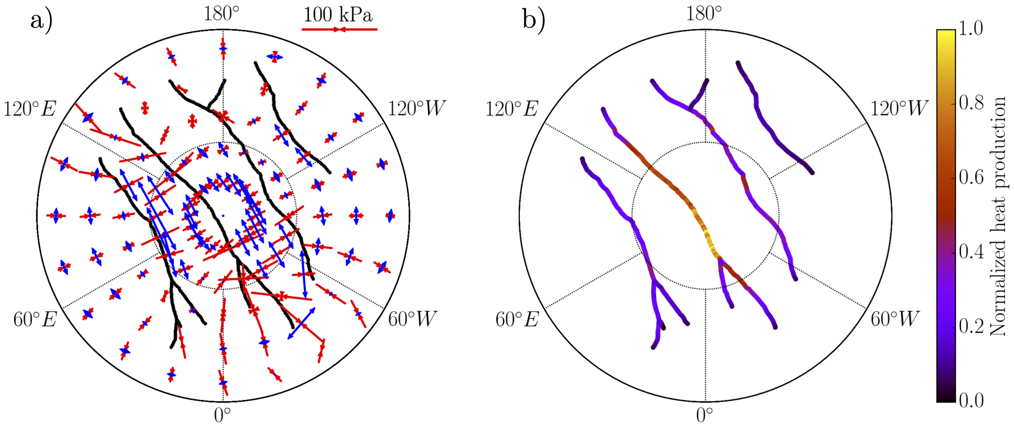

Figure 3.11: Background static stress at the surface (a) and normalized heat production along the faults (b) obtained for the model with μ_f=0.2. In panel a, red and blue arrows correspond to compression and tension, respectively. Maps showing the stress at different depths and illustrating the dependence of tidal heating on the friction coefficient can be found in the Supporting Information, see Section 3.4.

a magnitude of $10-100\,$kPa, which is comparable with the amplitude of the cyclic stress shown in Figure 3.9. A detailed analysis of the static stress field and its relationship to the tectonics of Enceladus' SPT is beyond the scope of the present study and will be pursued in a future paper.

The model developed here takes into account the dissipative nature of the fault motions, allowing us, for the first time, to estimate the heat generated along the tiger stripes. The heat production is evaluated by integrating the time-averaged mechanical dissipation over the thickness of the ice shell. The relative variations of the heat production along the faults are shown in Figure 3.11 b. Our model suggests that most of the frictional heat is generated in the central parts of the faults, the heat production decreases to zero near the fault tips.

While the relative variations in the frictional heating along the faults can be determined with a high degree of confidence, the evaluation of the total heat generated on the faults is challenging because it strongly depends on implementation details, in particular on the thickness of the fault zones. Considering the uncertainties, we can conclude with a high degree of confidence that the total heat production on the faults is less than 1 GW. This suggests that the frictional heating represents only a small fraction of the heat power observed over the SPT ($13-19\,$GW, Howett et al. (2011)), emitted from the tiger stripes ($\sim 5\,$GW, Spencer et al. (2018)) or predicted in the SPT from heat transfer models ($6-7\,$GW, Souček et al. (2019)). The dependence of the frictional heating on the value of the friction coefficient is relatively weak and is shown in the SI (see Figure 3.18 in Section 3.4.3). The largest frictional heating is found for $\mu_f\approx0.1-0.2$. When the friction coefficient increases, the segment of the fault where the frictional heating occurs is shortened, and the total heat production decreases.

3.3.4 Conclusions

In this part of the thesis, we evaluated the response of Enceladus to periodic tidal loading, assuming that the tiger stripes are fault zones of finite thickness whose strength depends on the normal stress acting on the fault planes. In contrast to the previous studies, in which the tiger stripes were included as frictionless fractures or were not included at all, the model provides a framework for understanding the role of contact friction in tidal deformation and for quantifying the mechanical dissipation in the fault zones. We find that the diurnal tides produce a complex pattern of stress anomalies, characterized by a length scale of $\sim$10 km and the peak values exceeding 100 kPa (Figure 3.9). The stress reaches a maximum in the central parts of the faults and decreases towards their tips.

The friction on the faults tends to slow down the response of the system to tidal loading, leading to an asymmetry between the compression and extension phases (Figure 3.9). This asymmetry results in additional stress, which is constant in time and comparable in magnitude to the cyclic stress (Figure 3.11 a). The static stress field is characterized by compression in the direction perpendicular to the faults. This stress orientation is independent of the friction coefficient and is likely to be controlled by the orientation of the faults relative to the tidal loading.

The frictional heating is concentrated in the central parts of the faults (Figure 3.11 b). We estimate that the total heat flow generated on Enceladus' faults is $0.1 - 1$ GW, accounting for only a small fraction of the heat power emitted from the tiger stripes (Spencer et al., 2018). A comparison of the predicted fault motion with the observed variations of Enceladus' plume activity may indicate that the permeability of the faults depends not only on whether the ice shell is in extension or compression but also on the total strain experienced by the material in the fault zones.

Since the mechanical properties of Enceladus' fault zones are largely unknown, we assume that the friction coefficient is constant. This is obviously a simplification of reality, see Sections 4.2 and 4.2.3, but it allows us to gain insight into the processes occurring in the SPT without performing an extensive parametric study.

In the first approximation, the south polar region of Enceladus can be regarded as an elastic system with frictional interfaces subjected to periodic loading. These systems have received considerable attention from the engineering community (e.g., Barber, 2016), but they have rarely been studied in the context of icy moons. This study shows that such systems' behavior may be surprising and counterintuitive in many ways. The existence of a static stress field generated by periodic tidal deformation is unexpected and has not been reported previously in the literature. Future research should answer the question of whether this field can influence the tectonic processes in the SPT and how much it is affected by temporal variations of the friction coefficient.

3.4 Supporting information for "Enceladus' tiger stripes as frictional faults: Effect on stress and heat production" (Pleiner Sládková et al., 2021)

In this section, we provide additional details on the model formulation and its numerical implementation. For the sake of completeness, we also show several additional results that complement those presented in the main text of the article (Pleiner Sládková et al., 2021) or shown in Section 3.3.

3.4.1 Model description

Here, we recapitulate the governing equations, and the boundary conditions. Model parameters used in the simulations are summarized in Table 3.1.

Symbol	Variable	Value	Unit
e	eccentricity	0.0047	
g	surface gravity	0.113	$\mathrm{m\,s^{-2}}$
K	bulk modulus of ice	8.8	GPa
n	parameter controlling the onset of yielding	2	-
Δ	fault zone half-width	1	km
η_{Max}	background value of the viscosity	10^{20}	Pa s
μ	shear modulus of ice	3.3	GPa
μ_f	coefficient of friction of ice	0.1, 0.2, 0.4, 0.8	-
ϱ_i	density of ice	926	$\mathrm{kg\,m^{-3}}$
ϱ_w	density of water	1010	$\mathrm{kg\,m^{-3}}$
ω	orbital frequency	5.3×10^{-5}	$\mathrm{s^{-1}}$

Table 3.1: Model parameters

Governing equations

We solve tidal deformation of a compressible Maxwell viscoelastic continuum in a hydrostatically pre-stressed state. A detailed derivation of the governing equation is provided in Souček et al. (2019), in a more general setting also involving temperature evolution. Here, we only recapitulate the model equations and boundary conditions. In the actual (Eulerian) configuration, the system of governing equations comprising the quasi-static force balance and the Maxwellian rheology reads as follows

$$\nabla \cdot \mathbb{T} - \varrho_i \nabla V_{\mathrm{tidal}} = \mathbf{0}\,, \tag{3.37a}$$

$$\dot{\mathbb{T}} = K(\nabla \cdot \dot{\mathbf{u}})\mathbb{I} + \mu \left(\nabla \dot{\mathbf{u}} + (\nabla \dot{\mathbf{u}})^{\mathrm{T}} - \frac{2}{3} (\nabla \cdot \dot{\mathbf{u}})\, \mathbb{I} \right) - \frac{\mu}{\eta} \mathbb{S}. \tag{3.37b}$$

For synchronous eccentric orbit and to the first order in eccentricity, the time-varying tidal potential is given by:

$$V_{\mathrm{tidal}}(\mathrm{r},\vartheta,\phi,t) = \mathrm{r}^2\omega^2 e \times \Bigg(\frac{3}{2}P_2^0(\cos\vartheta)\cos\omega t \\ -\frac{1}{4}P_2^2(\cos\vartheta)(3\cos\omega t\cos 2\phi + 4\sin\omega t\sin 2\phi)\Bigg), \tag{3.38}$$

where ω is the angular frequency, e is the eccentricity; $(\mathrm{r},\vartheta,\phi)$ are the radius, co-latitude and longitude, respectively; P_2^0 and P_2^2 are the associated Legendre functions. See Table 3.1 for the values used.

In the above equations, we neglect the effects of self-gravitation, the inertial force, and the body forces associated with density variations arising from the deformation, all negligible in the considered application. Note that we do not explicitly consider the balance of mass, assuming density to be constant. Also, the Maxwell rheology is not written in a frame-indifferent form since we consider only small deformations in our application, and the corresponding additional terms in the time derivative operator have been dropped. Taking the trace and the deviatoric part of (3.37b), we get, respectively,

$$\frac{1}{3}\mathrm{tr}\dot{\mathbb{T}} = K\nabla\cdot\dot{\mathbf{u}}\,, \qquad \dot{\mathbb{S}} = 2\mu\mathbb{D}^{\mathrm{d}} - \frac{\mu}{\eta}\mathbb{S}\,. \tag{3.39}$$

Thus, the isotropic part of the response is purely elastic (i.e., corresponding to an infinite bulk viscosity), while the shear deformation is Maxwellian.

On the boundaries of the shell, characterized by position vectors (from the origin), $\boldsymbol{r}_{\mathrm{s}}(\vartheta,\phi)$ (surface) and $\boldsymbol{r}_{\mathrm{b}}(\vartheta,\phi)$ (ice/water interface), the boundary conditions linking the surface stress and the radial displacement u_r are imposed. On the upper surface, we prescribe

$$\mathbb{T}(\boldsymbol{r}_{\mathrm{s}},t)\cdot\boldsymbol{n}_{\mathrm{s}} + u_{\mathrm{r}}(\boldsymbol{r}_{\mathrm{s}},t)\,\varrho_i\,g\,\boldsymbol{n}_{\mathrm{s}} = \boldsymbol{0}\,, \tag{3.40}$$

corresponding to the stress-free condition on the upper surface mapped to an undeformed shape of the shell and where $\boldsymbol{n}_{\mathrm{s}}$ is the outer normal to the surface. At the ice-ocean interface, traction equals the pressure in the ocean, which (again mapped on the undeformed surface) reads

$$\mathbb{T}(\boldsymbol{r}_{\mathrm{b}},t)\cdot\boldsymbol{n}_b - u_r(\boldsymbol{r}_{\mathrm{b}},t)\,(\varrho_w-\varrho_i)\,g\,\boldsymbol{n}_b = \varrho_w\,V(\boldsymbol{r}_{\mathrm{b}},t)\,\boldsymbol{n}_b\,, \tag{3.41}$$

where $\boldsymbol{n}_b$ is the outer normal to the ice-ocean boundary. For a detailed derivation of these boundary conditions, please see Souček et al. (2019), Appendix A.3.

Friction at the faults

For the description of how we approximate the friction at the fault, see Section 3.1.2.

Note that we keep the elastic parameters in the fault zone unaltered with respect to the rest of the shell in the current approach. This is in contrast with the approach in our previous work (Souček et al., 2016; Běhounková et al., 2017; Souček et al., 2019), where the elastic moduli were reduced in the fault zone to mimic a frictionless contact. In the current model, elasticity is unaffected, and

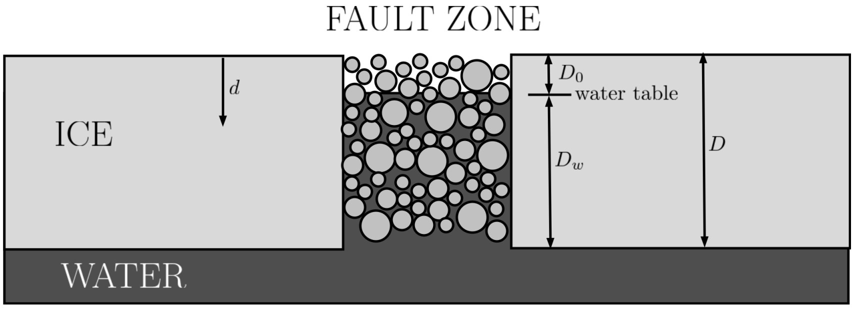

Figure 3.12: Sketch of the fault zone cross-section.

all the yield effects and mechanical weakening/strengthening are associated with the (dynamic) drop/increase in viscosity. In reality, a combination of both the viscosity and the elastic modulus reduction is plausible. Nevertheless, we chose the adopted approach for numerical reasons, and it is consistent in the sense that it provides a reasonable approximation of the Coulomb-type frictional contact.

Yield stress

In order to mimic the Coulomb-type friction, the yield stress σ_Y is taken proportional to the total compressive normal stress within the fault zone, i.e., we prescribe:

$$\sigma_Y = -\mu_f \left(\mathbb{T}^{\text{tot}}_{\text{nn}}\right)^- \quad \text{where} \quad \mathbb{T}^{\text{tot}}_{\text{nn}} = \tilde{\boldsymbol{n}} \cdot \mathbb{T}^{\text{tot}} \tilde{\boldsymbol{n}} \ , \quad \text{and} \quad (\bullet)^- = \min(\bullet, 0). \tag{3.42}$$

Here $\tilde{\boldsymbol{n}}$ is an approximation of the unit normal to the idealized fault surface, defined everywhere within the fault zone, see also Section 3.4.2; $\mathbb{T}^{\text{tot}}$ is the total Cauchy stress, composed of a static and a dynamic (time-dependent) part:

$$\mathbb{T}^{\text{tot}} = \mathbb{T}^{\text{static}} + \mathbb{T}, \tag{3.43}$$

where $\mathbb{T}$ stems from the solution of (3.37)-(3.41).

For the static part of the stress, we assume that the fault zone is composed of a damaged porous ice matrix, partially flooded (to the hydrostatic height) by water from the internal ocean, as in Figure 3.12. We adopt the simple Terzaghi effective stress approach (Terzaghi, 1925), assuming that the static normal stress $\mathbb{T}^{\text{static}}$ is given by the *effective pressure* p^{eff}, given by the ice overburden pressure minus the water pore pressure p^w:

$$\mathbb{T}^{\text{static}}(d) = -p^{\text{eff}}(d)\mathbb{I}\,, \qquad \text{where} \qquad p^{\text{eff}}(d) = \varrho_i g d - p^w(d). \tag{3.44}$$

Assuming that the water table is in hydrostatic equilibrium (which need not to be exactly true if the dynamic effects become significant, see, e.g., Kite and Rubin (2016)), it holds

$$p^w(d) = \begin{cases} 0 & d \le D_0 \\ \varrho_w g(d - D_0) & D_0 \le d \le D \end{cases} . \tag{3.45}$$

In order to reduce the resolution requirements in the radial direction, we further approximate the effective pressure by its depth-averaged form (denoted by overbar), which, given (3.44) and (3.45) reads:

$$\overline{p^{\text{eff}}} = \frac{\varrho_i g D}{2} - \frac{\varrho_w g D_w}{2} \frac{D_w}{D}. \tag{3.46}$$

Employing the assumption of hydrostatically equilibrated water table:

$$\varrho_i g D = \varrho_w g D_w \Longrightarrow \frac{D_w}{D} = \frac{\varrho_i}{\varrho_w}\,, \tag{3.47}$$

we get

$$\overline{p^{\text{eff}}} = \frac{gD}{2}(\varrho_w - \varrho_i)\frac{\varrho_i}{\varrho_w}\,. \tag{3.48}$$

This expression, applied in (3.43) gives

$$\sigma_Y = \begin{cases} \mu_f \left(\overline{p^{\text{eff}}} - \tilde{\boldsymbol{n}} \cdot \mathbb{T}\tilde{\boldsymbol{n}}\right) & \text{if} \quad \overline{p^{\text{eff}}} \geq \tilde{\boldsymbol{n}} \cdot \mathbb{T}\tilde{\boldsymbol{n}} \\ 0 & \text{otherwise} \end{cases}\,. \tag{3.49}$$

For numerical reasons, we use a cut-off at 10 Pa instead of 0. Note that the thickness of the shell is spatially variable. The above derivation holds locally, and the average effective pressure $\overline{p}^{\text{eff}}$ depends on the co-latitude and longitude.

3.4.2 Numerical implementation

This section provides additional information on the model geometry and numerical implementation.

Fault geometry and representation

The representation of the fault zones in our model is done via a smoothed indicator function χ defined as

$$\chi(\vartheta, \phi) = \exp\left(-\frac{\mathcal{D}^2(\vartheta, \phi)}{2\Delta^2}\right), \tag{3.50}$$

where $\mathcal{D}$ denotes the spherical distance to a curve approximating the fault – processed from data by Porco et al. (2014), and Δ denotes the half-width of χ. The indicator function is shown in Figures 3.13 and 3.14.

In the formula for viscosity (3.35), we need to evaluate $\tilde{\boldsymbol{n}} \cdot \mathbb{T}\tilde{\boldsymbol{n}}$ due to its presence in the expression for the yield stress (see (3.49)), where $\tilde{\boldsymbol{n}}$ is the approximation of the unit normal to the idealized fault surface. We approximate this field as a normalized gradient of an oriented distance function

$$\tilde{\boldsymbol{n}} = \frac{\nabla d_s}{\|\nabla d_s\|}\,, \tag{3.51}$$

where d_s is an oriented distance function. The unit normal field in the fault zones is depicted by arrows in Figure 3.14 for one-fault model (top) and four-fault model (bottom).

The indicator function is also used to interpolate the Maxwell viscosity η between an external value η_{Max} outside the fault zones and an effective viscosity η_{eff} in the fault zone:

$$\log \eta(r, \vartheta, \phi) = (1 - \chi(\vartheta, \phi)) \log \eta_{\text{Max}} + \chi(\vartheta, \phi) \log \eta_{\text{eff}}\,. \tag{3.52}$$

We interpolate logarithms of viscosity for numerical reasons.

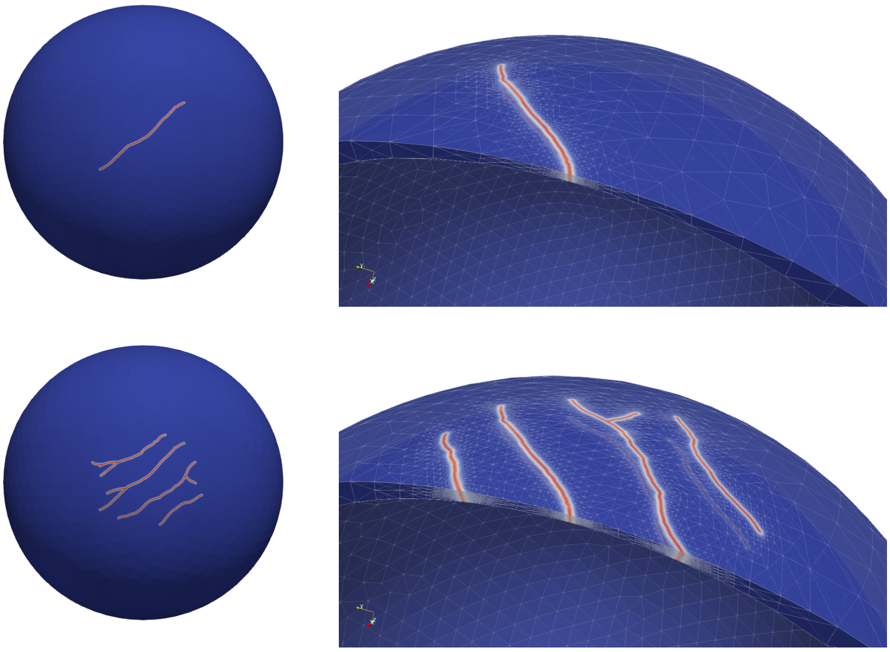

Figure 3.13: Indicator function χ defining the faults, for the one-fault model - main branch of Baghdad Sulcus (*top*) and the four-fault model (*bottom*) together with the mesh.

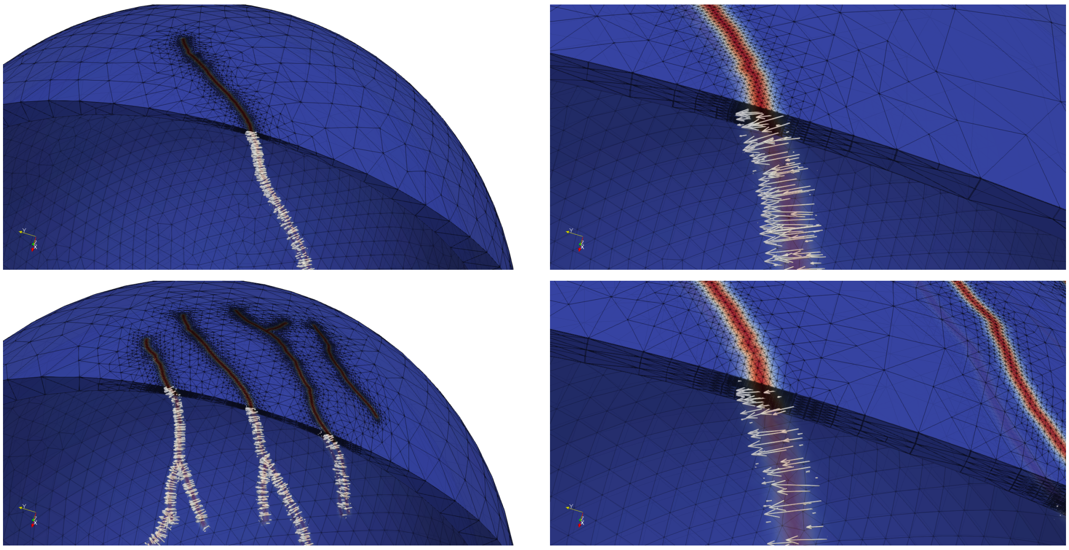

Figure 3.14: Indicator function χ together with the computational mesh and the approximation of oriented normal function $\tilde{\boldsymbol{n}}$ (arrows).

Finite element model

The weak formulation of the problem (3.37)-(3.41), and the details on the temporal and spatial discretization, together with specifics on the numerical implementation by finite element library FEniCS, can be found in Souček et al. (2019). The only difference here (from the numerical point of view) lies in the dynamic stress $\mathbb{T}$ entering the viscosity η through the effective viscosity formula (3.35) and the yield stress expression (3.49).

This implies that the problem (3.37)-(3.41) becomes strongly nonlinear. To deal with the nonlinearity, we adopt a fixed point iteration scheme on each discrete time level. For numerical reasons and due to technical problems with identifying the optimal convergence measure for the fixed point iteration scheme, we adopt a fixed number of 5 fixed point iterations for each time step, which has proven to be sufficient in the investigated problem.

The initial computational mesh is generated using the open-source `gmsh` library (see `www.gmsh.info`) and then iteratively refined in the fault zone. Finally, it is mapped to an approximation of the realistic shape based on the shape model of Čadek et al. (2019). The resolution is the finest in the fault zone (approximately 500 m). However, far away from the faults, the average resolution is significantly coarser (approximately 30 km). The computational mesh contains approximately 1.5 million tetrahedral elements. Each simulation (with a specific setup) was run for 4 tidal periods, using 20 time steps per period. As the surrounding of the fault zone behaves effectively elastic, convergence to a periodic solution is sufficiently fast. We used the computational capabilities of a supercomputer at IT4Innovations National Supercomputing Center, Czech Republic, running the jobs typically on 16 or 24 nodes, each node composed of two twelve-core Intel Xeon processors equipped with an 128 GB RAM. The average time required for one simulation was between 20 and 30 hours.

3.4.3 Supplementary results

In this section, we first demonstrate, using a simple ordinary differential equation (ODE) toy problem, that the development of background stress is natural for periodically loaded systems with Coulomb-type friction. Next, we show how frictional heating and the static background stresses depend on the coefficient of friction.

Stationary pre-stress arising from friction asymmetry

Let us demonstrate that the compressive background stress observed in our simulations (see Figures 3.11 a, 3.16, 3.17) is, in fact, a feature inherent to models with asymmetry in the frictional response. The asymmetry can be either directional (different friction coefficient in one direction than in the other) or related to the forcing – friction coefficient depending on the load. The latter case corresponds to the Coulomb-type friction used in Section 3.3, where we consider the yield stress to be modulated by the normal stress at the fault.

We show that even for a perfectly symmetric periodic forcing, the above-mentioned asymmetry in the dependence of friction coefficient necessarily leads to the development of background stress that compensates it, thus allowing for a periodic response. Consider a simplified problem in the form of one scalar ODE, which captures the essential features of our three-dimensional continuum model:

- Model 1

$$\beta\Big(y'(t)\Big)y'(t) = -ky(t) + \cos(\omega t)\,, \tag{3.53a}$$

- Model 2

$$\beta\Big(cos(\omega t)\Big)y'(t) = -ky(t) + \cos(\omega t)\,, \tag{3.53b}$$

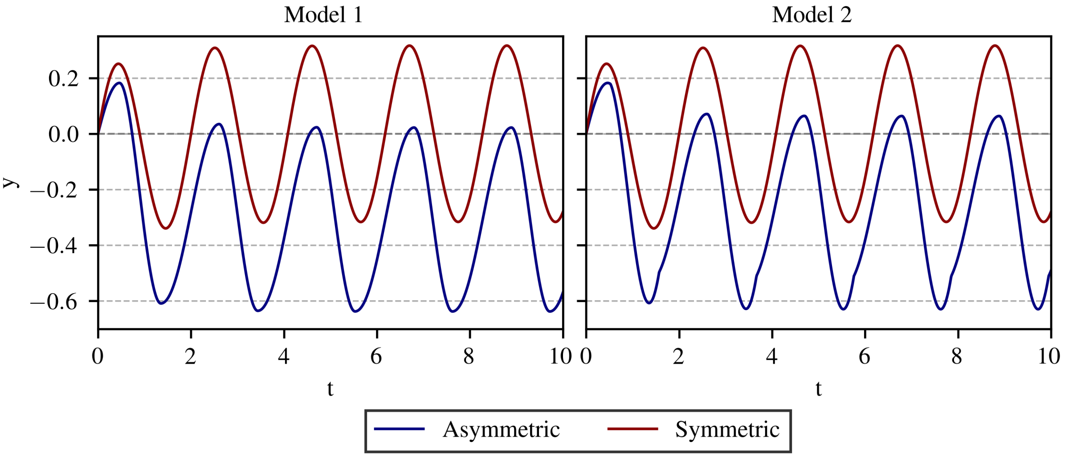

Figure 3.15: Numerical solution of equations 3.53a and 3.53b via Wolfram Mathematica.

solved for $t>0$, assuming $y(0)=0$ and considering k, and ω constant and

$$\beta(z) = \begin{cases} \beta_1 & \text{if} \quad z < 0 \\ \beta_2 & \text{if} \quad z \geq 0 \end{cases} . \tag{3.54}$$

This model describes a stationary force balance between the frictional force on the left-hand side, the elastic response (first term on the r.h.s), and the periodic loading force (second term on the r.h.s.). In this regard, it corresponds well to our model setting.

Solving numerically these two ODE's in Wolfram Mathematica, for k=1, ω=3, for two cases: symmetric case β_1=β_2=1, or asymmetric response β_1=$\frac{1}{2}$, β_2=$\frac{3}{2}$, yields the outputs presented in Figure 3.15.

The asymmetry in the frictional response leads to an offset of the periodic solution with respect to the symmetric case for both considered models. This behavior is rather intuitive since a periodic solution exists; it cannot be symmetric due to the asymmetry of the frictional response. Consequently, an offset develops, compensating the asymmetry, which allows for a periodic-in-time solution. This static offset in the displacement then contributes to the stress field, representing a static background stress.

Depth-dependence of the background stress

To complement the result in the main text, Figure 3.16 shows the background stress for a four-fault model in three different depths (at the surface, mid-shell, and bottom of the shell). While the stress is for any depth compressional in the direction perpendicular to the faults compensating for the response asymmetry, the stress regime in the direction parallel to the faults changes with depth. In the inter-faults region, the stress parallel with the faults changes from extensional (at the surface) to compressional (at the bottom) as a consequence of the bending stress (cf., Souček et al., 2019).

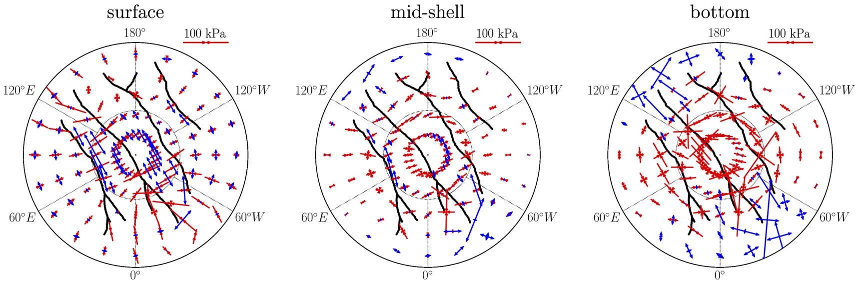

Figure 3.16: The background stress for the four-fault model (with $\mu_f = 0.2$), at three different depths.

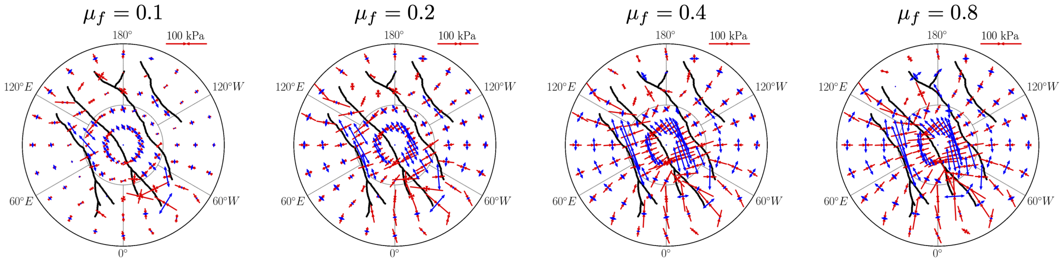

Figure 3.17: Dependence of the background stress on the friction coefficient μ_f for the four-fault model.

Parametric study for friction coefficient

Figure 3.17 depicts the static background stress field on the surface as a function of the friction coefficient μ_f ranging between μ_f=0.1 and μ_f=0.8. The stress orientation is consistent for all cases. With an increasing friction coefficient, the magnitude of background stress increases as expected. Remarkably, the largest background stress develops for μ_f=0.8 model, whereas the periodic part of the solution is similar to the solution without the faults.

Figure 3.18 shows the normalized heat production along the faults for models with different coefficients of friction. The largest dissipation is observed along the Baghdad sulcus for all values of the friction coefficient. Moreover, with the increasing friction coefficient, the heat production is getting more localized near the south pole, where the thickness also reaches its minimum. The dominance of the heating along the Baghdad sulcus further increases with the friction coefficient.

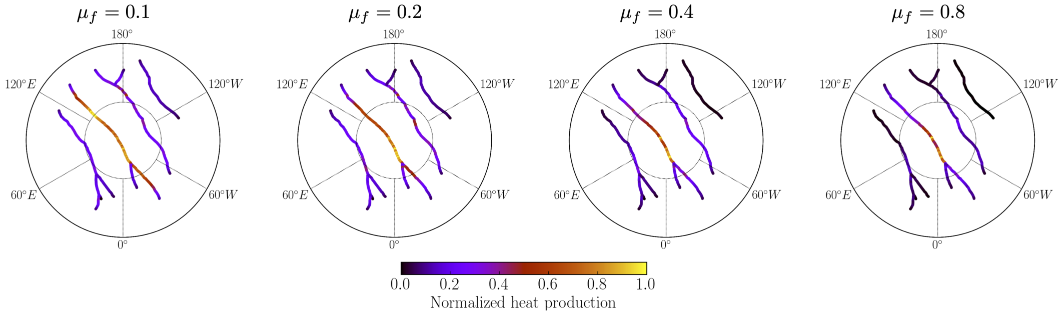

Figure 3.18: Dependence of the normalized heat production on the friction coefficient μ_f for the four-fault model.

4. Outlooks for a more realistic description of ice-ice contact

In this chapter, we present an outlook towards a more realistic description of the ice-ice contact in the visco-elasto-plastic framework presented in Chapter 3. We begin by introducing the concept known as the ”rate-and-state friction law”, which was developed by the seismological community in the 1970s and 1980s as a means of describing the frictional behavior of rocks. Subsequently, we provide a concise overview of experimental research conducted on ice-ice friction. We conclude the theoretical section by presenting a rate and state friction model specifically designed for ice-ice contact, and we discuss some of its fundamental characteristics. Following the theoretical discussion, we present two benchmark tests that assess the performance of the more realistic friction models integrated into the test case described in Chapter 3, with a focus on planar fault zone geometry (please refer to Section 3.1 for further details).

4.1 The historical development of rate and state friction model

From 1978 to 1982, a deeper understanding of the rock-rock contact was provided by the pioneering works of James H. Dieterich, Ernest Rabinowicz, and Andy Ruina, who developed a general class of friction laws using so-called internal state variables. These variables characterize changes in the properties of the faults during the dynamical contact and allow one to describe many of the experimentally observed characteristics of real-world frictional contacts (Dieterich and Kilgore, 1994). In this section, we summarize the articles of J. H. Dieterich and A. Ruina (Dieterich (1978, 1979); Ruina (1983)) developing the rate and state friction model.

4.1.1 Friction model by James H. Dieterich (Dieterich, 1978, 1979)

In 1979 Dieterich presented a study based on shear experiments on ground surfaces of granodiorite from Raymond, California (Dieterich, 1979) in which he described how time, displacement, and velocity affect the friction on the rock-rock contact in laboratory conditions. He also pointed out a resemblance between laboratory friction experiments and natural faults that allows for extrapolation of the laboratory results onto natural faults even though the laboratory experiments cannot capture the complexity of real-world conditions.

First, the stick-slip instability observed in the laboratory can be related to the mechanism of the crustal earthquake caused by an unstable slip. Second, the stable frictional slip in laboratory measurements exhibits similarities with the aseismic fault creep. Finally, the insensitivity of laboratory friction measurements to rock type, test conditions, and the character of the surface suggests that laboratory measurements can be relevant to the natural faults subjected to more complex conditions.

Observations arising from the experiments in Dieterich's paper (Dieterich, 1979) can be summarized into a few points, which are more thoroughly discussed in the following lines and which laid grounds to a novel frictional model, see Figure 4.2 (top curve for experimental results and the lowermost for the new model):

1. Including a healing mechanism in the frictional model is necessary to explain the data.
2. Certain finite slip is required for the friction coefficient to stabilize after an abrupt change in sliding velocity.
3. Such a slip does not depend on the amplitude of the slip velocity change.
4. A transient rise in friction develops after the increase of velocity, followed by a subsequent decrease.
5. After an abrupt change of velocity, the coefficient of friction decreases with increasing velocity.
6. Static friction increases with a growing loading rate in the experiments, where the contact is held still and then loaded with different velocities.

Now, let us concentrate more thoroughly on the above points. Since all the existing theories for frictional contact adopted a displacement or strain weakening mechanism, without an additional healing mechanism, repeated earthquakes on a particular fault would entail repeated weakening, eventually leading to zero strength of the fault. Since this is not observed, the inclusion of healing mechanisms in the frictional models seemed inevitable. In 1978, Dieterich introduced the following temporal dependence of the coefficient of static friction representing such a healing mechanism (Dieterich, 1978):

$$\frac{\tau}{\sigma_n} =: \mu_f = \mu_f^0 + A\log(Bt_c + 1). \tag{4.1}$$

Here τ represents the shear stress, σ_n is the normal stress, and t_c is the time of contact. Based on the observations, the constants A, B and μ_f^0 (the static coefficient of friction) have values of $0.01 - 0.02$, $1 - 2$ and $0.6 - 0.8$, respectively (Dieterich, 1978).

After performing measurements of sliding friction at different slip velocities, the time of contact has been replaced by

$$t_c = \frac{d_c}{\mathrm{v_{slip}}}, \tag{4.2}$$

where $\mathrm{v_{slip}}$ is the slip velocity and d_c is an experimental displacement parameter - the critical displacement characterizing the slip necessary for the coefficient of friction to stabilize after the change of slip velocity $\mathrm{v_{slip}}$. Measured values for d_c were of the order of 10^{-4}cm.

Apart from the velocity weakening resulting from combining (4.2) with (4.1), the critical displacement d_c also introduces the displacement (slip) dependence to the friction law. According to the experiments, d_c corresponds to surface roughness and does not depend on the amplitude of slip velocity change. Dieterich (1979) interprets the values of t_c as the average lifetime of a population of contacts, and d_c as the displacement required to change the population of contact points completely. Thus, according to Dieterich (1979), two processes compete on the frictional contact: first, the population of contacts ages, thus increasing the coefficient of friction as in equation 4.1; second, the displacement destroys the existing population of contacts and creates new, weaker ones, thus reducing the coefficient of friction.

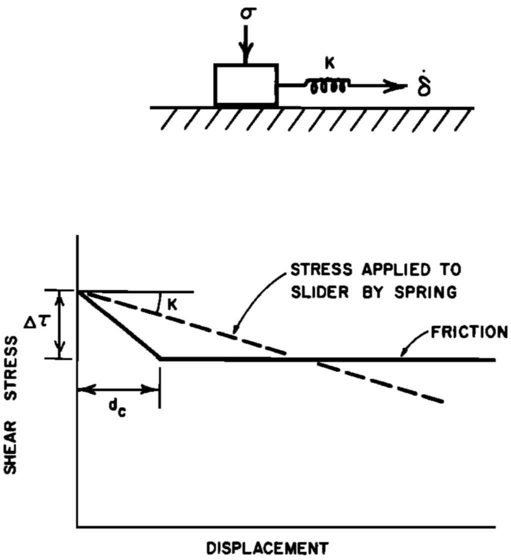

Figure 4.1: The instability model from Dieterich (1979).

Based on this interpretation, a simple spring-slider model of mechanically loaded frictional contact has been proposed to explain the experimental results, showing the transition from stable sliding to stick-slip (Dieterich, 1978), see Figure 4.1 or Section 3.1.2 for more information about the spring slider model. However, such a model was not able to capture the preseismic slip; hence, the pursuit of a more suitable model continued in the article Dieterich (1979).

From an abrupt change of loading velocity experiment, Dieterich (1979) inferred that the friction coefficient decreases with increasing velocity. On the other hand, a second type of experiment, in which the contact is held still for some time and then is loaded with different velocities, revealed that static friction increases with increasing loading velocity. Dieterich (1979) assumed that the adhesion at the actual points of contact (between the sliding surfaces directly or between the gouge particles separating the surfaces) controls the friction of rocks. According to Bowden and Tabor (1964), the actual contact of two surfaces is limited to asperities. Thus, when the normal stress rises, the contact area increases. The measure of contact area per unit surface $\mathcal{A}$ may be approximated as

$$\mathcal{A} = \mathcal{C}\sigma_n, \tag{4.3}$$

where σ_n is the average normal stress applied over the entire surface assuming perfect (100%) contact, $\mathcal{C}$ is a material constant inversely proportional to indentation hardness or yield stress.

Furthermore, Bowden and Tabor (1964) assert that the resistance to the slip is controlled by the adhesive strength of the junctions. Therefore, the average shear stress τ is proportional to the real area of contact: $\tau = F\mathcal{A}$, where F is the adhesive strength per unit area of contact. Then the friction coefficient is given as the shear stress divided by the normal stress; thus:

$$\mu_f = \frac{\tau}{\sigma_n} = \frac{F\mathcal{A}}{\mathcal{A}/\mathcal{C}} = \mathcal{C}F. \tag{4.4}$$

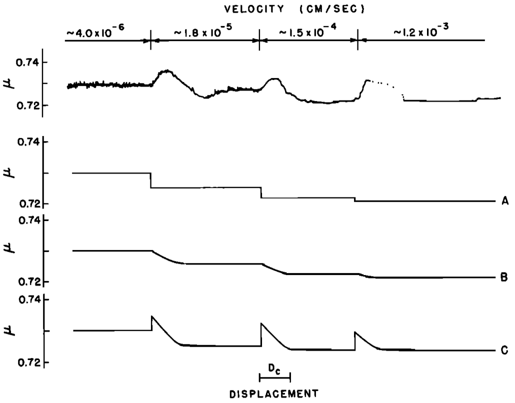

Figure 4.2: Figure 3 from Dieterich (1979): Comparison of experimental results (top curve) with empirical friction laws (the three bottom curves). Curve A employs (4.2) and (4.5), curve B uses (4.5) and (4.6). Curve C is based on (4.8) with $d_c = 2 \times 10^{-3}$cm, $c_1 = 0.68$, $c_2 = 0.01, c_3 = 0.5$, $f_1 = 1.0$, $f_2 = 25$, and $f_3 = 2 \times 10^{-3}$.

The time dependence in eq. (4.1) is related to an increase in the area of contact, or sometimes the depth of penetration of asperities (Dieterich, 1978). In response to the stress concentration at the contact points, creep deformation occurs, causing an increase in the contact area. Consequently, in view of (4.3), $\mathcal{C}$ should be time-dependent. The application of the following empirical relationship

$$\mathcal{C} = c_1 + c_2 \log(c_3 t + 1)$$

leads to the following time-dependent formula for the friction coefficient

$$\mu_f = \Big[c_1 + c_2 \log(c_3 t + 1)\Big] F, \tag{4.5}$$

which corresponds to equation (4.1) with $c_1 F = \mu_f^0, c_2 F = \mathcal{A}, c_3 = B$. Consequently, the last equation describes either the static friction if t is the time of stationary contact t_c or the sliding coefficient if t is the average time of contact.

To account for the observation that the displacement d_c is necessary for the coefficient of friction to change and stabilize after the velocity change, Dieterich (1979) presents an updated formula for t:

$$t = \frac{d_c}{\mathrm{v}_{\text{slip}}} \left(\frac{\mathrm{v}_{\text{slip}}}{d_c} t_0 \right)^{\exp\left(\frac{\delta_0 - \delta}{d_c}\right)}, \tag{4.6}$$

where t_0 and δ_0 are the average contact time and displacement needed for the stabilization of μ_f after the velocity change.

Moreover, Dieterich (1979) observed a transient rise in friction after the increase of velocity, probably not related to the variation of surface area with displacement and hence interpreted it as an effect of a loading rate dependence of the strength term F, cf. Dieterich (1979):

$$F = f_1 + \frac{1}{f_2 \log\left(\frac{d_c}{\mathrm{v_{slip}}} + 10\right)}, \tag{4.7}$$

where f_1, f_2 are constants. This equation states that for a constant area of contact, the strength of contact increases as the velocity of loading rises. Combining the formulae for $\mathcal{C}$ and F:

$$\mu_f = \Big[c_1 + c_2 \log(c_3 t + 1)\Big]\left[f_1 + \frac{1}{f_2 \log\left(\frac{d_c}{\mathrm{v_{slip}}} + 10\right)}\right], \tag{4.8a}$$

$$\text{where } t = \frac{d_c}{\mathrm{v_{slip}}}\left(\frac{\mathrm{v_{slip}}}{d_c} t_0\right)^{\exp\left(\frac{\delta_0 - \delta}{d_c}\right)} \tag{4.8b}$$

gives us an equation for the coefficient of friction representing adequately the static, transient, and steady state sliding friction observations presented in the article of Dieterich (1979), see Figure 4.2 for comparison with experiments.

Summarizing Dieterich (1979): the coefficient of friction can be expressed as the product of parameters $\mathcal{C}$ and F, where $\mathcal{C}$ depends on the time of contact, and F depends on slip velocity. During the slip $t \sim \mathrm{v_{slip}^{-1}}$ and in the case of velocity change, t relaxes to the new value after the displacement d_c. Hence two effects can be described: i) transient increase of μ_f for rising velocity, ii) indirect decrease in contact time (hence μ_f) with increasing velocity, which becomes apparent only after the displacement d_c.

Unstable slip in Dieterich's friction model

Dieterich (1979) discusses the possibility of an unstable slip for the proposed friction model and its implications for modeling earthquakes. For this purpose, he employs a simple mechanical analogue to the gradually loaded mechanical contact - a spring slider with a spring stiffness k_{sp} and coefficient of friction that depends on time and velocity as in (4.8), see Figure 4.1 with $K = k_{sp}$.

In this setting, an unstable slip occurs when the decrease of frictional strength $\Delta\tau$ over the critical displacement d_c has a slope that exceeds the slope of the unloading curve of the spring $-k_{sp}$, see Figure 4.1. Then the stress applied to the slider by the string is bigger than the frictional resistance, and an acceleration of the slider and consequently an instability follows; hence $k_{sp} \leq \frac{\Delta\tau}{d_c}$ leads to unstable behavior.

For stable sliding, the opposite inequality holds. The transition between the two states occurs for $k_{sp}^{crit} = \frac{\Delta\tau}{d_c}$. Since $\Delta\tau = \Delta\mu_f\sigma_n$, where $\Delta\mu_f$ is the change of the coefficient of friction depending on changes in time of contact and slip velocity, we have:

$$k_{sp}^{crit} = \frac{\Delta\mu_f\sigma_n}{d_c} \tag{4.9}$$

for the transition from stable sliding to stick-slip.

For a real fault, the stiffness of the spring k_{sp} needs to be replaced by the fault's slip stiffness, Dieterich (1978) proposed the following formula for confined slip on a fault segment:

$$k_{sp}^{crit} = \frac{\Delta\tau}{d_f} = \frac{\mu}{\nu}\frac{1}{L_s}, \tag{4.10}$$

where L_s is the length of the slipped zone as given by the fault dislocation relationship, $\Delta\tau$ is the change of stress caused by the average slip displacement d_f on a fault length L_s, μ is the shear modulus and $\nu \simeq 1$ is a geometric constant. Combining the instability inequality together with the last equation for fault's slip stiffness we obtain:

$$\frac{\mu}{\nu}\frac{1}{L_s} < \frac{\Delta\mu_f \sigma_n}{d_c} \tag{4.11}$$

for the unstable slip on a fault.

4.1.2 Friction model by Andy Ruina (Ruina, 1980, 1983)

The research of Dieterich was followed by Andy Ruina, whose work relies mostly on Dieterich's experiments at the turn of the seventies and eighties of the last century. Ruina synthesized the experiments based mainly on the change of loading velocity to several observations:

1. A steady state friction stress τ_{ss} is associated with every slip rate $\mathrm{v}_{\mathrm{slip}}$.
2. Frictional stress has a positive instantaneous slip rate dependence, i.e., exhibits a positive jump in τ for increasing $\mathrm{v}_{\mathrm{slip}}$ and negative for decreasing $\mathrm{v}_{\mathrm{slip}}$.
3. There is a long term increase/decrease in τ following the negative/positive jump in $\mathrm{v}_{\mathrm{slip}}$, which may/may not be larger than the instantaneous increase in τ.
4. A decay of stress value after the step change in $\mathrm{v}_{\mathrm{slip}}$ has a characteristic length independent of $\mathrm{v}_{\mathrm{slip}}$.

Ruina also mentioned two specific observations concerning the slip rates around $1\,\mu\mathrm{ms}^{-1}$:

5. The instantaneous rate dependence of the friction force is proportional to the logarithm of the ratio of velocities before and after the velocity change, i.e., $\triangle\tau \sim \log\left(\frac{\mathrm{v}^1_{\mathrm{slip}}}{\mathrm{v}^2_{\mathrm{slip}}}\right)$.
6. A steady state frictional stress $\tau_{ss} \sim C\log(\mathrm{v}_{\mathrm{slip}}) + \mathrm{const.}$, C can be positive or negative depending on the material and environment.

The aim of Ruina (1983) was to identify a mathematical description capable of reproducing these observations, especially the first three (fading memory, steady state, positive instantaneous slip rate dependence, and subsequent negative long-term dependence on slip rate). In order to do so, he developed a frictional model involving the state of the fault, for which several assumptions had to be made:

1. The surface (or its region) has at any instant in time a specific state.
2. The stress due to friction depends exclusively on the normal stress, slip velocity, and the state of the contact, i.e.,
$$\tau = \mathcal{F}(\sigma_n,\ \mathrm{v}_{\mathrm{slip}},\ \text{state}).$$
3. The state varies as a continuous function of time for finite $\mathrm{v}_{\mathrm{slip}}$ (i.e., continuous displacement).
4. The state's rate of change depends only on the normal stress, slip rate, and the instantaneous state at the points, i.e., it holds
$$\frac{d(\text{state})}{\mathrm{dt}} = \mathcal{G}(\sigma_n, \mathrm{v}_{\mathrm{slip}}, \text{state}).$$

A particular finite-dimensional representation of the state was proposed by (Ruina, 1983), who assumed that it can be characterized by a collection of state variables θ_i, or collectively Θ. Thus:

$$\tau = \mathcal{F}(\sigma_n, \mathrm{v}_{\mathrm{slip}}, \theta_1, \theta_2, \theta_3, \ldots) \tag{4.12}$$

$$\frac{d\theta_i}{dt} = \mathcal{G}_i(\sigma_n, \mathrm{v}_{\mathrm{slip}}, \theta_1, \theta_2, \theta_3, \ldots). \tag{4.13}$$

Let us note that the applicability of the model does not require a clear physical interpretation of the state variables, they can be treated formally as so-called "internal" variables.

Since the observations often indicate that the frictional stress τ is proportional to the normal stress σ_n the above sliding law can often be simplified as:

$$\tau = \sigma_n \mathcal{F}(\Theta, \mathrm{v}_{\mathrm{slip}}). \tag{4.14}$$

Since, in a geological context, one can often assume a constant normal loading history, the state equation reduces to:

$$\frac{d\theta_i}{\mathrm{dt}} = \mathcal{G}_i(\Theta, \mathrm{v}_{\mathrm{slip}}), \text{ where } \Theta = \theta_1, \theta_2, \theta_3, \ldots \tag{4.15}$$

Here the state variables θ_i characterize the surface's memory of the previous sliding.

The extensive experiments of Dieterich and Ruina have revealed that for every slip velocity $\mathrm{v}_{\mathrm{slip}}$, there exists a steady state represented by the steady state values of stress and state $(\tau^{ss}(\mathrm{v}_{\mathrm{slip}}),\ \theta_i^{ss}(\mathrm{v}_{\mathrm{slip}}))$. The stress and state at a specific constant slip rate approach the steady state values after sufficient time or displacement, i.e., θ_i^{ss} solve $\mathcal{G}_i(\theta_1^{ss}, \theta_2^{ss}, \ldots, \mathrm{v}_{\mathrm{slip}}) = 0$ for $i = 1, 2, \ldots$. In addition, according to experiments of Ruina (1980) θ_i can be chosen in such a way that they evolve independently of each other, i.e.,:

$$\dot{\theta}_i = \mathcal{G}_i(\theta_i, \mathrm{v}_{\mathrm{slip}}).$$

Ruina further assumes:

$$\infty > \frac{\mathcal{G}_i(\theta_i, \mathrm{v}_{\mathrm{slip}})}{\theta_i^{ss}(\mathrm{v}_{\mathrm{slip}}) - \theta_i} > 0 \quad \forall \theta_i,$$

ensuring that θ_i has a unique steady state for a constant slip rate imposed after an arbitrary slip history. Moreover, according to Ruina (1983), the asymptotic convergence to the steady state is exponential.

Based on previous assumptions, Ruina (1983) proposes a new version of the friction law with just one internal state variable:

$$\tau = \sigma_n \mathcal{F}(\theta, \mathrm{v}_{\mathrm{slip}}), \tag{4.16a}$$

$$\dot{\theta} = \mathcal{G}(\theta, \mathrm{v}_{\mathrm{slip}}). \tag{4.16b}$$

The difficulty in precisely defining $\mathcal{F}$ and $\mathcal{G}$ lies in the fact that the state variable cannot be measured. Thus, Ruina (1983) first defined sets of test conditions to confirm the one state friction law (4.16) and then sets of experiments to find the functions $\mathcal{F}$ and $\mathcal{G}$.

Consequently, he presented a couple of laws based on the early work of other authors, e.g., **"Simplified Dieterich's Law"**:

$$\tau = \sigma_n \left[\mu_f^0 + \theta + A \log\left(\frac{\mathrm{v}_{\mathrm{slip}}}{\mathrm{v}_{\mathrm{ref}}}\right) \right], \tag{4.17a}$$

$$\dot{\theta} = -\frac{\mathrm{v}_{\mathrm{slip}}}{d_c} \left[\theta + B \log\left(\frac{\mathrm{v}_{\mathrm{slip}}}{\mathrm{v}_{\mathrm{ref}}}\right) \right], \tag{4.17b}$$

where $\mathrm{v}_{\mathrm{ref}}$ is a reference value of the slip velocity and whose apparent deficiency is the singularity for zero sliding velocity (static contact).

Alternatively, a **"Two state variable friction law"** has been proposed by Ruina (1983) to explain some of the experiments performed on quartzite which cannot be described by the one-state law above:

$$\tau = \sigma_n \left[\mu_f^0 + \theta_1 + \theta_2 + A \log\left(\frac{\mathrm{v}_{\mathrm{slip}}}{\mathrm{v}_{\mathrm{ref}}}\right) \right], \tag{4.18a}$$

$$\dot{\theta}_1 = -\frac{\mathrm{v}_{\mathrm{slip}}}{d_c^1} \left[\theta_1 + B_1 \log\left(\frac{\mathrm{v}_{\mathrm{slip}}}{\mathrm{v}_{\mathrm{ref}}}\right) \right], \tag{4.18b}$$

$$\dot{\theta}_2 = -\frac{\mathrm{v}_{\mathrm{slip}}}{d_c^2} \left[\theta_2 + B_2 \log\left(\frac{\mathrm{v}_{\mathrm{slip}}}{\mathrm{v}_{\mathrm{ref}}}\right) \right]. \tag{4.18c}$$

The two-state variable friction law used in a spring slider model with a very stiff spring is able to reproduce the quartzite results nicely; see Figure 4.3. However, such a model still has the same problematic property as the "Simplified Dieterich's Law".

Unstable slip for Ruina's friction model

Similarly, as in the case of Dieterich's model, the frictional model by Ruina also admits unstable slip in a certain range of model parameters and thus is capable of reproducing earthquake-like response. Ruina (1983) presents a study of stability for constant force loading and the one state variable law, i.e., eqs. 4.17. He shows that for $B < A$, the solution converges to the steady-state solution. However, for $B > A$, the friction stress τ decreases with steady-state slip speed, and the steady sliding is extremely unstable.

The second stability study in Ruina (1983) concerns a steady sliding with a spring slider model. The model is unstable for the stiffness of the spring lower

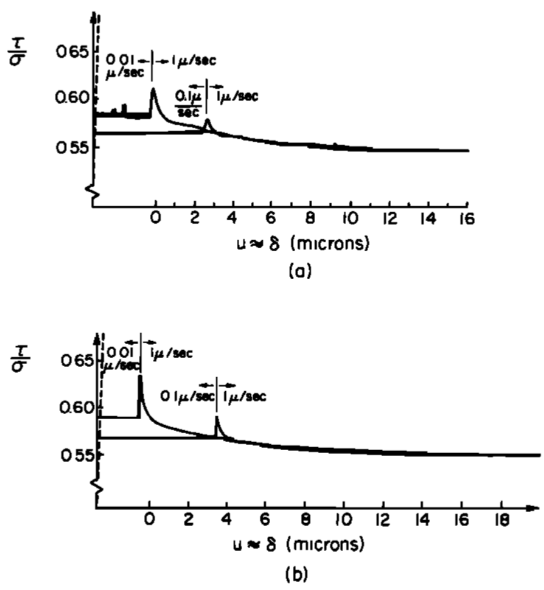

Figure 4.3: Figure 2 from Ruina (1983): Friction force variation due to step change in slip rate: (a) Quartzite polished with # 90 grit abrasive and about 30 bars normal stress. Experimental results from two tests in which the slip rate was changed from 0.01 $\mu\,\mathrm{m\,s}^{-1}$ to $1\mu\,\mathrm{m\,s}^{-1}$; (b) numerical simulation of the two tests using equation 4.18.

than the critical value: $k_{sp} < k_{sp}^{crit}$, where $k_{sp}^{crit} = -\frac{\mathrm{v_{slip}}}{d_c}\frac{d\tau_{ss}}{d\mathrm{v_{slip}}}$. If we apply this condition to the simplified Dieterich law, cf. eqs. 4.17, we obtain:

$$k_{sp}^{crit} = \sigma_n \frac{B-A}{d_c}. \tag{4.19}$$

The formula (4.19) can be derived through the theory of asymptotic linear stability for ordinary differential equations. We present this approach in Section 4.2.3.

4.2 Experimental data for the ice-ice frictional contact

The study of ice friction was in the early days motivated by understanding the behavior of skis, skates, etc.; hence most of the published papers considered the friction between ice and other materials, e.g., Joly (1899). The ice-ice frictional contact has been studied more extensively in the last forty years: including the theoretical/experimental work of Oksanen and Keinonen (1982), continuing with several articles around the group of Fortt and Schulson (Kennedy et al. (2000); Montagnat and Schulson (2003); Fortt et al. (2003); Fortt and Schulson (2007, 2009); Schulson and Fortt (2012); Schulson (2018)) and the group of Maeno and Arakawa (Maeno et al. (2003); Maeno and Arakawa (2004)). This section compiles the (primarily experimental) studies of ice-ice frictional contact.

Most of the research concentrated on the behavior of ice at moderate temperature, usually −10°C, sometimes expanding down to −40°C, except for Schulson and Fortt (2012), who tested the behavior of ice at temperatures as low as −175°C

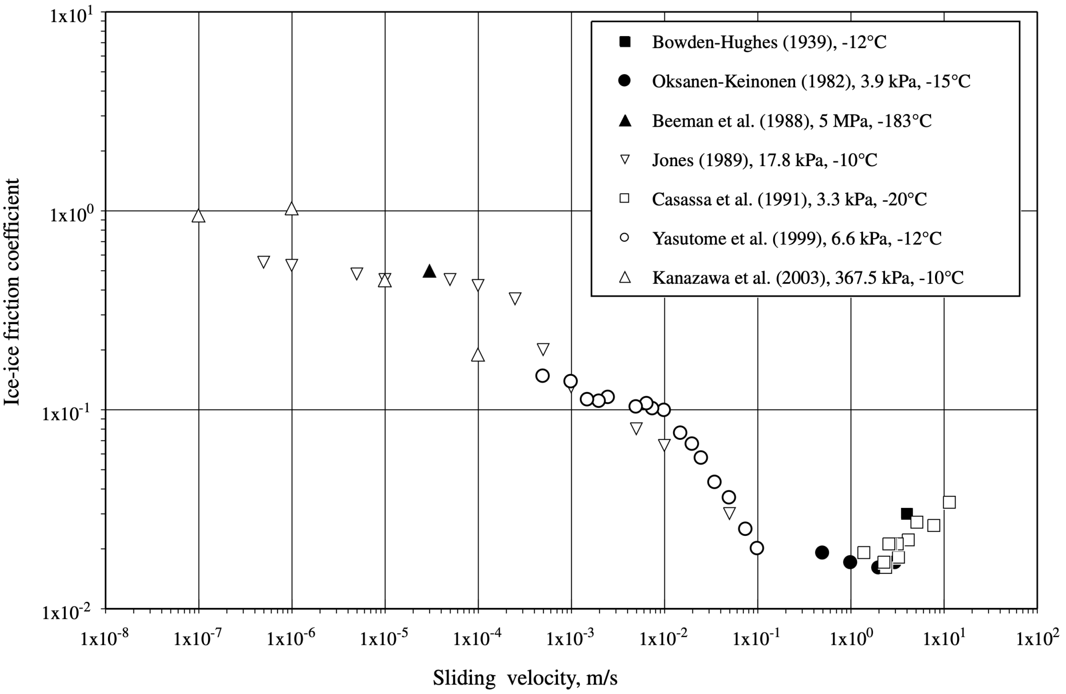

Figure 4.4: Figure 10 from Maeno et al. (2003) comprising measured friction coefficients' dependency on sliding velocity.

and Beeman et al. (1988) measuring at −183°C, cf. Figure 4.4 from Maeno et al. (2003). Consequently, the friction measurements relevant for the near-surface regions of icy moons such as Europa and Enceladus, where the temperature drops down to -223°C and -198°C, respectively, are lacking.

4.2.1 Slip rate regimes

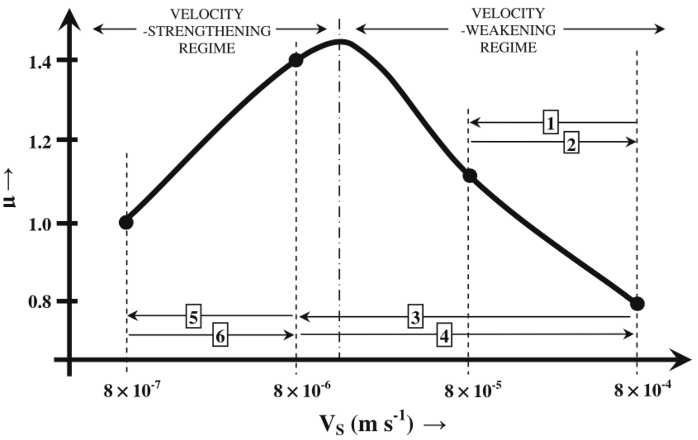

Figure 4.5: Slip rate dependence of ice friction coefficient (Figure taken from Fortt and Schulson (2009)).

The coefficient of friction primarily depends on the slip rate, but the nature of this dependence varies, with most studies distinguishing between two regimes: velocity-weakening and velocity-strengthening, see Figure 4.5. Schulson (2018) explains the shift from velocity-strengthening to velocity-weakening by the amount of meltwater present on the contact; see Figure 4.6.

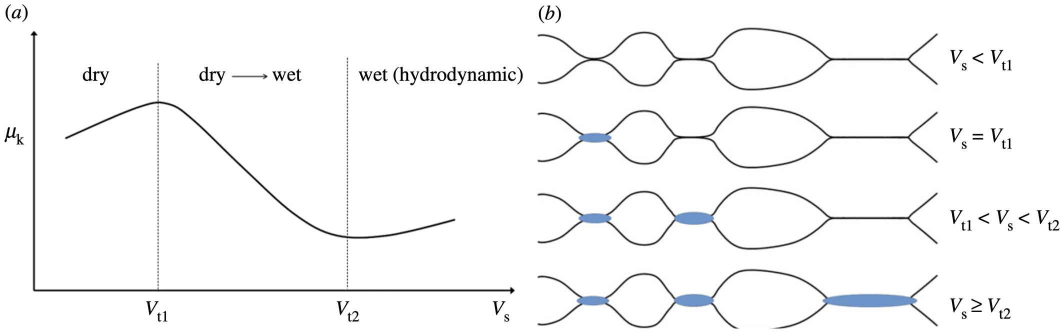

Figure 4.6: Figure taken from Schulson (2018) explaining that the coefficient of friction is driven by the development of a liquid layer on the contact surface. Thus, three regions are defined by the magnitude of slip velocity: The first boundary is at V_{t_1}, where the smallest contacts melt. The second is set by V_{t_2}, where all (even the largest) contacts melt, leaving the friction to be ruled by hydrodynamics.

As for the rock friction, see Section 4.1, the interaction between the asperities drives the frictional behavior (Schulson, 2018); however, due to lower melting temperature of ice compared to rocks, such interaction changes with velocity. For a low slip rate, one asperity passes over another one slowly enough for the frictional heating to be conducted away (no meltwater is produced); see the uppermost image on Figure 4.6 b), the friction follows velocity-strengthening regime, see left part of Figure 4.6 a). At the speed V_{t1}, the time of passage is not slow enough for sufficient conductive cooling; hence some meltwater is created, and the resistance to sliding decreases, see the middle parts of Figures 4.6 a) and b). For the velocity of V_{t2} and greater, the amount of produced meltwater is big enough to cover all the contact points. Hence hydrodynamics starts to govern the process while sliding resistance increases with velocity again; see the right part of Figure 4.6 a) and the lowermost part of Figure 4.6 b).

Fortt et al. (2003) and Schulson and Fortt (2012) agree that the transition happens at approximately $v_{\text{trans}} \sim 10^{-5} - 10^{-4} \text{m}\,\text{s}^{-1}$, while the latter study suggests that temperature dependence is also involved, see below. This statement is also supported by Oksanen and Keinonen (1982), who divide the slip-rate regions mainly based on temperature; however, their measurements involve only temperatures higher than -15°C. As a point of interest, the slip rate in the Enceladus model, see Chapter 3, reaches values up to $\sim 5 \times 10^{-5}\,\text{ms}^{-1}$.

Velocity-weakening

Oksanen and Keinonen (1982) proposed that the coefficient of friction decreases with the square root of the slip rate for ice at -15°C and that it exhibits velocity-weakening also for temperatures between -10°C up to -2°C and velocities $\lesssim 1\,\text{m}\,\text{s}^{-1}$. According to Schulson (2018), this region is probably operated by brittle-like behavior and local melting, see middle parts of Figures 4.6 a) and b), and it operates for elevated temperatures above -50°C and velocities higher than v_{trans}.

Velocity-strengthening

In the velocity-strengthening region coefficient of friction grows as the square root of slip rate according to Oksanen and Keinonen (1982) at temperatures around the melting point (0°C). It also exhibits velocity strengthening from -10°C up to -2°C for a higher slip rate ($\gtrsim 1\,\mathrm{m\,s^{-1}}$). Here, friction is driven by ductile-like behavior, dislocation creep, and fault healing. Schulson and Fortt (2012) distinguish this region for temperatures higher than -50°C and velocities lower than v_{trans} or for the lowermost temperature measured $T = -175$°C and velocities below $10^{-6}\,\mathrm{m\,s^{-1}}$ or higher than $10^{-4}\,\mathrm{m\,s^{-1}}$. At this temperature and in between these velocity values, the friction is indifferent to the slip rate (Schulson and Fortt, 2012).

4.2.2 Other dependencies

As mentioned, the temperature of the ice may determine the mode in which friction depends on the slip rate, but there might be other effects. According to Fortt and Schulson (2007), the friction coefficient grows by 20 - 40 % with temperature decreasing from values around 0°C to -40°C. Schulson (2018) later specified, that the friction coefficient grows (by 20 - 40 %) for temperature decreasing from -10°C to -40°C and decreases (by 10 - 20 %) for temperature increasing from -10°C to 0°C.

In addition, a couple of studies confirm that ice type and grain size do not affect the coefficient of friction, e.g., Schulson and Fortt (2012), while roughness and salinity have a weak effect, see Schulson (2018).

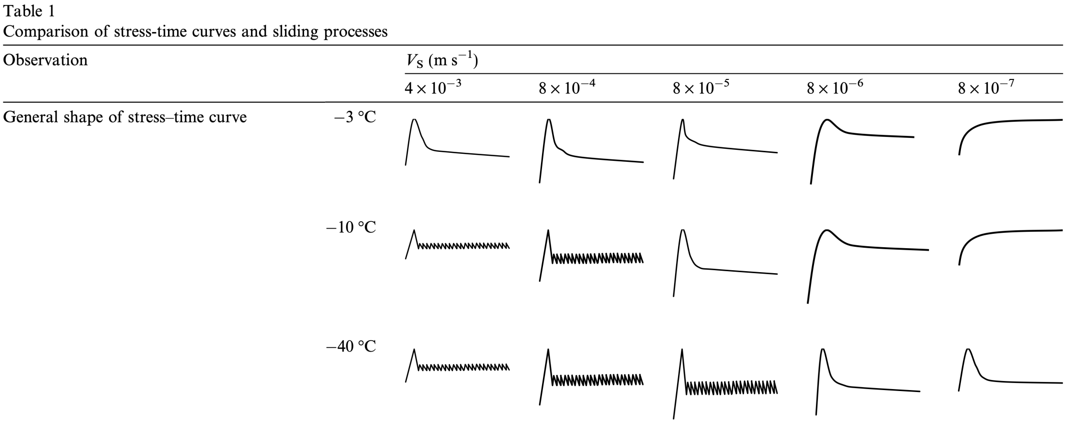

Table 1
Comparison of stress-time curves and sliding processes

Observation		V_S (m s^{-1})				
		4×10^{-3}	8×10^{-4}	8×10^{-5}	8×10^{-6}	8×10^{-7}
General shape of stress–time curve	−3 °C					
	−10 °C					
	−40 °C					

Figure 4.7: Figure taken from Fortt and Schulson (2007) showing a comparison of stress-time curves for different temperatures and velocities.

Displacement dependence

Fortt and Schulson (2007) present a behavior similar to rock-rock friction experiments when they include displacement dependence, see Figure 4.7. Except for the two top cases with slip velocity equal to $8 \times 10^{-7}\mathrm{m\,s^{-1}}$ velocity-weakening evolution of the stress-time curves is very similar to the rate and state model of Ruina (1983): a transient increase of stress is followed by a decay (mostly slower), sometimes followed by a statistical steady-state value. While for the velocity-strengthening regime (slip velocity equal to $8 \times 10^{-7}\,\mathrm{m\,s^{-1}}$ and temperature of -3°C and -10°C), the displacement dependence can be described as high transient growth followed by a slower logarithmic-type growth.

The recent observations by Fortt and Schulson (2009) reporting that ice friction exhibits memory, as well as the results of Schulson and Fortt (2012) with Fortt et al. (2003) who observe that the coefficient of friction exhibits power-law dependence for a subcritical displacement (with the threshold value of 2 mm) and then obeys Coulomb's law, seem to support the thesis of Lishman et al. (2011), that ice on ice friction can be described by the rate and state friction law.

4.2.3 Rate and state friction model for ice-ice contact

Lishman et al. (2011) presented the rate and state model for ice-ice contact similar to the simplified Dieterich model in eqs. 4.17, see Section 4.1:

$$\mu_f = \mu_f^0 + \theta + A \log\left(\frac{\mathrm{v_{slip}}}{\mathrm{v_{ref}}}\right), \tag{4.20a}$$

$$\dot{\theta} = -\frac{\mathrm{v_{slip}}}{d_c}\left(\theta + B\,\log\left(\frac{\mathrm{v_{slip}}}{\mathrm{v_{ref}}}\right)\right), \tag{4.20b}$$

where the values of constants for saline ice are $A = 0.310, B = 0.382, \mu_f^0 = 0.872$, and d_c varies with scale ($d_c = 0.2$ mm in the lab measurements - 0.1 m scale - and $d_c = 5$ mm for the ice tank measurements - 1 m scale). Since here $B > A$, the ice-ice frictional contact lies in the unstable velocity-weakening regime; see the section below. Lishman et al. (2011) measured ice response for temperature equal to -10°C and velocities from 10^{-5} to $10^{-1}\mathrm{m\,s^{-1}}$, hence, their results correspond to the findings of others, see Section 4.2.1.

The asymptotic linear stability of the rate and state friction model

In this section, we derive the conditions for the asymptotic linear stability of the rate and state friction model given by (4.20) in the setting of the spring-slider experiment in order to understand the behavior of such a system. We consider the sliding regime corresponding to equality in equation 3.28 and $\mathrm{v_{ref}}=\mathrm{v_0}$. Using $u_0 = \mathrm{v_0}t$, we obtain:

$$\mu_f \sigma_n = k_{sp}(\mathrm{v_0}t - u_{sl}), \tag{4.21}$$

To simplify the system into a system of two ordinary differential equations of the form $\frac{d\mathbf{a}}{dt} = f(\mathbf{a}, t)$, we differentiate the equation (4.21) with respect to time ($\frac{d}{dt}$) while setting $\mathrm{v_{slip}} = \frac{du_{sl}}{dt}$ and $\mathrm{v_{ref}} = \mathrm{v_0}$:

$$\frac{d\mu_f}{dt}\sigma_n = k_{sp}(\mathrm{v_0} - \mathrm{v_{slip}}). \tag{4.22}$$

We express the time derivative of the coefficient of friction from (4.20a), and further on, we denote the time derivative by dot, i.e., $\dot{a} := \frac{da}{dt}$:

$$\left(\dot{\theta} + A\frac{\mathrm{v_0}}{\mathrm{v_{slip}}}\frac{1}{\mathrm{v_0}}\dot{\mathrm{v}}_{\mathrm{slip}}\right)\sigma_n = k_{sp}(\mathrm{v_0} - \mathrm{v_{slip}}) \tag{4.23}$$

Now we substitute the time derivative of the state variable by the right side of (4.20b):

$$\left[-\frac{\mathrm{v}_{\mathrm{slip}}}{d_c}\left(\theta + B\,\log\frac{\mathrm{v}_{\mathrm{slip}}}{\mathrm{v}_0}\right) + A\frac{\dot{\overline{\mathrm{v}_{\mathrm{slip}}}}}{\mathrm{v}_{\mathrm{slip}}}\right]\sigma_n = k_{sp}(\mathrm{v}_0 - \mathrm{v}_{\mathrm{slip}}). \tag{4.24}$$

As a last step, we express the above equation in the required form, obtaining the following system:

$$\begin{aligned} \dot{\overline{\mathrm{v}_{\mathrm{slip}}}} &= f_V := \frac{k_{sp}\mathrm{v}_{\mathrm{slip}}}{A\,\sigma_n}(\mathrm{v}_0 - \mathrm{v}_{\mathrm{slip}}) + \frac{\mathrm{v}_{\mathrm{slip}}^2}{Ad_c}\left(\theta + B\log\frac{\mathrm{v}_{\mathrm{slip}}}{\mathrm{v}_0}\right), && (4.25a)\\ \dot{\theta} &= f_\theta := -\frac{\mathrm{v}_{\mathrm{slip}}}{d_c}\left(\theta + B\,\log\frac{\mathrm{v}_{\mathrm{slip}}}{\mathrm{v}_0}\right). && (4.25b) \end{aligned}$$

In order to investigate the asymptotic linear stability for a system of ordinary differential equations (ODEs) in the form (4.25), one has to investigate the eigenvalues of the matrix of first derivatives (Jacobian) of the system around the steady state. If all the eigenvalues have a negative real part, the system is asymptotically stable, while if some eigenvalue has a positive real part, the system is unstable (Lyapunov theorem, Lyapunov (1992)). Thus, we first evaluate the derivatives of the right-hand sides:

$$\begin{aligned} \frac{\partial f_V}{\partial \mathrm{v}_{\mathrm{slip}}} &= \frac{k_{sp}}{A\sigma_n}(\mathrm{v}_0 - \mathrm{v}_{\mathrm{slip}}) - \frac{k_{sp}\mathrm{v}_{\mathrm{slip}}}{A\sigma_n} + \frac{2\mathrm{v}_{\mathrm{slip}}}{Ad_c}\left(\theta + B\log\frac{\mathrm{v}_{\mathrm{slip}}}{\mathrm{v}_0}\right) + \frac{\mathrm{v}_{\mathrm{slip}}^2}{Ad_c}B\frac{1}{\mathrm{v}_{\mathrm{slip}}}\\ &= \frac{k_{sp}}{A\sigma_n}\mathrm{v}_0 - 2\frac{k_{sp}\mathrm{v}_{\mathrm{slip}}}{A\sigma_n} + \frac{2\mathrm{v}_{\mathrm{slip}}}{Ad_c}\left(\theta + B\log\frac{\mathrm{v}_{\mathrm{slip}}}{\mathrm{v}_0}\right) + \frac{B\mathrm{v}_{\mathrm{slip}}}{Ad_c}, && (4.26a)\\ \frac{\partial f_\theta}{\partial \mathrm{v}_{\mathrm{slip}}} &= -\frac{1}{d_c}\left(\theta + B\log\frac{\mathrm{v}_{\mathrm{slip}}}{\mathrm{v}_0}\right) - \frac{\mathrm{v}_{\mathrm{slip}}}{d_c}B\frac{1}{\mathrm{v}_{\mathrm{slip}}}\\ &= -\frac{1}{d_c}\left(\theta + B\log\frac{\mathrm{v}_{\mathrm{slip}}}{\mathrm{v}_0}\right) - \frac{B}{d_c}, && (4.26b)\\ \frac{\partial f_V}{\partial\theta} &= \frac{\mathrm{v}_{\mathrm{slip}}^2}{Ad_c}, && (4.26c)\\ \frac{\partial f_\theta}{\partial\theta} &= -\frac{\mathrm{v}_{\mathrm{slip}}}{d_c}. && (4.26d) \end{aligned}$$

The steady state of equations (4.25a) and (4.25b) corresponds to $\mathrm{v}_{\mathrm{slip}} = \mathrm{v}_0, \theta = -B\log\frac{\mathrm{v}_{\mathrm{slip}}}{\mathrm{v}_0} = 0$, thus the Jacobian of the system in the steady state $\nabla f|_{ss}$ is:

$$\nabla f|_{ss} = \begin{bmatrix} -\frac{k_{sp}\mathrm{v}_0}{A\sigma_n} + \frac{B\mathrm{v}_0}{Ad_c} & \frac{\mathrm{v}_0^2}{Ad_c}\\ -\frac{B}{d_c} & -\frac{\mathrm{v}_0}{d_c} \end{bmatrix}.$$

Second, we compute the eigenvalues of the steady state Jacobian:

$$\begin{aligned} \det(\nabla f|_{ss} - \lambda\mathbb{I}) &= \det\begin{bmatrix} -\frac{k_{sp}\mathrm{v}_0}{A\sigma_n} + \frac{B\mathrm{v}_0}{Ad_c} - \lambda & \frac{\mathrm{v}_0^2}{Ad_c}\\ -\frac{B}{d_c} & -\frac{\mathrm{v}_0}{d_c} - \lambda \end{bmatrix} && (4.27)\\ &= \lambda^2 + \left(\frac{\mathrm{v}_0}{d_c} - \frac{B\mathrm{v}_0}{Ad_c} + \frac{k_{sp}\mathrm{v}_0}{A\sigma_n}\right)\lambda + \frac{k_{sp}\mathrm{v}_0^2}{A\sigma_n d_c}. && (4.28) \end{aligned}$$

Finally, we find its root solution:

$$\lambda_{1,2} = \frac{-\mathrm{v}_0\left(\frac{k_{sp}}{A\sigma_n}+\frac{1}{d_c}-\frac{B}{Ad_c}\right)\pm \mathrm{v}_0\sqrt{\left(\frac{k_{sp}}{A\sigma_n}+\frac{1}{d_c}-\frac{B}{Ad_c}\right)^2-4\frac{k_{sp}}{A\sigma_n d_c}}}{2} \tag{4.29}$$

$$= -\frac{\mathrm{v}_0}{2}\left(\frac{k_{sp}}{A\sigma_n}+\frac{1}{d_c}-\frac{B}{Ad_c}\right)\left(1\pm\sqrt{1-\frac{4k_{sp}Ad_c\sigma_n}{(k_{sp}d_c+A\sigma_n-B\sigma_n)^2}}\right). \tag{4.30}$$

It holds: $\frac{4k_{sp}Ad_c\sigma_n}{(k_{sp}d_c+A\sigma_n-B\sigma_n)^2} > 0$, hence $1-\frac{4k_{sp}Ad_c\sigma_n}{(k_{sp}d_c+A\sigma_n-B\sigma_n)^2} \leq 1$, thus the square root is either real and smaller than one or purely imaginary; therefore, the last bracket always has a positive real part.

Thus, we concern ourselves only with the first part of the expression (4.30). We can derive that the real part of $\lambda_{1,2} < 0$ if and only if $\frac{\mathrm{v}_0}{2}\left(\frac{k_{sp}}{A\sigma_n}+\frac{1}{d_c}-\frac{B}{Ad_c}\right) > 0$, which corresponds to $k_{sp} > \frac{\sigma_n(B-A)}{d_c}$. Thus, we denote the critical stiffness as:

$$k_{sp}^{crit} = \frac{\sigma_n(B-A)}{d_c}. \tag{4.31}$$

The system is linearly asymptotically stable if the real part of all its eigenvalues in the steady state is negative, i.e., if $k_{sp} > k_{sp}^{crit}$ and it is unstable otherwise.

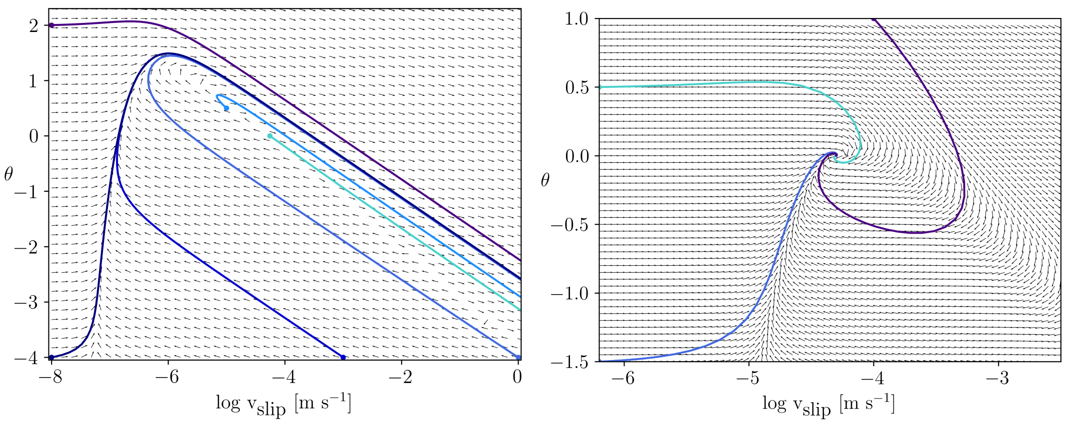

Figure 4.8: Several time evolutions (colored lines, from different initial states - corresponding colored dots) of the system describing the behavior of a rate and state model when applied to the friction in the spring slider are shown in the space of state variable and slip velocity for *(a)* a sub-critical k_{sp} leading to unstable (diverging) evolution and *(b)* a super-critical k_{sp} leading to linearly asymptotic stable evolution. Any time evolution can be traced by following the direction of the arrows.

In Figure 4.8, several trajectories for the spring slider model with the friction described via rate and state model (4.20) are plotted in the space of slip velocity and state variable, see Section 4.3.2 for information about the details of the numerical calculations. On the left, a sub-critical spring stiffness has been chosen. Each of the runs starts from different initial conditions (denoted by a colored dot); however, all diverge away from the plotted area. Whereas in Figure 4.8 b) run with a super-critical spring stiffness converges to the steady state from any chosen initial state.

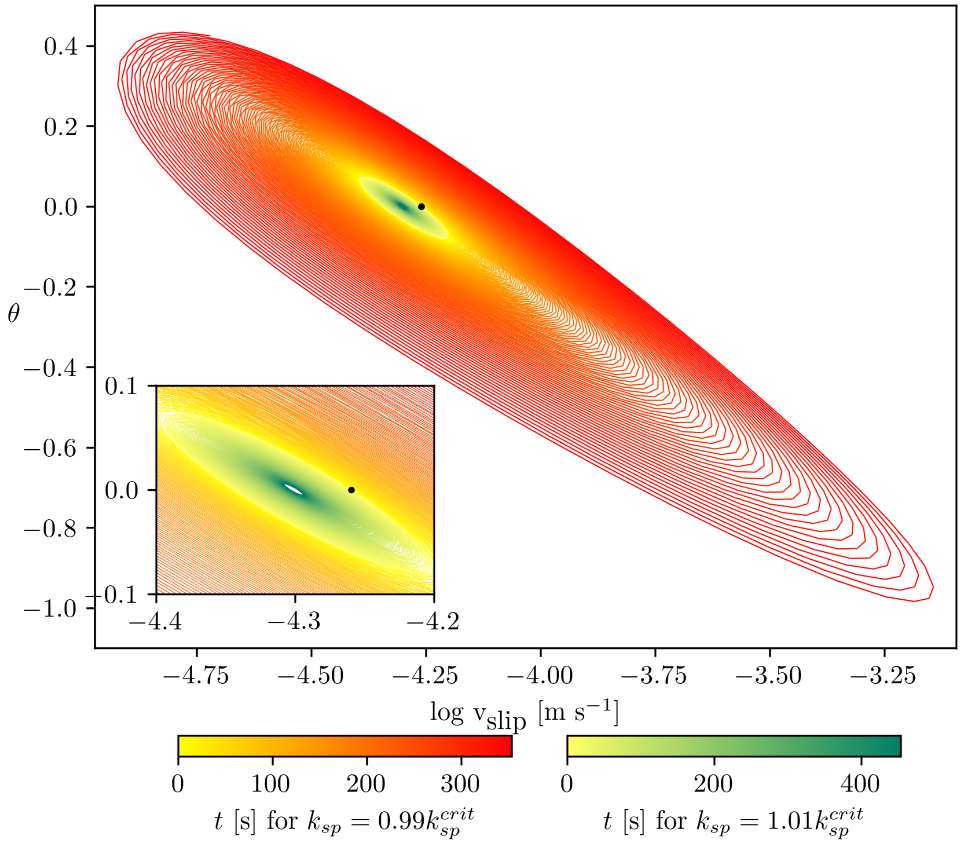

Figure 4.9: We display two possible time evolutions of the spring-slider model where the friction coefficient is described by the rate and state model. Both evolutions start from the same initial conditions (black dot): the first model has a super-critical spring stiffness $k_{sp} = 1.01k_{sp}^{crit}$ leading to the stable solution (circling towards the center of the ellipse - yellow to green color), whereas in the second case, the model with a sub-critical stiffness $k_{sp} = 0.99k_{sp}^{crit}$ diverges (spiraling out of the ellipse - yellow to orange to red color).

Even more illustrative are the results shown in Figure 4.9: two runs are started from the same initial state (black dot) with slightly different spring stiffnesses. Again, time evolutions in the space of slip velocity and state variable are shown. The sub-critical spring stiffness ($k_{sp} = 0.99k_{sp}^{crit}$) spirals away from the starting point. While the run with slightly super-critical spring stiffness ($k_{sp} = 1.01k_{sp}^{crit}$) converges.

Regularization of Lishman's rate and state friction model

As mentioned in Section 4.1.2, the rate and state friction model suffers from singularity for zero sliding velocity. Since non-sliding fault is a viable option in our model, we need to prevent the cases where the slip velocity (argument of the logarithm function in the Lishman's rate and state friction model, see equations 4.20) is zero. Therefore, we add a small positive regularizing velocity $\mathrm{v}_{\mathrm{reg}}$ to the actual slip velocity $\mathrm{v_{slip}}$ in the logarithm, obtaining:

$$\mu_f = \mu_f^0 + \theta + A \log \frac{\mathrm{v_{slip}} + \mathrm{v_{reg}}}{\mathrm{v_0}}, \tag{4.32}$$

$$\dot{\theta} = -\frac{\mathrm{v_{slip}}}{d_c}\left(\theta + B \log \frac{\mathrm{v_{slip}} + \mathrm{v_{reg}}}{\mathrm{v_0}}\right). \tag{4.33}$$

To avoid a nonphysical negative coefficient of friction, we choose $\mathrm{v_{reg}} = 0.06$ assuring for μ_f to be positive for $\theta = 0$ and $\mathrm{v_0} = 1$ and other parameters set as in Lishman et al. (2011) [1].

Further on, we use the following regularized system for the spring slider with the friction described by the rate and state model:

$$\dot{\mathrm{v}}_{\mathrm{slip}} = \frac{k_{sp}\mathrm{v_{slip}}}{A\sigma_n}(\mathrm{v_0} - \mathrm{v_{slip}}) + \frac{\mathrm{v_{slip}^2}}{AL}\left(\theta + B \log \frac{\mathrm{v_{slip}} + \mathrm{v_{reg}}}{\mathrm{v_0}}\right) \tag{4.34a}$$

$$\dot{\theta} = -\frac{\mathrm{v_{slip}}}{L}\left(\theta + B \log \frac{\mathrm{v_{slip}} + \mathrm{v_{reg}}}{\mathrm{v_0}}\right). \tag{4.34b}$$

4.3 Benchmarks

In this section, we use the benchmark settings as defined in Section 3.2 to test the variable friction coefficient for the 3D model with planar fault zone geometry, see Section 3.1.

4.3.1 Velocity-dependent friction coefficient: velocity-strengthening regime

First, we aim to incorporate the velocity dependence into the model. Since the ice-ice contact probably exhibits both velocity-strengthening and velocity-weakening behavior (Lishman et al., 2011; Fortt and Schulson, 2009), and since the velocity-weakening dependence can lead to infinite velocity in finite time (see the asymptotic stability section in 4.2.3), we were not able to benchmark such a setting, and we opted for a simple velocity-strengthening model to benchmark the velocity dependence:

$$\mu_f = \mathrm{c}\,\mathrm{v_{slip}}, \tag{4.35}$$

where $\mathrm{c} = 0.1$ and the model is loaded with $\mathrm{v_0} = 1\mathrm{m\,s^{-1}}$.

We compare three approaches in this setting - the spring slider model, the 1D Maxwell model with suitable effective viscosity, and, finally, the 2D Mawell model representative of the 3D finite-element approach that has been applied in the planetary applications discussed before. In the case of Maxwell models (1D and 2D/3D), the relationship for the coefficient of friction translates into the formula for the yield stress:

$$\sigma_Y = \sigma_Y^0 \mathrm{c}\,\mathrm{v_{slip}}, \tag{4.36}$$

where σ_Y^0 is the background yield stress equal to $\sigma_Y^0 = 5 \times 10^7\mathrm{Pa}$.

---

[1] $(0 < 0.872 + 0 + 0.31 \log(\mathrm{v_{reg}}) \Leftrightarrow -2.81 < \log(\mathrm{v_{reg}}))$

Spring slider

For the spring slider model, see Section 3.2.1, and the velocity-strengthening coefficient of friction, we are interested in the sliding regime only; thus, we take into account the equality in equation 3.29 with $\mu_f = \mathrm{c}\mathrm{v}_{\mathrm{slip}}$, and we derive obtained equation in time getting:

$$\mathrm{c}\,\dot{\overline{\mathrm{v}_{\mathrm{slip}}}}\sigma_Y = k_{sp}(\mathrm{v}_0 - \mathrm{v}_{\mathrm{slip}}). \tag{4.37}$$

From which we have:

$$\dot{\overline{\mathrm{v}_{\mathrm{slip}}}} = \frac{k_{sp}}{\mathrm{c}\,\sigma_n}(\mathrm{v}_0 - \mathrm{v}_{\mathrm{slip}}), \tag{4.38}$$

We solve equation 4.38 by a Runge-Kutta's solver written in Fortran 90 using subroutines from Numerical Recipes (Press et al., 1993). For results, see the full turquoise line in Figure 4.10.

1D Maxwell model

In the case of velocity strengthening for the 1D Maxwell model, we aim at approximating the equation 3.32 as similar as possible to the 2D/3D test case with planar fault zone geometry, see Section 3.1. Hence, we derive equation 3.32 in time with $\mathrm{v} := \dot{u}$ and $\mathrm{v}_{\mathrm{slip}} := \mathrm{v}$:

$$\eta_{\mathrm{eff}}^{\mathrm{1D}}\dot{\overline{\mathrm{v}_{\mathrm{slip}}}} = k_{sp}(\mathrm{v}_0 - \mathrm{v}_{\mathrm{slip}}). \tag{4.39}$$

We apply the Euler method:

$$\frac{\mathrm{v}_{\mathrm{slip}}^{k+1} - \mathrm{v}_{\mathrm{slip}}^{k}}{\mathrm{dt}} = \frac{k_{sp}}{\eta_{\mathrm{eff}}^{\mathrm{1D}}}(\mathrm{v}_0 - \mathrm{v}_{\mathrm{slip}}^{k+1}). \tag{4.40}$$

Furthermore, we do several fittings:

$$\mathrm{v}_{\mathrm{slip}}^{k+1}\left(1 + \frac{\mathrm{dt}\,k_{sp}}{\eta_{\mathrm{eff}}^{\mathrm{1D},k+1}}\right) = \frac{\mathrm{dt}\,k_{sp}}{\eta_{\mathrm{eff}}^{\mathrm{1D},k+1}}\mathrm{v}_0 + \mathrm{v}_{\mathrm{slip}}^{k}, \tag{4.41}$$

from which we obtain the expression for slip velocity in the next step:

$$\mathrm{v}_{\mathrm{slip}}^{k+1} = \frac{\mathrm{dt}\,k_{sp}}{\eta_{\mathrm{eff}}^{\mathrm{1D},k+1} + \mathrm{dt}\,k_{sp}}\mathrm{v}_0 + \frac{\eta_{\mathrm{eff}}^{\mathrm{1D},k+1}}{\eta_{\mathrm{eff}}^{\mathrm{1D},k+1} + \mathrm{dt}\,k_{sp}}\mathrm{v}_{\mathrm{slip}}^{k}, \tag{4.42a}$$

Since nonlinearity is present through the dependence of viscosity and yield stress on velocity, fixed point iterations are employed:

$$\eta_{\mathrm{eff}}^{\mathrm{1D},k+1} = \frac{\eta_{\mathrm{Max}}}{\left[1 + \left(\frac{\eta_{\mathrm{Max}}\mathrm{v}_{\mathrm{slip}}^{k,\eta}}{\sigma_Y^{k,\eta}}\right)^{2n}\right]^{1/(2n)}}, \tag{4.42b}$$

$$\sigma_Y^{k,\eta} = \sigma_Y^0\mathrm{c}\,\mathrm{v}_{\mathrm{slip}}^{k,\eta}, \tag{4.42c}$$

where $\mathrm{v}_{\mathrm{slip}}^{k,\eta}$ denotes the auxiliary velocity for fixed point iteration, which is updated as $\mathrm{v}_{\mathrm{slip}}^{k+1}$ every step of the iteration, together with the viscosity and the yield stress. For the results see blue dashed line on Figure 4.10.

2D Maxwell model

As in Section 3.2, the 2D model is used to substitute for the results of the complete 3D model; see Section 3.1 for model description. For the 2D Maxwell model with velocity strengthening, equations (3.23) are supplemented with:

$$\sigma_Y = \sigma_Y^0 (2\,\mathrm{c}\,h \|\mathbb{D}^\eta_{\mathrm{visc}}\|). \tag{4.43}$$

For the results, see the purple cross-hatched line in Figure 4.10.

Results

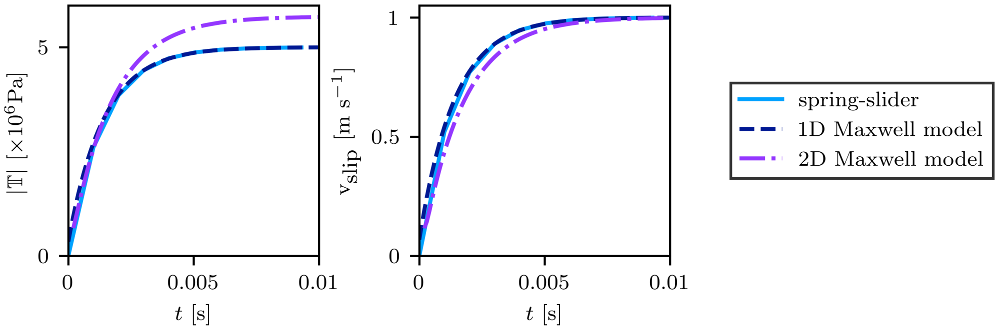

Figure 4.10: We display the time evolution of the stress magnitude/friction force (on the left) and slip velocity (on the right) for the three models with a velocity-strengthening coefficient of friction and constant velocity loading. The turquoise full line denotes the results of the spring slider model solved with Runge-Kutta's solver in a Fortran code, the blue dashed line symbolizes the 1D Maxwell model computed with a Fortran code using finite differences, the purple cross-hatched line depicts the result of 2D Maxwell model written in Fenics Project (Alnaes et al., 2015) using finite element method.

In the velocity-strengthening benchmark setting, the comparison of slip velocities for the models of spring slider, 1D and 2D Maxwell displayed on Figure 4.10 shows a nice fit, although really fine mesh was needed for the 2D model (481 per 241 elements). Another possibility to obtain precise results for the 2D model is to use a sharp interface, i.e., a step function, instead of the characteristic function. The stress from the 2D Maxwell model differs a little from the other two models; however, it has only a mild impact on the slip velocity.

4.3.2 The rate and state friction model according to Lishman et al. (2011)

Second, we benchmark the regularized form of Lishman's rate and state friction model (4.34). For the Maxwell model, the first equation transforms into a relation for the yield stress:

$$\sigma_Y = \sigma_Y^0 \left(\mu_f^0 + \theta + A \log \frac{|\mathrm{v_{slip}} + \mathrm{v_{reg}}|}{\mathrm{v_0}} \right), \tag{4.44}$$

where σ_Y^0 is the background/stick state yield stress and following values for the parameters are used: $\mu_f^0 = 0.862, A = 0.31, B = 0.382, d_c = 0.005\,\mathrm{m}, \sigma_Y^0 = 10^4\,\mathrm{Pa}, \mathrm{v_0} = 1\,\mathrm{m\,s^{-1}}$.

Spring slider

In the spring slider model with friction described by the rate and state friction, we solve equations 4.34 by accordingly adjusted Runge-Kutta's solver mentioned in the previous Section 4.3.1. For results, see the full turquoise line in Figure 4.11.

1D Maxwell model

In the 1D Maxwell model with rate and state friction, we keep the expression for velocity from the previous case, see eq. 4.42a, and we change the formulas for viscosity (4.42b) and yield stress (4.42c) to:

$$\eta_{\text{eff}}^{\text{1D},k+1} = \frac{\eta_{\text{Max}}}{\left[1+\left(\frac{\eta_{\text{Max}}(\mathrm{v}_{\text{slip}}^{k,\eta}+\mathrm{v}_{\text{reg}})}{\sigma_Y}\right)^{2n}\right]^{1/(2n)}} \tag{4.45a}$$

$$\sigma_Y^{k,\eta} = \sigma_Y^0\left(\mu_f^0+\theta^{k+1}+A\log\frac{\mathrm{v}_{\text{slip}}^{k,\eta}+\mathrm{v}_{\text{reg}}}{\mathrm{v}_0}\right). \tag{4.45b}$$

We supplement these equations with the evolution equation for state variable approximated via the Euler method:

$$\theta^{k+1} = -\frac{\mathrm{dt}\,\mathrm{v}_{\text{slip}}^{k+1}}{d_c}\left(\theta^k+B\log\frac{\mathrm{v}_{\text{slip}}^{k+1}+\mathrm{v}_{\text{reg}}}{\mathrm{v}_0}\right)+\theta_k. \tag{4.46}$$

See the blue dashed line in Figure 4.11 for results.

2D Maxwell model

As in the 1D version of the Maxwell model, the yield stress follows the rate and state formula:

$$\sigma_Y = \sigma_Y^0\left(\mu_f^0+\theta^{k+1}+A\,\log\frac{2h\|\mathbb{D}_{\text{visc}}^{\eta}\|+\mathrm{v}_{\text{reg}}}{\mathrm{v}_0}\right), \tag{4.47}$$

where we use the approximation of slip velocity through the symmetric gradient of velocities as in Section 3.1.2. The rest of the equations (3.23) remains the same, and we supplement them with the state variable's evolution. To obtain the weak formulation of equation 4.34b we multiply it by a test function θ' and integrate over the computational domain Ω:

$$\int_\Omega \dot{\theta}\,\theta'\ \mathrm{dx}+\int_\Omega\frac{\mathrm{v}_{\text{slip}}}{d_c}\left(\theta+B\ \log\frac{|\mathrm{v}_{\text{slip}}|+\mathrm{v}_{\text{reg}}}{\mathrm{v}_0}\right)\theta'\ \mathrm{dx}=0. \tag{4.48}$$

We approximate the time derivative by the Euler method:

$$\int_\Omega\frac{\theta^{k+1}-\theta^k}{\mathrm{dt}}\theta'\ \mathrm{dx}+\int_\Omega\frac{\mathrm{v}_{\text{slip}}^{k+1}}{d_c}\left(\theta+B\ \log\frac{|\mathrm{v}_{\text{slip}}^{k+1}|+\mathrm{v}_{\text{reg}}}{\mathrm{v}_0}\right)\theta'\ \mathrm{dx}=0. \tag{4.49}$$

Furthermore, the slip velocity is approximated as $\mathrm{v}_{\text{slip}} \sim 2h\|\mathbb{D}_{\text{visc}}\|$; thus, the final version for the evolution of the state variable is:

$$\int_\Omega\frac{\theta^{k+1}-\theta^k}{\mathrm{dt}}\theta'\ \mathrm{dx}+\int_\Omega\frac{2h\|\mathbb{D}_{\text{visc}}^{\eta}\|}{d_c}\left(\theta+B\ \log\frac{2h\|\mathbb{D}_{\text{visc}}\|+\mathrm{v}_{\text{reg}}}{\mathrm{v}_0}\right)\theta'\ \mathrm{dx}=0. \tag{4.50}$$

We use the discontinuous Galerkin elements of zero degree DG_0 for the state function. For the results, see the purple cross-hatched line in Figure 4.11.

Results

The rate and state friction results, see Figure 4.11 fit reasonably well: All the models provide similar evolution of the stress/friction force. The slip velocity is slightly overestimated in the Maxwell models' results; however, the difference in the steady state value corresponds to the regularization velocity $v_{reg}=0.06\,\mathrm{m\,s^{-1}}$. Thus, after the correction, all the models converge to the same slip velocity value (the loading velocity). The state variable evolution and steady-state value differ the most among all the models; nevertheless, since the stress and the limit of slip velocity correspond well and since we use the state variable only to compute the slip velocity, this difference is not a critical one.

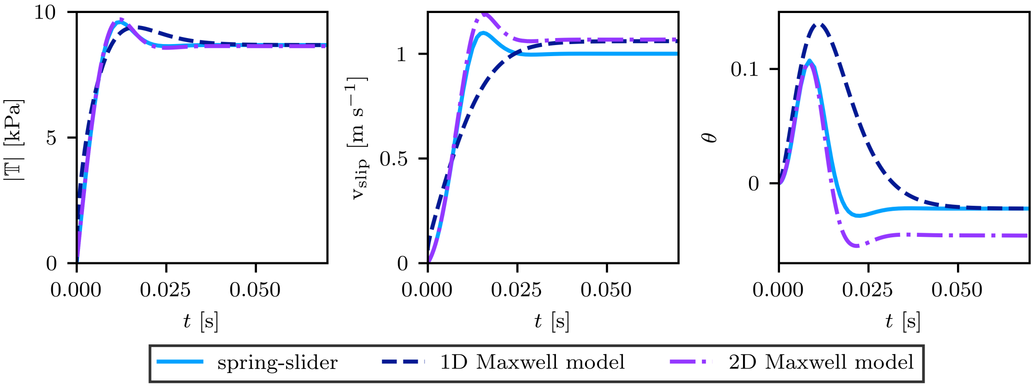

Figure 4.11: From left: time evolution of the friction force/stress, the slip velocity, and the state variable for the three models with a rate and state friction coefficient and constant velocity loading. The turquoise full line denotes the results of spring slider model solved with Runge-Kutta's solver in a Fortran code, the blue dashed line symbolizes the one-dimensional Maxwell model computed with a Fortran code using finite differences, the purple cross-hatched line depicts the result of two-dimensional Maxwell model written in Fenics Project (Alnaes et al., 2015) using finite element method.

This benchmark demonstrated that the inclusion of the rate and state friction model in a 3D model of the Enceladus's ice shell is a viable option; however, a complete reformulation of the tidal deformation model in terms of velocity instead of displacement would be necessary.

Conclusion

This thesis, titled "Tidally induced deformation of icy moons," aims to enhance existing models of the tidal response of icy moons. In particular, our focus is directed towards Europa and Enceladus, two moons currently believed to harbor global liquid water oceans maintained by dissipative processes driven by tidal forces. Both these moons emanate vapor plumes, whose properties and composition might lead to information about their internal dynamics and conditions. Consequently, Europa and Enceladus are subjects of significant geophysical and astrobiological interest. The general idea behind this Ph.D. project was to focus primarily on incorporating the description of friction into existing models of these moons, such as Kalousová et al. (2016) and Souček et al. (2019).

As a first step, we have concentrated on strike-slip faults on Europa. The dissipative effects of the strike-slip motion driven by tidal forces might produce near-surface meltwater on these faults. By integrating and enhancing the studies conducted by Nimmo and Gaidos (2002) and Kalousová et al. (2016), we have successfully developed a model that simulates the reactivation of a planar fault in the ice shell of Europa. The model involves the thermal and mechanical evolution of its two-phase surroundings (ice, water). Furthermore, it enables the calculation of the associated dissipative heating, encompassing both the frictional heating occurring along the fault and the viscous dissipation in the surrounding bulk. Even though we have conducted a thorough parametric study comprising diverse boundary conditions, forcing scenarios, and varying rheological assumptions, our findings indicate that meltwater generation at strike-slip faults is relatively limited. Specifically, our simulations demonstrate that only a small amount of meltwater, $\lesssim 4\%$ porosity localized at the fault plane, can be generated under these conditions. As a consequence, our simulations seem to discredit the strike-slip fault heating scenario as a viable mechanism for producing a substantial near-surface water source on Europa. As to the reasoning, several lines of evidence come together: The primary heating source (frictional heating) is a surface one (creating water only at the fault); moreover, the additional heating source (viscous dissipation) is relatively feeble since most of the deformation is elastic. Also, the slip velocity drops to zero with depth in a continuous manner; hence, there is no shear singularity below the fault as in Nimmo and Gaidos (2002). Several more reasons further contribute: The simulated depth of the fault is smaller than in Nimmo and Gaidos (2002), decreasing the total frictional power. The phase change consumes part of the dissipated heat since we calculate the two-phase evolution of the fault's surroundings. Finally, the produced porosity gives negative feedback on the two heating sources by lowering the ice viscosity and frictional coefficient. Our findings might prove relevant in the context of the recently launched JUwICE mission's search for subsurface water reservoirs.

In the second step, we have developed a numerical model to validate or disprove the mechanism of "tidal walking" - a theoretical concept for producing observable lateral offset on strike-slip faults of Europa. The model is based on the numerical tool described above with the following specific adjustments: We have simplified the material model to a one-phase setting while adding normal and shear loading of the fault's neighborhood, mimicking the tides. Unlike previous purely mechanical studies (Preblich et al., 2007), we have also investigated the role of thermal effects. In particular, we identified thermo-mechanical coupling as a possible key mechanism that may trigger the development of a visible offset. Notably, dissipative heating promoted the creation of a low-viscosity zone near the fault, which appears to be critical for producing an observable lateral offset. Our simulations indicate that apart from this thermally triggered case, it seems unlikely to produce a visible offset under current europan conditions. In particular, without a low viscosity zone, the penetration of the whole ice shell would be required. Although this seems unlikely with the present-day amplitude of tidal forcing and with the current estimates of the shell thickness, it may have been possible in Europa's geological past. Additionally, we have studied the thermal signature on the surface for reactivated faults, and we observed that moderate surface heat flux anomalies could be obtained even for cases where the accumulated offset is negligible. Therefore, surface temperature measurements by future missions could represent one possible way to distinguish between active and inactive faults.

In the third step, our focus shifted to Enceladus, where the measured activity of the jets in the south-polar region remains unexplained by existing models. Despite the precise localization of the source of these jets, known as tiger stripes, and the strong indication of a link to tidal forces due to observed temporal variations in activity, a comprehensive explanation has yet to be found. We have enhanced the recent numerical model by Souček et al. (2019) by incorporating friction on the tiger stripes; up to now, the physical description of the tiger stripes has been limited to the model of frictionless water-filled cracks. By adopting friction mimicked through a specific stress-dependent viscosity in the fault zones, we hoped to explain the activity timing better. While this specific goal was not achieved, our results suggested an intriguing connection between the plume's brightness' and tangential displacement's maxima. Our enhanced model uncovers that due to the friction on the faults, the symmetry in the mechanical response with respect to the closing and opening phases of the tidal period may be disrupted. In our model, this leads to a specific redistribution of the stress in the south polar region of Enceladus with possible geomorphological consequences. In addition, we have shown that the overall mechanical response of Enceladus's shell strongly depends on the choice of the effective friction coefficient, making this parameter accessible to future missions' measurements.

In the final chapter, we have provided an outlook toward models with more realistic frictional laws. In particular, experimental studies indicate that ice-ice friction strongly depends on the slip rate, exhibiting both velocity-weakening and velocity-strengthening, depending on local conditions and, very likely, on temperature. Lishman et al. (2011) even suggested that ice-ice friction can behave according to the so-called rate and state friction model presented originally to describe friction experiments with rocks. In this case, the friction coefficient depends on the slip rate but also shows a memory of the contact zone's history by including state variable(s). Even though no measurements of ice-ice friction at icy moons' surface temperatures are available, we have attempted to test the concept and to implement the rate and state model into a test case presented in the third chapter. We have successfully benchmarked the results against two 1D models, providing a proof-of-concept for including the rate and state frictional model in the future 3D models of Enceladus' ice shell.

Lastly, we note that although our results and models focused explicitly on Europa and Enceladus, the developed methodology holds potential for application to other intriguing ocean worlds. Celestial bodies such as Ganymede or Triton, and potentially many others, share similar scientific interests. The insights gained from our research can serve as a foundation for investigating and understanding the geological processes and phenomena within these bodies, expanding our knowledge and opening paths for further exploration and discoveries.

Bibliography

M. S. Alnaes, J. Blechta, J. Hake, A. Johansson, B. Kehlet, A. Logg, C. Richardson, J. Ring, M. E. Rognes, and G. N. Wells. The FEniCS Project Version 1.5. *Archive of Numerical Software*, 3(100):9–23, 2015. doi: 10.11588/ans.2015.100.20553.

E. M. Anderson. The dynamics of faulting. *Transactions of the Edinburgh Geological Society*, 8(3):387–402, 1905. doi: 10.1144/transed.8.3.387.

J. D. Anderson, E. L. Lau, W. L. Sjogren, G. Schubert, and W. B. Moore. Europa's Differentiated Internal Structure: Inferences from Two Galileo Encounters. *Science*, 276(5316):1236–1239, 1997. doi: 10.1126/science.276.5316.1236.

L.-E. Andersson, J. Barber, and Y. Ahn. Attractors in frictional systems subjected to periodic loads. *SIAM Journal on Applied Mathematics*, 73:1097–1116, 2013. doi: 10.2307/23479966.

G. Angelis, G. G. Kordopati, E. Zingkou, A. Karioti, G. Sotiropoulou, and G. Pampalakis. Plausible emergence of biochemistry in Enceladus based on chemobrionics. *Chemistry – A European Journal*, 27:600–604, 2021. doi: 10.1002/chem.202004018.

C. E. Bader and S. A. Kattenhorn. Formation Mechanisms of Europan Ridges with Apparent Lateral Offsets. In *39th Annual Lunar and Planetary Science Conference*, Lunar and Planetary Science Conference, page 2036, 2008.

R.-M. Baland, M. Yseboodt, and T. Van Hoolst. The obliquity of Enceladus. *Icarus*, 268:12–31, 2016. doi: 10.1016/j.icarus.2015.11.039.

J. R. Barber. Nominally static frictional contacts under periodic loading. *The Journal of Strain Analysis for Engineering Design*, 51:270–278, 2016. doi: 10.1177/0309324715602844.

A. C. Barr, A. P. Showman, and R. Dotson. *Heat Transfer in Europa's Icy Shell*, pages 405–430. University of Arizona Press, 2009. ISBN 9780816528448.

M. Beeman, W. B. Durham, and S. H. Kirby. Friction of ice. *Journal of Geophysical Research: Solid Earth*, 93(B7):7625–7633, 1988. doi: 10.1029/JB093iB07p07625.

M. Beuthe. Enceladus's crust as a non-uniform thin shell: I tidal deformations. *Icarus*, 302:145 – 174, 2018. doi: 10.1016/j.icarus.2017.11.009.

M. Beuthe. Enceladus's crust as a non-uniform thin shell: II tidal dissipation. *Icarus*, 332:66 – 91, 2019. doi: 10.1016/j.icarus.2019.05.035.

E. B. Bierhaus, K. Zahnle, C. R. Chapman, and R. Dotson. *Europa's Crater Distributions and Surface Ages*, pages 161–180. University of Arizona Press, 2009. ISBN 9780816528448.

S. E. Billings and S. A. Kattenhorn. Comparison between terrestrial explosion crater morphology in floating ice and Europan chaos. *Lunar and Planetary Science XXXIV*, 1955:15–16, 2003.

S. E. Billings and S. A. Kattenhorn. The great thickness debate: Ice shell thickness models for Europa and comparisons with estimates based on flexure at ridges. *Icarus*, 177(2):397–412, 2005. doi: 10.1016/j.icarus.2005.03.013.

B. G. Bills, F. Nimmo, Ö. Karatekin, T. Van Hoolst, N. Rambaux, B. Levrard, J. Laskar, and R. Dotson. *Rotational Dynamics of Europa*, pages 119–134. University of Arizona Press, 2009. ISBN 9780816528448.

M. T. Bland and W. B. McKinnon. Forming Europa's folds: Strain requirements for the production of large-amplitude deformation. *Icarus*, 221(2):694–709, 2012. doi: 10.1016/j.icarus.2012.08.029.

F. P. Bowden and D. Tabor. *The Friction and Lubrication of Solids. Part 2*. Oxford University Press, oct 1964. ISBN 9780198507772.

B. Buratti and J. Veverka. Voyager photometry of europa. *Icarus*, 55(1):93–110, 1983. doi: 10.1016/0019-1035(83)90053-2.

M. Běhounková, G. Tobie, O. Čadek, G. Choblet, C. Porco, and F. Nimmo. Timing of water plume eruptions on Enceladus explained by interior viscosity structure. *Nature Geoscience*, 8:601–604, 2015. doi: 10.1038/ngeo2475.

M. Běhounková, O. Souček, J. Hron, and O. Čadek. Plume activity and tidal deformation on Enceladus influenced by faults and variable ice shell thickness. *Astrobiology*, 17:941–954, 2017. doi: 10.1089/ast.2016.1629.

O. Čadek, O. Souček, M. Běhounková, G. Choblet, G. Tobie, and J. Hron. Long-term stability of Enceladus' uneven ice shell. *Icarus*, 319:476–484, 2019. ISSN 10902643. doi: 10.1016/j.icarus.2018.10.003.

R. W. Carlson, R. E. Johnson, and M. S. Anderson. Sulfuric acid on Europa and the radiolytic sulfur cycle. *Science*, 286(5437):97–99, 1999. ISSN 00368075. doi: 10.1126/science.286.5437.97.

R. W. Carlson, W. M. Calvin, J. B. Dalton, G. B. Hansen, R. L. Hudson, R. E. Johnson, T. B. McCord, and M. H. Moore. *Europa's Surface Composition*, pages 283–328. University of Arizona Press, 2009. ISBN 97808165284. doi: 10.2307/j.ctt1xp3wdw.18.

M. H. Carr, M. J. S. Belton, C. R. Chapman, M. E. Davies, P. Geissler, R. Greenberg, A. S. McEwen, B. R. Tufts, R. Greeley, R. Sullivan, J. W. Head, R. T. Pappalardo, K. P. Klaasen, T. V. Johnson, J. Kaufman, D. Senske, J. Moore, G. Neukum, G. Schubert, J. A. Burns, P. Thomas, and J. Veverka. Evidence for a subsurface ocean on Europa. *Nature*, 391:363–365, 1998. doi: 10.1038/34857.

E. M. A. Chen and F. Nimmo. Obliquity tides do not significantly heat Enceladus. *Icarus*, 214(2):779–781, 2011. doi: 10.1016/j.icarus.2011.06.007.

G. Choblet, G. Tobie, C. Sotin, M. Běhounková, O. Čadek, F. Postberg, and O. Souček. Powering prolonged hydrothermal activity inside Enceladus. *Nature Astronomy*, 2017. doi: 10.1038/s41550-017-0289-8.

COMSOL Multiphysics. Introduction to COMSOL multiphysics®. *COMSOL Multiphysics, Burlington, MA*, 9:2018, 1998.

Z. A. Crawford, M. E. Mullen, and R. T. Pappalardo. SatStress: A Web-Accessible Model of Viscoelastic Tidal Stresses in Icy Satellites. In *Lunar and Planetary Science Conference*, Lunar and Planetary Science Conference, page 2326, Mar 2007.

E. N. Crow-Willard and R. T. Pappalardo. Structural mapping of Enceladus and implications for formation of tectonized regions. *Journal of Geophysical Research E: Planets*, 120(5):928–950, 2015. doi: 10.1002/2015JE004818.

S. De La Chapelle, H. Milsch, O. Castelnau, and P. Duval. Compressive creep of ice containing a liquid intergranular phase: Rate-controlling processes in the dislocation creep regime. *Geophysical Research Letters*, 26(2):251–254, 1999. doi: 10.1029/1998GL900289.

J. H. Dieterich. Time-dependent friction and the mechanics of stick-slip. *Pure and Applied Geophysics*, 116(4-5):790–806, 1978. doi: 10.1007/BF00876539.

J. H. Dieterich. Modeling of rock friction: 1. Experimental results and constitutive equations. *Journal of Geophysical Research: Solid Earth*, 84(B5):2161–2168, 1979. doi: 10.1029/JB084iB05p02161.

J. H. Dieterich and B. D. Kilgore. Direct observation of frictional contacts: New insights for state-dependent properties. *Pure and Applied Geophysics*, 143(1-3): 283–302, 1994. doi: 10.1007/BF00874332.

A. J. Dombard. Planetary science - cracks under stress. *Nature*, 447:276–7, 2007. doi: 10.1038/447276a.

A. J. Dombard and W. B. McKinnon. Folding of Europa's icy lithosphere: an analysis of viscous-plastic buckling and subsequent topographic relaxation. *Journal of Structural Geology*, 28(12):2259–2269, 2006. ISSN 01918141. doi: 10.1016/j.jsg.2005.12.003.

A. J. Dombard, G. W. Patterson, A. P. Lederer, and L. M. Prockter. Flanking fractures and the formation of double ridges on Europa. *Icarus*, 223(1):74–81, 2013. doi: 10.1016/j.icarus.2012.11.021.

M. K. Dougherty, B. J. Buratti, P. K. Seidelmann, J. R. Spencer, and Renée Dotson. *Enceladus as an Active World: History and Discovery*, pages 3–16. University of Arizona Press, 2018. ISBN 9780816537075.

A. L. Fortt and E. M. Schulson. The resistance to sliding along Coulombic shear faults in ice. *Acta Materialia*, 55(7):2253–2264, 2007. doi: 10.1016/j.actamat.2006.11.022.

A. L. Fortt and E. M. Schulson. Velocity-dependent friction on Coulombic shear faults in ice. *Acta Materialia*, 57(15):4382–4390, 2009. doi: 10.1016/j.actamat.2009.06.001.

A. L. Fortt, E. M. Schulson, and E. Russell. Sliding along Coulombic shear faults in ice. *Canadian Journal of Physics*, 81(1-2):519–527, 2003. doi: 10.1139/p02-146.

D. L. Goldsby and D. L. Kohlstedt. Superplastic deformation of ice: Experimental observations. *Journal of Geophysical Research: Solid Earth*, 106(B6):11017–11030, 2001. doi: 10.1029/2000JB900336.

D. B. Goldstein, M. Hedman, M. Manga, M. Perry, J. Spitale, and B. Teolis. *Enceladus Plume Dynamics: From Surface to Space*, pages 175–194. University of Arizona Press, 2018. ISBN 9780816537075.

R. Greenberg, P. Geissler, G. V. Hoppa, B. R. Tufts, D. D. Durda, R. Pappalardo, J. W. Head, R. Greeley, R. Sullivan, and M. H. Carr. Tectonic Processes on Europa: Tidal Stresses, Mechanical Response, and Visible Features. *Icarus*, 135(1):64–78, 1998. doi: 10.1006/icar.1998.5986.

R. Greenberg, G. V. Hoppa, B. R. Tufts, P. Geissler, J. Riley, and S. Kadel. Chaos on Europa. *Icarus*, 141(2):263–286, 1999. doi: 10.1006/icar.1999.6187.

P. K. Haff, A. Eviatar, and G. L. Siscoe. Ring and plasma: The enigmae of Enceladus. *Icarus*, 56(3):426–438, 1983. doi: 10.1016/0019-1035(83)90164-1.

M. M. Hedman, C. M. Gosmeyer, P. D. Nicholson, C. Sotin, R. H. Brown, R. N. Clark, K. H. Baines, B. J. Buratti, and M. R. Showalter. An observed correlation between plume activity and tidal stresses on Enceladus. *Nature*, 500 (7461):182–184, 2013. doi: 10.1038/nature12371.

D. J. Hemingway, L. Iess, R. Tajeddine, and G. Tobie. *The Interior of Enceladus*, pages 57–78. University of Arizona Press, 2018. ISBN 9780816537075.

R. Herrendörfer, T. Gerya, and Y. van Dinther. An invariant rate- and state-dependent friction formulation for viscoelastoplastic earthquake cycle simulations. *Journal of Geophysical Research: Solid Earth*, 123:5018–5051, 2018. doi: 10.1029/2017JB015225.

W. Herschel. I. Account of the discovery of a sixth and seventh satellite of the planet Saturn; with remarks on the construction of its ring, its atmosphere, its rotation on an axis, and its spheroidical figure. *Philosophical Transactions of the Royal Society of London*, 80:1–20, 1790. doi: 10.1098/rstl.1790.0001.

C. A. Hobbs and P. V. Hobbs. *Ice Physics*. Clarendon Press, 1974. ISBN 9780198519362.

G. V. Hoppa, B. R. Tufts, R. Greenberg, and P. Geissler. Strike-slip faults on Europa: Global shear patterns driven by tidal stress. *Icarus*, 141(2):287–298, 1999a. ISSN 00191035. doi: 10.1006/icar.1999.6185.

G. V. Hoppa, B. R. Tufts, R. Greenberg, and P. E. Geissler. Formation of cycloidal features on Europa. *Science*, 285(5435):1899–1902, 1999b. doi: 10.1126/science.285.5435.1899.

G. V. Hoppa, R. Greenberg, B. R. Tufts, P. Geissler, C. Phillips, and M. Milazzo. Distribution of strike-slip faults on Europa. *Journal of Geophysical Research: Planets*, 105(E9):22617–22627, 2000. doi: 10.1029/1999JE001156.

S. M. Howell and R. T. Pappalardo. Band Formation and Ocean-Surface Interaction on Europa and Ganymede. *Geophysical Research Letters*, 45(10): 4701–4709, 2018. doi: 10.1029/2018GL077594.

C. J. A. Howett, J. R. Spencer, J. Pearl, and M. Segura. High heat flow from Enceladus' south polar region measured using 10-600 cm^{-1} Cassini/CIRS data. *Journal of Geophysical Research E: Planets*, 116(3):1–15, 2011. doi: 10.1029/2010JE003718.

H.-W. Hsu, F. Postberg, Y. Sekine, T. Shibuya, S. Kempf, M. Horányi, A. Juhász, N. Altobelli, K. Suzuki, Y. Masaki, T. Kuwatani, S. Tachibana, S. Sirono, G. Moragas-Klostermeyer, and R. Srama. Ongoing hydrothermal activities within Enceladus. *Nature*, 519(7542):207–10, 2015. doi: 10.1038/nature14262.

T. A. Hurford, P. Helfenstein, G. V. Hoppa, R. Greenberg, and B. G. Bills. Eruptions arising from tidally controlled periodic openings of rifts on Enceladus. *Nature*, 447(7142):292–294, 2007. doi: 10.1038/nature05821.

T. A. Hurford, B. Bills, P. Helfenstein, R. Greenberg, G.V. Hoppa, and D.P. Hamilton. Geological implications of a physical libration on Enceladus. *Icarus*, 203:541–552, 2009. doi: 10.1016/j.icarus.2009.04.025.

T. A. Hurford, P. Helfenstein, and J. N. Spitale. Tidal control of jet eruptions on Enceladus as observed by Cassini ISS between 2005 and 2007. *Icarus*, 220: 896–903, 2012. doi: 10.1016/j.icarus.2012.06.022.

H. Hussmann and T. Spohn. Thermal-orbital evolution of Io and Europa. *Icarus*, 171(2):391–410, 2004. doi: 10.1016/j.icarus.2004.05.020.

L. Iess, D. J. Stevenson, M. Parisi, D. Hemingway, R. A. Jacobson, J. I. Lunine, F. Nimmo, J. W. Armstrong, S. W. Asmar, M. Ducci, and P. Tortora. The Gravity Field and Interior Structure of Enceladus. *Science*, 344:78 – 80, 2014. doi: 10.1126/science.1225053.

A. P. Ingersoll, S. P. Ewald, and S. K. Trumbo. Time variability of the Enceladus plumes: Orbital periods, decadal periods, and aperiodic change. *Icarus*, 344: 113345, 2020. doi: 10.1016/j.icarus.2019.06.006.

X. Jia, M. G. Kivelson, K. K. Khurana, and W. S. Kurth. Evidence of a plume on Europa from Galileo magnetic and plasma wave signatures. *Nature Astronomy*, 2(6):459–464, 2018. doi: 10.1038/s41550-018-0450-z.

J. Joly. The phenomena of skating and Professor J. Tomson's thermodynamic relation. *Nature*, 59(1534):485–486, 1899. doi: 10.1038/059485b0.

K. Kalousová, O. Souček, G. Tobie, G. Choblet, and O. Čadek. Water generation and transport below Europa's strike-slip faults. *Journal of Geophysical Research: Planets*, 121(12):2444–2462, 2016. doi: 10.1002/2016JE005188.

K. Kalousová, O. Souček, G. Tobie, G. Choblet, and O. Čadek. Ice melting and downward transport of meltwater by two-phase flow in Europa's ice shell. *Journal of Geophysical Research: Planets*, 119(3):532–549, 2014. doi: 10.1002/2013JE004563.

S. A. Kattenhorn. Strike-slip fault evolution on Europa: Evidence from tailcrack geometries. *Icarus*, 172(2):582–602, 2004. doi: 10.1016/j.icarus.2004.07.005.

S. A. Kattenhorn and K. M. Prockter. Evidence for subduction in the ice shell of Europa. *Nature Geoscience*, 7(10):762–767, 2014. doi: 10.1038/ngeo2245.

S. A. Kattenhorn, T. Hurford, and R. Dotson. *Tectonics of Europa*, pages 199–236. University of Arizona Press, 2009. ISBN 9780816528448.

J. P. Kay and S. A. Kattenhorn. An Open-Source GUI for Calculating Icy Moon Tidal Stresses Using SatStress. In *Lunar and Planetary Science Conference*, Lunar and Planetary Science Conference, page 2046, 2010.

S. Kempf, U. Beckmann, and J. Schmidt. How the Enceladus dust plume feeds Saturn's E ring. *Icarus*, 206(2):446–457, 2010. doi: 10.1016/j.icarus.2009.09.016.

F. E. Kennedy, E. M. Schulson, and D. E. Jones. The friction of ice on ice at low sliding velocities. *Philosophical Magazine A: Physics of Condensed Matter, Structure, Defects and Mechanical Properties*, 80(5):1093–1110, 2000. doi: 10.1080/01418610008212103.

K. K. Khurana, M. G. Kivelson, D. J. Stevenson, G. Schubert, C. T. Russell, R. J. Walker, and C. Polanskey. Induced magnetic fields as evidence for subsurface oceans in Europa and Callisto. *Nature*, 424, 1998. doi: 10.1038/nature01828.

M. J. Kinczyk, G. W. Patterson, R. P. Perkins, G. C. Collins, M. Borrelli, T. L. Becker, M. T. Bland, and R. T. Pappalardo. Evaluation of Impact Crater Distributions for Geological Terrains on Enceladus. In *48th Annual Lunar and Planetary Science Conference*, Lunar and Planetary Science Conference, page 2926, 2017.

E. S. Kite and A. M. Rubin. Sustained eruptions on Enceladus explained by turbulent dissipation in tiger stripes. *Proceedings of the National Academy of Sciences*, 113(15):201520507, 2016. doi: 10.1073/pnas.1520507113.

M. G. Kivelson, K. K. Khurana, C. T. Russell, M. Volwerk, R. J. Walker, and C. Zimmer. Galileo Magnetometer Measurements: A Stronger Case for a Subsurface Ocean at Europa. *Science*, 289:1340–1343, 2000.

K. Kleer, A. McEwen, R. Park, C. Bierson, A. Davies, D. DellaGustina, A. Ermakov, J. Fuller, C. Hamilton, C. Harris, H. Hay, R. Jacobson, J. T. Keane, L. Kestay, K. Khurana, K. Kirby, V. Lainey, I. Matsuyama, C. McCarthy,

F. Nimmo, M. Panning, A. Pommier, J. Rathbun, G. Steinbrügge, D. Stevenson, V. Tsai, E. Turtle, J. Eiler, E. Young, K. Zahnle, J. Adkins, K. Mandt, M. McGrath, A. Moullet, J. Waite, and N. Schneider. Tidal Heating: Lessons from Io and the Jovian System. *Final Report for the Keck Institute for Space Studies*, 06 2019.

V. Lainey, J.-E. Arlot, Ö. Karatekin, and T. Van Hoolst. Strong tidal dissipation in Io and Jupiter from astrometric observations. *Nature*, 459(7249):957–959, Jun 2009. doi: 10.1038/nature08108.

S. Lee, R. T. Pappalardo, and N. C. Makris. Mechanics of tidally driven fractures in Europa's ice shell. *Icarus*, 177(2):367–379, 2005. doi: 10.1016/j.icarus.2005.07.003. Europa Icy Shell.

B. Lishman, P. Sammonds, and D. Feltham. A rate and state friction law for saline ice. *Journal of Geophysical Research: Oceans*, 116(5):1–13, 2011. doi: 10.1029/2010JC006334.

A. Logg, K.-A. Mardal, and G. N. Wells. *Automated Solution of Differential Equations by the Finite Element Method*, volume 84. Springer Berlin Heidelberg, 2012. ISBN 978-3-642-23098-1. doi: 10.1007/978-3-642-23099-8.

A. M. Lyapunov. The general problem of the stability of motion. *International Journal of Control*, 55(3):531–534, 1992. doi: 10.1080/00207179208934253.

N. Maeno and M. Arakawa. Adhesion shear theory of ice friction at low sliding velocities, combined with ice sintering. *Journal of Applied Physics*, 95(1):134–139, 2004. doi: 10.1063/1.1633654.

N. Maeno, M. Arakawa, A. Yasutome, N. Mizukami, and S. Kanazawa. Ice-ice friction measurements, and water lubrication and adhesion-shear mechanisms. *Canadian Journal of Physics*, 81(1-2):241–249, 2003. doi: 10.1139/p03-023.

A. G. Marusiak, S. Vance, M. P. Panning, M. Běhounková, P. K. Byrne, G. Choblet, M. Melwani Daswani, K. Hughson, B. Journaux, A. H. Lobo, B. E. Schmidt, K. Pleiner Sládková, K. M. Soderlund, W. Song, O. Souček, G. Steinbrügge, A. F. Thompson, and S. Wang. Exploration of icy ocean worlds using geophysical approaches. *The Planetary Science Journal*, 2(4):150, 2021. doi: 10.3847/PSJ/ac1272.

T. B. McCord, G. B. Hansen, F. P. Fanale, R. W. Carlson, D. L. Matson, T. V. Johnson, W. D. Smythe, J. K. Crowley, P. D. Martin, A. Ocampo, C. A. Hibbitts, J. C. Granahan, and NIMS Team. Salts on Europa's Surface Detected by Galileo's Near Infrared Mapping Spectrometer. *Science*, 280(5367):1242–1245, 1998. doi: 10.1126/science.280.5367.124.

M. T. Mellon, D. J. Zanko, and S. M. Hörst. Thermal conductivity of water-ice regolith and application to the outer solar system. *Lunar Planet. Sci. IL, 2083 (abstract)*, 2018. doi: 10.1186/1471-2369-14-81.

H. J. Melosh and E. P. Turtle. Ridges on Europa: Origin by Incremental Ice-Wedging. In *Lunar and Planetary Science Conference*, Lunar and Planetary Science Conference, page 2029, 2004.

M. Montagnat and E. M. Schulson. On friction and surface cracking during sliding of ice on ice. *Journal of Glaciology*, 49(166):391–396, 2003. doi: 10.3189/172756503781830647.

F. Nimmo and E. Gaidos. Strike-slip motion and double ridge formation on Europa. *Journal of Geophysical Research*, 107(E4):1–8, 2002. doi: 10.1029/2000JE001476.

F. Nimmo and B. Giese. Thermal and topographic tests of Europa chaos formation models from Galileo E15 observations. *Icarus*, 177(2):327 – 340, 2005. doi: 10.1016/j.icarus.2004.10.034. Europa Icy Shell.

F. Nimmo and P. M. Schenk. Normal faulting on Europa: implications for ice shell properties. *Journal of Structural Geology*, 28(12):2194–2203, 2006. doi: 10.1016/j.jsg.2005.08.009.

F. Nimmo, R. T. Pappalardo, and B. Giese. On the origins of band topography, Europa. *Icarus*, 166(1):21 – 32, 2003. doi: 10.1016/j.icarus.2003.08.002.

F. Nimmo, M. Manga, and R. Dotson. *Geodynamics of Europa's Icy Shell*, pages 381–404. University of Arizona Press, 2009. ISBN 9780816528448.

F. Nimmo, C. Porco, and C. Mitchell. Tidally modulated eruptions on Enceladus: Cassini ISS observations and models. *The Astronomical Journal*, 148(3):46, 2014. doi: 10.1088/0004-6256/148/3/46.

P. Oksanen and J. Keinonen. The mechanism of friction of ice. *Wear*, 78(3):315–324, 1982. doi: 10.1016/0043-1648(82)90242-3.

K. D. Pang, C. C. Voge, J. W. Rhoads, and J. M. Ajello. The E ring of Saturn and satellite Enceladus. *Journal of Geophysical Research: Solid Earth*, 89(B11):9459–9470, 1984. doi: 10.1029/JB089iB11p09459.

R. Pappalardo. Seeking Europa's Ocean. *Proceedings of the International Astronomical Union*, 6:101 – 114, 01 2010. doi: 10.1017/S1743921310007325.

R. T. Pappalardo, J. W. Head, R. Greeley, R. J. Sullivan, C. Pilcher, G. Schubert, W. B. Moore, M. H. Carr, J. M. Moore, M. J. S. Belton, and D. L. Goldsby. Geological evidence for solid-state convection in Europa's ice shell. *Nature*, 391 (6665):365–368, 1998. doi: 10.1038/34862.

R. T. Pappalardo, M. J. S. Belton, H. H. Breneman, M. H. Carr, C. R. Chapman, G. C. Collins, T. Denk, S. Fagents, P. E. Geissler, B. Giese, R. Greeley, R. Greenberg, J. W. Head, P. Helfenstein, G. Hoppa, S. D. Kadel, K. P. Klaasen, J. E. Klemaszewski, K. Magee, A. S. McEwen, J. M. Moore, W. B. Moore, G. Neukum, C. B. Phillips, L. M. Prockter, G. Schubert, D. A. Senske, R. J. Sullivan, B. R. Tufts, E. P. Turtle, R. Wagner, and K. K. Williams. Does Europa have a subsurface ocean? Evaluation of the geological evidence. *Journal of Geophysical Research: Planets*, 104(E10):24015–24055, 1999. doi: 10.1029/1998JE000628.

G. W. Patterson, S. A. Kattenhorn, P. Helfenstein, G. C. Collins, R. T. Pappalardo, and R. Dotson. *The Geology of Enceladus*, pages 95–126. University of Arizona Press, 2018. ISBN 9780816537075.

D. A. Patthoff and S. A. Kattenhorn. A fracture history on Enceladus provides evidence for a global ocean. *Geophysical Research Letters*, 38(18), 2011. doi: 10.1029/2011GL048387.

D. A. Patthoff, S. A. Kattenhorn, and C. M. Cooper. Implications of nonsynchronous rotation on the deformational history and ice shell properties in the south polar terrain of Enceladus. *Icarus*, 321:445 – 457, 2019. doi: 10.1016/j.icarus.2018.11.028.

K. Pleiner Sládková, O. Souček, and M. Běhounková. Enceladus' tiger stripes as frictional faults: Effect on stress and heat production. *Geophysical Research Letters*, 48(19), 2021. doi: 10.1029/2021GL094849.

C. Porco, P. Helfenstein, P. C. Thomas, A. P. Ingersoll, J. Wisdom, R. West, G. Neukum, T. Denk, R. Wagner, T. Roatsch, S. Kieffer, E. Turtle, A. McEwen, T. V. Johnson, J. Rathbun, J. Veverka, D. Wilson, J. Perry, J. Spitale, A. Brahic, J. A. Burns, A. D. DelGenio, L. Dones, C. D. Murray, and S. Squyres. Cassini Observes the Active South Pole of Enceladus. *Science*, 311(5766):1393–1401, 2006. doi: 10.1126/science.1123013.

C. Porco, D. DiNino, and F. Nimmo. How the Geysers, Tidal Stresses, and Thermal Emission Across the South Polar Terrain of Enceladus Are Related. *The Astronomical Journal*, 148(3):45, 2014. doi: 10.1088/0004-6256/148/3/45.

F. Postberg, S. Kempf, J.K. Hillier, R. Srama, S.F. Green, N. McBride, and E. Grün. The E-ring in the vicinity of Enceladus: II. Probing the moon's interior—The composition of E-ring particles. *Icarus*, 193(2):438–454, 2008. doi: 10.1016/j.icarus.2007.09.001.

B. Preblich, R. Greenberg, J. Riley, and D. O'Brien. Tidally driven strike-slip displacement on Europa: Viscoelastic modeling. *Planetary and Space Science*, 55(10):1225–1245, 2007. doi: 10.1016/j.pss.2007.01.018.

W. H. Press, S. A. Teukolsky, W. T. Vetterling, and B. P. Flannery. *Numerical Recipes in FORTRAN; The Art of Scientific Computing.* Cambridge University Press, USA, 2nd edition, 1993. ISBN 0521437164.

A. R. Rhoden, B. Militzer, E. M. Huff, T. A. Hurford, M. Manga, and M. A. Richards. Constraints on Europa's rotational dynamics from modeling of tidally-driven fractures. *Icarus*, 210(2):770 – 784, 2010. doi: 10.1016/j.icarus.2010.07.018.

A. R. Rhoden, G. Wurman, E. M. Huff, M. Manga, and T. A. Hurford. Shell tectonics: A mechanical model for strike-slip displacement on Europa. *Icarus*, 218(1):297–307, 2012. doi: 10.1016/j.icarus.2011.12.015.

A. R. Rhoden, T. A. Hurford, J. Spitale, W. Henning, E. M. Huff, M. T. Bland, and S. Sajous. The formation of Enceladus' Tiger Stripe Fractures from eccentricity tides. *Earth and Planetary Science Letters*, 544:116389, 2020. doi: 10.1016/j.epsl.2020.116389.

L. Roth, J. Saur, K. D. Retherford, D. F. Strobel, P. D. Feldman, M. A. McGrath, and F. Nimmo. Transient water vapor at Europa's south pole. *Science*, 343: 171–174, 2014. doi: 10.1126/science.1247051.

A. Ruina. *Friction laws and instabilities: A quasistatic analysis of some dry frictional behavior.* PhD thesis, Brown University, Providence, 1980.

A. Ruina. Slip instability and state variable friction laws. *Journal of Geophysical Research: Solid Earth*, 88(B12):10359–10370, 1983. doi: 10.1029/JB088iB12p10359.

A. R. Sarid, R. Greenberg, G. V. Hoppa, T. A. Hurford, B. R. Tufts, and P. Geissler. Polar Wander and Surface Convergence of Europa's Ice Shell: Evidence from a Survey of Strike-Slip Displacement. *Icarus*, 158(1):24 – 41, 2002. doi: 10.1006/icar.2002.6873.

B. E. Schmidt, D. D. Blankenship, G. W. Patterson, and P. M. Schenk. Active formation of 'chaos terrain' over shallow subsurface water on Europa. *Nature*, 479(7374):502–505, 2011. doi: 10.1038/nature10608.

A. M. Schoenfeld, E. K. Hawkins, K. M. Soderlund, S. D. Vance, E. Leonard, and A. Yin. Particle entrainment and rotating convection in Enceladus' ocean. *Communications Earth & Environment*, 4(1):28, 2023. doi: 10.1038/s43247-023-00674-z.

E. M. Schulson. Friction of sea ice. *Philosophical Transactions of the Royal Society A: Mathematical, Physical and Engineering Sciences*, 376(2129), 2018. doi: 10.1098/rsta.2017.0336.

E. M. Schulson and A. L. Fortt. Friction of ice on ice. *Cold Regions Science and Technology*, 117, 2012. doi: 10.1029/2012JB009219.

M. R. Showalter, J. N. Cuzzi, and S. M. Larson. Structure and particle properties of saturn's e ring. *Icarus*, 94(2):451–473, 1991. doi: 10.1016/0019-1035(91)90241-K.

A. P. Showman and L. Han. Effects of plasticity on convection in an ice shell: Implications for Europa. *Icarus*, 177:425–437, 2005. doi: 10.1016/j.icarus.2005.02.020.

K. Sládková, O. Souček, K. Kalousová, and M. Běhounková. Tidal walking on Europa's strike slip faults - insight from numerical modeling. *Journal of Geophysical Research: Planets*, 125, 2020. doi: 10.1029/2019je006327.

B. A. Smith, L. A. Soderblom, R. Beebe, J. Boyce, G. Briggs, M. Carr, S. A. Collins, A. F. Cook, G. E. Danielson, M. E. Davies, G. E. Hunt, A. Ingersoll, T. V. Johnson, H. Masursky, J. McCauley, D. Morrison, T. Owen, C. Sagan,

E. M. Shoemaker, R. Strom, V. E. Suomi, and J. Veverka. The Galilean Satellites and Jupiter: Voyager 2 Imaging Science Results. *Science*, 206(4421): 927–950, 1979a. doi: 10.1126/science.206.4421.927.

B. A. Smith, L. A. Soderblom, T. V. Johnson, A. P. Ingersoll, S. A. Collins, E. M. Shoemaker, G. E. Hunt, H. Masursky, M. H. Carr, M. E. Davies, A. F. Cook, J. Boyce, G. E. Danielson, T. Owen, C. Sagan, R. F. Beebe, J. Veverka, R. G. Strom, J. F. McCauley, D. Morrison, G. A. Briggs, and V. E. Suomi. The Jupiter System Through the Eyes of Voyager 1. *Science*, 204(4396):951–972, 1979b. doi: 10.1126/science.204.4396.951.

B. A. Smith, K. A. Soderblom, R. M. Batson, P. Bridges, J. L. Inge, H. Masursky, E. M. Shoemaker, R. Beebe, J. M. Boyce, G. A. Briggs, A. Bunker, S. A. Collins, C. J. Hansen, T. V. Johnson, J. L. Mitchell, R. Terrile, A. F. Cook, J. C. Cuzzi, J. B. Pollack, G. E. Danielson, A. P. Ingersoll, N. E. Davies, G. E. Hunt, D. R. Morrison, T. R. E. Owen, C. E. Sagan, J. F. Veverka, R. Strom, and V. E. Suomi. A New Look at the Saturn System: The Voyager 2 Images. *Science*, 215:504 – 537, 1982.

B. Smith-Konter and R. T. Pappalardo. Tidally driven stress accumulation and shear failure of Enceladus's tiger stripes. *Icarus*, 2008. doi: 10.1016/j.icarus.2008.07.005.

C. Sotin, G. Tobie, J. Wahr, W. B. McKinnon, and R. Dotson. *Tides and Tidal Heating on Europa*, pages 85–118. University of Arizona Press, 2009. ISBN 9780816528448.

O. Souček, J. Hron, M. Běhounková, and O. Čadek. Effect of the tiger stripes on the deformation of Saturn's moon Enceladus. *Geophysical Research Letters*, 43 (14):7417–7423, 2016. doi: 10.1002/2016GL069415.

O. Souček, M. Běhounková, O. Čadek, J. Hron, G. Tobie, and G. Choblet. Tidal dissipation in Enceladus' uneven, fractured ice shell. *Icarus*, 328:218 – 231, 2019. doi: 10.1016/j.icarus.2019.02.012.

W. B. Sparks, K. P. Hand, M. A. McGrath, E. Bergeron, M. Cracraft, and S. E. Deustua. Probing for Evidence of Plumes on Europa with HST/STIS. *The Astrophysical Journal*, 829(2):121, 2016.

W. B. Sparks, B. E. Schmidt, M. A. McGrath, K. P. Hand, J. R. Spencer, M. Cracraft, and S. E. Deustua. Active Cryovolcanism on Europa? *The Astrophysical Journal*, 839(2):L18, 2017. doi: 10.3847/2041-8213/aa67f8.

N. A. Spaun, J. W. Head, G. C. Collins, L. M. Prockter, and R. T. Pappalardo. Conamara Chaos Region, Europa: Reconstruction of mobile polygonal ice blocks. *Geophysical Research Letters*, 25(23):4277–4280, 1998. doi: 10.1029/1998GL900176.

J. R. Spencer, F. Nimmo, A. P. Ingersoll, T. A. Hurford, E. S. Kite, A. R. Rhoden, J. Schmidt, and C. J. A. Howett. *Plume Origins and Plumbing: From Ocean to Surface*, pages 163–174. University of Arizona Press, 2018. ISBN 9780816537075.

R. Tajeddine, K. M. Soderlund, P. C. Thomas, P. Helfenstein, M. M. Hedman, J. A. Burns, and P. M. Schenk. True polar wander of Enceladus from topographic data. *Icarus*, 295:46–60, 2017. doi: 10.1016/j.icarus.2017.04.019.

K. Terzaghi. *Erdbaumechanik auf Bodenphysikalischer Grundlage.* Franz Deuticke, Liepzig-Vienna, 1925.

P. C. Thomas, R. Tajeddine, M. S. Tiscareno, J. A. Burns, J. Joseph, T. J. Loredo, P. Helfenstein, and C. Porco. Enceladus's measured physical libration requires a global subsurface ocean. *Icarus*, 264:37–47, 2016. doi: 10.1016/j.icarus.2015.08.037.

G. Tobie. Tidally heated convection: Constraints on Europa's ice shell thickness. *Journal of Geophysical Research*, 108(E11):5124, 2003. doi: 10.1029/2003JE002099.

N. Tosi, C. Stein, L. Noack, C. Hüttig, P. Maierová, H. Samuel, D. R. Davies, C. R. Wilson, S. C. Kramer, C. Thieulot, A. Glerum, M. Fraters, W. Spakman, A. Rozel, and P. J. Tackley. A community benchmark for viscoplastic thermal convection in a 2-D square box. *Geochemistry, Geophysics, Geosystems*, 16: 2175–2196, 2015. doi: 10.1002/2015GC005807.

R. Trompert and U. Hansen. Mantle convection simulations with rheologies that generate plate-like behaviour. *Nature*, 395:686–689, 1998. doi: 10.1038/27185.

B. R. Tufts, R. Greenberg, G. Hoppa, and P. Geissler. Astypalaea linea: A large-scale strike-slip fault on europa. *Icarus*, 141(1):53–64, 1999. doi: 10.1006/icar.1999.6168.

B. R. Tufts, R. Greenberg, G. Hoppa, and P. Geissler. Lithospheric Dilation on Europa. *Icarus*, 146(1):75–97, 2000. doi: 10.1006/icar.2000.6369.

S. Vance, M. Běhounková, B. G. Bills, P. Byrne, O. Čadek, J. Castillo-Rogez, G. Choblet, K. Hughson, T. Hurford, S. Kedar, K. Keane, E. Kite, A. H. Lobo, A. G. Marusiak, M. Melwani Daswani, M. P. Panning, R. S. Park, B. E. Schmidt, K. Sládková, K. M. Soderlund, C. Sotin, O. Souček, S. Stähler, G. Steinbrügge, S. Tharimena, A. Thompson, G. Tobie, W. Song, and S. Wang. Distributed geophysical exploration of Enceladus and other ocean worlds. *Bulletin of the AAS*, 53, 2021. doi: 10.3847/25c2cfeb.a07234f4.

J. Vetter. Evaluating displacements along Europan ridges. Master's thesis, Universit of Idaho, 2005.

J. Wahr, Z. A. Selvans, M. E. Mullen, A. C. Barr, G. C. Collins, M. M. Selvans, and R. T. Pappalardo. Modeling stresses on satellites due to nonsynchronous rotation and orbital eccentricity using gravitational potential theory. *Icarus*, 200(1):188–206, 2009. doi: 10.1016/j.icarus.2008.11.002.

J. H. Waite, C. R. Glein, R. S. Perryman, B. D. Teolis, B. A. Magee, G. Miller, J. Grimes, M. E. Perry, K. E. Miller, A. Bouquet, J. I. Lunine, T. Brockwell, and S. J. Bolton. Cassini finds molecular hydrogen in the Enceladus plume: Evidence for hydrothermal processes. *Science*, 356:155–159, 2017. doi: 10.1126/science.aai8703.

A. Yin and R. T. Pappalardo. Gravitational spreading, bookshelf faulting, and tectonic evolution of the South Polar Terrain of Saturn's moon Enceladus. *Icarus*, 260:409–439, 2015. doi: 10.1016/j.icarus.2015.07.017.

List of Symbols

$\dot{} = \frac{d}{dt}$	time derivative
$\lvert \bullet \rvert$	magnitude
$\lVert \bullet \rVert_2$	second invariant of a tensor
$\overline{\bullet}$	average
$(\bullet)^-$	minimum from $\bullet$ and zero
$\mathbf{O}$	zero vector
a	the distance between the centers of the two bodies
a	constant in the simple shear velocity
A	constant parameter in friction models
$\mathcal{A}$	real area of contact
a'	aspect ratio
A_i	prefactor in viscosity formula (2.24b)
b	constant in the simple shear velocity
B	constant parameter in friction models
B_1, B_2	constant parameters in friction models
B_N	parameter in equation 2.42
c	the specific heat of ice
c	constant
C	material constant denoting the dependence of steady state stress on slip velocity
$\mathcal{C}$	material constant for computing the real area of contact
c_1, c_2, c_3	parameters in coefficient of friction formula
d	depth (of the Cartesian domain)
D	ice shell thickness
$\mathcal{D}$	spherical distance to a curve approximating the fault
$\mathbb{D}$	symmetric part of the velocity gradient
d_0	depth, where the fault stops being stress free in the tangential direction
d_a	activation depth
d_c	critical displacement
d_c^1, d_c^2	critical displacements in the “Two state variable friction law”
d_f	the average slip displacement on a fault length L_s
d_g	grain size
d_s	oriented distance function
$d_{\max}$	analytical estimate of activation depth
$d_{\max}(t)$	the maximum activation depth at a given time
d_{rego}	depth of the regolith layer
D_0	depth of the unwatered part of the fault zone
D_w	depth of water in the fault zone
$\mathbb{D}^d$	deviatoric part of $\mathbb{D}$
$\mathbb{D}_{\mathrm{elast}}$	elastic part of $\mathbb{D}$
$\mathbb{D}_{\mathrm{visc}}$	viscous part of $\mathbb{D}$
$\mathbb{D}^{\mathrm{d}}_{\mathrm{visc}}$	deviatoric part of the viscous strain rate tensor
dt	time step
e	eccentricity

$\mathbf{e}_x$	unit vector in the direction of axis x
E, E_i	activation energy
$\mathbf{f}$	body force
F	strength per unit area of contact
$\mathcal{F}$	function describing the friction stress dependence on other variables
f_1, f_2	parameters in coefficient of friction formula
f_V, f_θ	right hand sides of the rate and state spring slider model ODE
$\lvert F_t^F(t)\rvert/D$	absolute value of the average tangential stress at the fault
$\lvert F_t^R(t)/D\rvert$	absolute value of the average tangential stress at the right boundary
$\nabla f\rvert_{ss}$	gradient of the rate and state spring slider system in the steady state
g	magnitude of gravity acceleration
$\mathbf{g}$	gravity acceleration
G	universal gravitational constant
$\mathcal{G}$	function describing the state's rate of change
h	height of the narrow fault zone
$\mathbb{I}$	identity matrix
k	parameter in ODE toy problem
$^{k}, ^{k+1}$	current and previous time step
K	total number of time steps
K	bulk modulus
$\mathcal{K}$	coefficient in the numerical approximation of stress tensor/vector
k_1, k_2	constant parameters in eq. 2.27
k_{sp}	spring stiffness
k_{sp}^{crit}	critical stiffness
k_{rego}	thermal conductivity of the regolith
$k(T)$	temperature-dependent thermal conductivity
^{l}	current time step in the convection model
^{lt}	time step when the tidal model was run for the last time
L	characteristic length
$\boldsymbol{\mathcal{L}}$	coefficient in the numerical approximation of stress tensor/vector
l_i	exponent in viscosity formula (2.24b)
L_h	latent heat of melting of ice
L_s	length of the slipped zone
m	mass of the parent body
m_i	exponent in viscosity formula (2.24b)
n	parameter in the formula for β_{eff} and η_{eff}
$\mathbf{n}$	outer normal vector
$\tilde{\boldsymbol{n}}$	approximation of the unit normal to the idealized fault surface
n_i	exponent in viscosity formula (2.24b)
$\boldsymbol{n}_b$	outer normal to the ice-ocean boundary
$\boldsymbol{n}_{\mathrm{s}}$	outer normal to the surface
p	excess water pressure with respect to the hydrostatic equilibrium pressure of pure ice
p	pressure in tidal model
P	orbital period
p_0	constant parameter for fixating pressure
p^w	water pore pressure
$\overline{p^{\text{eff}}}$	effective pressure

P_2	degree-2 Legendre polynomial
P_2^0, P_2^2	associated Legendre functions
q	heat flux
Δq	heat flux anomaly
Q	heating
Q_{fric}	frictional heating
Q_{shear}	shear heating
r	melt production rate (positive for melting)
r	radius
R	universal gas constant
$\mathcal{R}$	radius of the satellite
$\boldsymbol{r}_{\mathrm{b}}$	position vector for ice/water interface
$\boldsymbol{r}_{\mathrm{s}}$	position vector for surface
$\mathbf{s}$	stress vector
$\mathbb{S}$	deviatoric part of Cauchy stress tensor
t	time
T	temperature
$\mathbb{T}$	Cauchy stress tensor
ΔT	$= T - T_{\mathrm{m}}$ - temperature difference from the melting temperature
t_0	average contact time
t_c	time of contact
t_s	time of the start of the sliding
$\mathbb{T}^{1\mathrm{D}}$	Cauchy stress tensor in 1D formulation
T_e	external (insolation) temperature
T_{m}	melting temperature
T_{s}	surface temperature
$\mathbb{T}_\eta$	stress on the dashpot
$\mathbb{T}_{sp}$	stress on the spring
$\mathbb{T}^{\mathrm{static}}$	static part of Cauchy stress
$\mathbb{T}^{\mathrm{tot}}$	total Cauchy stress
$\mathbb{T}^{\mathrm{tot}}_{nn}$	$\tilde{\boldsymbol{n}} \cdot \mathbb{T}^{\mathrm{tot}} \tilde{\boldsymbol{n}}$
u	displacement of the dashpot
$\mathbf{u}$	(tidal) displacement
u_0	forcing displacement in the spring-slider and Maxwell model
Δu_{n}	jump in the displacement component normal to the fault
u_r	radial displacement
u_{sl}	displacement of the slider
$\mathrm{u}_{\mathrm{slip}}$	total slip
u_{slip}	the magnitude of the jump in the displacement component parallel to the fault
u_{sp}	displacement of the spring
v	velocity in the model of Nimmo and Gaidos (2002)
v	1D velocity in mechanical analogues
$\boldsymbol{v}$	ice matrix velocity
$\mathbf{v}$	tidal velocity
$\mathbf{v}'$	test function for the tidal velocity
v^+, v^-	loading velocities for the fault zone
v_0	forcing velocity in the spring slider and Maxwell model

$\mathrm{v}_{\mathrm{load}}$	loading velocity
$\mathrm{v}_{\mathrm{load}}^{0}$	loading velocity amplitude
$\mathrm{v}_{\mathrm{ref}}$	reference value of slip velocity
$\mathrm{v}_{\mathrm{reg}}$	regularizing slip velocity
$\mathrm{v}_{\mathrm{slip}}$	slip velocity
v_{slip}	magnitude of the jump across the fault in the velocity component parallel to the fault
v_{trans}	velocity at which velocity-strenghtening regime changes to velocity-weakening regime for ice-ice friction
v^{sp}	velocity of the spring
$\overline{\lvert\mathrm{v}_{\mathrm{slip}}\rvert}$	slip velocity averaged over one period
Δv_{n}	jump in the velocity component normal to the fault
V_{t1}, V_{t2}	velocities at which velocity-strenghtening regime changes to velocity-weakening regime and back for ice-ice friction
V_{tidal}	tidal potential
w	width of the Cartesian domain
x	horizontal coordinate, distance from the fault
$\mathbf{x}$	unit vector in direction of axis x
y	horizontal coordinate
y_f	y coordinate of the center of the fault zone
Y_{20}, Y_{22}	spherical harmonics functions
z	vertical coordinate
α	ice thermal expansivity
β	parameter in ODE toy problem
β^*	parameter in the formula for β_{eff}
β_1, β_2	parameters in ODE toy problem
β_{eff}	effective sliding coefficient
γ	viscosity reduction parameter
γ_f	yield stress reduction coefficient
γ_s	stabilization parameter in the case of fully activated fault
$\Gamma_{\mathrm{O}}, \Gamma_{\mathrm{R}}, \Gamma_{\mathrm{S}}, \Gamma_{\mathrm{F}}$	bottom, right, top, left boundary
δ	displacement; mutual offset
Δ	the half-width of χ/fault zone
δ_0	average displacement
δ_s	accumulated surface offset
$\tilde{\delta}_s$	normalized surface offset per period
ϵ	numerical zero
ϵ^k	2% of maximal slip velocity over the previous time steps
ϵ_{Φ}	smoothening parameter for porosity
ϵ_{rad}	emissivity of Europa
η	viscosity
${}_{\eta},{}^{\eta}$	auxiliary variables defined for the fixed point iterations
η_i	viscosity of particular mechanism
η_{eff}	effective viscosity
η_{cut}	viscosity cut-off
η_{Max}	background viscosity in the Maxwell rheology
η_{pure}	unreduced viscosity
$\eta_{\mathrm{eff}}^{\mathrm{1D}}$	effective viscosity in the 1D Maxwell model

θ	state variable
ϑ	colatitude
Θ	collection of state variables
θ_i	state variables
θ_i^{ss}	steady state of the state variable
μ	shear modulus
μ_f	coefficient of friction
μ_f^0	static coefficient of friction
μ_f^{w}	lubricated coefficient of friction
$\Delta\mu_f$	change in μ_f
$\Delta\mu_f^{k,ss}$	change in the steady state coefficient of friction
ν	geometric constant
$\triangle\varrho$	$= \varrho_i - \varrho_w$ - density difference between the phases
ϱ_i	ice density
ϱ_w	water density
σ_0	loading stresses amplitude
σ_n	normal stress
σ_t	tangential stress
σ_Y	yield stress
$\widetilde{\sigma_Y}$	yield stress with the normal part of the diurnal tides included
σ_Y^0	background yield stress
$\sigma_{0,n}$	amplitudes of normal stresses induced on diurnal time scale
$\sigma_{0,t}$	amplitudes of tangential stresses induced on diurnal time scale
σ_n^{BG}	normal stresses induced on longer time scales
σ_t^{BG}	tangential stresses induced on longer time scales
σ_{nn}	normal component of the traction vector acting on the fault surface
σ_{rad}	Stefan-Boltzman constant
τ	shear stress
$\scriptstyle\tau$	tangential component of a vector
τ_0	internal cohesion along the sliding surface
τ_f	frictional force
τ_M	Maxwell time
τ_p	pulling force
τ_{ss}	steady state friction stress
$\Delta\tau$	decrease of friction strength
φ	phase shift
ϕ	longitude
Φ	porosity
Φ_s	regularized porosity
$\Delta\Phi_s$	difference in current time step porosity and the porosity from the time when the tidal model was run for the last time
χ	characteristic function / smoothened indicator function
χ_ϵ	thickness of the transient zone
Ψ	angle from the axis connecting the centers of the two bodies at an arbitrary point on the satellite's surface
ω	orbital frequency
Ω	computational domain
$\partial\Omega$	boundary of the computational domain

List of publications

1. Tidal walking on Europa's strike slip faults - insight from numerical modeling (Sládková et al., 2020)
2. Enceladus' tigers stripes as frictional faults: Effect on stress and heat production (Pleiner Sládková et al., 2021)
3. Exploration of Icy Ocean Worlds Using Geophysical Approaches (Marusiak et al., 2021)
4. Distributed Geophysical Exploration of Enceladus and Other Ocean Worlds (Vance et al., 2021)